DYNAMIC ANALYSIS OF FIBERGLASS-REINFORCED PLASTIC PIPES WITH THICKNESS DISCONTINUITY USING WAVELET-BASED FINITE ELEMENT

BY

WASIU ADEYEMI OKE

A Dissertation Presented to the
DEANSHIP OF GRADUATE STUDIES

KING FAHD UNIVERSITY OF PETROLEUM & MINERALS
DHAHRAN, SAUDI ARABIA

In Partial Fulfillment of the
Requirements for the Degree of

DOCTOR OF PHILOSOPHY
In

MECHANICAL ENGINEERING

MAY, 2016

KING FAHD UNIVERSITY OF PETROLEUM & MINERALS

DHAHRAN 31261, SAUDI ARABIA

DEANSHIP OF GRADUATE STUDIES

This dissertation, written by WASIU ADEYEMI OKE under the direction of his dissertation advisor and approved by his dissertation committee, has been presented to and accepted by the Dean of Graduate Studies, in partial fulfillment of the requirements for the degree of **DOCTOR OF PHILOSOPHY IN MECHANICAL ENGINEERING**.

Dr. Yehia A. Khulief
(Advisor)

Dr. Zuhair M. Gasem
Department Chairman

Dr. Mohamed A. El-Gebeily
(Member)

Dr. Salam A. Zummo
Dean of Graduate Studies

Dr. Abul Fazal M. Arif
(Member)

29/9/16

Date

Dr. Yagoub N. Al-Nassar
(Member)

Dr. Mehmet V. Sunar
(Member)

DEDICATION

This Dissertation work is dedicated to God Almighty the Lord of the world, to my parents, Mr. and Mrs. Koleoso Oke, my sisters and brothers and to my lovely wife and kids.

ACKNOWLEDGMENT

First and foremost, my gratitude goes to KFUPM administration for giving me the opportunity to finish my PhD program at KFUPM. I also acknowledge the support provided by King Abdulaziz City for Science & Technology (KACST) through the Science and Technology Unit at KFUPM for funding this work through project No. 12-ADV3005-04 as part of the National Science, Technology and Innovation Plan. Besides, I am extremely grateful to my advisor Prof. Yehia A. Khulief for his unquantifiable support, guidance and encouragement throughout my stay at KFUPM and the period of my research work. I also thank him for his patience, motivation, enthusiasm, insightful comments and mentorship during the research and dissertation writing. Indeed, I would like to express my appreciation to Prof. Mohammed A. El-Gebeily, Prof. Abul Fazal M. Arif, Dr. Yagoub N. Al-Nassar and Dr. Mehmet V. Sunar for their support, suggestions and encouragement.

Furthermore, I should like to thank my colleagues and friends at KFUPM for their support. Special thanks are due to the Nigerian Community at KFUPM & Environs (NCUPM) for providing home away from home. In the same way, I like to express my gratitude to my Mentor, Mr. Ogundiran Tayo for his constant support and encouragement. I am particularly grateful to my sister Mrs. Risikat Ibraheem, for her sincere caring and support all the times. The author would also like to thank his brothers and sisters for their unconditional support, patience and understanding.

No doubt, any river that forgets its source will dry away; I also want to thank my parents for their support, inspiration and prayer in spite of being far away from them. Above all, I would like to express my warm appreciation to my beloved wife, Zainab and my pretty kids, Khadeejah and Aisha for their moral support, patience, encouragement and understanding.

Above all, my gratefulness goes to God Almighty, for giving me life, wisdom, knowledge and guiding me to success. My past, present and future are with You God Almighty only, make my future better, brighter and shine longer.

TABLE OF CONTENTS

LIST OF TABLES

LIST OF FIGURES

LIST OF ABBREVIATIONS

BSWI	:	B-Spline Wavelet on the Interval
DOF	:	Degree of Freedom
EP	:	Euler-Bernoulli Pipe Element
FEM	:	Finite Element Method
FRP	:	Fiberglass Reinforced Plastic
LCSS	:	Laminated Composite Structure Stiffness
MRA	:	Multi-Resolution Analysis
THW	:	Trigonometric Hermite Wavelet
TP	:	Timoshenko Pipe Element
WBFEM	:	Wavelet-based Finite Element Method

ABSTRACT

FULL NAME : WASIU ADEYEMI OKE

TITLE : Dynamic Analysis of Fiberglass-Reinforced Plastic Pipes with
Thickness Discontinuity using Wavelet-based Finite Element

MAJOR : Mechanical Engineering

DATE : May, 2016

In the past few decades, Fiberglass-Reinforced Plastic (FRP) pipes have become a viable alternative to coated steel, stainless steel and other metallic pipes in many engineering applications related to power generation, chemical processing, oil and gas transportation, municipal wastewater drainage and treatment and other industrial applications. Internal surface attack, which can take several forms due to chemical reactions, heat, erosion, or a combination of such influences, is the main apparent type of aging damage in in-service FRP piping. This phenomenon will cause thickness discontinuity in pipes and fittings, which could compromise their structural integrity and could thereby lead to waste of resources, increase plant downtime, revenue loss and possible catastrophic failures.

In this work, the dynamic behavior of FRP pipes with internal thickness discontinuity (wall-thinning) of different geometries, which may occur at different locations along its span, has been investigated. In order to examine the structural integrity of the pipe, the wavelet-based finite element method (WBFEM) has been adopted to obtain a numerical model of high efficiency and fidelity. Wavelets have multi-resolution analysis and therefore possess unique advantages for capturing localized effects and structural discontinuities. The finite pipe element was constructed in the wavelet space and then transformed to the physical space. Detailed expressions of the required matrices are derived for the laminated composite pipe using the B-spline and Trigonometric hermite wavelets scaling functions. Both Euler-Bernoulli and Timoshenko beam theories are considered. The generalized eigenvalue problem has been formulated and solved to obtain the modal characteristics of the FRP pipe. The developed model is equally applicable to empty pipes as well as pipes conveying fluid; with or without internal thickness discontinuities.

To demonstrate the accuracy and efficiency of the developed approach, the results of the numerical simulations are compared with the available results in literature and those obtained by ANSYS. In addition to providing information related to the FRP pipe structural integrity, the developed dynamic model has been utilized to produce some benchmark solutions to fill a gap in the literature, which does not contain any published data pertinent to vibrations of composite pipes with internal surface defects. For future practical applications, the results of this investigation attested to the potential of using the vibration signature as a viable basis for establishing online schemes for detecting and monitoring the internal surface defects in pipelines.

ملخص الرسالة

الاسم الكامل: واسيو أديمي أوك

عنوان الرسالة: التحليل الديناميكي للأنابيب البلاستيكية المقواه بالألياف الزجاجية و المتقطعة السمك باستخدام العنصر المحدود المبني على المويجات.

التخصص: الهندسة الميكانيكية

تاريخ الدرجة العلمية: مايو ، 2016

لقد أصبحت الأنابيب البلاستيكية المقواه بالألياف الزجاجية (FRP) في العقود القليلة الماضية بديلا قابلا للتطبيق للصلب المطلي، والفولاذ المقاوم للصدأ وغيرها من الأنابيب المعدنية في العديد من التطبيقات الهندسية المتعلقة بتوليد الطاقة والمعالجة الكيميائية ونقل النفط والغاز وتصريف ومعالجة مياه الصرف الصحي وغيرها من التطبيقات الصناعية. تآكل السطح الداخلي، والذي يمكن أن يأخذ عدة أشكال بسبب التفاعلات الكيميائية والحرارة، أو مزيج من هذه التأثيرات، هو النوع الشائع والواضح لتلف الأنابيب البلاستيكية المقواه بالألياف الزجاجية (FRP) مع طول مدة استخدامها. وهذه الظاهرة تتسبب في تناقص سمك الأنابيب والتوصيلات، والتي يمكن أن تهدد سلامة هيكلها، و بالتالي قد تؤدي إلى إهدار الموارد، وزيادة فترة توقف المصنع، وفقدان الإيرادات و أحتمالية حدوث الأعطال الكارثية. في هذه الرسالة، تم دراسة السلوك الديناميكي لأنابيب الألياف الزجاجية (FRP) في وجود تآكل موضعي في السمك الداخلي (ترقق الجدار الداخلي) على أشكال هندسية مختلفة، والتي قد تحدث في مواقع مختلفة على طول فترة استخدامها. ومن أجل فحص السلامة الهيكلية للأنبوب، لقد تم اعتماد طريقة العنصر المحدود المبني على أساس المويجات (WBFEM) للحصول على نموذج عددي عالي الكفاءة والدقة. فالمويجات تستطيع عمل تحاليل متعددة الدقة، وبالتالي تمتلك مزايا فريدة لنمذجة التأثيرات الموضعية والتقطعات الهيكلية. وعنصر الأنابيب المحدود تم بناءه في حيز المويجات ثم يتم تحويله إلى الحيز المادي. ولقد تم التوصل الي صيغ مفصلة من المصفوفات اللازمة للأنابيب الرقائقية المركبة باستخدام المويجات المخددة (B-spline) ومويجات هيرميت المثلثية. كما تم تبني نظريات العتبات المرنة لكل من أويلر- برنولي وتيموشينكو. وقد تم صياغة و حل المشكلة العامة للقيمة الذاتية للحصول على الخصائص المرنة لأنابيب الألياف الزجاجية (FRP). والنموذج المطور في هذا البحث يمكن تطبيقه لدراسة الأنابيب الفارغة كما يمكن تطبيقه كذلك على أنابيب نقل السوائل وذلك في حالة وجود او عدم

وجود تآكلات داخلية في السُمك. وللتدليل على دقة وكفاءة النموذج المستحدث، تم مقارنة نتائج المحاكاة العددية مع نتائج الدراسات السابقة المنشورة، وأيضا النتائج التي تم الحصول عليها بواسطة ANSYS.

بالإضافة إلى توفير المعلومات المتعلقة بالسلامة الهيكلية للأنابيب الزجاجية، قد تم استخدام النموذج الديناميكي المستحدث لإنتاج بعض الحلول القياسية لسد فراغ في الدوريات المنشورة، والتي لا تحتوي على أية بيانات قد تكون وثيقة الصلة باهتزازات الأنابيب المركبة التي تحوي عيوب سطحية داخلية. كما تشير نتائج هذه الدراسة إلى إمكانية استخدام إشارات الإهتزاز، كأساس عملي لاستحداث انظمة مراقبة دائمة في المستقبل لكشف ورصد العيوب السطحية الداخلية في خطوط الأنابيب، وذلك من أجل التطبيقات العملية في الصناهة.

CHAPTER 1

INTRODUCTION

1.1 Fiberglass-Reinforced Plastic (FRP) Pipes

Composite pipes like FRP pipes have become a viable alternative to protected steel, stainless steel and other metallic pipes in several applications. Indeed, no doubt about it that for some decades, there has been an exceptional increase in the usage and development of fiber-reinforced multi-layer composite materials as a result of their lightweight, high strength, corrosion resistance and high-temperature performance [1, 2]. These properties offer composite materials advantages over conventional materials and make composite materials more desired in modern technology [3]. Laminated composites are designed in different geometries but laminated composite cylindrical pipes or shells (thin, moderately thick and thick) have been of great interest to a large number of fields, such as aeronautics and astronautics engineering [3, 4] and other industries such as Oil and gas, marine systems and offshore applications [5-7]. The pipes produced from laminated composite materials are usually called [8]: Fiberglass Reinforced Plastic or polyester or Fiber Reinforced Plastic (FRP) pipes (European standards), Glass fiber Reinforce Plastic or polyester (GRP) (BS standards), Reinforced Thermosetting Resin Pipe (RTRP), Reinforced Plastic or polymer Mortar Pipe (American Standards), Fiberglass Reinforced Epoxy (FRE) and Glass fiber Reinforced Epoxy (GRE). Hence, all over the industries, the common term FRP refers to plastic that has been reinforced with glass fibers [9]. FRP contains **fiber** that is made of: Glass, Aramid, Carbon, Ceramic; **Matrix of Plastic**: Polyester, Pthalates, Epoxide, Polyurethane, HDPE, PTFE, etc. [10, 11] and **additives** like: colors, fire inhibitors, UV retardants, antiskid and conductivity agents, etc.

The FRP know-how came to be during World War II and the first machine (centrifugal casting) to produce pipe appropriate for chemical and commercial applications was developed in the 1950s [12]. The advantages of FRP material include corrosion resistance, economy, weight advantage, high strength, flexibility, easy to repair, thermal insulation and less conductivity [9, 13-15]. FRP pipes can be used for all types of fluids [8] and as a result, their utilization is growing and it will continue to grow in the following industries [14-16]: Oil and gas, petrochemical, water distribution, desalination and power, industrial, infrastructural and municipal and others (see Figs. 1.1-1.4).

In general, pipes in-service are exposed to different types of damage that may affect their operational performance. There are several defects (internal and external) that can be found in FRP pipes in-service due to the operational and environmental conditions. Internal surface defects may include erosion, cracks, crazes, ridges foreign inclusion, pits (pin holes), wear scratch, dents and wrinkles [10, 17-19]. However, these defects or damages can succinctly group into aging damage (surface Attack, erosion/corrosion, stress corrosion, etc.); mechanical damage (surface crazing, structural cracking, etc.) and heat-related damage (loss of strength, stiffness and hardness, thermal or Shrinkage Cracking, oxidation, etc.) [10]. According to Reichhold [10], among the aforementioned damages, surface attack, which can take several forms, is apparently the

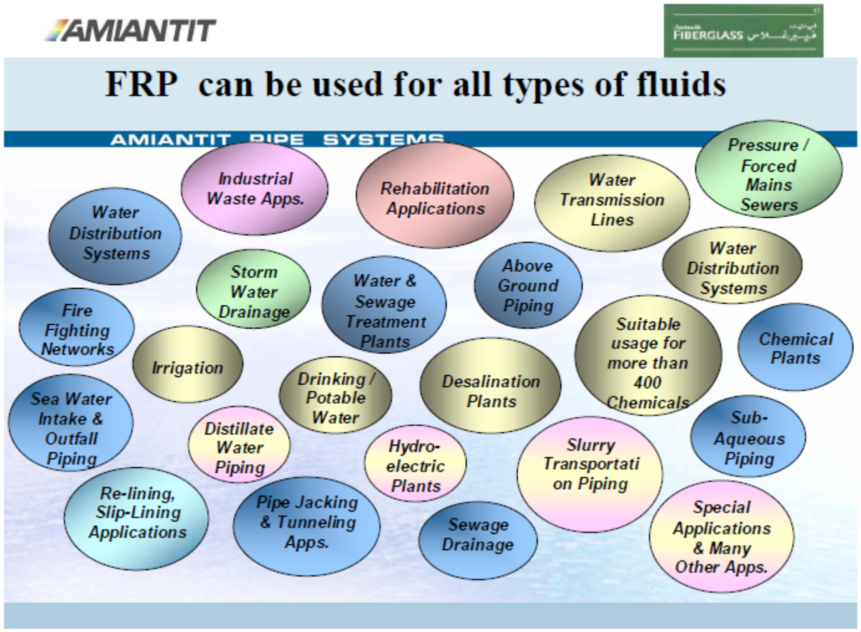
AMIANTIT

FIBERGLASS

FRP can be used for all types of fluids

AMIANTIT PIPE SYSTEMS

Industrial Waste Apps.

Rehabilitation Applications

Water Transmission Lines

Pressure / Forced Mains Sewers

Water Distribution Systems

Storm Water Drainage

Water & Sewage Treatment Plants

Above Ground Piping

Water Distribution Systems

Fire Fighting Networks

Irrigation

Suitable usage for more than 400 Chemicals

Chemical Plants

Sea Water Intake & Outfall Piping

Drinking / Potable Water

Desalination Plants

Distillate Water Piping

Hydro-electric Plants

Slurry Transportati on Piping

Sub-Aqueous Piping

Re-lining, Slip-Lining Applications

Pipe Jacking & Tunneling Apps.

Sewage Drainage

Special Applications & Many Other Apps.

Figure 1.1: Usage of FRP Pipes for fluid [8]

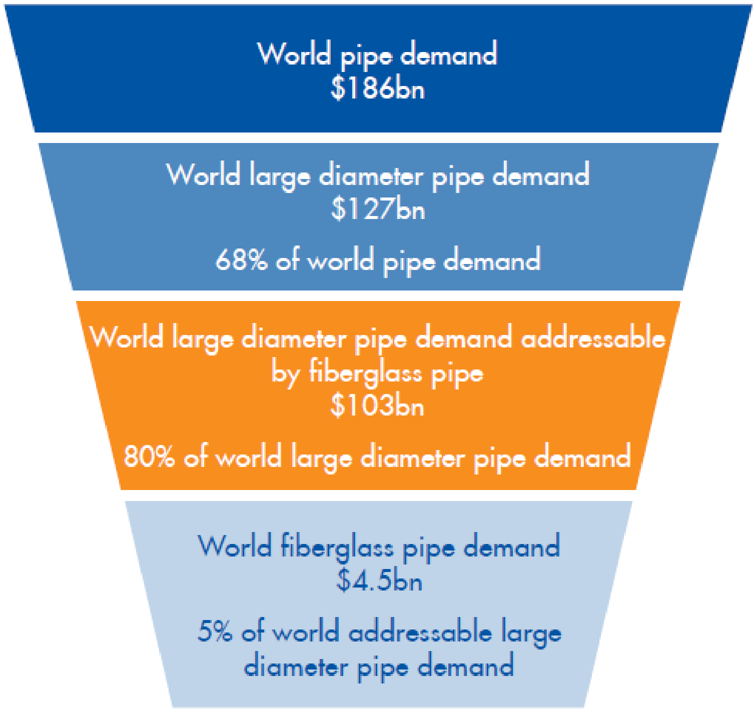

Figure 1.2: Global pipe Market (2010) [15]

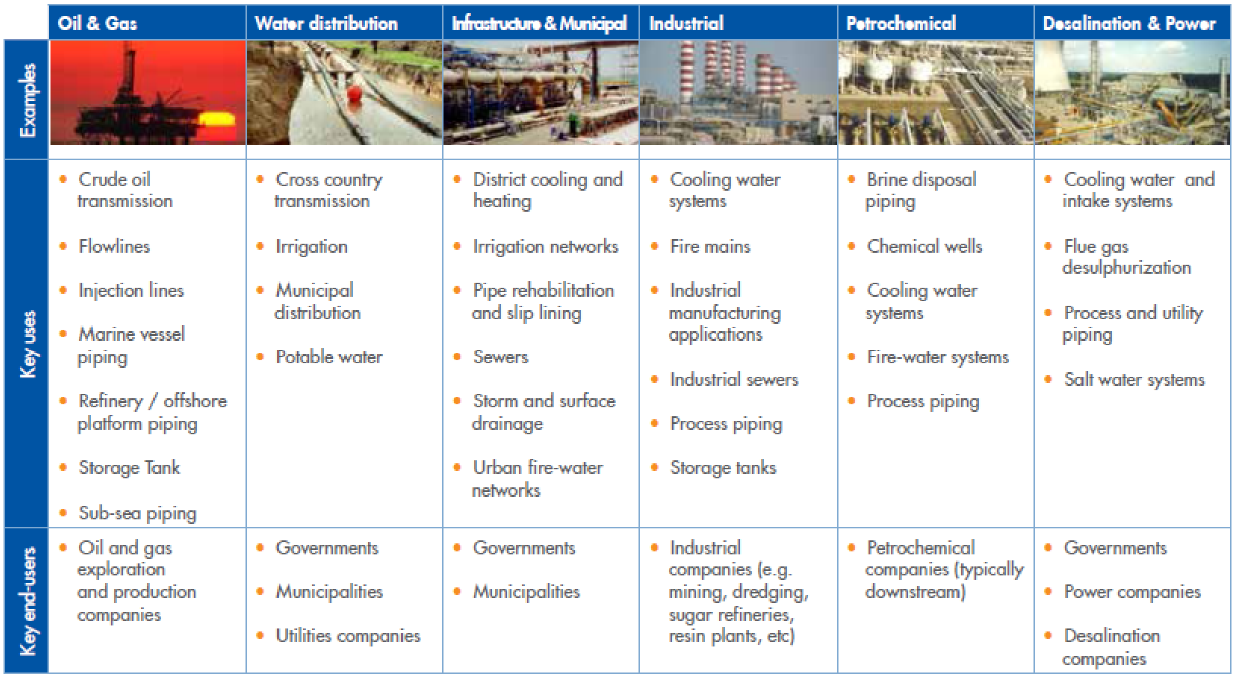

	Oil & Gas	Water distribution	Infrastructure & Municipal	Industrial	Petrochemical	Desalination & Power
Examples						
Key uses	• Crude oil transmission • Flowlines • Injection lines • Marine vessel piping • Refinery / offshore platform piping • Storage Tank • Sub-sea piping	• Cross country transmission • Irrigation • Municipal distribution • Potable water	• District cooling and heating • Irrigation networks • Pipe rehabilitation and slip lining • Sewers • Storm and surface drainage • Urban fire-water networks	• Cooling water systems • Fire mains • Industrial manufacturing applications • Industrial sewers • Process piping • Storage tanks	• Brine disposal piping • Chemical wells • Cooling water systems • Fire-water systems • Process piping	• Cooling water and intake systems • Flue gas desulphurization • Process and utility piping • Salt water systems
Key end-users	• Oil and gas exploration and production companies	• Governments • Municipalities • Utilities companies	• Governments • Municipalities	• Industrial companies (e.g. mining, dredging, sugar refineries, resin plants, etc)	• Petrochemical companies (typically downstream)	• Governments • Power companies • Desalination companies

Figure 1.3: Industries using FRP pipes [15]

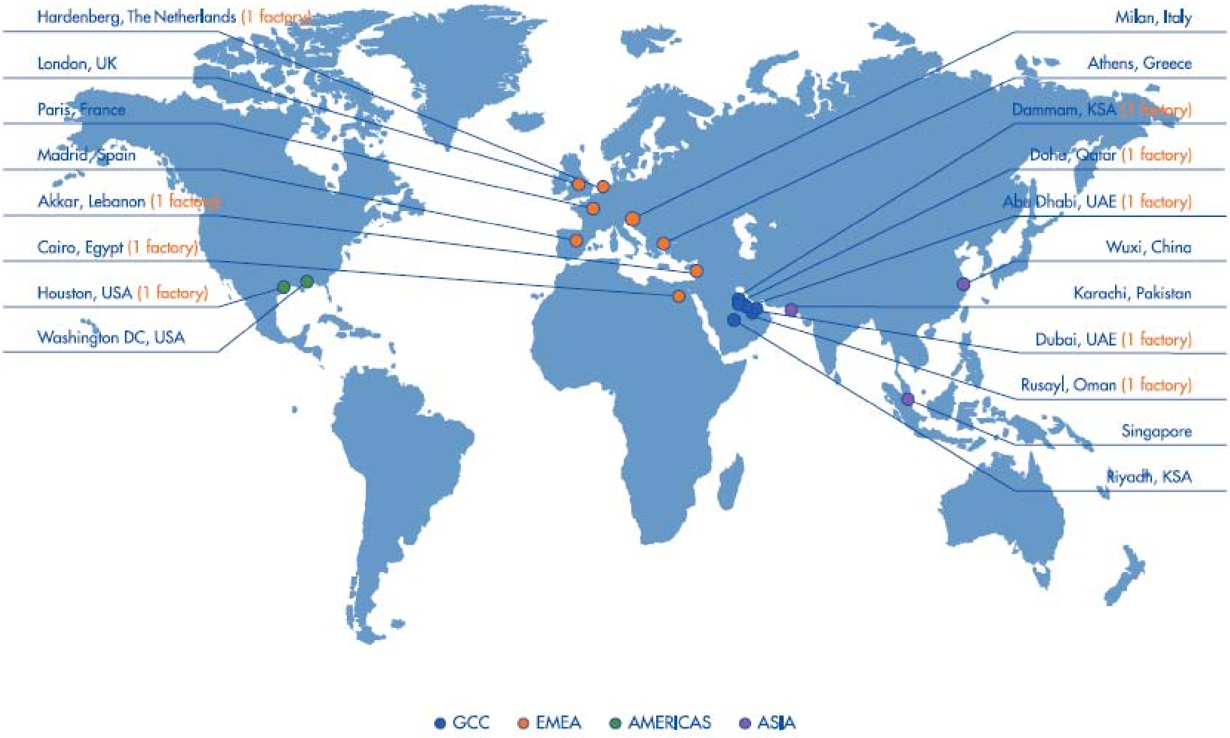

Figure 1.4: Global Research [15]

dominant type of aging damage in in-service FRP piping, which is normally caused by chemical reactions, heat, erosion, or a combination of such influences. This phenomenon will result in erosion-induced internal defects or thickness discontinuities in pipes and fittings, which could compromise their structural integrity and may lead to waste of resources, increase in plant downtime and possible catastrophic failures.

1.2 Motivation of the Study

Saudi Arabia is blessed with abundant resources of crude oil and natural gas. The Kingdom is ranked first among oil producing countries worldwide in terms of crude oil production and exports as well as natural gas production and exports. A gigantic pipeline network has been established throughout the regions in Saudi Arabia to support the oil and gas industry and provide infrastructure for future expansions. In addition, the Kingdom is becoming a leading country in petrochemical industries. Accordingly, a greater demand for the utilization of composite pipes has been manifested in the current pipeline network, as well as its future expansion and replacement these pipeline networks. In order to meet the increasing demands for oil, gas and petrochemical products, the industrial sector in Saudi Arabia needs to be at the forefront of the industrial countries and share the leading the effort in developing detection techniques for the internal pipe defects. Monitoring and early detection of such concealed defects in pipeline systems is crucial to minimize waste of resources, reduce plant downtime, and possible sudden failures. Vibration-based techniques have a great potential to serve as a basis for reliable and nondestructive detection schemes. Moreover, detection methods based on vibration measurements are well-oriented to establishing online monitoring systems. To this end, the understanding of the vibration behavior and stability of the laminated composite pipes is essential to developing such detection schemes. To gain more insight into the vibrational response of the piping system, an accurate and efficient dynamic model that accounts for the internal surface defects for a composite pipe conveying fluid must be established. In this context, the objectives of this investigation are detailed in the next section.

1.3 Objectives

This research work aimed to evaluate the potential of using the vibrational characteristics of the composite pipes (like FRP pipes) in monitoring the corrosion-induced thinning or internal defects. Accordingly, the objectives of this research are as follows:

1) Develop a dynamic model for vibration analysis of FRP pipes with thickness discontinuity using wavelet-based finite element method (WBFEM). The model allows for multi-layered composites with different ply angles.
2) Study the effect of the wall-thinning depth and location on the modal characteristics of the fluid-free FRP pipe.
3) Study the effect of the wall-thinning depth and location on the modal characteristics of an FRP pipe with internal flow.
4) Evaluate the wall-thinning effect on the impulse response of the FRP pipe.

1.4 Methodology

The methodology used to achieve the dissertation objectives is outlined as follows:

1) Three wavelets (trigonometric, Daubechies and B-spline) have been studied. The trigonometric and B-spline wavelets were initially selected. Thereafter, due to its superiority, the B-spline wavelet has been eventually utilized throughout the study.
2) The dynamic models for a uniform FRP pipe have been developed based on Euler-Bernoulli and Timoshenko beam theories. The pipe model has been discretized using the WBFEM.
3) The dynamic formulations account for internal surface discontinuities in an empty pipe, as well as a pipe conveying fluid.
4) The developed model has been extended to handle discontinuities of different geometries. In this context, the geometry of the discontinuity is permitted to vary within the cross section both in angular and radial directions, and to occupy any length of the pipe span.
5) The generalized eigenvalue problem, including all the aforementioned features of the pipe, has been formulated and solved to examine the vibrational behaviour of the composite pipe in terms of its modal characteristics.
6) The effectiveness of the developed model has been validated via comparisons with available results in literature, as well as results obtained by the traditional FEM method using ANSYS.
7) Finally, dynamic analysis is performed by integrating the model forward in time to calculate the time histories of the transient response of the composite FRP pipe.

Both initial conditions on displacement and velocity are considered. The impulse response is obtained either by applying an initial velocity condition or by applying a pulse excitation.

1.5 Dissertation Structure

This dissertation is divided into nine chapters as follows:

Chapter 1 contains the introduction, objectives and the methodology used in achieving the dissertation objectives. It also contains dissertation structure. In **Chapter 2**, a comprehensive review of previous work on the dynamic analysis of (i) health pipes ranging from thin to thick and (ii) pipes conveying fluid were presented. In the later part, the extensive review on the usage of wavelets in dynamic analysis of pipe structures was discussed. In **Chapter 3**, the components of composite materials and some terminologies that needed to know to be able to handle laminated composite pipes analyses effectively were reported. In addition, some equations needed for obtaining laminated composite pipes data that utilized in subsequent chapters were presented. The wavelets were discussed in **Chapter 4** and the discussion covered the history and some available wavelets that can be utilized in structural analyses. Besides, the two wavelets considered in this study were discussed and the procedures for involving them in FEM were given. In the later part of the chapter, the advantages of WBFEM over traditional FEM were made available. In **Chapter 5**, WBFEM models for laminated composite pipes with and without thickness discontinuity were presented. These models were based on Euler-Bernoulli and Timoshenko beam theories. Toward the end of the chapter, the models for the laminated pipe without discontinuity were validated and the results obtained with available results in literature and ANSYS FEM results were reported. The WBFEM used in Chapter 5 using Euler-Bernoulli theory was generalized in **Chapter 6** for composite pipe with and without thickness discontinuity. The model was later validated toward the end of the chapter. The generalized model that used B-spline wavelet used in Chapter 6 was extended to handle laminated composite pipes with and without thickness discontinuity conveying fluid in **Chapter 7**. The model was validated and the results obtained were compared and discussed thereafter. In **Chapter 8,** the effects of thickness discontinuity on the impulse response of the FRP pipes were presented using the model utilized in Chapter 7.

In the long run, the conclusions that emphasize the key findings in this work and recommendations for future work are reported in **Chapter 9.**

CHAPTER 2

LITERATURE REVIEW

2.1 General Background

As the usage of FRP pipes continue to grow in oil and gas, petrochemical, water distribution, desalination and power, industrial, infrastructural and municipal and other industries, the internal defects or thickness discontinuity in these pipes and fittings which could compromise their structural integrity need to be monitored through their dynamic analysis. This is crucial to minimize plant downtime, loss of revenues and possible catastrophic failures. Due to the importance of the vibrational behavior of the composite laminated pipes in the aforementioned industries, methods of vibration analysis of such pipes have received a substantial attention from researchers. Several methods have been developed for analyzing free vibrations of composite laminated cylindrical pipes; these include the finite element method, Ritz method, differential quadrature method, and other numerical discretization methods. These methods have been equally to both thin and thick pipes.

2.2 Dynamic Analysis of Laminated Cylindrical Composite Pipes without Fluid Flow

In this section, the dynamic analysis of a laminated composite empty pipe is reviewed. The pipes considered are classified into groups, namely thin, moderate and thick pipes.

2.2.1 Thin-walled Laminated Cylindrical Composite Pipes

Narita and Ohta [4] presented a finite element solution for the free vibration problem of cross-ply laminated closed cylindrical shells. They modelled cross-ply shell as an orthotropic thin shell by using classical lamination theory. The strain and kinetic energies were developed analytically in their formulation of ring element of the shell based on the energy expressions derived from the Flugge-type shell theory. They concluded that the results obtained were in good agreement with those in existing literature. In addition, it was reported that the lamination angles cause significant differences in frequencies. Soldatos and Messina [20, 21] used energy functional of the Love-type version of the unified shell theory to investigate the free vibration characteristics of transverse shear deformable cross-ply laminated circular cylindrical shells on the basis of the Ritz method. They used variational approach in their theoretical formulation and classical type with several shear deformable Love-type shell theories were considered. In their work, the shells with no external tractions at one or both edges were examined. They observed that the results obtained agree favourably with both analytical and experimental results in literature. On the other hand, it was stated that whenever higher vibration characteristics are required orthonormal polynomial bases should be employed. Furthermore, in another development they extended the applicability of the Ritz-type method towards an advanced study of the influence of the edge boundary conditions on the vibration characteristics of cross-ply laminated cylindrical shells. In their new analysis the energy functional of the two different types of love-type version of a unified shear-deformable shell theory was used. They found that the numerical results obtained were in agreement with corresponding numerical results in the literature. However, they reported that for further study particularly for short shells, perfect modelling of the inter-laminar stress distribution may become a serious issue. Civalek [22] carried out numerical study on the free vibration analysis for laminated conical and cylindrical shell. Love's first approximation thin shell theory was used in the analysis and discrete singular convolution (DSC) method was employed to solve the equations obtained. Researcher discovered that the results obtained by DSC compared well with those obtained by other researchers and the method offered a capable way of solving orthotropic laminated conical and cylindrical shells problems. Poore et al. [23] presented semi-analytical solution for obtaining the vibration characteristics of laminated cylindrical shells containing a circular cutout. The governing equations were obtained by Halmilton's principle and displacement conditions were relaxed through Lagrange multipliers. Fourier and Laurent series were employed for global and local functions used in their method to represent the mid-surface displacements. In their work, two different cases of simply supported boundary conditions were utilized. They observed that the natural frequencies of cylindrical composite shells with first kind of boundary conditions were much more sensitive to the existence of a cutout than shells with second kind. Also, it was stated that the cutout had little effect on the mode shapes of the shell when its size was small compared to the radius of the shell. Viswanathan et al. [24] investigated the vibration of multi-layered circular cylindrical shells with cross-ply walls using spline function method that included first-order shear deformation theory. They obtained the governing equilibrium equations in terms of displacement and rotational functions. The eigenvalue problem was then obtained by approximating these functions using Bickley-type splines of appropriate order. They found that as the thickness increases the frequency values also increase but reverse was the case when length parameter increases. Besides, it was stated that the effect of transverse shear deformation was more significant as it reduced frequency values. Naeem et al. [25] studies vibration characteristics of cylindrical shells that were presumed to be made from functionally graded materials. These shells were stiffened with isotropic rings on the outer surface. Sander's thin shell theory of first order was used to obtain strain energy and characteristic beam functions were used to estimate axial model dependence. The problem was then formulated through the principle of minimum energy of lagrangian function. They concluded that identical and equally spaced stiffeners located eccentrically on the cylindrical shell were very efficient than concentric ones. Jin et al. [6] developed a unified and exact solution method for the free vibration analysis of composite laminated cylindrical shells with general elastically restrained boundaries and arbitrary lamination schemes. In their theoretical model formulation, an arbitrarily laminated version of the Reissner– Naghdi's linear shell theory was considered. The shell displacements were constructed as a standard Fourier cosine series complemented with auxiliary functions. They observed that their results were comparable well with those available in literature and the method can be applied generally to different boundary conditions. Khalifa [26] studied the free vibration behaviour of orthotropic cylindrical shell with step or reduced thicknesses over parts of its circumference using Flügge's shell theory, the transfer matrix approach and the Romberg integration method together. The model was used to obtain the vibration frequencies and the equivalent mode shapes for symmetrical and antisymmetrical type-modes. Researcher found that when the step thickness ratios decrease, the vibration frequencies decrease and the mode shapes become more pronounced for two and four-stepped shells. Viswanathan et al. [5] used Spline approximation to study free vibration of symmetric angle-ply laminated circular cylindrical shells. Love's first approximation theory was employed to develop their equation of motions. They perform parametric studies and frequency response of the shell was investigated. They observed that relative thickness, the angle ply orientation and layering of the shell wall affected the natural frequencies of the vibration of the cylindrical shell.

2.2.2 Moderately Thick-Walled Laminated Cylindrical Composite Pipes

Soldatos [27] studied the free vibration problem of thin elastic cross-ply laminated circular cylindrical shells and panels using most commonly used four thin shell theories: Donnell's, Love's, Sanders' and Flugge's in a unified version. It was concluded that other theories gave similar results while results of Donnell's theory matched well with non-shallow theories only when short shells were considered. Nevertheless, it was recommended that Fluge's theory should be used in numerical applications particularly in a situation whereby effect of coupling between extension and bending is anticipated to be great. Ramesh and Ganesan [28] developed a semi-analytical finite element based on a discrete layer theory for the free vibration analysis of multi-layered composite circular cylindrical shells. They employed Fourier expansions in the circumferential direction, constant transverse displacement in the thickness direction and piece-wise approximations for the in-plane displacements in their formulation. They observed that their results agree favourably with other results in literature when shell thickness was 1 mm but there was small variation at higher modes when thickness was 10mm. Sun et al. [29] used nine-noded isoparametric quadratic finite elements based on extended Sanders' first order shear deformable shell theory to study the fundamental frequencies of laminated anisotropic circular cylindrical composite shells. The authors discovered that for fairly high accuracy, the number of elements needed in the circumferential direction of a cylinder is 5-10 for each half-wave. Also, it was stated that Donnell type theory was not adequate for vibration analysis of moderately thick composite cylinders. Singh and Gupta [30] examined the free vibration characteristics of cylindrical tubes in which first order shear deformation theory for moderately thick shells, Euler-Bernoulli and Timoshenko beam theories were considered. They concluded that flexural frequency results obtained from beam theory with Timoshenko type shear deformation compared favourably with those from shell theory without thickness shear deformation. Nonetheless, they also concluded that the results from beam theory are not correct at excessive low length to mean radius ratio and at thickness to mean radius ratio. Timarchi and Soldatos [31] investigated axisymmetric and the flexural free vibrations of shell. In their study, Love-type version of the unified shear-deformable shell theory was considered. Three shear-deformable shell theories were used and different edge boundary conditions were utilized. They examined cross and angle plies that were closed, circular cylindrical shells and made of one or more monoclinical layers. They found that all the theories were wrongly assumed that at the material interfaces of the angle-ply laminate interlaminar stresses are discontinuous. However, they stated that angle-ply lay-up numerical behaviour of the solution was not all the time stable. Jin et al. [3] developed a unified analytical technique for the vibration analysis of moderately thick composite laminated cylindrical shells based on the first-order shear deformation theory. The shells considered were subjected to different lamination schemes. In spite of boundary conditions, each of the displacements and rotation components of the shell was expanded as the linear combination of a standard Fourier series. They concluded that their results were comparable with results obtainable in literature and the method can be applied to shell with more complex boundaries. Qu et al. [32] presented variational formulation for calculating the free, steady-state and transient vibrations of composite laminated moderately thick shells of revolution under different combinations of boundary conditions. In their formulation, the first-order shear deformation theory was employed and Fourier series and four sets of polynomials were considered for admissible functions for each shell segment. In their study, angle-ply and cross-ply laminated cylindrical, spherical and conical shells with a variety of geometric and material parameters and different boundary conditions were examined. They concluded that their results were accurately compared with those available in literature.

2.2.3 Thick-Walled Laminated Cylindrical Composite Pipes

Khdeir et al. [33] used the classical, first order and third-order shell theories and the state-space method to develop analytical solutions for displacements, natural frequencies and buckling loads of cross-ply circular cylindrical shells under various boundary conditions. In their work, there is no need for shear correction factors because the third-order theory of shells of Reddy accounts for cubic variation of surface displacements through the thickness of the laminate. They observed that classical shell theory under predicted the deflections but over predicted frequencies compared to shear deformation theories. It was also discovered that the first-order shell theory produced results very close to those of the third-order theory, however, it slightly under predicted frequencies. Ye and Soldatos [34] presented a refined formulation of an approach appropriate for three-dimensional vibration analyses of homogeneous and cross-ply laminated thick cylinders and cylindrical panels. The refined formulation used a 6 x 6 frequency determinant based on a recursive formula. They found that the frequencies increased as number of layers increased but when the number of layers of an antisymmetric cross-ply laminate increased the bending-extensional coupling due to lamination dies out very quickly. Furthermore, they noticed that the first frequency parameters were always higher for $[0°/90^{o}]_{s}$ laminates than for $[90^{o}/0°]_{s}$ and the mode shapes of the fundamental frequencies were always dominated by the radial displacement component for laminates having either symmetric or anti symmetric lay-ups. Thinh and Nguyen [35] developed continuous element method from dynamic stiffness matrix that accounted for rotary inertia and shear deformations effects to study the vibration analysis of thick laminated cross-ply composite cylindrical shells. They utilized first order shear deformation theory of composite shells and Reissner–Mindlin assumption was considered. They concluded that the results obtained shown that their model can be used to solve the vibration analysis of thick cross-ply composite cylindrical shell efficiently with high accuracy for any frequency range. Moreover, it was stated that the model can be used effectively to analyze shell in medium and high frequencies where other methods failed.

Besides, among other methods used to study vibration characteristics of laminated cylindrical composite shells is optimization method. Koide and Luersen [36] maximizing the fundamental frequency of laminated cylindrical composite shells through the stacking sequence using Ant colony optimization. MATLAB platform was used to implement this algorithm coupled with a finite element code. The connection was established between algorithm and ABAQUS academic version in order to compute the structural response of the cylinder. In their study, cylindrical shells with and without a cutout geometry were examined. They concluded that for cylindrical shells with cutout or complex geometries, ant colony metaheuristic can be employed to find optimal stacking sequences.

From above discussions, it can be observed that there are available means of handling dynamic analyses of healthy fiberglass reinforce plastic (FRP) pipes without fluid. However, some researchers have gone further to investigate the dynamic analysis of healthy laminated composite pipe conveying fluid.

2.3 Dynamic Analysis of Pipes Conveying Fluid

In many engineering applications, the problems of vibration and dynamic stability of fluid pipe systems are of major concern. These systems include pipes conveying fluids for domestic usage and those transporting fluids to and out of industries. In addition, the systems also include risers/pipes in offshore platforms, tubes in power plants, pipes carrying fluids in chemical and power plants, hydropower systems, air-conditioning ducts, heat exchange pipes, nuclear reactor fuel elements, exhaust pipes in engines [37-39] and others. Fluid flows can be laminar or turbulent but laminar flows are uncommon. Although, there are some cases in which flows can be laminar, such as in food industries however flows are turbulent in most cases [40]. Generally, pipes conveying fluid can be grouped into two categories (isotropic and composite pipes) based on the materials from which they were produced.

2.3.1 Isotropic Pipes Conveying Fluid

In this section, analyses of isotropic pipe conveying fluid reported in the literature were presented. While majority of researchers have worked on fluid-pipe with turbulent flow some also have worked on fluid-pipe with laminar flow. Wang et al. [41] carried out analysis of vibration characteristics of fluid-conveying pipe of different shapes using ADINA system in order to ascertain its effectiveness. In their investigation, shell and 3D elements were utilized to model pipe and fluid respectively. The fluid flow considered was laminar and pipe and fluid were coupled through their interfaces. They did several transient analyses and they discovered that the natural frequencies calculated by dynamic stiffness or analytical methods in general were higher than results obtained through ADINA. In addition, they also observed and concluded that it was not easy in ADINA system to maintain numerical stability at high flow velocity. Al-Hashimy et al. [42] investigated the effects of fluid density on natural frequencies and mode shapes of sudden enlargement-sudden contraction pipe conveying fluid supported by flexible supports. They employed beam theory to develop the governing equations of motion and transfer matrix method (TMM) was employed to solve the mathematical model. In their study, two fluids and laminar flow were considered and external force was applied to excite the pipe. They observed that there was good agreement between the results obtained through TMM and those obtained from ANSYS. Besides, they also observed and concluded that density of different fluid has diverse effect on both pipe frequency and corresponding mode shape. Recently, Kutin and Bajsić [43] developed asymptotic model for the fluid-dynamic loading of the laminar and uniform mean flows that is relevant for any circumferential wavenumber of the mode shape of the pipe conveying fluid. The effects of velocity profile were defined in terms of the correction factors for the fluid-dynamic loading. Asymptotic model was developed from the solutions of the Pridmore-Brown equation for the Fourier transform of the vibrational fluid pressure and solution was obtained through the Frobenius power series method. The flow effects on the first-mode frequency of pipe with fixed-fixed support were obtained through this model. The results obtained were compared with available results in literature.

Besides, when dealing with pipe conveying fluid with laminar flow, stability is not an issue. However, when dealing with turbulence flow that is commonly in industries, stability will become a serious issue because of the consequences that will occur if the pipe lose its stability in service. As a result, so many researchers have studied the vibration and stability of pipe conveying fluid using its dynamic analysis. In other to achieve this, several methods have been identified or utilized for examining dynamic analysis of pipe conveying fluid. These methods include: Transfer matrix method, finite element method, Generalized Differential Quadrature method, spectral element method, spectral transfer matrix method and others. The most widely used among these methods is finite element method (FEM), Piet-Lahanier and Ohayon [44] studied an elastic pipe conveying a compressible fluid in which viscous damping and flow effects were considered. They employed FEM based on an appropriate variational analysis of the low-frequency modal responses in their investigation. They made it known that the results obtained for straight and elbow pipes agreed with available results in literature. Zhang et al. [45] utilized Lagrange principle, the Ritz method and the idea of fictitious loads to develop a finite element model for a pipe conveying fluid. The effects of rotary inertia and shear deformation were considered in their model. This model was then used to explore the vibratory behavior of the pipe conveying fluid. They concluded that the model can be used to study the linear and non-linear behavior of pipes conveying fluid. Hansson and Sandberg [46] presented finite element formulations for symmetric and unsymmetric elements for studying liquid-filled pipes in which fluid-structure interaction was considered. Axisymmetric fluid and axisymmetric shell elements were used in their study. These elements were assessed numerically including eigenvalue analysis and they concluded that both performed well. However, it was reported that requirement of a special equation solver is the shortcoming of unsymmetric form while weakness of symmetric form is that it contains an artificial damping matrix. Kaewunruena et al. [47] used Hamilton’s principle to develop nonlinear equations of motion coupled in axial and transverse displacements for marine risers/pipes conveying fluid. Finite element model obtained from the formulation was used to obtain nonlinear frequencies and corresponding mode shapes through modified direct iteration procedure in conjunction with the inverse iteration. They examined riser statics and linear and nonlinear free riser/pipe dynamics in order to ensure precise trend and vibration behaviour of riser. It was discovered that the results obtained by their model compared well with available results in literature. They concluded that the degree of vibration was harden by static offsets and shift of mode shapes serves as a signal of nonlinear dynamic behavior. Moreover, all the above studied in which FEM has been used are on the pipe conveying fluid only. Some researchers have also used FEM to investigate the dynamic analysis of pipe conveying fluid and rest on elastic foundations. Ryu et al. [37] examined the vibration and dynamic stability of cantilever pipes conveying fluid on elastic foundations. They used extended Hamilton's principle to obtain equations of motion and numerical scheme was developed using FEM. A range of mass ratios, structural damping coefficients and elastic foundation parameters were considered and pipe flutter was also explored. They concluded that elastic foundation parameter has stabilizing effect unlike structural damping that has both stabilizing and destabilizing effects depending on mass ratio and elastic foundation parameter. Mostafa [39] employed finite element analysis to examine the natural frequency of a simply supported pipeline conveying incompressible steady fluid flow rest on viscoelastic foundation or modified Winkler model. In the analysis, investigator studied the effect of pipe length, pipe thickness, fluid density and foundation damping and stiffness on critical velocity and pipe stability. It was reported that the results obtained were in good agreement with available results in literature and new ones were obtained. The author also concluded that foundation damping decreases the critical velocity while foundation stiffness increases it.

Although, FEM has been used far more than any other method in fluid pipe analysis, however, TMM also has been gaining ground among researchers. Li et al. [48] investigated vibration analysis of a pipe with many sections conveying fluid in frequency domain analysis of the fluid–structure interaction using TMM. All the three coupling mechanisms were considered in their method which was developed to be used for both free and forced vibrations of multi-pipe sections conveying fluid. Besides, the effects of the pipe radius and material on the dynamic behavior of a pipe system were also explored. Dai et al. [49] examined the effect of steady combined force due to the internal fluid flow on the natural frequencies and critical flow velocities of pipe conveying fluid. They employed TMM to model three-dimensional (3D) pipe and vibration analysis of straight and curved pipelines conveying fluid was conducted in which harmonic excitation force was applied. They concluded that their results compared well with available results in literature and made it known that if this force was neglected the results to be obtained might not be dependable. In addition, TMM was also employed in Al-Hashimy et al. [42].

Besides, apart from FEM and TMM commonly being used, some researchers have used other methods to study dynamic analysis of pipe conveying fluid with and without elastic foundations. Zhong-min et al. [50] developed governing equation of liquid solid couple vibration of pipe conveying fluid on the elastic foundation. They then utilized power series method to obtain complex frequency and critical velocity of pipe conveying fluid on two-parameter and Winkler elastic foundations. They concluded that elastic foundation has influence on stability of pipe conveying fluid. In addition, they also concluded that for a pipe conveying fluid at a certain velocity, its highest frequency will occur when it is on two-parameter foundation follows by Winkler foundation and zero elastic foundation. Kuiper and Metrikine [51] studied the stability of a tensioned clamped-pinned pipe conveying fluid at low speed analytically. The model was developed using plug flow model in conjunction with a tensioned Euler-Bernoulli beam and D-decomposition method was utilized to examine the pipe stability. They concluded that unlike under high fluid velocities the pipe is stable for small fluid velocities. Moreover, they also concluded that critical velocity does not depend on external linearised Morison damping. Tornabene et al. [52] used Generalized Differential

Quadrature method to investigate stability of a cantilever pipe conveying fluid. In their study, they converted differential governing equation into a discrete system of algebraic equations and pipe stability was reduced to an eigenvalue problem. Argand diagram was then employed to demonstrate the connection between the eigenvalue branches and the corresponding unstable flutter modes. They concluded that only one critical flow speed can exist for the pipe at a certain mass ratio and after that system will become unstable for flutter. García-Planas and Mediano-Valiente [53] developed a mathematical method for the dynamic behavior of a clamped-pinned pipeline conveying fluid as a replacement for the expensive tests being used to determine the stability of a pipe conveying fluid. The nonlinear equation obtained was linearized and the stability was investigated by using eigenvalues of Hamiltonian linear system that depended on material constants. They concluded that dynamics and stability of pipes conveying fluid also depend on fluid pressure and pipe material in addition to the boundary conditions.

2.3.2 Laminated Composite Pipes Conveying Fluid

Composite pipes such as fiberglass-reinforced plastic (FRP) pipes for some decades have become a viable alternative to protected steel, stainless steel and other metallic pipes in several applications. However, despite the fast usage of composite pipes, very few researchers have studied the dynamic analysis of composite pipe conveying fluid. Chang and Chiou [54] presented the natural frequencies and critical velocities of laminated circular cylindrical shells with fixed-fixed ends conveying fluids. In their study, Hamilton principle was used to derive the equations of motion under the scope of the Mindlin-type first-order transverse shear deformable cylindrical shell theory for the moderately thick cylindrical shells. They found that the thickness-to-radius and length-to-radius ratios have effect on the natural frequencies. In addition, it was observed that the layup angle affected not only the stiffness of the shell but also lowest fundamental frequencies. Zou et al. [55] developed a state-variable model for vibration analysis of laminated composite pipe conveying fluid. They utilized thin-walled composite theory in developing their formulation and Hamilton's principle was used to obtain the equation of motion. The equation was then solved by using Ritz method and solution was obtained through state-space. Numerical analyses with different boundary conditions were executed and they concluded that the results obtained were in good agreement with those obtained using ANSYS software. Duarte et al. [56] carried out simulation of a composite piping system under different flow velocities in which fluid and pipe domain are modeled as one-dimensional problem. The linearized system obtained from the couple problem was solved using FEM. Fiberglass with external pipe reinforcement and fiberglass reinforced piping under steady flow simulations were executed for several velocities. The system frequencies behavior under internal flow was then utilized to evaluate the reinforcement.

In the literature, there are available means of handling dynamic analyses of fiberglass reinforce plastic (FRP) pipes with and without fluid flow. Most of the works reported were on healthy uniform and laminated cylindrical shells or pipes which could be regarded as FRP pipes. However, the dynamic analysis of FRP pipes with thickness discontinuity and with and without fluid flow was not considered. In addition, it can also be observed from the survey that laminated composite pipe conveying fluid has not been examined like isotropic pipe. Majority of pipes studied with or without fluid flow are healthy pipes which have not being subjected to in-service surface attack due to fluid type, environmental conditions under which they are being used and other factors. This surface attack can take a number of forms due to chemical reactions, heat, erosion, or a combination of such influences. This phenomenon will cause thickness discontinuity in pipes and fittings which could compromise their structural integrity and could thereby lead to abrupt wastage or revenue loss, increase plant downtime and sometimes disastrous failures. It becomes imperative to study the dynamic analysis of FRP pipes with thickness discontinuity in order to ensure that the integrity of the FRP pipes has not been compromised and above all, to prevent the aforementioned effects in industries.

2.4 Transient Analysis of Pipe with and without Fluid Flow

Mohammad et al. [57, 58] examined the transient response of a cantilever and simply supported pipes conveying fluid under impulse loading. Euler-Bernoulli theory was employed and it was expanded to accommodate fluid flow effects. In their studies perturbation and numerical methods were employed to analysis the transient response of pipe under consideration. In addition, the influence of two non-dimensional parameters that include pipe properties and characteristics of fluid flow on pipe transient response were also examined. They observed that one of these parameters increased the damping properties. However, reverse was the case as second parameter increased and finally caused instability. Duan et al. [59] utilized experiment to study not only the upshot of wave scattering of uneven obstacles in pipe network but also its influence on the transient analysis of the pipe. In their experimental setup, three sections of pipe were used and obstacle was introduced in the middle section one after the other. In their investigation, two different types of obstacle were considered and the results obtained were utilized to authenticate the former numerical and analytical investigations. They concluded that in engineering systems, the influence of wave scattering of obstacles in pipeline may affect the transient-based fault discovery in the old pipe systems. Zheng et al. [60] proposed a formulation for expressing the vertical response of a thin pipe pile to a transient load. In their formulation, they considered the coupling between the pipe pile and the outer and inner viscoelastic soil vibrations. In both vertical and circumferential directions, wave propagation in thin pipe pile was considered. The governing equation was developed in the cylindrical coordinate and the inverse Fourier transform was employed to obtain the time domain results. The results obtained with their method in which Half-sine impact force was utilized were compared with that of FEM and it was concluded that their results matched well with those results obtained from FEM.

However, it can be noted from the above discussion that much has not been done on the transient analysis of the pipe with or without fluid flow. In addition, the transient analysis of not only the isotropic pipes but also the laminated composite pipes with thickness discontinuity with or without fluid flow has not been given much attention.

2.5 Wavelets in Dynamic Analysis of Pipes

Indeed, conventional FEM is one of the most numerical methods being used mostly in engineering but also being used in other fields such as applied mathematics. However, for some times researchers have been shifted from this FEM to FEM in which scaling or wavelet functions serve as interpolation function. The wavelets that have been used in the structural analyses include Daubechies, Trigonometric, Haar, B-spline and others. Among these wavelets, the most frequently used is B-spline wavelet and this may be attributed to the fact that B-spline wavelet on the interval (BSWI) is the best in approximation of numerical calculation [61-63]. In this section, only those that have been used to analyses pipes or shells that related to this study were presented. Xie et al. [1] applied Haar wavelet discretization method (HWDM) to the free vibration analysis of composite laminated cylindrical shells in which different boundary conditions were considered. They used Reissner–Naghdi's shell theory to formulate their theoretical model. The eigenvalue problem was then obtained by discretizations of governing equations and boundary conditions through HWDM. They concluded that their results were correct when comparison studied was done. Jiawei et al. [64] developed two kinds of truncated conical shell elements to solve axisymmetric problems using BSWI. They then performed dynamic and static analyzes to show the accuracy of the development and its superiority over traditional element.

As it has been found in literature, B-spline wavelets have been used to a greater extend in structural analysis and it was concluded that it gave accurate results when compared with the results obtained from traditional finite element, finite difference and other methods. However, it can be concluded that wavelets have not been used to a greater extend in analyzing pipe or pipe conveying fluid with or without thickness discontinuity.

CHAPTER 3

LAMINATED COMPOSITE STRUCTURES

3.1 Laminated Composites and Terminology

The study of the interactions of the composite components on the microscopic level is regarded as micromechanics. It concerns with the condition of deformation and stress in the components and local failures that include interphase /interface failure (debonding), matrix and fiber failures (compressive, tensile and shear). The different types of analysis regarding composite materials are shown in Fig. 3.1.

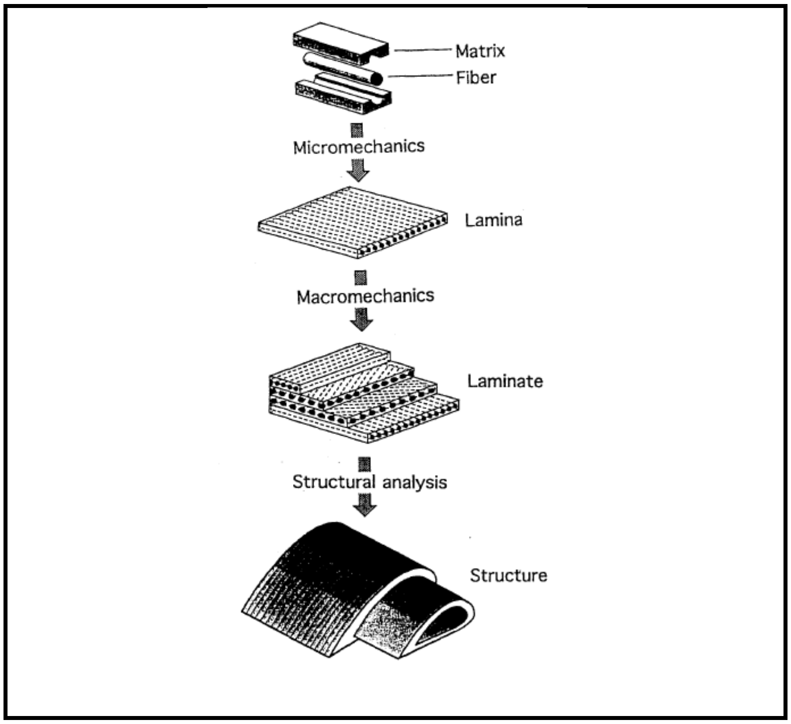

Figure 3.1: Different types of analysis regarding composite materials [65]

Composite material made up of several reinforcements combined with a well-suited matrix to attain greater performance from structure. Fiber orientation is mainly vital contributor to the material strength. There are several components that are needed to know in order to understand the composite systems; these components include matrix, fiber, layer, ply angle, laminate, and others. In composite system, fibers (e.g glass, boron, aramid, carbon, ceramic, etc) serve as reinforcement in composite and their required properties include high stiffness, high strength and moderately low density [65]. A layer or lamina may contain unidirectional continuous, short, bidirectional, randomly, braided or woven fibers implanted in a matrix [66, 67]. The layers (plies or laminae) can be of different thicknesses made of diverse materials. When these layers are bonded together at various orientations they will produce laminate of desired properties. Thus, composites are made up of plies (layers or laminae) united together to form a laminate (see Fig. 3.2).

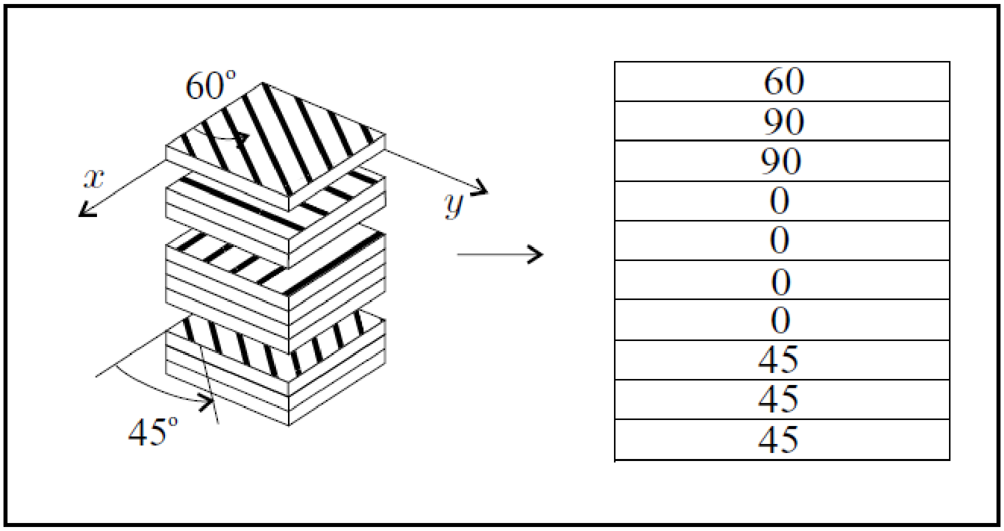

Figure 3.2: Layup in a laminate consisting of unidirectional plies [66]

There are four layer groups in Fig. 3.2 and the laminated code or stacking-sequence can be defined as $[60/90_2/0_4/45_3]$ from top to bottom or outer to inner for cylindrical or pipe structures. In addition, each layer group contains ply or plies, first group contains one ply, second group contains two plies, third group contains four plies and the fourth group contains three plies.

Furthermore, there are also some terminologies that can be used to classify laminates and they include symmetric, antisymmetric, balanced, unbalanced, cross-ply, angle-ply, etc. A laminate can be classified as symmetric laminate if it is symmetric with respect to the midplane otherwise its antisymmetric laminate [66]. That is, its laminated code is like $[-\phi_p]$ and $[\phi_p]$; $[\phi_n/\overline{\phi}_u/\phi_n]$, $[-\phi_n/-\overline{\phi}_u/-\phi_n]$, $[-\phi_n/\overline{\phi}_u/-\phi_n]$,$[\phi_n/-\overline{\phi}_u/\phi_n]$ and others. In this examples, p, n and u are number of plies in a group with $p > 1$, $n, u = 1, 2, ...$ and ϕ and $\overline{\phi}$ are ply angles.

In balanced laminates, there is an equal ply in the $-\phi$ direction for every ply in the $+\phi$ direction. Also, regarding the cross-ply laminates, the values of ϕ can only be 0^0 and 90^0 while angle-ply laminates are the opposite of cross-ply laminates. Besides, balanced, cross-ply and angle ply laminates can be symmetric or antisymmetric while angle-ply laminates can be any of aforementioned laminates except cross-ply laminates.

However, since fibers can be oriented in a random manner in a composite material, the composite can be described as isotropic, transversely isotropic, monoclinic, anisotropic, or orthotropic based on fibers behavior.

3.2 Generalized Hooke's Law and Plane Stress for Orthotropic Plates

The materials being used in engineering can be grouped into isotropic and composite materials. For laminated composites each lamina can be treated as a plate. One young modulus is needed to define the relationship between stress and strain for isotropic materials because the relationship does not depend on the direction of applied force. However, the composite materials required at least two young moduli to be able to establish the relationship between stress and strain [68]. As a result, there is going to be one modulus along the longitudinal and one along transverse directions of fibers of plate in order to be able to define the stiffness of orthotropic plate. Generally, the modulus along the longitudinal direction of fibers can be represented as E_1 or E_L while the one along transverse direction of fibers is represented as E_2 or E_T as shown in the Fig. 3.3.

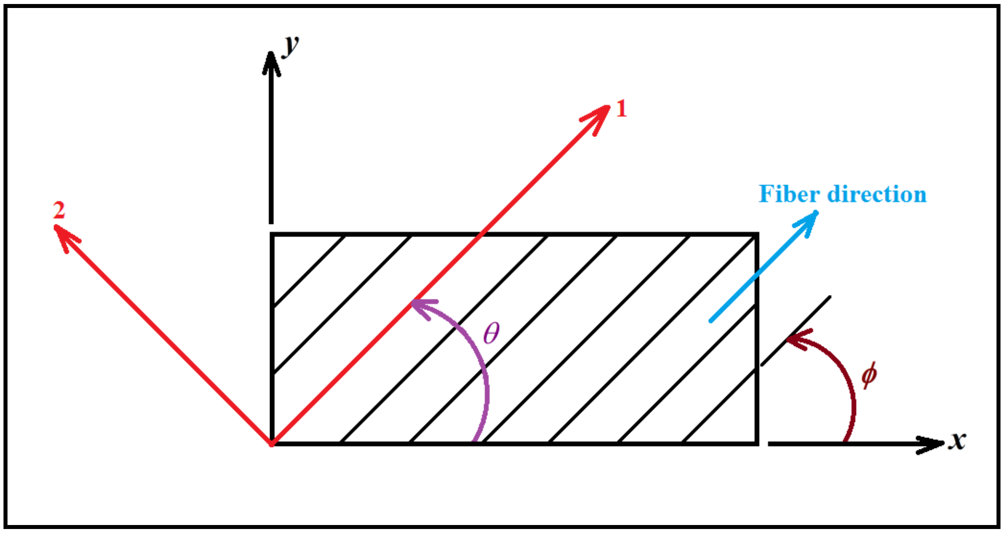

Figure 3.3: Orthotropic lamina with longitudinal and transverse directions

In the Fig. 3.3, angle ϕ describes the directions of fibers in the lamina from x-axis while θ that is the same as ϕ indicates the orientation of 1-axis from the x-axis. These angles are positive in anticlockwise direction. The relationship for the orthotropic plate can be defined as

$$\sigma_1 = E_1\varepsilon_1, \quad \sigma_2 = E_2\varepsilon_2 \tag{3.1}$$

In analysis of orthotropic plate, plane stress is being adopted due to the thickness of the lamina usually assumed to be thin and stress through the thickness will be small. In a thin fiber-reinforced composite plate, plane stress condition will approximate the stresses and it is a valuable approximation that produces results within acceptable accuracy for many thin wall structures [66]. In this case, stresses acting within the plate will be in more than one direction and this will make poisson's ratio to become significant. Thus, poisson's ratio ν_{12} for loading along the fibers directions and ν_{21} for loading perpendicular to the fibers directions can be defined as

$$\nu_{12} = \frac{\varepsilon_2}{\varepsilon_1} = \frac{\varepsilon_T}{\varepsilon_L}, \quad \nu_{21} = \frac{\varepsilon_1}{\varepsilon_2} = \frac{\varepsilon_L}{\varepsilon_T} \tag{3.2}$$

If a load is applied to the plate along the longitudinal direction and another load perpendicular to this load, then strain component will decrease due to contraction of poisson's effect as a result of perpendicular load. Hence, by subtracting strains in Eq. (3.2) form strains in Eq. (3.1), it will become

$$\varepsilon_1 = \frac{\sigma_1}{E_1} - \nu_{21}\varepsilon_2, \quad \varepsilon_2 = \frac{\sigma_2}{E_2} - \nu_{12}\varepsilon_1 \tag{3.3}$$

Upon substituting Eq. (3.1) in (3.3), new expressions will be obtained as

$$\varepsilon_1 = \frac{\sigma_1}{E_1} - \nu_{21}\frac{\sigma_2}{E_2}, \quad \varepsilon_2 = \frac{\sigma_2}{E_2} - \nu_{12}\frac{\sigma_1}{E_1} \tag{3.4}$$

Generally, the relationship between the Poisson's ratio and Young's modulus for orthotropic materials is given as [69]

$$\frac{\nu_{ij}}{E_i} = \frac{\nu_{ji}}{E_j},\ i, j = 1, 2, 3 \tag{3.5}$$

However, in each of these two directions ($i = 1, j = 2$), there is relationship between moduli and Poisson's ratios and Eq. (3.5) will become

$$\frac{\nu_{12}}{E_1} = \frac{\nu_{21}}{E_2} \tag{3.6}$$

In addition, there is a possibility of shear force present on the plate. The resulting shear stress τ_{12} is related to γ_{12} by the relationship

$$\tau_{12} = G_{12}\gamma_{12} = 2G_{12}\varepsilon_{12} \tag{3.7}$$

Equations (3.4) and (3.7) can be arranged in matrix form and the arrangement will yield strain-stress relationship from which coefficient matrix (compliance matrix$[S]$) can be obtained as

$$\{\varepsilon\} = [S]\{\sigma\} \tag{3.8}$$

where

$$\{\varepsilon\} = \{\varepsilon_1 \quad \varepsilon_2 \quad \gamma_{12}\}^T,\ \{\sigma\} = \{\sigma_1 \quad \sigma_2 \quad \tau_{12}\}^T$$

$$[S] = \begin{bmatrix} S_{11} & S_{12} & 0 \\ S_{12} & S_{22} & 0 \\ 0 & 0 & S_{66} \end{bmatrix} = \begin{bmatrix} 1/E_1 & -\nu_{21}/E_2 & 0 \\ -\nu_{12}/E_1 & 1/E_2 & 0 \\ 0 & 0 & 1/G_{12} \end{bmatrix}$$

Noting that $\nu_{12}/E_1 = \nu_{21}/E_2$ from Eq. (3.6), then $s_{12} = s_{21}$.

Inverting matrix in Eq. (3.8) will produce the stress-strain relationship as

$$\{\sigma\} = [\mathrm{Q}]\{\varepsilon\} \tag{3.9}$$

$$[Q]=\begin{bmatrix} Q_{11} & Q_{12} & 0 \\ Q_{12} & Q_{22} & 0 \\ 0 & 0 & Q_{66} \end{bmatrix}$$

where

$$Q_{11}=\frac{E_1}{\eta},\ Q_{12}=\frac{\nu_{12}E_2}{\eta}=\frac{\nu_{12}E_2}{\eta},\ Q_{22}=\frac{E_2}{\eta},\ Q_{66}=G_{12},\ \eta=1-\frac{E_2}{E_1}\nu_{12}^2=1-\nu_{12}\nu_{21}$$

Eq. (3.9) is for the situation whereby $\phi=0^0$, however, if $\phi\neq 0^0$, $\left[Q\right]$ needs to be transformed. Hence, after the transformation the constitutive relation transformed to the $x-y$ coordinate system is defined as [68, 70]

$$\begin{Bmatrix} \sigma_1 \\ \sigma_2 \\ \tau_{12} \end{Bmatrix}=\begin{bmatrix} \overline{Q}_{11} & \overline{Q}_{12} & \overline{Q}_{66} \\ \overline{Q}_{12} & \overline{Q}_{22} & \overline{Q}_{26} \\ \overline{Q}_{16} & \overline{Q}_{26} & \overline{Q}_{66} \end{bmatrix}\begin{Bmatrix} \varepsilon_1 \\ \varepsilon_2 \\ \gamma_{12} \end{Bmatrix},\ \begin{Bmatrix} \sigma_1 \\ \sigma_2 \\ \tau_{12} \end{Bmatrix}=\begin{bmatrix} \overline{Q}_{11} & \overline{Q}_{12} & 2\overline{Q}_{66} \\ \overline{Q}_{12} & \overline{Q}_{22} & 2\overline{Q}_{26} \\ \overline{Q}_{16} & \overline{Q}_{26} & 2\overline{Q}_{66} \end{bmatrix}\begin{Bmatrix} \varepsilon_1 \\ \varepsilon_2 \\ \varepsilon_{12} \end{Bmatrix}$$

or

$$\{\sigma\}=[\overline{Q}]\{\varepsilon\} \tag{3.10}$$

where $[\overline{Q}]$ is transformed reduced stiffness matrix of the ply/layer. It is constant across each ply and $\overline{Q}_{ij}$ ($i, j=1,2,6$) are the in-plane elements of the stiffness matrix. For an orthotropic or transversely isotropic materials, $\overline{Q}_{ij}$ are given as [65, 66, 71, 72]

$$\begin{aligned}
\overline{Q}_{11}&=Q_{11}c^4+2(Q_{12}+2Q_{66})c^2s^2+Q_{22}s^4\\
\overline{Q}_{12}&=(Q_{11}+Q_{22}-4Q_{66})c^2s^2+Q_{12}(c^4+s^4)\\
\overline{Q}_{22}&=Q_{11}s^4+2(Q_{12}+2Q_{66})c^2s^2+Q_{22}c^4\\
\overline{Q}_{16}&=(Q_{11}-\ Q_{12}-2Q_{66})c^3s+(Q_{12}-\ Q_{22}+2Q_{66})cs^3\\
\overline{Q}_{26}&=(Q_{11}-\ Q_{12}-2Q_{66})cs^3+(Q_{12}-\ Q_{22}+2Q_{66})c^3s\\
\overline{Q}_{66}&=(Q_{11}+Q_{22}-\ 2Q_{12}-2Q_{66})c^2s^2+Q_{66}(c^4+s^4)
\end{aligned}$$

where $s=\sin\theta,\ c=\cos\theta$ or $s=\sin\phi,\ c=\cos\phi$

It can be observed in Eq. (3.10) that normal stresses will be produced by shear strain and normal strains will contribute to a shear stress. This is termed as extensional shear coupling that will occur when a lamina is loaded at angle ϕ that is neither 0^0 nor 90^0. This indicates that as long as $\overline{Q}_{16}$ and/or $\overline{Q}_{26}$ are not zeros, this coupling will continue to exit [66].

3.3 Composite Material Properties

As it was reported earlier, those fibers can be oriented in a random manner in a composite material and as a result composite can be described as isotropic, transversely isotropic, monoclinic, anisotropic, orthotropic and so on based on fibers behavior. These are the different ways of simplifying the composite material and this will reduce the number of engineering constants to be determined during the composite structure analyses. Thus, for these materials whose properties can be described in three different directions (three-dimensional case with $i, j = 1, 2, 3$ in Eq. (3.5)), their engineering constants and their constraints are as presented in Tables 3.1 and 3.2 as given in [66]. In Table 3.1, the independent constants in each material are those constants that must be known whenever any of this material is to be considered. Thus, the more constants need to be known as one move from first material to the last in Table 3.1. Similarly, while obtaining these constants the corresponding constraints on each material listed in Table 3.2 must be satisfied before such material can be valid.

Table 3.1: Nonzero engineering constants for different materials

S/N	Material	Nonzero engineering constants	
		Independent	**Dependent**
1	Isotropic	$E_1 = E$	$E_2 = E_3 = E,\ \ \nu_{13} = \nu_{23} = \nu$
		$\nu_{12} = \nu$	$G_{23} = G_{13} = G_{12} = \dfrac{E}{2(1+\nu)}$
2	Transversely isotropic	E_1, E_2	$E_3 = E_2,\ \ G_{13} = G_{12}$
		G_{12}	$G_{23} = \dfrac{E_2}{2(1+\nu_{23})}$
		$\nu_{12},\ \nu_{13}$	$\nu_{13} = \nu_{12}$
3	Orthotropic	E_1, E_2, E_3	
		G_{23}, G_{13}, G_{12}	
		$\nu_{12}, \nu_{13}, \nu_{23}$	
4	Monoclinic	E_1, E_2, E_3	
		G_{23}, G_{13}, G_{12}	
		$\nu_{12}, \nu_{13}, \nu_{23}$	
		$\nu_{16}, \nu_{26}, \nu_{36}, \nu_{45}$	

Table 3.2: Constraints on engineering constants for different materials

S/N	Material	Constraint
1	Isotropic	$E_1 > 0$
		$-1 < \nu_{12} < 0.5$
2	Transversely isotropic	$E_1 > 0, E_2 > 0, G_{12} > 0$
		$-1 < \nu_{23} < 1 - 2\dfrac{E_2}{E_1}\nu_{12}^2$
		$\nu_{12}^2 < \dfrac{E_1}{E_2}$
3	Orthotropic	$E_1 > 0, E_2 > 0, E_3 > 0$
		$G_{23} > 0, G_{13} > 0, G_{12} > 0$
		$1 - \nu_{23}^2\dfrac{E_3}{E_2} - \nu_{12}^2\dfrac{E_2}{E_1} - 2\nu_{12}\nu_{13}\nu_{23}\dfrac{E_3}{E_1} - \nu_{13}^2\dfrac{E_3}{E_1} > 0$
		$\nu_{23}^2 < \dfrac{E_2}{E_3}, \nu_{13}^2 < \dfrac{E_1}{E_3}, \nu_{12}^2 < \dfrac{E_1}{E_2}$

3.4 Stiffness Matrices of Laminates

Generally, laminated composite structures are analyzed based on the laminated plate theory. As a result, thin laminates consist of three distinct stiffness matrices represented by $[A]$, $[B]$ and $[D]$ and they are functions of stacking sequence of all plies, geometry and material properties [65]. In addition, matrix $[D]$ depends on stacking sequence unlike matrix $[A]$ [67] while matrix $[B]$ will become zero when laminate is symmetric [3, 6, 73, 74]. Hence, when $[B]$ becomes zero, it is an indication that the midplane and reference plane are coincided. Similarly, $A_{i6} = B_{i6} = D_{i6} = 0$ when $i = 1, 2$ for cross-ply laminate [1, 24, 33, 74]. However, According to [73], A_{i6} and D_{i6} should not be neglected in analysis when they are not equal to zero no matter how small their values because they can make considerable difference in the results to be obtained. These matrices properties show that in the analysis of laminated composite structures, matrices $[A]$ and $[D]$ will always involve while matrix $[B]$ may or may not involve due to the classification of the laminate under consideration. Besides, the value of each element in these matrices can be higher or lower based on the assumption adopted under the laminated plate theory. These different assumptions will be dealt with in Chapter 5.

Moreover, for general structure, the detail can be obtained in literature and how the elements A_{ij}, B_{ij} and D_{ij} of each of these matrices can be obtained from a laminated composite pipe is presented here based on the works of [68, 72, 73, 75]. A small part of a laminate with N layers is shown in Fig. 3.4 in which h is the total thickness of the laminate while h_k is the thickness of the k_{th} layer. Also, z_k is the directed distance to

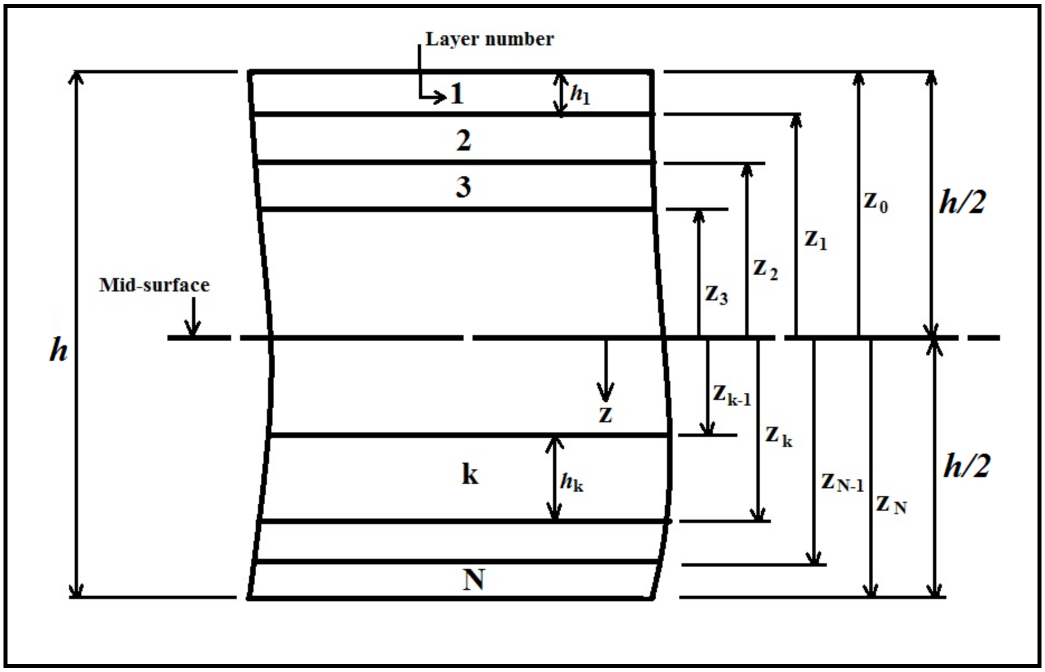

Figure 3.4: Part of a geometry of N-layers laminate

the bottom of the k_{th} layer and z_{k-1} is the directed distance to the top of the k_{th} layer. Hence, $z_k\ (k = 0,1,2,....,N)$ can be obtained as

$$\begin{aligned} z_0 &= -\frac{h}{2},\ z_1 = -\frac{h}{2} + h_1,\ \text{etc.} \\ z_N &= \frac{h}{2},\ z_{N-1} = \frac{h}{2} - h_N,\ \text{etc.} \end{aligned}, \tag{3.11}$$

It is imperative to know that if positive direction of z-axis was upward (opposite to what is in Fig. 3.4), then multiply the values of all the z_k obtained from Eq. (3.11) by minus sign in order to make them agree with z-axis direction. Hence, z_k can be positive or negative. In addition, z is general and it will becomes radius r when circular laminated composite structure (e.g. pipe) is to be considered. Thus, for laminated composite pipe, extensional stiffness A_{ij}, bending-coupling stiffness B_{ij} and bending stiffness D_{ij} can be obtained as

$$\begin{aligned} A_{ij} &= \int_{-h/2}^{h/2} \bar{\mathrm{Q}}_{ij}^{(k)} dr = \sum_{k=1}^{N} \bar{\mathrm{Q}}_{ij}^{(k)} (r_k - r_{k-1}) \\ B_{ij} &= \int_{-h/2}^{h/2} \frac{1}{2} \bar{\mathrm{Q}}_{ij}^{(k)} dr = \sum_{k=1}^{N} \frac{1}{2} \bar{\mathrm{Q}}_{ij}^{(k)} (r_k^2 - r_{k-1}^2) \\ D_{ij} &= \int_{-h/2}^{h/2} \frac{1}{3} \bar{\mathrm{Q}}_{ij}^{(k)} dr = \sum_{k=1}^{N} \frac{1}{3} \bar{\mathrm{Q}}_{ij}^{(k)} (r_k^3 - r_{k-1}^3) \end{aligned} \tag{3.12}$$

Besides, from Fig. 3.4,

$$h_k = r_k - r_{k-1}, \qquad \bar{r}_k = \frac{r_k + r_{k-1}}{2} \tag{3.13}$$

where $\bar{r}_k$ is the location of the centroid of the k_{th} lamina from the mid-plane/mid-surface of the laminate. Then, the expressions in Eq. (3.12) can be expanded as

$$\frac{1}{2}(r_k^2 - r_{k-1}^2) = \frac{(r_k + r_{k-1})}{2}(r_k - r_{k-1}) \tag{3.14}$$

$$\frac{1}{3}(r_k^3 - r_{k-1}^3) = (r_k - r_{k-1})\left(\frac{r_k + r_{k-1}}{2}\right)^2 + \frac{(r_k - r_{k-1})^3}{12} \tag{3.15}$$

Upon substituting Eq. (3.13) in Eqs. (3.14) and (3.15), they became

$$\frac{1}{2}(r_k^2 - r_{k-1}^2) = \bar{r}_k h_k \tag{3.16}$$

$$\frac{1}{3}(r_k^3 - r_{k-1}^3) = h_k \bar{r}_k^{\,2} + \frac{h_k^{\,3}}{12} \tag{3.17}$$

By substituting Eqs. (3.13), (3.16) and (3.17) in Eq. (3.12), it became

$$
\begin{aligned}
A_{ij} &= \int_{-h/2}^{h/2} \overline{\mathrm{Q}}_{ij}^{(k)} dr = \sum_{k=1}^{N} \overline{\mathrm{Q}}_{ij}^{(k)} (r_k - r_{k-1}) = \sum_{k=1}^{N} \overline{\mathrm{Q}}_{ij}^{(k)} h_k \\
B_{ij} &= \int_{-h/2}^{h/2} \frac{1}{2} \overline{\mathrm{Q}}_{ij}^{(k)} dr = \sum_{k=1}^{N} \frac{1}{2} \overline{\mathrm{Q}}_{ij}^{(k)} (r_k^2 - r_{k-1}^2) = \sum_{k=1}^{N} \overline{\mathrm{Q}}_{ij}^{(k)} \overline{r}_k h_k \\
D_{ij} &= \int_{-h/2}^{h/2} \frac{1}{3} \overline{\mathrm{Q}}_{ij}^{(k)} dr = \sum_{k=1}^{N} \frac{1}{3} \overline{\mathrm{Q}}_{ij}^{(k)} (r_k^3 - r_{k-1}^3) = \sum_{k=1}^{N} \overline{\mathrm{Q}}_{ij}^{(k)} \left(h_k \overline{r}_k^{\,2} + \frac{h_k^{\,3}}{12} \right)
\end{aligned}
\tag{3.18}
$$

Finally, Eq. (3.18) consists of different methods through which the elements in stiffness matrices can be obtained. These equations are very important to this study and it will be mentioned in the subsequent chapters.

Besides, it was assumed in this work that the layers in the laminate are bonded flawlessly, thickness of the laminate is small when compare to its remaining dimensions and delamination was not occurred before and after the pipe was attacked with thickness discontinuity.

CHAPTER 4

WAVELETS

4.1 Emergence of Wavelets

Wavelet analysis was introduced in 1987-88 as a new tool that emerged from mathematics and it has been adopted in different areas in science and engineering ever since, [76]. The analysis has played a significant role in area of engineering and several applications that include signal processing, data and image compression, solution of partial differential equations, statistics and modeling multiscale phenomena [76-84]. Multiscale processes or phenomena mean the structure of a physical system and a potential way of relating the structure. Also, multiscale representation is a selected representation for the ease of analyst because it offers a better depiction of information for calculation, storage and communication. Systematic and competent general representations are presented by wavelet analysis for a broad category of functions [76]. An essential option for capturing localized effects in many signals are offered by wavelets based representations. This is accomplished by employing representations through continuous transforms (double integrals) or discrete transforms (double series). The processes of scaling and shifting of a generating (mother) function are the influential to these representations. This remarkable mathematical development has benefited the field of vibration analysis in conjunction with vibration monitoring, system identification, damage detection, and quite a lot of other tasks [85].

According to [86], wavelet analysis was introduced firstly in seismology in order to provide a time dimension to seismic analysis which Fourier analysis lacked. Fourier analysis is not good for studying data with transient but appropriate for studying data that its statistical properties are invariant over time (stationary data). However, Wavelets were designed to be able to handle non-stationary data [85, 86]. Alfred Haar (Hungarian mathematician) was the first candidate in the wavelets that established functions that are now called Haar wavelets in 1909 [86, 87]. These functions consist merely of a short positive pulse followed by a short negative pulse. In teaching wavelet theory, the short pulses of Haar wavelets are exceptional but instead of smooth curves they yield jagged lines and this makes them less valuable for the majority of applications. After Haar wavelets, different communities came out with different versions of wavelet analysis the only thing they have in common is that further than individual specialized communities no one knew about them. This trend continues until 1984 when wavelet theory at last came into its own through Morlet and Grossmann. Yves Meyer who was generally acknowledged as one of the founders of wavelet theory was the first to recognize the connection between Morlet's wavelets and previous mathematical wavelets. A new kind of wavelet that has a mathematical property called orthogonality was also discovered by Meyer and this wavelet made the wavelet transform as simple to work with and manipulate as a Fourier transform. Orthogonality means that the information captured by one wavelet is totally autonomous of the information captured by another. In 1987, the ultimate greatest contribution in the wavelet revolution was emerged when Ingrid Daubechies discovered a whole new class of wavelets that were orthogonal (like Meyer's) and could be implemented using simple digital filtering ideas (short digital filters). The new wavelets were smooth without Jumps unlike Haar and they were almost as easy to program and use as Haar wavelets [86].

In the 1990s and 2000s, due to the popularity of wavelets there exist a large variety of standard wavelet basis functions and they include Haar, Daubechies, Coiflets and Mexican wavelets. However, because the basis function is normally meant to imitate localized information embedded in the signal, the selection of the wavelet basis is an essential issue [88].

Wavelet is defined as mathematical tools for waveform representations and segmentations, time-frequency analysis, and fast algorithms for easy implementation. For those signals that are periodic, a Fourier (or trigonometric) series is the standard mathematical tool for their representation. A mathematical model of the signal is provided by a finite sum (or truncation) of such an infinite series. The trigonometric models are formulated by taking the linear combinations of the trigonometric basis functions [89].

The principles of both signal addition and sequential shape representation are incorporated by wavelet analysis and this makes wavelets an appropriate method for signal analysis. Wavelet analysis represents signals by a series of orthogonal basis functions. The sinusoidal function is the basis function for Fourier analysis while the wavelet analysis basis function is mainly indeterminate with the exception that upon translation or dilation the basis function is localized and orthogonal onto itself [88].

The types of signals for which wavelet transforms are principally valuable include aperiodic, noisy, intermittent and transient signals. Applications of wavelet currently include condition monitoring of rotating machinery, crack surface characterization, seismic signal denoising, climate analysis, financial time series analysis, denoising of astronomical images, characterization of turbulent intermittency, heart monitoring, compression of medical and thump impression records, fast solution of partial differential equations, audio and video compression, computer graphics and many more [86]. The fast growing field is wavelets and it has being applied in almost all fields.

4.2 Wavelets Communities

In multi-resolution analysis (MRA) of data, several examples of functions (Fig. 4.1) can be used and they are regarded as wavelets. Those examples include [86]:

- *Dyadic translates and dilates of one junction: C*lassical wavelets.
- *Wavelet packets:* This is an extension of the classical wavelets and it can provide bases functions with better frequency localization.
- *Multi-wavelets:* This uses a finite number of wavelet functions instead of using one fixed function to translate and dilate for making basis functions
- *Second generation wavelets:* This provides extra flexibility which can be utilized to create wavelets adapted to irregular samples. Thus, the idea of translation and dilation is discarded.
- *Local trigonometric bases:* This makes use of cosines and sines defined on finite intervals combined with not only an easy but very great way to smoothly join the bases functions at the end points.

Moreover, there are families within the wavelets communities. While some wavelets are for continuous wavelet transform others are for discrete wavelet transform. The classical wavelets community consists of the following families [85, 86, 88]:

- Wavelets for continuous wavelet transform (Gaussian, Morlet, Mexican Hat see Fig. 4.1)

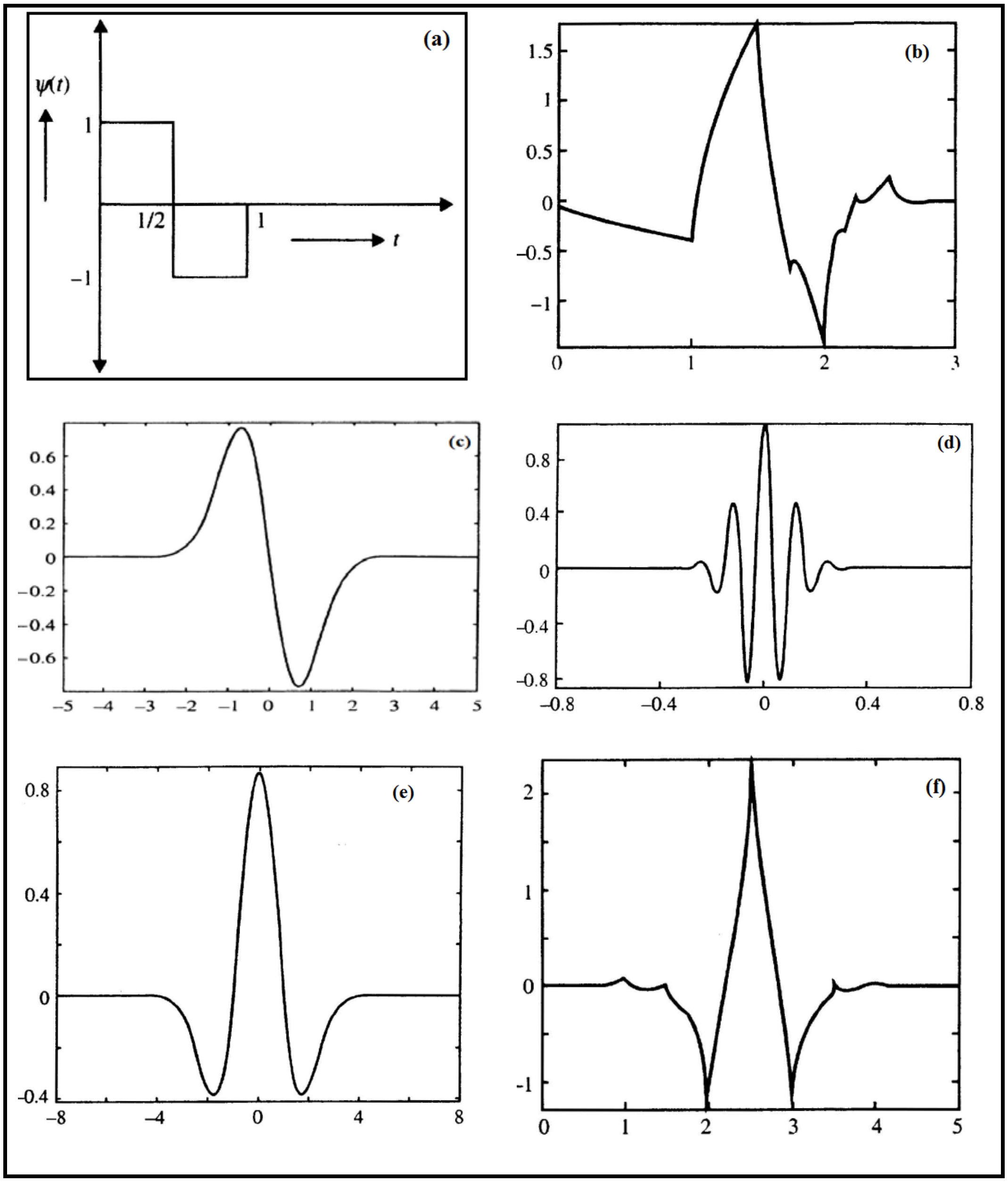

Figure 4.1: Graphs of several different types of wavelets: (a) Haar Wavelet (b) Daubechies' 4-tap Maxtlat wavelet (c) Gausian wavelet (d) Morlet wavelet (e) Mexican Hat wavelet and (f) Coiflet wavelet [86].

- Biorthogonal spline wavelets
- Complex wavelets
- Daubechies Maxflat wavelets
- Coiflets
- Symlets

Furthermore, wavelet means *small wave* and wavelet analysis is about analyzing signal with short period finite energy functions. Conversely, wavelength transform is defined as a tool that will slice data or functions or operators into various frequency components and then uses a resolution matched to its scale to study each component [80, 84]. Alternatively, wavelet transform is defined as transformation of the signal under investigation into another representation which presents the signal in a more valuable form. For signal analysis, there are varieties of wavelets that can be used but the choice of a particular wavelet depends on the type of application under consideration. There are several wavelet transforms and they include [84, 85, 90]:

1. The continuous wavelet transform: The translation and dilation parameters differ continuously over the real number.
2. The discrete wavelet transform (DWT): This transform map the continuous-time functions into a set of numbers much like the Fourier series maps continuous-time signals into a set of numbers.
3. The second type of wavelet transform maps continuous-time signals into functions much like the Fourier transform for continuous-time energy signals.
4. The last transform maps discrete-time signals into a set of numbers and it is similar to the discrete time Fourier series (DTFS).

4.3 Difference between Fourier and Wavelet Transforms

Fourier method can also be used in some areas where wavelets are being used. Even though there are four Fourier transforms, however, there are significant differences that make wavelets superior to Fourier method [78, 82, 88, 91, 92]:

1. Wavelets are mainly appropriate for analyzing systems involving suddenly varying functions.
2. Wavelets are localized in space, time and frequency unlike Fourier basis functions that localized in frequency domain only.
3. Due to wavelets localization in finite domains (compact support), they are more qualify for detecting both sharp irregularities and smooth oscillations in data.
4. No imaginary numbers are required in the calculation as a result they are computer-oriented method.
5. Wavelets can represent several groups of functions in a more compact way.
6. Wavelet transforms work better than Fourier transforms due to the following reasons [86]:

- In the computation they are much less sensitive to small errors.
- Unlike in wavelets, a smooth signal could be turn into a jumpy one or vice versa as a result of truncation or error of the Fourier coefficients.
- There are variety of wavelets unlike Fourier transform

4.4 Wavelets on the Interval [0,1]

In this section, the two wavelets (Trigonometric hermite and B-spline) considered in this work are discussed.

4.4.1 Trigonometric Hermite Wavelet (THW)

The THW are recognized to possess both good approximation characteristics of trigonometric function and multi-resolution, local characteristics of wavelet [93]. It has been utilized in the field of structural analysis by [93-95] to develop WBFEM. WBFEM was described to be a new numerical method using wavelet functions or scale functions as interpolation functions to construct the finite elements.

According to [93, 96], the scale functions of THW for any $j \in \mathbb{N}$ are defined

$$\Gamma^{0}_{j,0}(x)=\begin{cases}\dfrac{1}{2^{2j+1}}\dfrac{\sin^{2}(2^{j}x)}{\sin^{2}(x/2)} & x\notin 2\pi\mathbb{Z}\\ 1 & x\in 2\pi\mathbb{Z}\end{cases} \tag{4.1a}$$

$$\Gamma^{1}_{j,0}(x)=\begin{cases}\dfrac{1}{2^{2j+2}}\{1-\cos(2^{j+1}x)\}\cot\dfrac{x}{2} & x\notin 2\pi\mathbb{Z}\\ 1 & x\in 2\pi\mathbb{Z}\end{cases} \tag{4.1b}$$

The corresponding wavelet functions are

$$\psi^{0}_{j,0}(x)=\frac{1}{2^{j+1}}\cos(2^{j+1}x)+\frac{1}{3(2^{2j+1})}\sum_{l=2^{j+1}+1}^{2^{j+2}-1}(3(2^{j+1})-l)\cos(lx) \tag{4.2a}$$

$$\psi^{1}_{j,0}(x)=\frac{1}{2^{2j+3}}\sin(2^{j+2}x)+\frac{1}{3(2^{2j+1})}\sum_{l=2^{j+1}+1}^{2^{j+2}-1}\sin(lx) \tag{4.2b}$$

The node for the interpolation processes are equally spaced on the interval $[0,2\pi)$ with a dyadic step size:

$$x_{j,\delta}=\frac{\delta\pi}{2^{j}} \text{ for any } j\in\mathbb{N} \text{ and } \delta=0,1,........,2^{j+1}-1 \tag{4.3}$$

Then for s =0,1; $\Gamma^{s}_{j,\delta}(x)$ and $\psi^{s}_{j,\delta}(x)$ are defined as

$$\Gamma^{s}_{j,\delta}(x):=\Gamma^{s}_{j,0}(x-x_{j,\mu}) \text{ and } \psi^{s}_{j,\delta}(x):=\psi^{s}_{j,0}(x-x_{j,\delta}). \tag{4.4}$$

However, for example if $j=2$ and $\mathbb{Z}=1$, the scaling and wavelets functions $\Gamma^{s}_{j,\delta}$ and $\psi^{s}_{j,\delta}$ from Eqs. (4.1) and (4.2) for some δ are as shown in Figs. 4.2 and 4.3 in that order.

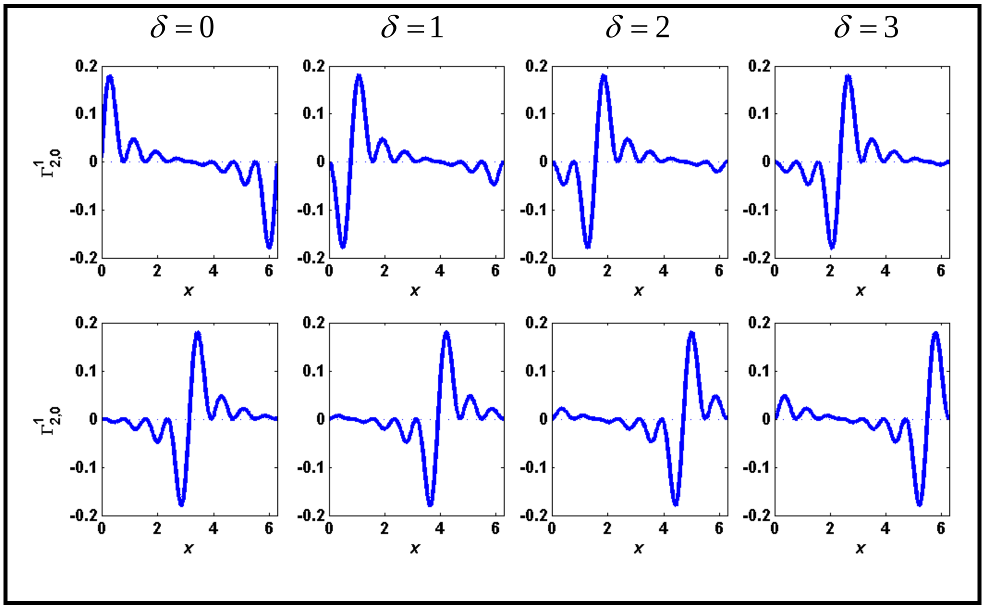

Figure 4.2: Scale functions $\Gamma^{0}_{2,0}$ and $\Gamma^{1}_{2,0}$

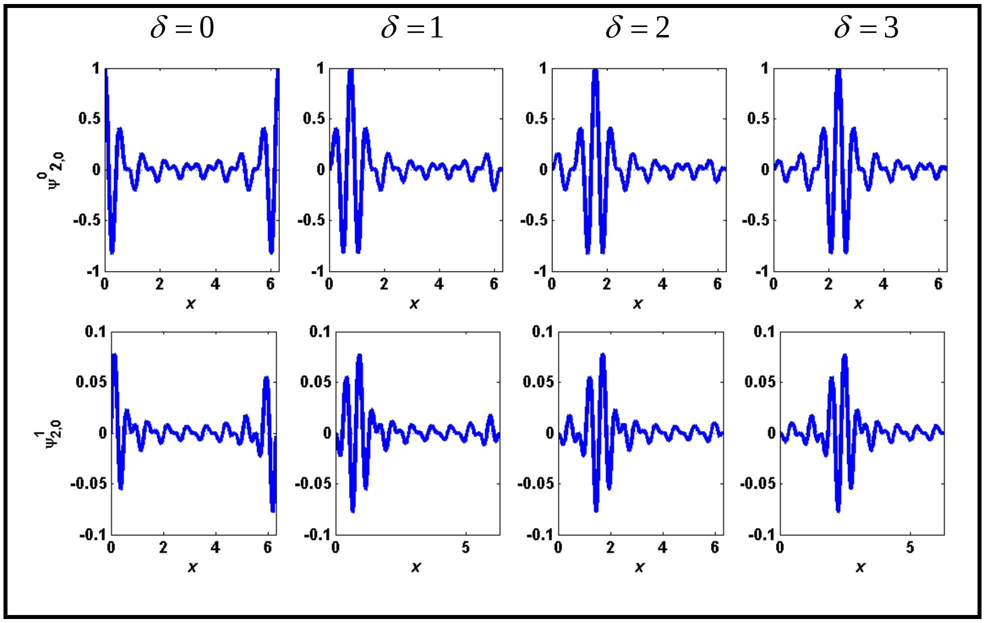

Figure 4.3: Wavelet functions $\psi^{0}_{2,0}$ and $\psi^{1}_{2,0}$

4.4.1.1 Interpolation Function based on Trigonometric Wavelets

One of the crucial steps in the finite element method is selection of interpolating functions. In order to construct finite element, wavelet finite element method utilizes wavelet or scale functions as interpolating functions. In the works of [93], the scale functions of trigonometric wavelets are employed as interpolation function for C^1 element in finite element method. Since the trigonometric wavelet is a periodic wavelet, to avoid the same results at the periodic points that are not required, they utilized only half a cycle of the trigonometric wavelet scale function and x was replaced by $x\pi$. Due to the translation modified scale function, the following groups of interpolation functions were then obtained [93-96]

$$\begin{aligned} &\Gamma^0_{j,n} = \cos^2\{(x-n)\pi\}\cos^2\{(x-n)\pi/2\} \\ &\Gamma^1_{j,n} = \sin\{(x-n)\pi\}\cos^2\{(x-n)\pi\}\cos^2\{(x-n)\pi/2\} \\ &0 \le x \le 1 \end{aligned} \tag{4.5}$$

where $\Gamma^s_{j,n}\,(s=0,1)$ have the following interpolatory properties:

$$\Gamma^s_{j,n}(0) = \begin{cases} 1 & \text{for } s=0 \text{ and } n=0 \text{ or } 1 \\ 0 & \text{else} \end{cases} \tag{4.6a}$$

$$\left\{\Gamma^s_{j,n}\right\}'(0) = \begin{cases} 1 & \text{for } s=1 \text{ and } n=0 \text{ or } 1 \\ 0 & \text{else} \end{cases} \tag{4.6b}$$

It is important to note that the higher the value of j in Eq. (4.3), the more the values of δ in Eq. (4.3) or values of $n=\delta/2$ in Eq. (4.5) and above all, the more the cost of computation when system matrices are to be computed. Thus, the scaling function with $j=1$ was considered in this study to avoid the consequences associated with higher value of j. Hence, by substituting $j=1$ in Eq. (4.3), the values of n will become $0, 1/2, 1, 3/2$

or $0,1/2,3/2,1$. The plot of the scaling functions of the trigonometric wavelet on the interval [0, 1] given in Eq. (4.5) is show in Fig. 4.4.

4.4.2 B-spline Wavelet

The B-spline wavelet is a piecewise defined polynomial with a compact support, which is normally represented by a linear combination of the basis functions. The B-wavelet is a linear combination of B-splines; thus the B-wavelet also has compact support. Although the orthogonal wavelets possess better numerical stability, they have poor smoothness and large support [97]. However, B-spline is semiorthogonal wavelet with compact support.

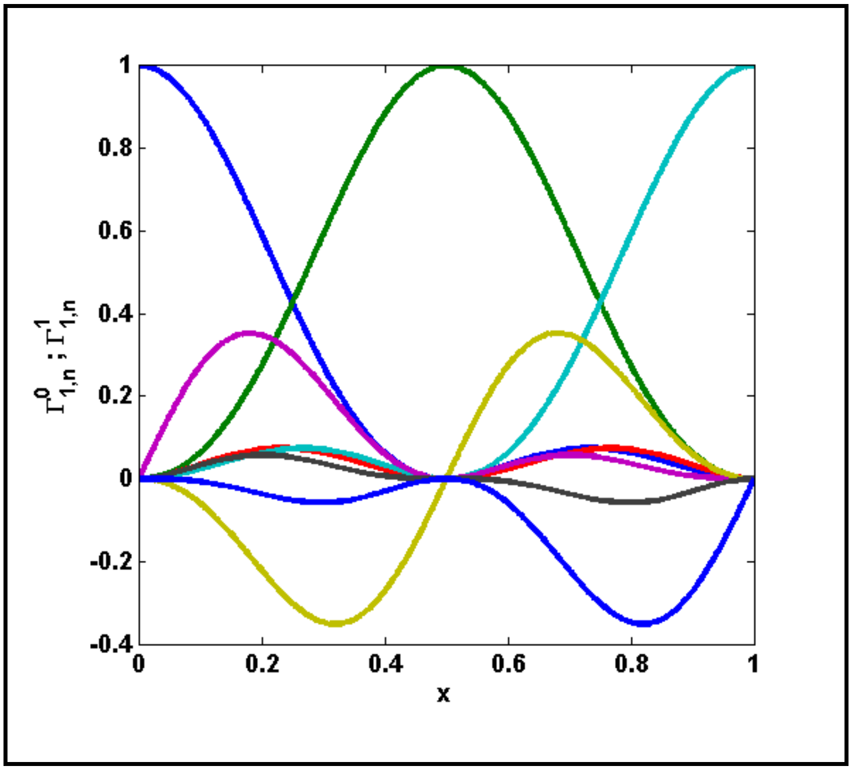

Figure 4.4: Scaling functions of trigonometric wavelet on the interval [0, 1]

In general, wavelets are manifested by some decomposition of the Hilbert space $L^2(\mathbb{R})$ into a nested sequence of subspaces. To construct wavelets, a set of scaling functions that generate MRA on the nested set of subspaces of the square integrable real space $L^2(\mathbb{R})$ are sought [97]. Typical scaling functions are the m^{th} order cardinal B-spline functions, which are polynomial functions with equally spaced knots. B-splines have the smallest possible support and B-spline wavelets of a given order m were found to achieve better approximation properties than other wavelets [98]. However, numerical instabilities may arise if the B-spline wavelets defined on $L^2(\mathbb{R})$ are utilized as interpolation functions [62, 99]. In order to alleviate this problem, Chui and Quak [100] introduced the B-spline wavelet on the bounded interval [0, 1], which is abbreviated by BSWI. Goswami et al. [101] utilized the BSWI to solve first-kind integral equations. B-spline employed in [100] are well-conditioned and can be easily adapted to the bounded interval by employing multiple knots at the endpoints. Hence, by the transformation $\zeta = (x - x_o)/(x_f - x_o)$, the function $g(\zeta)$ on interval $[x_o, x_f]$ can be transformed to the interval [0, 1]. One can then divide the interval [0, 1] into 2^j segments (where $j \in \mathbb{Z}^+$; $\mathbb{Z}^+ = 0,1,2,....$). If nodes are increased by $m-1$ at both endpoints, the resulting $2(m-1)$ nodes can be considered as multiple nodes, and the total node number becomes $(2^j + 2m - 1)$. Subsequently, the B-splines are constructed to the m^{th} order nested sequence of subspaces $V_j^{[0,1]}$, which are spanned by the basis functions [102]

$$B_{m,i}^j(\zeta) = N_m(2^j\zeta - i), \quad i = -m+1, ..., 2^j - 1 \tag{4.7}$$

where $N_m(2\zeta)$ is the cardinal splines with the support property $SuppB_{m,i}^j = [\zeta_i^j, \zeta_{m+i}^j]$. The MRA can be obtained on the interval [0, 1] if $\varphi_{m,i}^j(\zeta) = B_{m,i}^j(\zeta)$ where $\mathcal{d} = m-1$ is the smoothness order of the scaling functions $\varphi_{m,i}^{j}(\zeta)$. While m segments are occupied by support of the inner B-splines, $2m-1$ segments are occupied by the corresponding semi-orthogonal wavelets. Therefore, 2^j segments will be obtained on [0, 1] when $j>0$. Further, the following condition needs to be satisfied for one inner wavelet to have its support completely spanned by [0, 1]:

$$2^{j_o} \geq 2m-1, \quad j_o \in \mathbb{N} \tag{4.8}$$

The smallest value of j that satisfies Eq. (4.8) is j_o; i.e. $j \geq j_o$. For further details of the MRA on the interval, the reader is referred to [64, 101, 102]. The scaling functions $\varphi_{m,i}^{j}(\zeta)$ of m^{th} order B-spline wavelets on interval can be stated in the form introduced in [62]. These are restated here for completeness, as they are utilized in subsequent chapters.

$$\varphi_{m,i}^{j}(\zeta) = \begin{cases} \varphi_{m,i}^{q}(2^{j-q}\zeta); & \text{(0-boundary scaling functions)} \\ \quad i=-m+1,\ldots,-1 & \\ \varphi_{m,0}^{q}(2^{j-q}\zeta - 2^{-q}i); & \text{(inner scaling functions)} \\ \quad i=0,\ldots,2^j-m & \\ \varphi_{m,2^j-m-i}^{q}(1-2^{j-q}\zeta); & \text{(1-boundary scaling functions)} \\ \quad i=2^j-m+1,\ldots,2^j-1 & \end{cases} \tag{4.9}$$

and the corresponding wavelets $\psi_{m,i}^{j}(\zeta)$ are given by

$$\psi_{m,i}^{j}(\zeta) = \begin{cases} \psi_{m,i}^{q}(2^{j-q}\zeta); & \text{(0-boundary wavelets)} \\ i=-m+1,\ldots,-1 & \\ \psi_{m,0}^{q}(2^{j-q}\zeta - 2^{-q}i); & \text{(inner wavelets)} \\ i=0,\ldots,2^j-2m+1 & \\ \psi_{m,2^j-2m-i+1}^{q}(1-2^{j-q}\zeta); & \text{(1-boundary wavelets)} \\ \text{i}=2^j-2m+2,\ldots,2^j-m & \end{cases} \tag{4.10}$$

with their compact support defined by

$$\operatorname{supp}\psi_{m,i}^{j}(\zeta)=\begin{cases}[0,(2m-1+i)2^{-j}]; & \text{(0-boundary wavelets)}\\ [2^{-j}i,(2m-1+i)2^{-j}]; & \text{(inner wavelets)}\\ [2^{-j}i,1]; & \text{(1-boundary wavelets)}\end{cases} \tag{4.11}$$

The expressions in Eqs. (4.9) and (4.10) show that, there are $m-1$ boundary scaling and wavelet functions at the boundary points 0 and 1, in addition to 2^j-2m+2 inner wavelets and 2^j-m+1 inner scaling functions.

The scaling and wavelet functions for $q=0$ are directly obtained from the above equations. Generally, the BSWI of even order is commonly preferred in practical numerical calculations [61]. Thus, wavelets with $j=3$ and $m=4$ (cubic spline) was considered in this study. This is also due to the effectiveness and accuracy of this combination as demonstrated in the literature. In addition, according to Gallier [103], if d becomes large the curve construction tends to be excessively costly and may become computationally impossible. Moreover, the cubic spline represents an interpolation function that is continuous up to the second derivative. Unlike piecewise linear interpolation, the cubic spline interpolation gives smooth function approximation.

4.4.2.1 Interpolation Function based on B-spline Wavelet

Now, one may proceed to construct the scaling and wavelet functions on the interval. When $j\neq 0$, the functions $\varphi_{m,i}^{j}(\zeta)$ and $\psi_{m,i}^{j}(\zeta)$ can be obtained from Eqs. (4.9) and (4.10). For $m=4$, the condition in Eq. (4.8) results in $j_o=3$, which implies that in order to have one inner wavelet whose support lies completely in [0, 1], the minimum value for *j* is j_o; i.e. $j=3$. Accordingly, Eqs. (4.9) and (4.10) can be reconstructed for $j=3,\ m=4$ and $q=0$ to arrive at the following form:

$$\varphi_{4,i}^{3}(\zeta)=\begin{cases}\varphi_{4,i}^{0}(2^{3}\zeta); & \text{(0-bounary scaling functions)}\\ \quad i=-3,-2,-1 & \\ \varphi_{4,0}^{0}(2^{3}\zeta-1); & \text{(inner scaling functions)}\\ \quad i=0,1,2,3,4 & \\ \varphi_{4,2^{3}-4-i}^{0}(1-2^{3}\zeta); & \text{(1-bounary scaling functions)}\\ \quad i=5,6,7 & \end{cases} \tag{4.12}$$

$$\psi_{4,i}^{3}(\zeta)=\begin{cases}\psi_{4,i}^{0}(2^{3}\zeta); & \text{(0 boundary wavelets)}\\ \quad i=-3,-2,-1 & \\ \psi_{4,0}^{0}(2^{3}\zeta-i); & \text{(inner wavelets)}\\ \quad i=0,1 & \\ \psi_{4,2^{3}-6-i+1}^{0}(1-2^{3}\zeta); & \text{(1 boundary wavelets)}\\ \quad i=2,3,4 & \end{cases} \tag{4.13}$$

In order to generate the functions $\varphi_{4,t}^{0}(\zeta)$ and $\psi_{4,t}^{0}(\zeta)$ in Eqs. (4.12) and (4.13), one may simply utilize the data presented by Goswami et al. [101] for the scaling and wavelet functions for $j=0$ and $m=4$, respectively at $t=-3,-2,-1,0$. Consequently, the functions $\varphi_{4,i}^{3}(\zeta)$ and $\psi_{4,i}^{3}(\zeta)$ in Eqs. (4.12) and (4.13) are obtained for a given range of i. The expressions of the scaling functions $\varphi_{4,t}^{0}(\zeta)$ and $\varphi_{4,i}^{3}(\zeta)\ \forall i$ are given in the Appendices A and B, respectively. The scaling and wavelets functions for $j=3$ and $m=4$ are evaluated and displayed in Figs. 4.5 and 4.6 for length l_e respectively. These functions can be used as interpolation functions in FEM instead of classical polynomial functions.

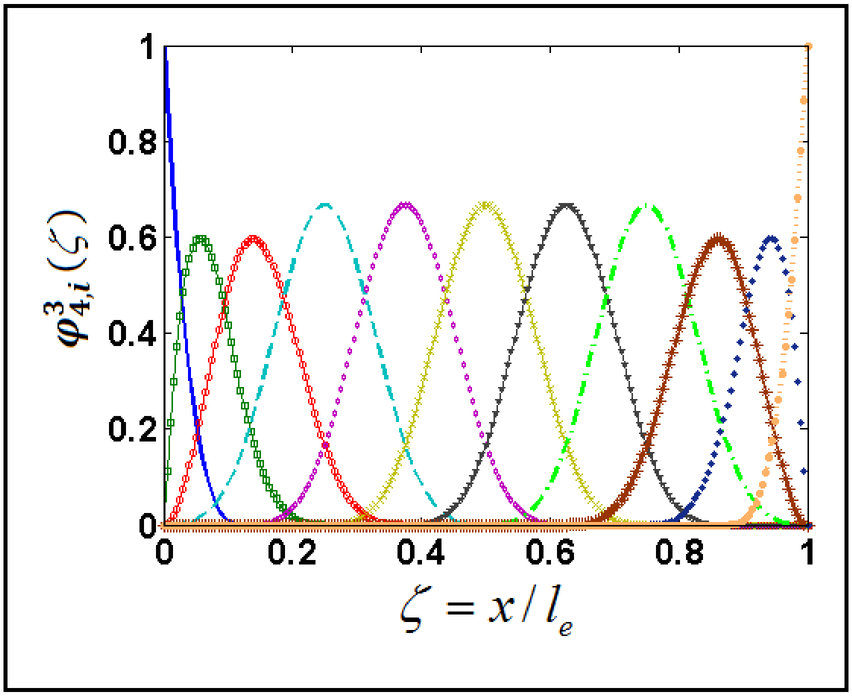

Figure 4.5: Scaling function of B-spline wavelet on the interval [0, 1]

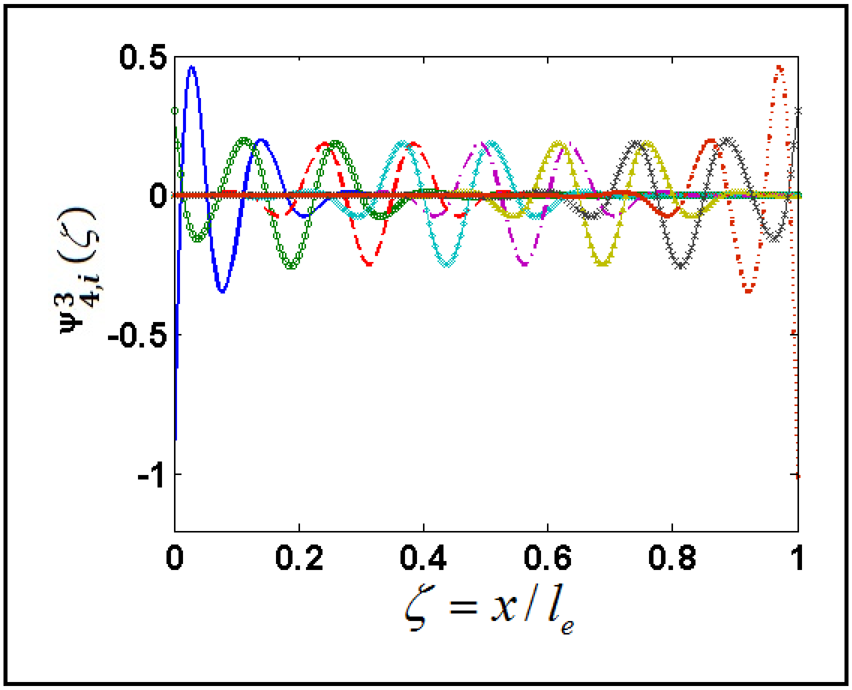

Figure 4.6: wavelet function of B-spline wavelet on the interval [0, 1]

4.5 Advantages of WBFEM over Conventional FEM

The conventional FEM is the most popular discretization technique and has been used for a very long time. However, due to the emergency of WBFEM with its superior accuracy, researchers became more inclined to prefer WBFEM over the conventional FEM. Thus, using the scale functions or wavelets functions as interpolation functions in FEM formulation give the WBFEM the following advantages [79, 82, 85, 93, 104-106]:

1. It requires smaller number of elements without compromising the accuracy.
2. It can reduce system degrees of freedom to a great extent, while retaining a high computational accuracy, especially for the free vibration and buckling analyses; compared to the traditional finite element that uses polynomial functions.
3. Wavelets have MRA property and different basis functions instead of polynomials for structure analysis.
4. It has high precision and fast convergence.
5. It has localization property in space, time and frequency.
6. It reduces computational time because it does not require denser mesh or higher order elements, even when dealing with high local gradient problems.
7. It can deal with the boundary conditions and connections between adjacent elements as the traditional finite element method.
8. Trigonometric wavelets make the best use of the high approximation accuracy of the trigonometric series.

4.6 Some Remarks on WBFEM

Despite the fact that wavelets can be used in almost all fields with excellent performance, wavelets still have their shortcomings. Yet, their favorable features overweigh their drawbacks. In WBFEM, computing stiffness matrix is more involved than in traditional FEM. For instance, when using THW it was observed that some computational difficulties exit due to the presence of sine and cosine functions. However, this can be handled by computing the matrices symbolically once and for all and then save them as functions. These functions will then be called whenever these matrices are required. Also, in WBFEM it is expected to use smaller number of elements, however if one decided to refine the elements, excessive refinement must be avoided when using THW to avoid computational difficulties. In addition, obtaining the connection coefficients is the major problem when using Daubechies wavelets in WBFEM, [78, 83, 93, 106, 107]. Similarly, like Daubechies, some of these wavelets have no explicit expressions [82]. However, in order to deal with such shortcomings, second-generation wavelets based on a lifting scheme have been introduced [76].

CHAPTER 5

DYNAMIC ANALYSIS OF LAMINATED COMPOSITE PIPE

5.1 Mechanics of Laminated Composite Pipes

The beam and plate theories are considered as classical strength of materials theories. In this context, the Euler-Bernoulli beam theory has been extended to Kirchhoff's plate theory in plate analysis [108]. Generally, laminated plate approach has being used to obtain stiffness of the composite structures. This may due to the fact that, the stress resultants in the classical laminated plate theory are the same as those acting on the wall of the beam [109]. As a result, this approach is employed in this work in which an infinitesimal section of plate of the laminated pipe with wall discontinuity shown in Fig. 5.1 is utilized as shown in Fig. 5.2. In addition to *x, y* and *z* global axes in Fig. 5.2, it also contains two set of local axes used for the laminate (segment) and ply (material) system. The laminate axes (*x, r, s*) are used to obtain the stiffness of laminate. These axes are inclined at angle θ to the pipe global y-axis and total stiffness of the composite pipe is obtained by integrating over the entire domain of θ. The ply axes (1, 2, and 3) are used to obtain stress-strain relation for each lamina that made up the section (see Fig. 5.2).

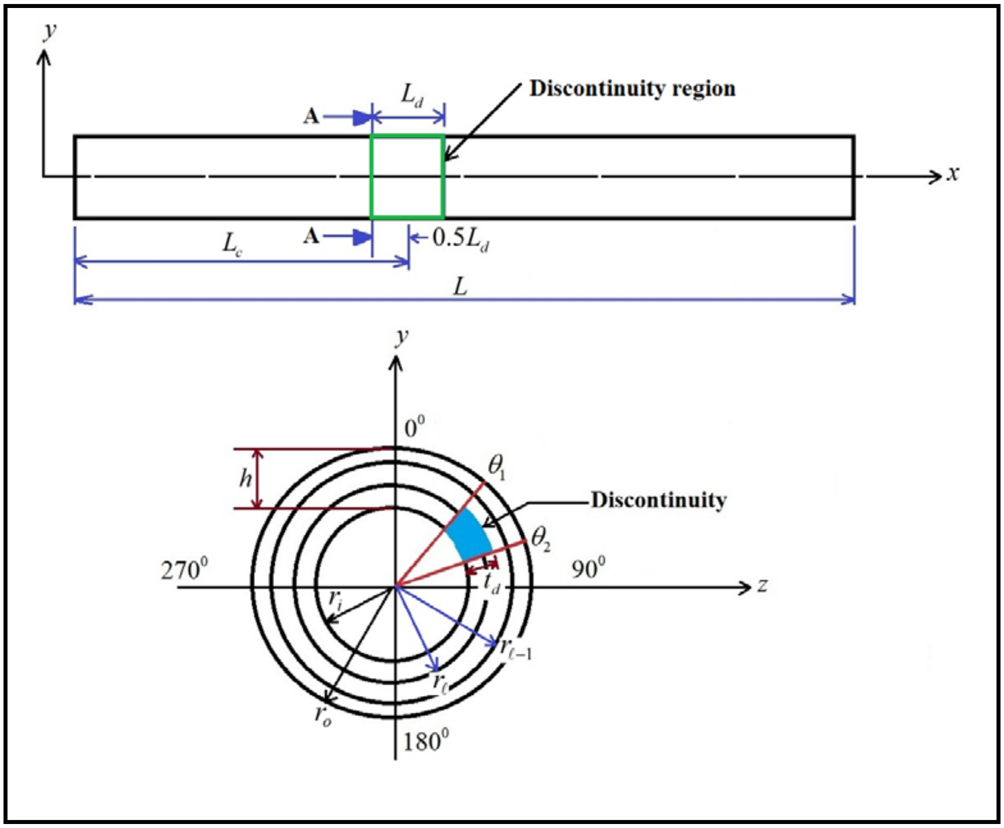

Figure 5.1: Composite pipe and its enlarged sectional view AA with discontinuity

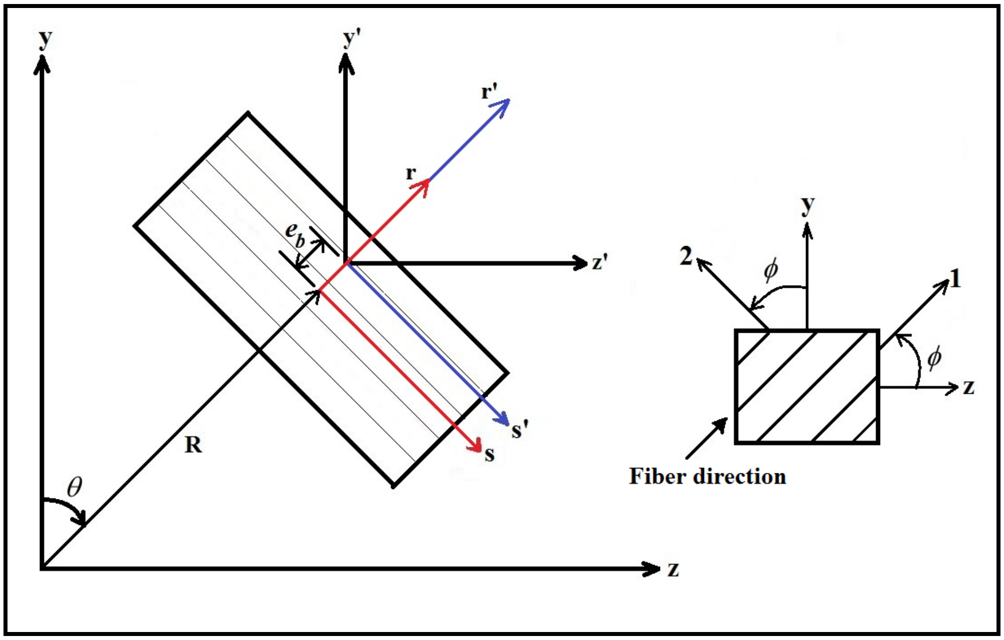

Figure 5.2: Enlarged Laminated pipe section

In orthotropic material analysis, each ply is treated as plate and this led to the usage of plane stress assumption. As a result, the relationship between stress and strain for orthotropic material is given by the generalize Hooke's law as

$$\begin{Bmatrix} \sigma_1 \\ \sigma_2 \\ \tau_{12} \end{Bmatrix} = \begin{bmatrix} \mathrm{Q}_{11} & \mathrm{Q}_{12} & 0 \\ \mathrm{Q}_{12} & \mathrm{Q}_{22} & 0 \\ 0 & 0 & \mathrm{Q}_{66} \end{bmatrix} \begin{Bmatrix} \varepsilon_1 \\ \varepsilon_2 \\ \gamma_{12} \end{Bmatrix} \tag{5.1}$$

where all elements in $[\mathrm{Q}]$ are as given in Eq. (3.9). Angle ϕ describes the orientation of each lamina with respect to the longitudinal direction. Thus, the constitutive relation transformed to the laminate system is given as [68, 70]

$$\{\sigma\} = [\bar{\mathrm{Q}}]\{\varepsilon\} \tag{5.2}$$

where $\{\sigma\} = [\sigma_x \quad \sigma_s \quad \tau_{xs}]^T$ and $\{\varepsilon\} = [\varepsilon_x \quad \varepsilon_s \quad \gamma_{xs}]^T$. The definitions of all elements in $[\bar{\mathrm{Q}}]$ are as defined in Eq. (3.10). The kinematic equations or strains at planes parallel to mid-plane surface of laminate are given according to the classical lamination theory as [70, 72]

$$\{\varepsilon\} = \{\varepsilon^0\} + r\{\kappa\} \tag{5.3}$$

Where $\{\varepsilon^0\} = [\varepsilon_x^0 \quad \varepsilon_s^0 \quad \gamma_{xs}^0]^T$ and $\{\kappa\} = [\kappa_x \quad \kappa_s \quad \kappa_{xs}]^T$ are strains at mid-plane (membrane strains) and change of slope (laminate curvature) of mid plane. Also, the force and moment resultants ($\{N\}$ and $\{M\}$) can be obtained. Upon substituting Eq. (5.3) in Eq. (5.2) and substitute the results obtained in force and moment resultants, constitutive equation will be produced which can be arranged as

$$\begin{Bmatrix} N_x \\ M_x \\ N_s \\ M_s \\ N_{xs} \\ M_{xs} \end{Bmatrix} = \begin{bmatrix} A_{11} & B_{11} & A_{12} & B_{12} & A_{16} & B_{16} \\ B_{11} & D_{11} & B_{12} & D_{12} & B_{16} & D_{16} \\ A_{12} & B_{12} & A_{22} & B_{22} & A_{26} & B_{26} \\ B_{12} & D_{12} & B_{22} & D_{22} & B_{26} & D_{26} \\ A_{16} & B_{16} & A_{26} & B_{26} & A_{66} & B_{66} \\ B_{16} & D_{16} & B_{26} & D_{26} & B_{66} & D_{66} \end{bmatrix} \begin{Bmatrix} \varepsilon_x^0 \\ \kappa_x \\ \varepsilon_s^0 \\ \kappa_s \\ \gamma_{xs}^0 \\ \kappa_{xs} \end{Bmatrix} \tag{5.4}$$

where N_x and N_s are axial forces, N_{xs} is in-plane shearing force, M_x and M_s are bending moments, and M_{xs} is twisting moment. The elements of coefficient matrix are from matrices $[A]$, $[B]$ and $[D]$. In composite laminates analysis, the most critical step is the formation of these three stiffness matrices. By employing Eq. (3.12) all the elements in coefficient or stiffness matrix in Eq. (5.4) for N plies will be obtained.

In addition, due to the inversion of Eq. (5.4) the compliance or flexibility matrix is obtained as

$$\begin{Bmatrix} \varepsilon_x^0 \\ \kappa_x \\ \varepsilon_s^0 \\ \kappa_s \\ \gamma_{xs}^0 \\ \kappa_{xs} \end{Bmatrix} = \begin{bmatrix} \alpha_{11} & \beta_{11} & \alpha_{12} & \beta_{12} & \alpha_{16} & \beta_{16} \\ \beta_{11} & \delta_{11} & \beta_{12} & \delta_{12} & \beta_{16} & \delta_{16} \\ \alpha_{12} & \beta_{12} & \alpha_{22} & \beta_{22} & \alpha_{26} & \beta_{26} \\ \beta_{12} & \delta_{12} & \beta_{22} & \delta_{22} & \beta_{26} & \delta_{26} \\ \alpha_{16} & \beta_{16} & \alpha_{26} & \beta_{26} & \alpha_{66} & \beta_{66} \\ \beta_{16} & \delta_{16} & \beta_{26} & \delta_{26} & \beta_{66} & \delta_{66} \end{bmatrix} \begin{Bmatrix} N_x \\ M_x \\ N_s \\ M_s \\ N_{xs} \\ M_{xs} \end{Bmatrix} \tag{5.5}$$

Besides, Ref. [110] assumed that the thin wall contour does not deform in its own plane and as a result it can be demonstrated that $\varepsilon_s^0 = \kappa_s = 0$. In addition, it was reported that for slender, thin-walled laminated beams/composites or when using the beam theory assumptions, it is proper to assume that $N_s = M_s = 0$ [70, 72, 109-111]. According to Ref. [110], the conditions $\varepsilon_s^0 = \kappa_s = 0$ will always true if and only if the beam cross sections are stiffened by ribs that are closely spaced. In the situation whereby there are no ribs or the cylindrical structure is being considered, they claimed that it is logical to assume $N_s = M_s = 0$. Similarly, it was also reported that this assumption will yield more accurate results than plane strain assumptions where $\varepsilon_s^0 = \kappa_s = 0$ [111]. Furthermore, the normal and shearing strains can be uncoupled [70, 111], this can be achieved by setting the bold elements in Eqs.(5.4) and (5.5) to zero. Hence, by applying $\varepsilon_s^0 = \kappa_s = 0$ to Eq. (5.4), $N_s = M_s = 0$ to Eq. (5.5) and assuming uncouple between normal and shearing strains in both equations, Eqs. (5.4) and (5.5) became

$$\begin{Bmatrix} N_x \\ M_x \\ N_{xs} \\ M_{xs} \end{Bmatrix} = \begin{bmatrix} A_{11} & B_{11} & 0 & 0 \\ B_{11} & D_{11} & 0 & 0 \\ 0 & 0 & A_{66} & B_{66} \\ 0 & 0 & B_{66} & D_{66} \end{bmatrix} \begin{Bmatrix} \varepsilon_x^0 \\ \kappa_x \\ \gamma_{xs}^0 \\ \kappa_{xs} \end{Bmatrix} \tag{5.6}$$

$$\begin{Bmatrix} N_x \\ M_x \\ N_{xs} \\ M_{xs} \end{Bmatrix} = \begin{bmatrix} \tilde{A}_{11} & \tilde{B}_{11} & 0 & 0 \\ \tilde{B}_{11} & \tilde{D}_{11} & 0 & 0 \\ 0 & 0 & \tilde{A}_{66} & \tilde{B}_{66} \\ 0 & 0 & \tilde{B}_{66} & \tilde{D}_{66} \end{bmatrix} \begin{Bmatrix} \varepsilon_x^0 \\ \kappa_x \\ \gamma_{xs}^0 \\ \kappa_{xs} \end{Bmatrix} \tag{5.7}$$

Nevertheless, it was stated that the uncoupled that was applied to Eqs. (5.4) and (5.5) is applicable only to antisymmetric angle-ply and cross-ply laminates that contain large number of plies [70]. Now, in order not to exclude the effects of normal and shearing strains, inverse of Eq. (5.5) needs to be done after N_s and M_s have been set to zero before uncoupled the equations. As a result, Eq. (5.5) yielded

$$\begin{Bmatrix} N_x \\ M_x \\ N_{xs} \\ M_{xs} \end{Bmatrix} = \begin{bmatrix} \vec{A}_{11} & \vec{B}_{11} & 0 & 0 \\ \vec{B}_{11} & \vec{D}_{11} & 0 & 0 \\ 0 & 0 & \vec{A}_{66} & \vec{B}_{66} \\ 0 & 0 & \vec{B}_{66} & \vec{D}_{66} \end{bmatrix} \begin{Bmatrix} \varepsilon_x^0 \\ \kappa_x \\ \gamma_{xs}^0 \\ \kappa_{xs} \end{Bmatrix} \tag{5.8}$$

It should be noted that while Eq. (5.6) did not undergo any inversion process, Eqs. (5.7) and (5.8) passed through two inversions. In addition, it was observed from these three equations that

$$A_{11} > \vec{A}_{11} > \tilde{A}_{11},\ \tilde{B}_{11} > \vec{B}_{11} > B_{11},\ D_{11} > \vec{D}_{11} > \tilde{D}_{11},\ A_{66} > \vec{A}_{66} > \tilde{A}_{66},\ \tilde{B}_{66} > \vec{B}_{66} > B_{66} \text{ or}$$
$$\left|B_{66}\right| > \left|\vec{B}_{66}\right| > \left|\tilde{B}_{66}\right|,\ D_{66} > \vec{D}_{66} > \tilde{D}_{66}$$

Eqs. (5.7) and (5.8) gave approximately the same results as number of layers in the laminate increases unlike Eq. (5.6). Also, these three equations gave roughly the same results for A_{66}, B_{66} and D_{66} as number of layers increases.

Moreover, Eq. (5.6), (5.7) and (5.8) for conciseness can be generalized to be

$$\begin{Bmatrix} N_x \\ M_x \\ N_{xs} \\ M_{xs} \end{Bmatrix} = \begin{bmatrix} A_x & B_x & 0 & 0 \\ B_x & D_x & 0 & 0 \\ 0 & 0 & A_{xs} & B_{xs} \\ 0 & 0 & B_{xs} & D_{xs} \end{bmatrix} \begin{Bmatrix} \varepsilon_x^0 \\ \kappa_x \\ \gamma_{xs}^0 \\ \kappa_{xs} \end{Bmatrix} \tag{5.9}$$

Henceforth, Eq. (5.9) is going to be focused because it gives the stiffness coefficients A_x, B_x, D_x, A_{xs}, B_{xs} and D_{xs} that needed to solve general bending and other problems in laminated composite structures.

Regarding the bending problem, in accordance with the equation that produced Eq. (5.9), the force N_x occurs at mid-surface s will cause a bending curvature κ_x [72]. Hence, in order to obtain the bending stiffness at neutral axis s' where there is no N_x, setting $N_x = 0$ in Eq. (5.9) and from the first two equations to be obtained $\varepsilon_x^0 = -B_x \kappa_x / A_x$ and

$$M_x = \bar{D}_x \kappa_x,\ \bar{D}_x = D_x - A_x \left(B_x / A_x\right)^2 \tag{5.10}$$

where $\bar{D}_x$ is the bending stiffness of the segment per unit length re-computed with respect to s'-axis. Similarly, if a state of deformation was assumed such that only $\varepsilon_x^0 \neq 0$ while all others equal zero, the first two equations in Eq. (5.9) produced

$$M_x = N_x (B_x / A_x) \tag{5.11}$$

Comparing Eq. (5.11) with definition of moment, it will be realized that

$$e_b = B_x / A_x \tag{5.12}$$

where e_b is the eccentricity (see Fig. 5.2) i.e., the location of neutral axis of bending s' where force N_x will create $\varepsilon_x^0 \neq 0$ without curvature. Also, substituting Eq. (5.12) in the second part of Eq. (5.10) produces

$$\bar{D}_x = D_x - A_x \left(B_x / A_x \right)^2 = D_x - A_x e_b^2 \tag{5.13}$$

5.2 Relationship between Mechanical Properties of Isotropic and Composite Structures

The relationship between the stiffness of isotropic and composite structures can be deduced from Eq. (5.9). The first two equations in Eq. (5.9) are

$$\begin{aligned} N_x &= A_x \varepsilon_x^0 + B_x \kappa_x \\ M_x &= B_x \varepsilon_x^0 + D_x \kappa_x \end{aligned} \tag{5.14}$$

Also, for isotropic structure,

$$\sigma = E\varepsilon \equiv E\varepsilon^0 \tag{5.15}$$

Substituting (5.3) in (5.15) leads to

$$\sigma = E\left(\varepsilon^0 + r\kappa\right) \tag{5.16}$$

Upon substituting Eq. (5.16) in force resultant equations in Eq. (5.4) and then compared the result produced to the first part of Eq. (5.14) showed that

$$A_x = \int_{-h/2}^{h/2} E_x dr, \; B_x = \int_{-h/2}^{h/2} E_x r dr \tag{5.17}$$

Where A_x and B_x are the laminate axial stiffness per unit length and the coupling between the twisting curvature κ_y and the shear force per unit length N_y [111]. Also, substituting Eq. (5.16) in moment resultant equations in Eq. (5.4) and compared the result to second part in Eq. (5.14) produced

$$D_x = \int_{-h/2}^{h/2} E_x r^2 dr \tag{5.18}$$

Thus, the results obtained from Eqs. (5.17) and (5.18) are tabulated in Table 5.1 for composite pipe with their equivalents in isotropic structure. Where A, b and h are area, width and thickness for the isotropic material.

Table 5.1: Equivalent isotropic structures stiffness per unit length.

Stiffness per unit length	**Composite as isotropic**	**Equivalent in isotropic**
A_x	Eh	EA/b
B_x	0	0
D_x	$Eh^3/12$	EI/b

5.3 Properties of the Laminated Composite Pipe

In Fig. 5.2, if laminate ds with respect to $s'-r'$ axis was considered, we can have

$$ds = Rd\theta \tag{5.19}$$

Consequently, according to the beam theory the second moment of areas and their products for isotropic structure using $s'-r'$ axis can be obtained. The bending stiffness of isotropic structure using $s'-r'$ axis will be produced when these moments are multiplying by E as

$$dEI_{s'} = \frac{Eh^3(ds)}{12},\ dEI_{r'} = \frac{Eh(ds)^3}{12},\ dEI_{s'r'} = 0 \tag{5.20}$$

Then, by substituting parameters in Table 5.1 along with Eq. (5.13) in Eq. (5.20), its equivalent for composite structure with respect to $s'-r'$ axis will be obtained as

$$d\widehat{EI}_{s'} = \overline{D}_x ds,\ d\widehat{EI}_{r'} = \frac{A_x(ds)^3}{12},\ d\widehat{EI}_{s'r'} = 0 \tag{5.21}$$

Furthermore, due to the rotation around $x-\text{axis}$ (in anticlockwise direction) with respect to $y'-z'$ axis, the mechanical moments of inertia and product of inertia of a segment are obtained. When the moments obtained are multiplied by E, the bending stiffnesses of the segment with respect to $y'-z'$ axes are produce as

$$\begin{aligned}
d\widehat{EI}_{z'} &= d\widehat{EI}_{s'}\cos^2\theta + d\widehat{EI}_{r'}\sin^2\theta - 2d\widehat{EI}_{s'r'}\cos\theta\sin\theta \\
d\widehat{EI}_{y'} &= d\widehat{EI}_{s'}\sin^2\theta + d\widehat{EI}_{r'}\cos^2\theta + 2d\widehat{EI}_{s'r'}\cos\theta\sin\theta \\
d\widehat{EI}_{y'z'} &= d\widehat{EI}_{s'r'}(\cos^2\theta - \sin^2\theta) + \left(d\widehat{EI}_{s'} - d\widehat{EI}_{r'}\right)\cos\theta\sin\theta
\end{aligned} \tag{5.22}$$

However, $d\widehat{EI}_{r'}$ can be neglected due to the fact that it contains higher order differential $(ds)^3$ [70]. Then, substituting Eq. (5.21) in Eq. (5.22) with $d\widehat{EI}_{r'} = 0$ leads to

$$\begin{aligned} d\widehat{EI}_{z'} &= \bar{D}_x \cos^2\theta ds \\ d\widehat{EI}_{y'} &= \bar{D}_x \sin^2\theta ds \\ d\widehat{EI}_{y'z'} &= \bar{D}_x \sin\theta\cos\theta ds \end{aligned} \tag{5.23}$$

Then, by employing the parallel axis theorem the bending stiffness of the segment per unit length $\mathcal{H}$ with respect to the global axes obtained as:

$$\begin{aligned} d\mathcal{H}_z &= d\widehat{EI}_{z'} + EA\left(y(s')\right)^2 \\ d\mathcal{H}_y &= d\widehat{EI}_{y'} + EA\left(z(s')\right)^2 \\ d\mathcal{H}_{yz} &= d\widehat{EI}_{y'z'} + EAz(s')y(s') \end{aligned} \tag{5.24}$$

and from Fig. 5.2

$$A = h(ds),\ \ y(s') = y(s) + e_b\cos\theta,\ \ z(s') = z(s) + e_b\sin\theta \tag{5.25}$$

where $z(s) = R\sin\theta,\ y(s) = R\cos\theta$. Upon substituting Eqs. (5.23) and (5.25) and parameter from Table 5.1 in Eq. (5.24), it becomes

$$\begin{aligned} d\mathcal{H}_z &= \left(\bar{D}_x\cos^2\theta + A_x\left(R\cos\theta + e_b\cos\theta\right)^2\right)ds \\ d\mathcal{H}_y &= \bar{D}_x\left(D_x\sin^2\theta + A_x\left(R\sin\theta + e_b\sin\theta\right)^2\right)ds \\ d\mathcal{H}_{yz} &= \left(\bar{D}_x\sin\theta\cos\theta + A_x(R\cos\theta + e_b\cos\theta)(R\sin\theta + e_b\sin\theta)\right)ds \end{aligned} \tag{5.26}$$

Hence, the bending stiffness of the composite pipe will be obtained by integrating Eq. (5.26) over the mid-surface using Eq. (5.19) with θ varying from θ_1 to θ_2 ($0^0 \le \theta_1 < \theta_2$ and $\theta_1 < \theta_2 \le 360^0$). Then, substituting Eqs. (5.19), (5.13) and (5.12) in Eq. (5.26) and integrate leads to

$$\begin{aligned} \mathcal{H}_z &= \mathcal{H}_y = \left(A_xR^3 + 2B_xR^2 + D_xR\right)\psi \\ \mathcal{H}_{yz} &= \frac{1}{2}(A_xR^3 + 2B_xR^2 + D_xR)\bar{\psi} \end{aligned} \tag{5.27}$$

where

$$R = \frac{D_o + D_i}{4}, \ \psi = \left[\frac{\theta}{2} + \frac{\sin 2\theta}{4} \right]_{\theta_1}^{\theta_2}, \ \bar{\psi} = \left[-\frac{1}{2}\cos(2\theta) \right]_{\theta_1}^{\theta_2}, 0^0 \le \theta_1 < \theta_2, \theta_1 < \theta_2 \le 360^0$$

It should be noted that Eq. (5.27) is applicable to composite pipe with/without wall discontinuity. For instance, for thin-walled composite pipe, $L_d = t_d = 0,\ \theta_1 = 0^0$ and $\theta_2 = 360^0$ for the part of laminate that does not contain discontinuity (see Fig. 5.1).

Furthermore, the mass per unit length $\mathcal{M}$ of the segment of the laminated composite pipe can be defined as

$$\mathcal{M} = \iint_{A_p} \rho_p dA_p = 2\pi \int_{r_i}^{r_o} \rho_k r dr = \sum_{k=1}^{N} \pi \rho_k (r_k^2 - r_{k-1}^2) \tag{5.28}$$

In addition, the rotational inertia γ can be expressed as

$$\gamma = \sum_{k=1}^{N} \rho_k I_k \tag{5.29}$$

and the second moment of area for k^{th} layer in the pipe can be described as

$$I_k = A_k \left[\frac{1}{16} \left(D_k^2 + D_{k-1}^2 \right) \right] \tag{5.30}$$

where A_k is the cross-sectional area of the k^{th} layer . Substituting Eq. (5.30) in Eq. (5.29) produced

$$\gamma = \sum_{k=1}^{N} \rho^{(k)} \frac{\pi}{4} \left(D_k^2 - D_{k-1}^2 \right) \left[\frac{1}{16} \left(D_o^2 + D_i^2 \right) \right] \tag{5.31}$$

Then, by substituting Eq. (5.28) in Eq. (5.31), it becomes

$$\gamma = \mathcal{M} D_m \tag{5.32}$$

where

$$D_m = (D_i^2 + D_o^2) / 16$$

Similarly, from Eq. (5.30), the second moment of area I_p for the laminated composite pipe can be expressed as

$$I_p = \sum_{k=1}^{N} I_k = \sum_{k=1}^{N} A_k (D_k^2 + D_{k-1}^2)/16 = \left[\sum_{k=1}^{N} A_k\right]\left[(D_o^2 + D_i^2)/16\right] = AD_m$$

from which

$$A = I_p / D_m \tag{5.33}$$

Multiplying Eq. (5.33) through by the shear modulus G resulted into

$$GA = GI_p / D_m \tag{5.34}$$

where

$$G = G_{12} \text{ or } G = G_e \tag{5.35}$$

Then, for laminated composite pipe of N layers

$$G_e = \sum_{k=1}^{N} \frac{E_k}{2(1+\nu_{12}^k)} \tag{5.36}$$

Besides, the equivalent modulus of elasticity $\bar{E}_k$ for k^{th} layer is given as [112, 113]

$$\bar{E}_k = \left[\frac{\cos^4 \phi_k}{E_1} + \left\{\frac{1}{G_{12}} - \frac{2\nu_{12}}{E_1}\right\}\cos^2 \phi_k \sin^2 \phi_k + \frac{\sin^4 \phi_k}{E_2}\right]^{-1} \tag{5.37}$$

Thus, $\bar{E}_k$ can be expressed using other data as $E_k = \bar{E}_k = \overline{\mathrm{Q}}_{11}^{k}$. In addition, GA can be stated differently, hence, upon substituting Eq. (5.36) in Eq. (5.34), it gives

$$G_A = GA = \left(\sum_{k=1}^{N} \frac{E_k}{2(1+\nu_{12}^k)}\right)\frac{I_p}{D_m} = \frac{E_p}{2(1+\nu_{12})}\frac{I_p}{D_m} \tag{5.38}$$

where

$$E_p = \sum_{k=1}^{N} E_k$$

but $\mathcal{H}_z = E_p I_p$, substituting it in Eq.(5.39) shows that

$$GA = \frac{\mathcal{H}_z}{2D_m(1+\nu_{12})} \tag{5.39}$$

However, since A_x, B_x and D_x can take different values based on Eqs. (5.6), (5.7), (5.8), (5.37) and (5.38), at least six models can be produced for obtaining stiffness terms of laminated composite structures. These models include $LCSS_1$, $LCSS_2$,....., $LCSS_6$ and they are defined as

$$\begin{aligned}
&LCS\ _1 : SA_x = A_{11},\ B_x = B_{11},\ D_x = D_{11} \\
&LCS\ _2 : SA_x = \tilde{A}_{11},\ B_x = \tilde{B}_{11},\ D_x = \tilde{D}_{11} \\
&LCS\ _3 : SA_x = \vec{A}_{11},\ B_x = \vec{B}_{11},\ D_x = \vec{D}_{11} \\
&LCSS_4 : LCSS_1 \text{ with } \overline{\mathrm{Q}}^{(\ell)} = \overline{E}_\ell \\
&LCSS_5 : LCSS_2 \text{ with } \overline{\mathrm{Q}}^{(\ell)} = \overline{E}_\ell \\
&LCSS_6 : LCSS_3 \text{ with } \overline{\mathrm{Q}}^{(\ell)} = \overline{E}_\ell
\end{aligned} \tag{5.40}$$

Nevertheless, the first four methods in Eq. (5.40) were considered in this dissertation.

5.4 Modeling of Composite Pipe using Wavelets on the Interval [0, 1]

In this section, the two Wavelets (trigonometric hermite and B-spline) discussed in Chapter 4 were used. In this case, the solving domain of laminated composite pipe like FRP pipe can be divided into subdomains, wherein each subdomain is mapped into the standard solving domain. The composite pipe of length L in Fig. 5.1 can be discretized into n_e number of element. When the scaling functions of the wavelets on the interval are used as interpolation functions, each element of length l_e can be subsequently divided equally into $\hbar$ segments with total number of nodes equals n_d. The $\hbar$ may be defined by the following general expression:

$$\hbar = 2^j + m - \mu,\ j \geq j_o\ ,\ n_d = \hbar + 1 \tag{5.41}$$

In the MRA, each element is divided into $\hbar$ segments with n_d nodes, which are associated with the proper degrees of freedom (DOF). In Chapter 4, the index i in the expressions for B-spline scaling functions can be written in a general form as $i = -m+1, -m+2, ..., 2^j - 1$. For the selected $m = 4$ and $j = 3$ in this study, the index i is equal to 11. This means that each element must have at least 11λ DOF, where $\lambda = 1, 2, ...$. In the case of Euler-Bernoulli beam, each of inner nodes (nodes between points $\zeta = 0$ and $\zeta = 1$) has 1 DOF, while each of the end nodes has 2 DOF. However, for Timoshenko beam, each node has 2 DOF. In order for Eq. (5.41) to produce a number of segments that is consistent with 11λ DOF, one needs to set $\mu = 4$ for EP, and $\mu = 2$ for TP.

In order to demonstrate the element segmentation, one of the elements is selected and its segments, nodes and nodal coordinates are shown in Fig. 5.3.

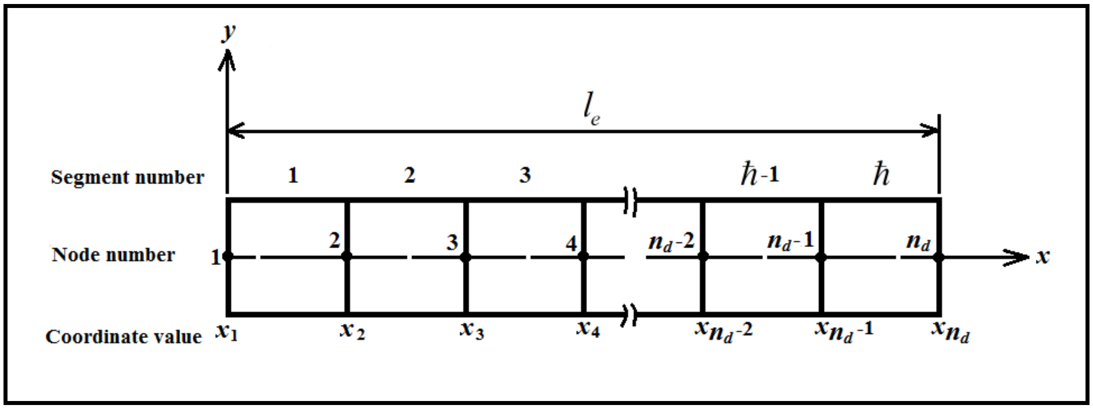

Figure 5.3: Segment numbers, node numbers and x coordinates on element of length l_e

If non-dimensional coordinate ζ is defined as

$$\zeta = (x - x_1)/l_e,\ dx = l_e d\zeta,\ 0 \le \zeta \le 1 \tag{5.42}$$

then, Eq. (5.42) maps x into the standard interval [0, 1]. Thus, for each node shown in Fig. 5.3 for element under consideration, Eq. (5.42) can be expressed as

$$\zeta_\varepsilon = (x_\varepsilon - x_1)/l_e,\ \varepsilon = 1, 2, ..., n_d \tag{5.43}$$

5.4.1 Euler-Bernoulli Pipe Element (EP)

The generalized potential energy function of the pipe element under the assumptions of the linear theory of elasticity as manifested by Euler-Bernoulli beam theory for a homogeneous beam (e.g. [93, 114]) can be restated for a composite FRP pipe as

$$\pi_p(\mathcal{W}) = \int_0^{l_e} \frac{\mathcal{H}(x)}{2}\left(\frac{d^2\mathcal{W}}{dx^2}\right)^2 dx - \frac{1}{2}\int_0^{l_e} \lambda \mathcal{M}(x)\mathcal{W}^2 dx \tag{5.44}$$

where $\lambda = \omega^2$. Substituting Eq. (5.42) in (5.44), one gets

$$\pi_p(\mathcal{W}) = \frac{1}{l_e^3}\int_0^1 \frac{\mathcal{H}(\zeta)}{2}\left(\frac{d^2\mathcal{W}}{d\zeta^2}\right)^2 d\zeta - \frac{1}{2} l_e \int_0^1 \lambda \mathcal{M}(\zeta)\mathcal{W}^2 d\zeta \tag{5.45}$$

The expressions of $\mathcal{H}(\zeta)$ and $\mathcal{M}(\zeta)$ are given in Eqs. (5.27) and (5.28), respectively.

5.4.1.1 EP with B-spline Wavelet Scaling Function (EP_1)

In Eq. (5.45), $\mathcal{W}(\zeta)$ is the only unknown field function which can be represented by the scaling functions of the B-spline wavelet on the interval as

$$\mathcal{W}(\zeta) = \sum_i^{\eta} \alpha_{m,i}^j \varphi_{m,i}^j(\zeta) = \{\Phi\}\{\Lambda\} \tag{5.46}$$

where

$$\eta = 2^j - 1,\ \ i = -m + 1$$

$$\{\Phi\} = \{\varphi^j_{m,-m+1}(\zeta) \quad \varphi^j_{m,-m+2}(\zeta) \quad \cdots \quad \varphi^j_{m,2^j-1}(\zeta)\}$$

$$\{\Lambda\} = \{\alpha^j_{m,-m+1} \quad \alpha^j_{m,-m+2} \quad \cdots \quad \alpha^j_{m,2^j-1}\}^T$$

Here, $\{\Phi\}$ and $\{\Lambda\}$ are the row vector of the scaling functions and the column vector of the wavelet coefficients, respectively. The elements in $\{\Phi\}$ were obtained from Eq. (4.12). Noting that Eq. (5.46) is in the wavelet-space, each of the two end nodes (nodes 1 and n_d in Fig. 5.3) according to Euler-Bernoulli beam theory has two degrees of freedom ($\mathcal{W}$ and $\Theta = d\mathcal{W}/dx$) in physical space to satisfy the compatibility of the displacement field $\mathcal{W}$. Thus, for Euler-Bernoulli beam $\mu = 4$ needs to be substituted in Eq. (5.41) to obtain $\hbar$ and n_d for each element as

$$\hbar = 2^j + m - 4,\ j \geq j_o\ ,\ n_d = \hbar + 1 \tag{5.47}$$

Accordingly, the total number of DOF per element is given by $n_d + 2$ and the vector of nodal DOF of the element is defined as

$$\{\mathcal{W}\}_e = \{\mathcal{W}_1 \quad \Theta_1 \quad \mathcal{W}_2 \quad \mathcal{W}_3 \quad \cdots \quad \mathcal{W}_{n_d-2} \quad \mathcal{W}_{n_d-1} \quad \mathcal{W}_{n_d} \quad \Theta_{n_d}\}^T \tag{5.48}$$

where

$$\Theta_1 = \frac{1}{l_e}\frac{d\mathcal{W}(\zeta_1)}{d\zeta},\ \ \Theta_{n_d} = \frac{1}{l_e}\frac{d\mathcal{W}(\zeta_{n_d})}{d\zeta}$$

The plot of scaling functions shown in Fig. 4.5 will change due to the theory employed. For the Euler-Bernoulli pipe element, this figure changed to Fig. 5.4.

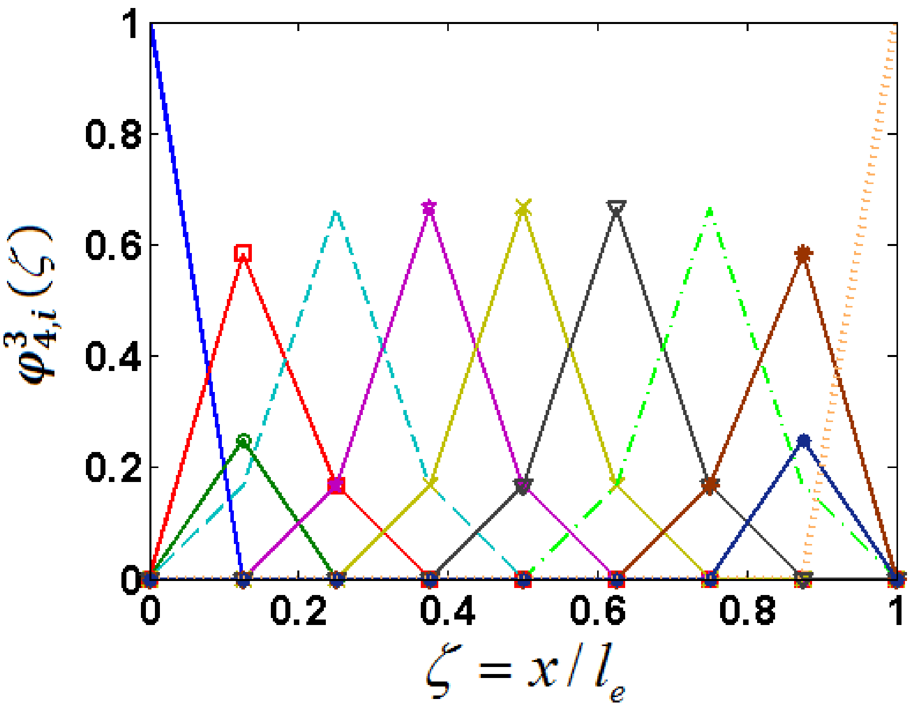

Figure 5.4: Scaling function on the interval [0, 1] for Euler beam l_e.

Substituting Eq. (5.43) into Eq. (5.46), one can write Eq. (5.48) in the form

$$\begin{Bmatrix} \mathcal{W}(\zeta_1) \\ \Theta(\zeta_1) \\ \mathcal{W}(\zeta_2) \\ \mathcal{W}(\zeta_3) \\ \vdots \\ \mathcal{W}(\zeta_{n_d-2}) \\ \mathcal{W}(\zeta_{n_d-1}) \\ \mathcal{W}(\zeta_{n_d}) \\ \Theta(\zeta_{n_d}) \end{Bmatrix} = \begin{bmatrix} \{\Phi(\zeta_1)\} \\ \frac{1}{l_e}\frac{\{\Phi(\zeta_1)\}}{d\zeta} \\ \{\Phi(\zeta_2)\} \\ \{\Phi(\zeta_3)\} \\ \vdots \\ \{\Phi(\zeta_{n_d-2})\} \\ \{\Phi(\zeta_{n_d-1})\} \\ \{\Phi(\zeta_{n_d})\} \\ \frac{1}{l_e}\frac{\{\Phi(\zeta_{n_d})\}}{d\zeta} \end{bmatrix} \begin{Bmatrix} \alpha^j_{m,-m+1} \\ \alpha^j_{m,-m+2} \\ \vdots \\ \alpha^j_{m,2^j-1} \end{Bmatrix} \tag{5.49}$$

Let the coefficient matrix in Eq. (5.49) be expressed as

$$[\Re_E] = \begin{bmatrix} \{\Phi(\zeta_1)\}^T & \left\{\dfrac{1}{l_e}\dfrac{\{\Phi(\zeta_1)\}}{d\zeta}\right\}^T & \{\Phi(\zeta_2)\}^T & \{\Phi(\zeta_3)\}^T \\ \cdots & \{\Phi(\zeta_{n_d-1})\}^T & \{\Phi(\zeta_{n_d})\}^T & \left\{\dfrac{1}{l_e}\dfrac{\{\Phi(\zeta_{n_d})\}}{d\zeta}\right\}^T \end{bmatrix}^T \tag{5.50}$$

Then, Eq. (5.49) can be rewritten in the augmented matrix form as

$$\{\mathcal{W}\}_e = [\Re_E]\{\Lambda\} \tag{5.51}$$

where

$$\{\Lambda\} = [T_E]\{\mathcal{W}\}_e,\ [T_E] = [\Re_E]^{-1} \tag{5.52}$$

By substituting Eq. (5.52) in Eq. (5.46), one gets

$$\mathcal{W}(\zeta) = [N_E]\{\mathcal{W}\}_e,\ [N_E] = \{\Phi\}[T_E] \tag{5.53}$$

Substituting (5.53) in Eq. (5.45) and rearranging yields

$$\begin{aligned} \pi_p(\mathcal{W}) = {} & \frac{1}{l_e^3}\int_0^1 \frac{\mathcal{H}(\zeta)}{2}\{\mathcal{W}\}_e^T[T_E]^T\left(\frac{d^2\{\Phi\}}{d\zeta^2}\right)^T\left(\frac{d^2\{\Phi\}}{d\zeta^2}\right)[T_E]\{\mathcal{W}\}_e\,d\zeta \\ & -\frac{l_e}{2}\int_0^1 \lambda\mathcal{M}(\zeta)\{\mathcal{W}\}_e^T[T_E]^T\{\Phi\}^T\{\Phi\}[T_E]\{\mathcal{W}\}_e\,d\zeta \end{aligned} \tag{5.54}$$

Utilizing the principle of minimum potential energy $(\delta\pi_p = 0)$, one obtains n_d equations. These can be expressed in the following matrix form:

$$\left([K]_e - \lambda[M]_e\right)\{\mathcal{W}\}_e = 0 \tag{5.55}$$

where

$$[K]_e = \frac{1}{l_e^3}\int_0^1 \mathcal{H}(\zeta)[T_E]^T\left(\frac{d^2\{\Phi\}}{d\zeta^2}\right)^T\left(\frac{d^2\{\Phi\}}{d\zeta^2}\right)[T_E]\,d\zeta$$

$$[M]_e = l_e\int_0^1 \mathcal{M}(\zeta)[T_E]^T\{\Phi\}^T\{\Phi\}[T_E]\,d\zeta$$

Eq. (5.55) is the eigenvalue problem of a laminated composite pipe without thickness discontinuity. In this case, one can simply apply the same procedure used in the conventional finite element method for handling the boundary conditions.

5.4.1.2 EP with Trigonometric Hermite Wavelet Scaling Function (EP_2)

In the previous sub section, the scaling function of B-spline wavelet was utilized to represent the unknown field $\mathcal{W}(\zeta)$ in Eq. (5.45). In this section, the scaling functions of trigonometric hermite wavelet were used. For trigonometric wavelet, Eq. (5.47) becomes $\hbar = 2^{j+1} - 1,\ j \in \mathbb{N}$, $n_d = \hbar + 1$ and for $j = 1$ (see Eq. (4.5)), $\hbar = 3$ and $n_d = 4$. Hence, $i = 1$, $\eta = 2n_d$ and Eq. (5.46) changed to

$$\mathcal{W}(\zeta) = \sum_{i=1}^{8} \beta_i \Gamma_i(\zeta) = \{\Phi\}\{\Lambda\} \tag{5.56}$$

where $\{\Lambda\}$ and $\{\Phi\}$ are as described earlier. The two vectors have smaller number of elements and they can be defined as

$$\{\Lambda\} = [\beta_1 \quad \beta_2 \quad \cdots \quad \beta_8]^T,\ \{\Phi\} = [\Gamma_1 \quad \Gamma_2 \quad \cdots \quad \Gamma_8] \tag{5.57}$$

in which

$$\Gamma_\alpha = \Gamma_{1,n}^{0}(\zeta);\ \Gamma_\delta = \Gamma_{1,n}^{1}(\zeta);\ \alpha = 1,3,5,7;\ \delta = 2,4,6,8$$

and the elements in $\{\Phi\}$ were obtained from Eq.(4.5).

Besides, the element shown in Fig. 5.3 under Trigonometric hermite wavelets was treated in such a way that two DOFs ($\mathcal{W}$ and $\Theta = d\mathcal{W}/dx$) were considered at each node leading to $2n_d$ total DOF per element. This will satisfy the compatibility of the displacement field $\mathcal{W}$. Then, the column vector of physical DOFs in each element can be expressed as

$$\{\mathcal{W}\}_e = \left[\mathcal{W}_1 \quad \Theta_1 \quad \mathcal{W}_2 \quad \Theta_2 \quad \mathcal{W}_3 \quad \Theta_3 \quad \mathcal{W}_4 \quad \Theta_4\right]^T \tag{5.58}$$

where

$$\Theta_p = \frac{1}{l_e}\frac{d\mathcal{W}(\zeta_p)}{d\zeta}, \;\; p = 1, 2, 3, 4$$

The results obtained by substituting Eq. (5.43) in Eq. (5.56) in order to compute each element in Eq. (5.58) were arranged as

$$\{\mathcal{W}\}_e = [T]\{\Lambda\} \tag{5.59}$$

where

$$[T] = \left[\{\Phi(\zeta_1)\}^T \quad \frac{1}{l_e}\frac{d\{\Phi(\zeta_1)\}^T}{d\zeta} \quad \{\Phi(\zeta_2)\}^T \quad \frac{1}{l_e}\frac{d\{\Phi(\zeta_2)\}^T}{d\zeta} \quad \cdots \right.$$
$$\left. \{\Phi(\zeta_3)\}^T \quad \frac{1}{l_e}\frac{d\{\Phi(\zeta_3)\}^T}{d\zeta} \quad \{\Phi(\zeta_4)\}^T \quad \frac{1}{l_e}\frac{d\{\Phi(\zeta_4)\}^T}{d\zeta} \right]^T$$

Also, one can have from Eq. (5.59)

$$\{\Lambda\} = [T_H]\{\mathcal{W}\}_e, \;\; [T_H] = [T]^{-1} \tag{5.60}$$

Substituting Eq. (5.60) into Eq. (5.56) yields

$$\mathcal{W}(\zeta) = \{N_T\}\{\mathcal{W}\}_e, \;\; \{N_T\} = \{\Phi\}[T_H] \tag{5.61}$$

However, by substituting Eq. (5.61) in Eq. (5.45), a new equations were produced that eventually resulted into new Eq. (5.55) in which

$$[K]_e = \frac{1}{l_e^3}\int_0^1 \mathcal{H}(\zeta)[T_H]^T \left(\frac{d^2\{\Phi\}}{d\zeta^2}\right)^T \left(\frac{d^2\{\Phi\}}{d\zeta^2}\right)[T_H]d\zeta$$

$$[M]_e = l_e\int_0^1 \mathcal{M}(\zeta)[T_H]^T\{\Phi\}^T\{\Phi\}[T_H]d\zeta$$

It becomes crucial to make it known that the size of each matrix for an element will be 11x11 and 8x8 for B-spline and Trigonometric hermite wavelets for EP respectively.

5.4.2 Timoshenko pipe element (TP)

If the composite pipe in Fig. 5.1 is treated under the hypothesis of Timoshenko beam theory [115], the generalized potential energy function including shear deformation and rotary inertia can be rewritten as

$$\begin{aligned}\pi_p(\mathcal{W},\Theta) = \frac{1}{2}\int_0^{l_e}\left[\mathcal{H}(x)\left(-\frac{d\Theta}{dx}\right)^2 + \frac{GA}{\kappa}\left(\frac{d\mathcal{W}}{dx}-\Theta\right)^2\right]dx \\ -\frac{1}{2}\int_0^{l_e}\lambda\left[\mathcal{M}(x)\mathcal{W}^2+\gamma(x)\Theta^2\right]dx\end{aligned} \tag{5.62}$$

where λ is as defined in Eq. (5.44). Substitute Eq. (5.42) in (5.62) yields

$$\begin{aligned}\pi_p(\mathcal{W},\Theta) = \frac{1}{2}\int_0^{1}\left[\mathcal{H}(\zeta)\frac{1}{l_e}\left(-\frac{d\Theta}{d\zeta}\right)^2 + \frac{GA}{\kappa}\left(\frac{1}{l_e}\left(\frac{d\mathcal{W}}{d\zeta}\right)^2 - 2\Theta\left(\frac{d\mathcal{W}}{d\zeta}\right)+l_e\Theta^2\right)^2\right]d\zeta \\ -\frac{1}{2}l_e\int_0^{1}\lambda\left[\mathcal{M}(\zeta)\mathcal{W}^2+\gamma(\zeta)\Theta^2\right]d\zeta\end{aligned} \tag{5.63}$$

$\mathcal{H}(\zeta)$, $\mathcal{M}(\zeta)$ and $\gamma(\zeta)$ are defined in Eqs. (5.27), (5.28) and (5.32), respectively, while G and GA are defined in Eqs. (5.35) and (5.38). The displacement fields $\mathcal{W}(\zeta)$ and $\Theta(\zeta)$ in Eq. (5.63) can be represented by the scaling functions of the B-spline wavelet on the interval. Accordingly, the deflection and rotation of the finite element are defined as

$$\mathcal{W}(\zeta) = \sum_{i=-m+1}^{2^j-1}\alpha_{m,i}^j\varphi_{m,i}^j(\zeta) = \{\Phi\}\{\Lambda\} \tag{5.64}$$

$$\Theta(\zeta) = \sum_{i=-m+1}^{2^j-1}\beta_{m,i}^j\varphi_{m,i}^j(\zeta) = \{\Phi\}\{\aleph\} \tag{5.65}$$

where

$$\{\Phi\} = \{\varphi_{m,-m+1}^j(\zeta) \quad \varphi_{m,-m+2}^j(\zeta) \quad \cdots \quad \varphi_{m,2^j-1}^j(\zeta)\}$$

$$\{\Lambda\} = \{\alpha_{m,-m+1}^j \quad \alpha_{m,-m+2}^j \quad \cdots \quad \alpha_{m,2^j-1}^j(\zeta)\}^T$$

$$\{\aleph\} = \{\beta^{j}_{m,-m+1} \quad \beta^{j}_{m,-m+2} \quad \cdots \quad \beta^{j}_{m,2^{j}-1}(\zeta)\}^{T}$$

Upon substituting $\mu = 2$ for the case of Timoshenko pipe in Eq. (5.41), the parameters $\hbar$ and n_d are determined for each element shown Fig. 5.3 as

$$\hbar = 2^{j} + m - 2, \; j \geq j_o \;, \; n_d = \hbar + 1 \tag{5.66}$$

The total number of DOF per element is $2n_d$ and the vectors of the element nodal coordinates are given by

$$\{\mathcal{W}\}_e = \{\mathcal{W}_1 \quad \mathcal{W}_2 \quad \cdots \quad \mathcal{W}_{n_d-1} \quad \mathcal{W}_{n_d}\}^{T} \tag{5.67}$$

$$\{\Theta\}_e = \{\Theta_1 \quad \Theta_2 \quad \cdots \quad \Theta_{n_d-1} \quad \Theta_{n_d}\}^{T} \tag{5.68}$$

Similarly, the plot of the scaling functions shown in Fig. 4.5 changed to Fig. 5.5 for TP. Substituting Eq. (5.43) in Eqs. (5.64) and (5.65), one can write Eqs. (5.67) and (5.68) as

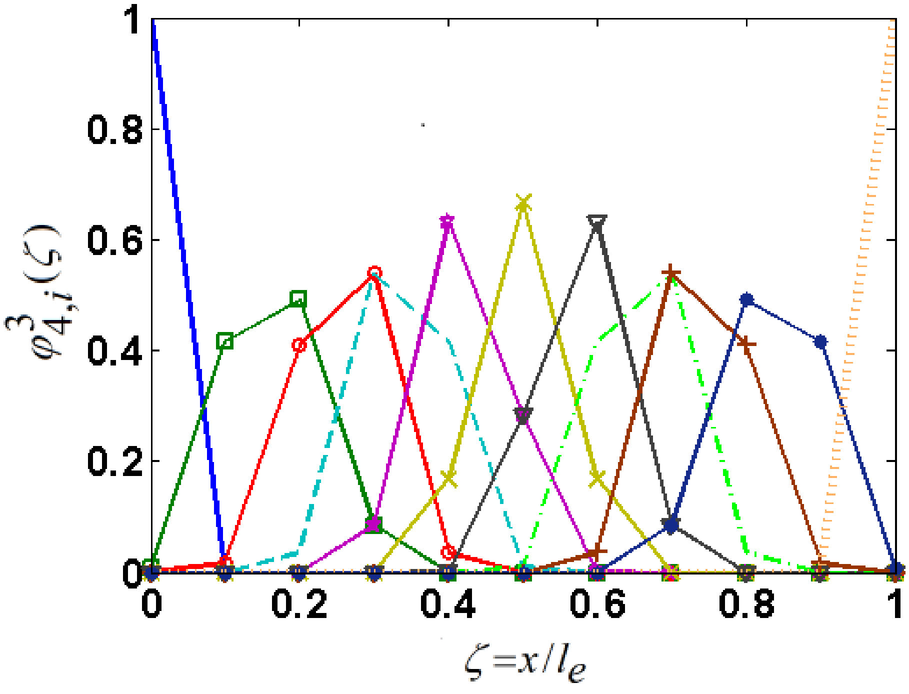

Figure 5.5: Scaling function on the interval [0, 1] for Timoshenko beam l_e.

$$\begin{Bmatrix} \mathcal{W}(\zeta_1) \\ \mathcal{W}(\zeta_2) \\ \vdots \\ \mathcal{W}(\zeta_{n_d-1}) \\ \mathcal{W}(\zeta_{n_d}) \end{Bmatrix} = \begin{bmatrix} \{\Phi(\zeta_1)\} \\ \{\Phi(\zeta_2)\} \\ \vdots \\ \{\Phi(\zeta_{n_d-1})\} \\ \{\Phi(\zeta_{n_d})\} \end{bmatrix} \begin{Bmatrix} \alpha^j_{m,-m+1} \\ \alpha^j_{m,-m+2} \\ \vdots \\ \alpha^j_{m,2^j-2} \\ \alpha^j_{m,2^j-1} \end{Bmatrix},$$
$$\begin{Bmatrix} \Theta(\zeta_1) \\ \Theta(\zeta_2) \\ \vdots \\ \Theta(\zeta_{n_d-1}) \\ \Theta(\zeta_{n_d}) \end{Bmatrix} = \begin{bmatrix} \{\Phi(\zeta_1)\} \\ \{\Phi(\zeta_2)\} \\ \vdots \\ \{\Phi(\zeta_{n_d-1})\} \\ \{\Phi(\zeta_{n_d})\} \end{bmatrix} \begin{Bmatrix} \beta^j_{m,-m+1} \\ \beta^j_{m,-m+2} \\ \vdots \\ \beta^j_{m,2^j-2} \\ \beta^j_{m,2^j-1} \end{Bmatrix} \tag{5.69}$$

Let

$$[\Re_T] = \left[\{\Phi(\zeta_1)\}^T \quad \{\Phi(\zeta_2)\}^T \quad \ldots \quad \{\Phi(\zeta_{n_d-1})\}^T \quad \{\Phi(\zeta_{n_d})\}^T \right]^T$$

then Eq. (5.69) can be expressed as

$$\{\mathcal{W}\}_e = [\Re_T]\{\Lambda\},\ \{\Theta\}_e = [\Re_T]\{\aleph\},$$

and

$$\{\Lambda\} = [T_T]\{\mathcal{W}\}_e,\ [T_T] = [\Re_T]^{-1} \tag{5.70}$$

$$\{\aleph\} = [T_T]\{\Theta\}_e \tag{5.71}$$

Utilizing Eqs. (5.70) and (5.71) in Eqs. (5.64) and (5.65), one obtains

$$\{\mathcal{W}\}(\zeta) = [N_T]\{\mathcal{W}\}_e,\ [N_T] = \{\Phi\}[T_T] \tag{5.72}$$

$$\Theta(\zeta) = [N_T]\{\Theta\}_e \tag{5.73}$$

Using Eqs. (5.72), (5.73) and (5.63), one can write the generalized potential energy function as

$$
\begin{aligned}
\pi_p(\mathcal{W},\ \Theta) = \frac{1}{2}\int_0^1 \Bigg[& \mathcal{H}(\zeta)\, \frac{1}{l_e}\{\Theta\}_e^T [T_T]^T \left(\frac{d\{\Phi\}}{d\zeta}\right)^T \left(\frac{d\{\Phi\}}{d\zeta}\right)[T_T]\{\Theta\}_e \\
& + \frac{GA}{\kappa}\left(\frac{1}{l_e}\{\mathcal{W}\}_e^T [T_T]^T \left(\frac{d\{\Phi\}}{d\zeta}\right)^T \left(\frac{d\{\Phi\}}{d\zeta}\right)[T_T]\{\mathcal{W}\}_e \right. \\
& - 2\{\Theta\}_e^T [T_T]^T \{\Phi\}^T \left(\frac{d\{\Phi\}}{d\zeta}\right)[T_T]\{\mathcal{W}\}_e \\
& \left. + l_e\{\Theta\}_e^T [T_T]^T \{\Phi\}^T \{\Phi\}[T_T]\{\Theta\}_e \right) \Bigg]\, d\zeta \\
& - \frac{1}{2} l_e \int_0^1 \lambda \Big[\mathcal{M}(\zeta)\{\mathcal{W}\}_e^T [T_T]^T \{\Phi\}^T \{\Phi\}[T_T]\{\mathcal{W}\}_e \\
& + \gamma(\zeta)\{\Theta\}_e^T [T_T]^T \{\Phi\}^T \{\Phi\}[T_T]\{\Theta\}_e \Big]\, d\zeta
\end{aligned}
\qquad (5.74)
$$

Invoking the principle of minimum potential energy $(\delta\pi_p = 0)$, the variations $\delta\pi_p / \partial\mathcal{W}_i$ and $\delta\pi_p / \partial\Theta_i$ vanish for all i; thus producing n_d equations, where $n_d = 11$ for $m = 4$ and $j = 3$.The n_d equations produced by $\delta\pi_p / \partial\mathcal{W}_i = 0$ can be arranged in matrix form as

$$
[K_{\mathcal{W}}^{1,1}]_e\{\mathcal{W}\}_e - [K_{\Theta}^{1,2}]_e\{\Theta\}_e - \lambda[M_{\mathcal{W}}]_e\{\mathcal{W}\}_e = 0 \qquad (5.75)
$$

where

$$
[K_{\mathcal{W}}^{1,1}]_e = \int_0^1 \frac{GA}{\kappa}\frac{1}{l_e}[T_T]^T \left(\frac{d\{\Phi\}}{d\zeta}\right)^T \left(\frac{d\{\Phi\}}{d\zeta}\right)[T_T]d\zeta
$$

$$
[K_{\Theta}^{1,2}]_e = \int_0^1 \frac{GA}{\kappa}[T_T]^T \left(\frac{d\{\Phi\}}{d\zeta}\right)^T \{\Phi\}[T_T]d\zeta \equiv [K_{\mathcal{W}}^{2,1}]_e^T
$$

$$
[M_{\mathcal{W}}]_e = \int_0^1 \Big[l_e\mathcal{M}(\zeta)[T_T]^T \{\Phi\}^T \{\Phi\}[T_T]d\zeta
$$

and $[K_{\mathcal{W}}^{1,1}]_e$, $[K_{\Theta}^{1,2}]_e$ and $[K_{\mathcal{W}}^{2,1}]_e$ are the element stiffness sub-matrices and $[M_{\mathcal{W}}]_e$ is the element mass sub-matrix. Similarly, the n_d equations resulting from $\delta\pi_p / \partial\Theta_i = 0$ are obtained as

$$[K_{\Theta}^{2,2}]_e\{\Theta\}_e - [K_{\mathcal{W}}^{2,1}]_e\{\mathcal{W}\}_e - \lambda[M_{\Theta}]_e\{\Theta\}_e = 0 \tag{5.76}$$

where

$$\begin{aligned}
[K_{\Theta}^{2,2}]_e &= \frac{1}{l_e}\int_0^1 \mathcal{H}(\zeta)[T_T]^T \left(\frac{d\{\Phi\}}{d\zeta}\right)^T \left(\frac{d\{\Phi\}}{d\zeta}\right)[T_T]\, d\zeta \\
&\quad + \int_0^1 \frac{GA}{\kappa} l_e [T_T]^T\{\Phi\}^T\{\Phi\}[T_T]\, d\zeta
\end{aligned}$$

$$[K_{\mathcal{W}}^{2,1}]_e = \int_0^1 \frac{GA}{\kappa}[T_T]^T\{\Phi\}^T\left(\frac{d\{\Phi\}}{d\zeta}\right)[T_T]d\zeta \equiv [K_{\Theta}^{1,2}]_e^T$$

$$[M_{\Theta}]_e = \int_0^1 l_e\,\gamma(\zeta)[T_T]^T\{\Phi\}^T\{\Phi\}[T_T]\,d\zeta$$

$[K_{\Theta}^{1,2}]_e$, $[K_{\Theta}^{2,2}]_e$ and $[K_{\mathcal{W}}^{2,1}]_e$ are the element stiffness sub-matrices and $[M_{\Theta}]_e$ is the element mass sub-matrix. Utilizing Eqs. (5.75) and (5.76), the eigenvalue problem is written as

$$\left([\bar{K}]_e - \lambda[\bar{M}]_e\right)\{\bar{\mathcal{W}}\}_e = 0 \tag{5.77}$$

where

$$[\bar{K}]_e = \begin{bmatrix} [K_{\mathcal{W}}^{1,1}]_e & -[K_{\Theta}^{1,2}]_e \\ -[K_{\mathcal{W}}^{2,1}]_e & [K_{\Theta}^{2,2}]_e \end{bmatrix}$$

$$[\bar{M}]_e = \begin{bmatrix} [M_{\mathcal{W}}]_e & [0] \\ [0] & [M_{\Theta}]_e \end{bmatrix}$$

$$\{\bar{\mathcal{W}}\}_e = \begin{bmatrix} \{\mathcal{W}\}_e & \{\Theta\}_e \end{bmatrix}^T \tag{5.78}$$

The matrices $[\bar{K}]_e$ and $[\bar{M}]_e$ are element stiffness and mass matrices. One may rearrange Eq. (5.78) in the following form:

$$\{W_e\} = \begin{bmatrix} \mathcal{W}_1 & \Theta_1 & \mathcal{W}_2 & \Theta_2 & \cdots & \mathcal{W}_{n_d-1} & \Theta_{n_d-1} & \mathcal{W}_{n_d} & \Theta_{n_d} \end{bmatrix}^T \tag{5.79}$$

Based on the rearrangement of the generalized nodal coordinates of Eq. (5.79), one can rewrite Eq. (5.77) as

$$\left([K]_e - \lambda [M]_e\right)\{W_e\} = 0 \tag{5.80}$$

where $[K]_e$ and $[M]_e$ are the corresponding element stiffness and mass matrices.

5.5 Programming the Wavelet-based Finite Element Scheme

The developed analytical model has been programmed using MATLAB code. In this context, the trigonometric hermite and the B-spline wavelets are generated. Further, the augmented mass and stiffness matrices are programmed in terms of the wavelets-based finite pipe element. Both Euler-Bernoulli and Timoshenko formulations are considered. The MATLAB code is written in a fairly general way that permits any type of boundary conditions, uniform pipe, stepped pipe, and any predetermined profile of the internal surface defect. The generalized eigenvalue problem, such as given by Eq. (5.80), is numerically assembled and solved to obtain the corresponding modal characteristics (eigenvalues and eigenvectors). The programmed numerical scheme also allows for performing dynamic response analysis by invoking the numerical integration routines of the Math library within MALAB. Besides, the program was developed in such a way that it can be easily updated to meet demands of each part of this investigation.

5.6 Numerical Results and Discussion

In this section, laminated composite pipes without thickness discontinuity were considered, while composite pipes with thickness discontinuities were considered in the subsequent chapters. In order to validate the accuracy of the developed finite element using Trigonometric hermite and B-spline wavelets on the interval, the pipe described in Table 5.2, which was modeled by several investigators using different beam and shell models was considered. The composite multilayer pipe is made of 10 layers with equal thickness. The results obtained by the present method together with other reported results for this pipe are presented in Table 5.3, wherein the results obtained by the present method using three elements are shown to have good agreement with other results. It was noted, according to [116] that the value of 98.65 Hz is the most accurate prediction of the first natural frequency of the pipe. In this case, the present method using the EP and TP with the generalized elastic moduli Q or E produced a much closer value to 98.65Hz than other reported methods in the table.

Table 5.2: Laminated composite pipe properties (Boron-epoxy) [113, 117, 118].

Property	**Value**
Mean diameter	126.9e-3m
Pipe thickness, h	1.321e-3m
Ply angles/ stacking sequence $(^{o})$	[90/ 45/ -45/0_6/90] (inner to outer layers)
Length of Pipe, L	2.470m
E_{11}	211 GPa
E_{22}	24.1 GPa
$G_{12} = G_{13} = G_{23}$	6.9 GPa
Poisson ratio, ν_{12}	0.36
Density, ρ	1967 kg / m^3

Table 5.3: Natural frequencies (Hz) of simply-supported pipe [113, 116].

Ref.	Authors	Frequency (Hz)	Method used
[**]	Zinberg, Symonds, 1970	91.67	Measured experimentally
	Dos Reis et al., 1987	82.37	Bernoulli–Euler beam theory. Stiffness determined by shell finite elements
	Kim and Bert, 1993	97.87	Sanders shell theory
		106.65	Donnell shallow shell theory
	Bert and Kim, 1995	96.47	Bresse–Timoshenko beam theory
	Singh and Gupta, 1996	95.78	Effective Modulus Beam Theory
	Chang et al., 2004	96.03	Continuum based Timoshenko Beam
	Qatu and Iqbal, 2010	95.4	Finite element analysis using ABAQUS
		102.47	Euler–Bernoulli beam theory
	Hajianmaleki and Qatu, 2011	95.89	Finite element analysis using ANSYS
		96.12	CBT using V-S
		94.71	SDBT using V-S
	Bert,1992	$98.65^{\$}$	Bernoulli–Euler beam theory
	Kim et al., 2004	91.43	Timoshenko beam model
Present study		98.11, 99.92	Present EP_1
		98.12, 99.91	Present EP_2
		99.58	Present TP

[**] stands for [113, 116]. $^{\$}$ most accurate according to [116]

For further numerical validation, a comparison that addresses the effect of the ply angle ϕ on the modal frequencies of a geometrically similar pipe (with material properties given in Table 5.4) is considered. The results reported by other researchers including results by the present method for different ϕ are presented in Table 5.5. It can be seen that the results obtained by present method are in very good agreement with the other reported solutions.

Table 5.4: Material properties (Graphite-epoxy) [113, 118].

Property	**Value**
Ply angles/ stacking sequence	$[\phi^o]$
E_{11}	$139\,\text{GPa}$
E_{22}	$11\,\text{GPa}$
$G_{12} = G_{13}$	$6.05\,\text{GPa}$
G_{23}	$3.78\,\text{GPa}$
Poisson ratio, ν_{12}	0.313
Density, ρ	$1578\,kg/m^3$

Table 5.5: Effect of ply angle on natural frequencies of simply-supported pipe.

Ref.	**Theory**	**Lamination angle (^{o})**						
		0	**15**	**30**	**45**	**60**	**75**	**90**
[113]	FEM analysis	100.28	68.8	45.51	35.9	31.96	30.57	30.27
	CBT approach	108.42	71.12	46.05	36.15	32.17	30.78	30.5
	SDBT approach	104.43	70.5	45.91	39.06	32.09	30.7	30.36
[118]	First-order beam theory	101.2	88.85	70.10	52.07	38.07	31.50	30.27
[116]	Bernoulli–Euler	108.68	NA	NA	NA	NA	NA	30.55
[**]	Sanders shell	92.12	72.75	50.13	39.77	35.33	33.67	33.22
	Bernoulli–Euler	107.08	89.88	71.15	52.85	38.2	31.42	30.22
	Bresse–Timoshenko	101.2	86.82	69.95	52.38	37.97	32.9	30.05
Present EP$_1$ ($\overline{Q}^{\ell}_{11} = \overline{E}_{\ell}$)		108.42	71.12	46.05	36.15	32.17	30.79	30.50
Present EP$_1$		108.76	102.30	84.89	62.04	41.95	32.13	30.60
Present EP$_2$		109.23	102.71	85.25	62.85	44.50	37.31	36.84
Present TP ($G = G_e$)		106.67	69.97	45.31	35.56	31.65	30.29	30.01
Present TP ($GA = G_A$)		105.35	69.10	44.75	35.12	31.26	29.92	29.64

[**] stands for [113, 116, 119]. NA refers to unavailable

Moreover, the three different definitions for the shear modulus G defined in Section 5.3 are examined. The computational significance of using different definitions of G on the natural frequencies of the two pipes (with properties given in Tables 5.2 and 5.4) is investigated and the results obtained are given in Tables 5.6 and 5.7. One can observe that the values of first frequency presented in Tables 5.6 and 5.7 are very close to those in Tables 5.3 and 5.5, respectively. This indicates that the different definitions of G lead to almost the same result. Also, it can be seen that all the results obtained using TP are lower than that of EP, which is attributed to the softening effect induced by shear and rotary inertia effects in Timoshenko beams.

Table 5.6: Natural frequencies of multi-layer simply-supported pipe.

Present study	**No. of element used**	**Natural frequency (Hz)**		
		1st	**2nd**	**3rd**
EP_1	3	99.92	399.80	900.84
EP_2	4	99.91	399.64	899.19
$\mathrm{EP}_1(\overline{\mathrm{Q}}_{11}^{\ell} = \bar{E}_{\ell})$ 、	3	95.77	383.09	861.97
$\mathrm{TP}(G = G_{12})$	3	89.54	284.28	503.38
$\mathrm{TP}(G = G_e)$	3	99.58	394.49	873.93
$\mathrm{TP}(GA = G_A)$	3	97.08	359.84	730.36

Table 5.7: Natural frequencies for single-layer simply-supported pipe.

Present study	**Lamination angle (^{o})**						
	0	**15**	**30**	**45**	**60**	**75**	**90**
EP_1	108.42	71.12	46.05	36.15	32.17	30.79	30.50
$\mathrm{TP}(G = G_{12})$	96.44	67.34	44.94	35.58	31.75	30.42	30.14
$\mathrm{TP}(G = G_e)$	106.67	69.97	45.31	35.56	31.65	30.29	30.01
$\mathrm{TP}(GA = G_A)$	105.35	69.10	44.75	35.12	31.26	29.92	29.64

In addition, the effect of boundary conditions on the natural frequencies was examined for the composite pipe described in Table 5.2. The pipe model used in ANSYS is shown in Fig. 5.6 while the results obtained by the present method as well as the conventional FEM using ANSYS are given in Table 5.8. It can be observed that the results obtained in the present study are very close to that of ANSYS except when $G=G_{12}$ where the results are lower. Besides, the results for the simply-supported case listed in Table 5.8 are in close agreement with those reported by other investigators in Table 5.3. In the present analysis, only three wavelet-based finite elements are used, while over 8000 elements were employed to generate the finite element mesh in ANSYS using 2D SHELL281 elements. In this context, as a result of wavelets MRA, the EP and TP models have 9 and 11 nodes per element, respectively. In terms of DOF, the 3-element mesh considered has 25 nodes (29 DOF) for the EP model and 31 nodes (62 DOF) for the TP model. However, in ANSYS the mesh has 26,640 nodes. Accordingly, the B-spline wavelet method demonstrated a great saving in computational time by consuming about 3% of the CPU time used by ANSYS.

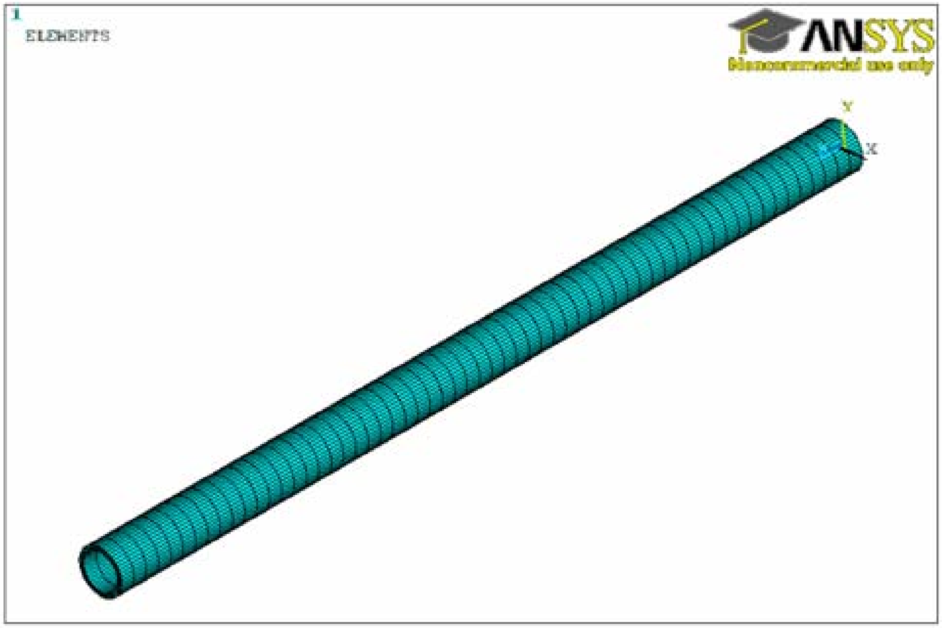

Figure 5.6: Laminated composite model in ANSYS using SHELL281.

Table 5.8: First natural frequency of composite pipe with different boundary conditions

Method	First Natural frequency (Hz)		
	SS	**CS**	**CF**
ANSYS	96.05	143.51	34.80
EP$_1$	99.92	156.09	35.60
EP$_2$	99.91	156.08	35.60
EP$_1$($\overline{Q}_{11}^{\ell} = \overline{E}_{\ell}$)	95.77	149.62	34.12
TP($G = G_{12}$)	89.54	120.55	33.69
TP($G = G_e$)	99.58	155.07	35.54
TP($GA = G_A$)	97.08	150.14	35.10

SS,CS and CF are Pinned-Pinned, Clamped-Pinned and Clamped-Free

Furthermore, the cardinal B-spline always has equal spacing between the knots [61, 97]. This equal spacing discretization scheme for both elements and knots is considered in the previous solutions. However, when elements of different lengths are considered, the entire pipe length will have knots with non-uniform separations. The effect of the non-uniform discretization using the developed wavelet-based element is examined and found to have no noticeable effect on the solutions.

Moreover, to complete the validation of the obtained modal characteristics, the first four mode shapes of the laminated composite pipe considered in Table 5.8, under different boundary conditions using EP, are obtained, normalized and displayed in Figs. 5.7 to 5.10. The mode shapes are constructed from the corresponding eigenvectors, which are normalized to highlight the pattern of the mode shapes rather than the relative amplitudes of different modes.

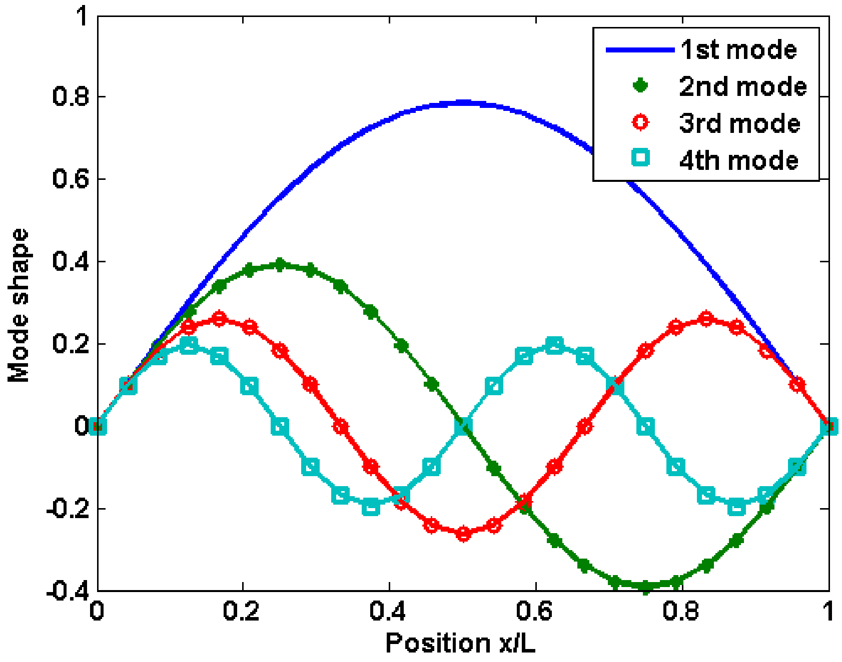

Figure 5.7: Mode shapes for SS composite pipe.

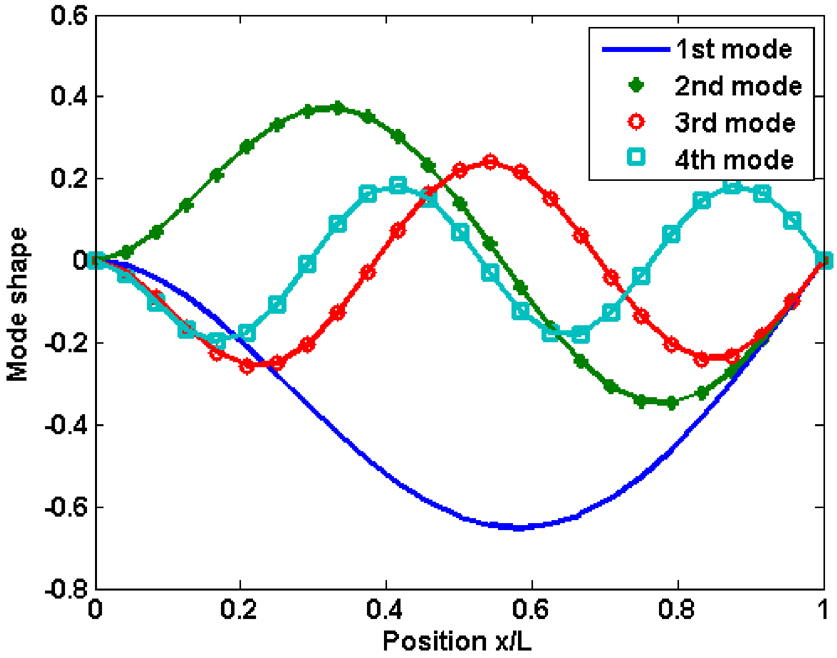

Figure 5.8: Mode shapes for CS composite pipe.

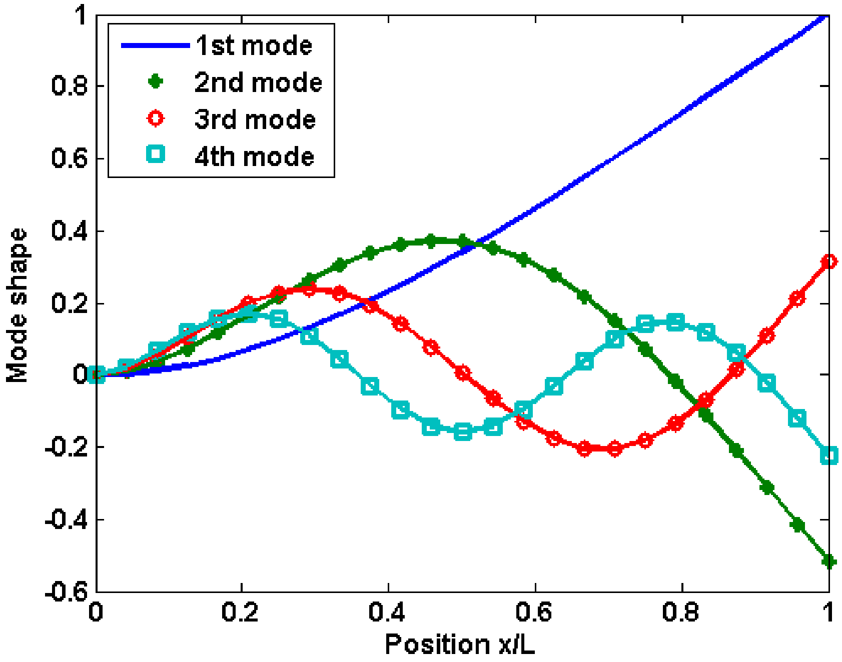

Figure 5.9: Mode shapes for CF composite pipe.

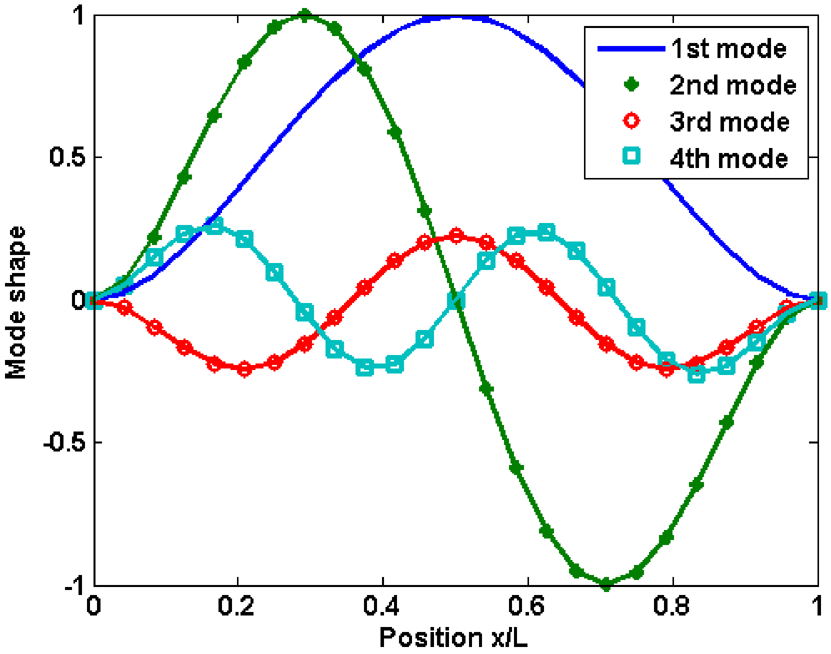

Figure 5.10: Mode shapes for CC composite pipe.

The obtained mode shapes are consistent with the pattern of the mode shapes obtained for a homogeneous beam-type structure. It is noted that the obtained mode shapes are almost identical to those obtained for the same composite pipe using the conventional FEM.

For further verification of the developed wavelet method, a third composite pipe (11-layer laminated glass reinforced epoxy pipe) with properties as given in Table 5.9 was studied. Using the EP, the first five natural frequencies are obtained for different boundary conditions and tabulated in Table 5.10. The obtained solution is in good agreement with ANSYS solution.

The effect of ply angle on natural frequency of the laminated composite structures was extended here. The two cases considered were laminated homogeneous and laminated composite pipes that are simply supported at both ends but both pipes have the same geometry. The data for both pipes are as shown in Tables 5.11 and 5.12 in that order and

ϕ range is from 0^0 to 90^0. The first natural frequency results obtained for each pipe using WBFEM and two types of ANSYS models are shown in Figs. 5.11-5.13.

Table 5.9: Laminated glass reinforced epoxy pipe material properties.

Property	**Value**
D_i	0.1016 m
D_o	0.1126 m
h	0.55e-2m
Ply angles/ stacking sequence $(^o)$	$[\pm 54_5 / 54]$ (inner to outer layers)
L	2 m
E_{11}	12.5 GPa
E_{22}	7. 1429GPa
$G_{12} = G_{13} = G_{23}$	3.3194 GPa
Poisson ratios: ν_{12}, ν_{21}	0.56, 0.32
Density, ρ	1730 kg / m^3

Table 5.10: First five natural frequencies of glass reinforced epoxy pipe.

Boundary Condition	**Authors**	**No. of element**	**Natural frequency (Hz)**				
			1	**2**	**3**	**4**	**5**
SS	EP_1	2	37.09	148.35	333.81	593.57	927.90
	EP_2	4	37.09	148.35	333.78	593.39	927.17
	ANSYS	8,880	36.03	136.95	359.18	571.87	945.82
CS	EP_1	2	57.94	187.76	391.78	670.14	1023.20
	EP_2	4	57.94	187.75	391.73	669.88	1022.21
	ANSYS	8,880	54.86	197.77	367.23	577.40	1025.80
CF	EP_1	2	13.21	82.80	231.85	454.39	751.38
	EP_2	4	13.21	82.80	231.84	454.31	751.01
	ANSYS	8,880	12.59	78.57	209.21	386.17	774.92

Table 5.11: Material properties of laminated homogeneous pipe.

Property	**Value**
D_i	0.1016 m
D_o	0.1126 m
h	0.55e-2m
Ply angles/ stacking sequence $(^o)$	$[\pm\phi_5 / \phi]$ (inner to outer layers)
L	2 m
E	12.5 GPa
Poisson ratios: ν	0.32
Density, ρ	1730 kg / m^3

Table 5.12: Material properties of laminated composite pipe.

Property	**Value**
D_i	0.1016 m
D_o	0.1126 m
h	0.55e-2m
Ply angles/ stacking sequence $(^o)$	$[\pm\phi_5 / \phi]$ (inner to outer layers)
L	2 m
E_{11}	12.5 GPa
E_{22}	7. 1429 GPa
$G_{12} = G_{13} = G_{23}$	3.3194 GPa
Poisson ratios: ν_{12}, ν_{21}	0.56, 0.32
Density, ρ	1730 kg / m^3

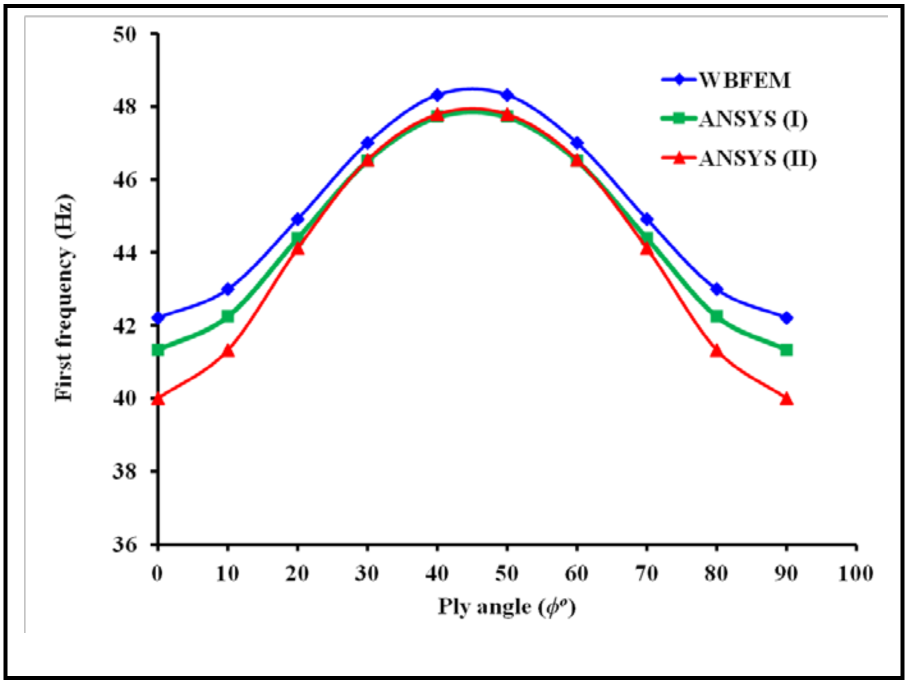

Figure 5.11: Effect of ply angle on natural frequency of laminated homogeneous pipe.

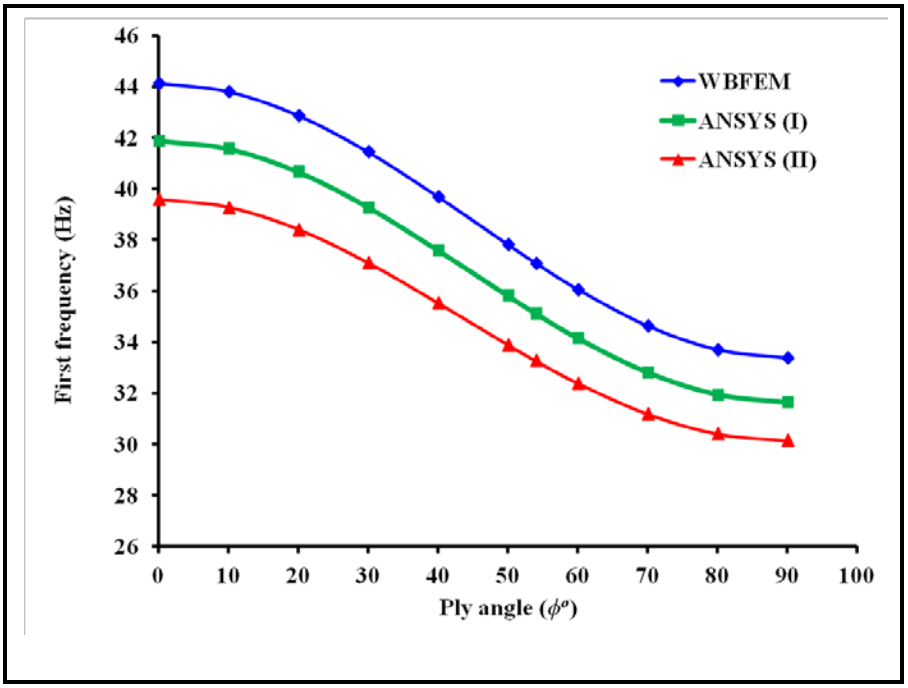

Figure 5.12: Effect of positive and negative ply angles on natural frequency of laminated composite pipe

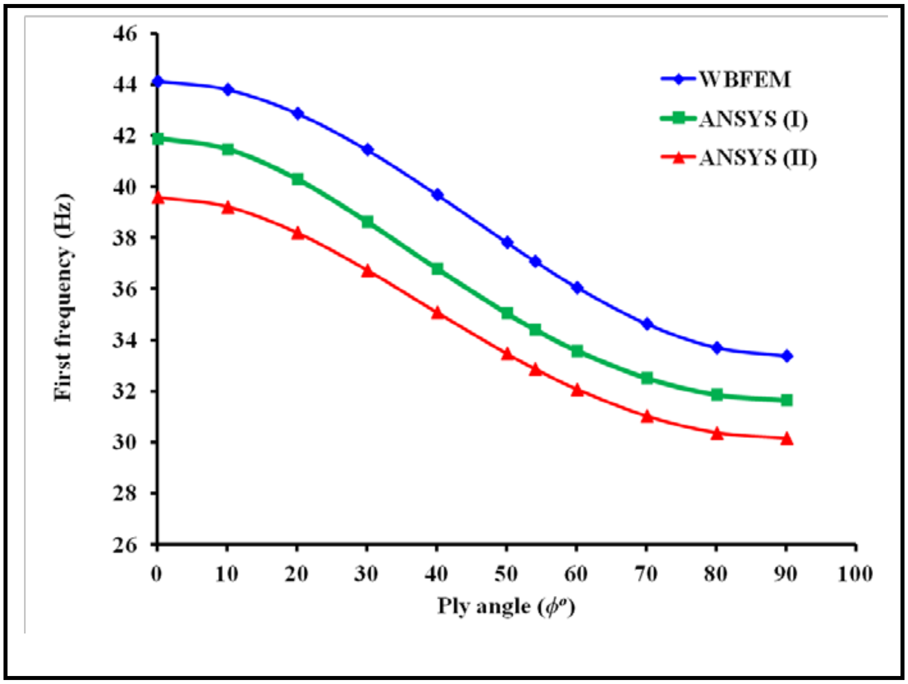

Figure 5.13: Effect of positive ply angle on natural frequency of laminated composite pipe

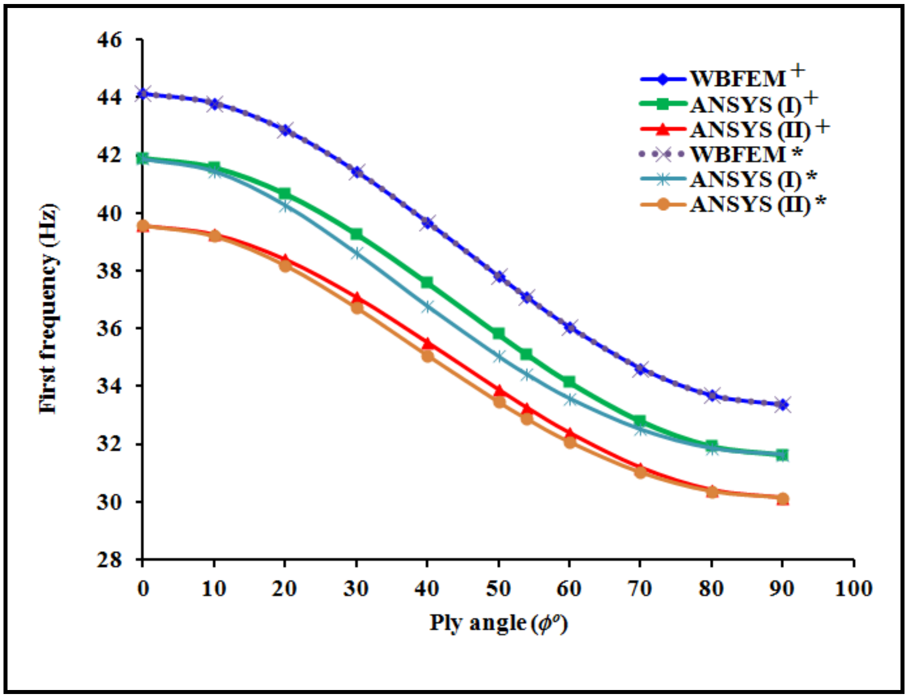

Figure 5.14: Comparison of natural frequency for different types of ply angle: $^{+}=[\pm\phi_5/\phi]$ and $^{*}=[\phi_{11}]$

It can be viewed from Fig. 5.11 that for homogeneous pipe, as ϕ increases from 0^o to 90^o, the frequency also increases until $\phi = 45^0$ and decreases afterward. It can also be deducted that the frequencies of ϕ and $90-\phi$ are the same which indicate that the properties of laminated homogenous pipe described in Table 5.11 are symmetric on $\phi = 45^0$ (see Fig. 5.11). This also means that this kind of pipe can exist or design in two forms: first with ply angle ϕ and the second with ply angle $90-\phi$. Conversely, Figs. 5.12 and 5.13 behaved differently, that is, frequency decreases as ϕ increases throughout the range. The scenarios in Figs. 5.11-5.13 can be summarized that for the kind of this laminated homogeneous pipe, the maximum frequency will occur when $\phi = 45^0$ and when $\phi = 0^0$ for laminated composite pipe.

Moreover, in these figures, ANSYS (I) is the first FRP pipe model in ANSYS whereby only three DOFs out of 6 DOFs of SHELL 281 element were considered while ANSYS (II) is the second model in which all DOFs were utilized at each node. It was found that the first model did not only produced results that closer to those obtained from WBFEM but also faster than second model in term of computational time when compared to the second model.

In addition, as it can be seen from Eq. (3.10) that $\overline{Q}_{11}$ will treat $[-\phi]$ as $[+\phi]$ during the analysis of composite structure, the effect of this on natural frequency was investigated and the results obtained are shown in Fig 5.14. This figure is equivalent to the combination of Figs. 5.12 and 5.13. It can be observed that the difference in treating $[\pm\phi_5 / \phi]$ as $[\phi_{11}]$ is negligible. Thus, it can be deduced that the natural frequency is not depends so much on the sign of ply angle ($+\phi$ or $-\phi$) but on the value of ply angle ϕ.

Generally, it can be seen that the results for WBFEM (based Euler-Bernoulli beam theory) are higher than that of ANSYS, the differences between the WBFEM and ANSYS FEM results may be due to the fact that 1D element was used in WBFEM while 2D element was used in ANSYS FEM. In addition, the SHELL281 employed in ANSYS FEM is based on Timoshenko theorem.

Besides, the convergence of the two wavelets considered was investigated using the pipe in Tables 5.2 and 5.9. The results obtained for the first frequency were shown in Fig. 5.15 and it was observed that WBFEM with B-spline wavelet converged quickly more than WBFEM with Trigonometric hermite wavelet. This shows the superiority of B-spline wavelet over Trigonometric hermite wavelet.

Finally, both the accuracy and efficiency of the model developed in this chapter are validated by comparisons with numerical solutions published in the available literature as well as results obtained by the conventional FEM using ANSYS.

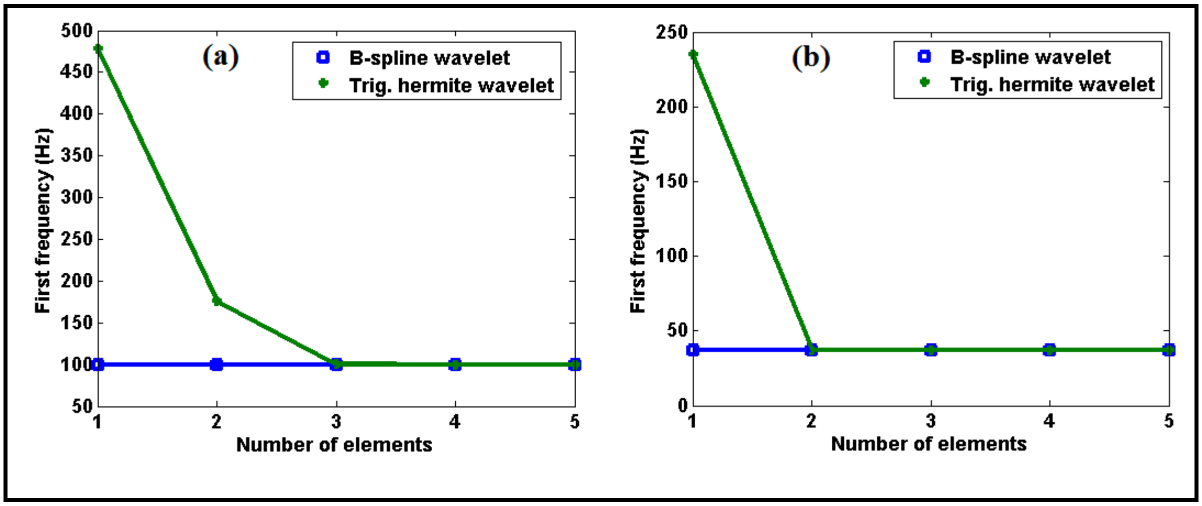

Figure 5.15: Convergence plot for pipes using different wavelets: (a) Table 5.2 and (b) Table 5.9

The comparisons demonstrate the accuracy of the developed wavelet-based finite pipe element, as it converged closer to the target value than other reported solutions in Table 5.3. In addition, the efficiency of computations when modeling composite multilayer pipes using the wavelets is demonstrated by using only three or four elements in comparisons to over 8000 elements when ANSYS shell element was utilized. In terms of CPU time, the present method used 3% of the CPU time consumed by ANSYS. Hence, the results produced by the developed element offer some benchmark solutions using wavelets on the interval in conjunction with the composite multilayer pipes.

In this chapter, laminated composite pipes without wall defect were investigated; in the next chapter laminated composite pipes with and without thickness discontinuity were studied. In addition, only the first $LCSS$ was majorly utilized here, all $LCSS$ and two wavelets were used in the next chapter. Besides, since most of the pipes that are being used in real life are long enough, henceforth, only EP was considered after this chapter.

CHAPTER 6

DYNAMIC ANALYSIS OF COMPOSITE PIPE WITH AND WITHOUT THICKNESS DISCONTINUITY

6.1 Laminated Composite Pipe with and without Thickness Discontinuity

In the previous chapter, the expressions related to bending stiffness and mass of the laminated composite pipe per unit length are given. In addition, due to various assumptions employed, six models that can be used to obtain stiffness terms of laminated composite structures were produced. Also, in previous chapter laminated composite pipes without thickness discontinuity (healthy pipe) or internal defect were investigated using mainly $LCSS_1$. In this chapter, laminated composite pipes with and without discontinuity were studied using EP and first four $LCSS$ ($LCSS_1$, $LCSS_2$, $LCSS_3$ and $LCSS_4$).

If the pipe structure contains thickness discontinuity, the dynamic and vibration characteristics of the structures will be affected. Discontinuity may occur in different forms, yet majority of them tend to affect the stiffness and mass of the structure under attack. A lot of types of damage that include aging damage may affect composite pipes while in-service. Surface attack which can take numerous forms is the mainly apparent type of aging damage in in-service composite piping. This phenomenon will cause internal wall discontinuity in pipes and fittings which could compromise their structural integrity and could thereby lead to increase plant downtime, revenue loss and sometimes catastrophic failures. Thus, equations given in Chapter 5 for EP and TP need to be modified to be able to handle pipes like laminated composite pipe shown in Fig. 6.1 that contains internal wall defect.

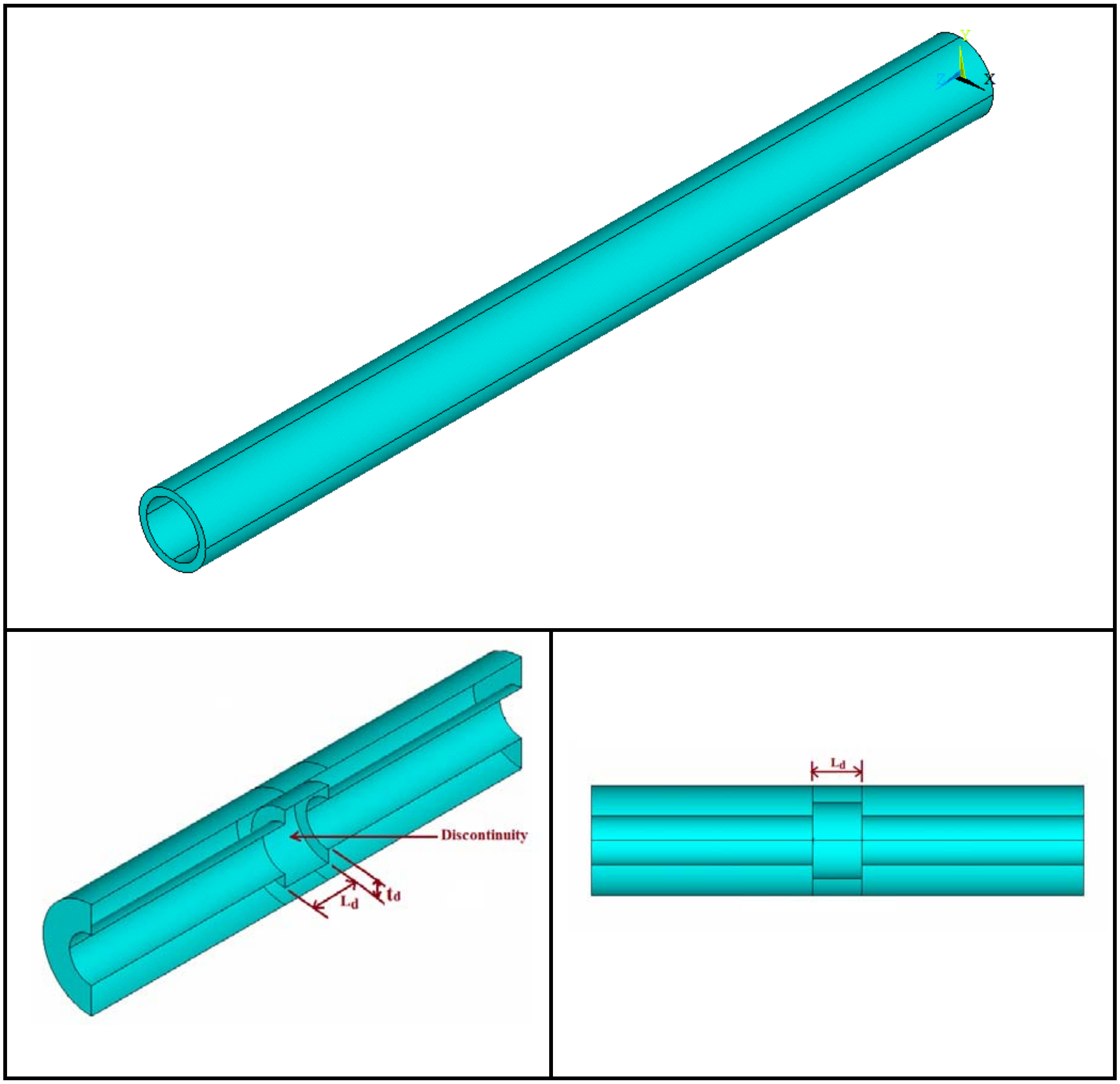

Figure 6.1: Magnified FRP pipe and its sectional views with discontinuity.

6.2 Euler-Bernoulli Pipe element (EP)

In composite FRP pipe analysis, the generalized potential energy function of the pipe element given in Chapter 5 for healthy pipe under the classical assumptions of Euler-Bernoulli beam theory can be generalized for the pipe with and without discontinuity or internal defect as

$$\pi_p(\mathcal{W}) = \int_0^{l_e} \frac{\overline{\mathcal{H}}(x)}{2}\left(\frac{d^2\mathcal{W}}{dx^2}\right)^2 dx - \frac{1}{2}\int_0^{l_e} \lambda \overline{\mathcal{M}}(x)\mathcal{W}^2 dx \tag{6.1}$$

where

$$\overline{\mathcal{H}}(x) = \mathcal{H}_z - \mathcal{H}_z^{(d)},\ \overline{\mathcal{M}}(x) = \mathcal{M}_z - \mathcal{M}_z^{(d)},\ \lambda = \omega^2$$

and $\mathcal{H}_z$,and $\mathcal{M}_z$ are stiffness and mass per unit length of an element without thickness discontinuity while $\mathcal{H}_z^{(d)}$ and $\mathcal{M}_z^{(d)}$ are stiffness and mass per unit length of discontinuity geometry in an element. However, for healthy pipe or pipe that does not contain thickness discontinuity, then, $\mathcal{H}_z^{(d)} = \mathcal{M}_z^{(d)} = 0$ and $L_d = t_d = 0$ respectively. Substituting Eq. (5.42) in (6.1), one gets

$$\pi_p(\mathcal{W}) = \frac{1}{l_e^3}\int_0^{1} \frac{\overline{\mathcal{H}}(\zeta)}{2}\left(\frac{d^2\mathcal{W}}{d\zeta^2}\right)^2 d\zeta - \frac{1}{2}l_e\int_0^{1} \lambda \overline{\mathcal{M}}(\zeta)\mathcal{W}^2 d\zeta \tag{6.2}$$

where $\mathcal{H}_z(\zeta)$ and $\mathcal{H}_z^{(d)}(\zeta)$, and $\mathcal{M}(\zeta)$ and $\mathcal{M}_z^{(d)}(\zeta)$ can be obtained from Eqs. (5.27) and (5.28) respectively. In Eq. (6.2), the only unknown field function is $\mathcal{W}(\zeta)$ and it can be expressed by the scaling functions of Trigonometric hermite and B-spline wavelets on the interval. Utilizing the principle of minimum potential energy $(\delta\pi_p = 0)$, one obtains n_d equations and they can be expressed in matrix form as in Eq. (5.55). Similarly, the same procedures are required for Timoshenko pipe element TP. However, as it was stated in Chapter 5, only EP were considered for the rest of this dissertation.

6.3 Results and Discussion

First, the numerical accuracy of using any of the four $LCSS$ with either B-spline or Trigonometric hermite wavelet was investigated. The numerical results obtained by the developed WBFEM formulation using any of these methods converged very closely to the same values as compared to ANSYS results and other published test cases. On FEM solution by ANSYS, the 6-DOF SHELL281 element was considered. To verify the accuracy of the proposed methods, a composite tube without wall discontinuity was considered. The tube has 10 layers, with material properties and dimensions as presented in Table 5.2. In Chapter 5, the mean diameter and thickness of this pipe were supplied to the MATLAB program developed for this work and D_i and D_o were obtained at run time. However, in order to be consistent with these diameters when it contains thickness discontinuity, these diameters were obtained from the pipe mean diameter and its thickness; they were then supplied to the program. The results obtained for all $LCSS$ (with B-spline and Trigonometric wavelets) and ANSYS are tabulated in Table 6.1 along with some results from the available literature. In the table, all of the $LCSS$ rows contain results for both B-spline and Trigonometric hermite wavelets. Similarly, the present ANSYS results also contained two results of two different models that were utilized. The results presented by researchers that lie in the range from 90.00 to 101.00Hz are tabulated in Table 6.1 while other researchers' results below or above this range are excluded. It

Table 6.1: Natural frequencies of simply-supported (SS) tube with 10 layers.

Ref.	Authors	Frequency (Hz)	Method used
[113, 116]	Zinberg, Symonds, 1970	91.67	Measured experimentally
	Kim and Bert, 1993	97.87	Sanders shell theory
	Bert and Kim, 1995	96.47	Bresse–Timoshenko beam theory
	Singh and Gupta, 1996	95.78	Effective Modulus Beam Theory
	Chang et al., 2004	96.03	Continuum based Timoshenko Beam
	Hajianmaleki and Qatu, 2011	95.89	Finite element analysis using ANSYS
		94.71	SDBT using V-S
	Bert,1992	98.65$^{\#}$	Bernoulli–Euler beam theory
	Kim et al., 2004	91.43	Timeshenko beam model
Present study		100.59, 100.59	LCSS_1
		98.72, 98.72	LCSS_2
		98.76, 98.76	LCSS_3
		96.41, 96.41	LCSS_4
		96.05, 94.23	ANSYS (I & II)

$^{\#}$ most accurate according to [116]

can be seen that all the results obtained by the present methods (with 3 and 4 elements) and ANSYS (with over 8,000 elements) compared well with the other published results. Referring to the most accurate frequency value for the pipe (98.65Hz) according to [116], one observes that among the results in Table 6.1, the closest to that value are 98.72 and 98.76 Hz, which are produced by the WBFEM methods in present study. In addition, it can be observed that both wavelets gave the same results all through and LCSS_2 and LCSS_3 have the same results. Also, among the LCSS types, LCSS_1 produced the highest result while LCSS_4 generated the smallest result.

Besides, in order to investigate the accuracy of the developed model further, the simply supported pipes studied in [55] using Ritz method were also considered. The three different reinforcements they considered include 18-oz woven roving glass mat (#1), 28.6-oz woven roving glass mat (#2), and pure epoxy resin (#3). The first three frequencies obtained are compared in Table 6.2 where $\mathcal{H}_z = \Re$. It can be found that the results obtained in the present study agreed with that of [55].

Table 6.2: Composite pipe made of fiberglass epoxy [55]

S/N	D_o (mm)	L (m)	Pipe wall layup configuration (from outside to inside)			Laminate stiffness			Natural Frequency (Hz)	
			#1 (mm)	#2 (mm)	#3 (mm)	$A_{11}*10^7$ (N/m)	D_{11} (Nm)	$\Re*10^3$ (Nm^2)	Ref. [55]	Present work
1	60.22	1.30	1.98	0	2.41	5.0566	87.1528	3.4632	58.63	57.76
									NA	231.03
									NA	519.83
2	88.62	1.33	1.98	0	2.36	5.5305	90.8353	11.8550	83.51	83.71
									NA	334.85
									NA	753.41
3	114.30	5.60	2.24	0	2.21	7.6281	161.5345	28.8050	6.38	6.04
									NA	24.17
									NA	54.37
4	168.28	5.60	2.41	0	2.54	7.363	216.7862	102.8600	9.28	9.10
									NA	36.41
									NA	81.93
5	219.08	5.60	3.25	0	2.13	5.0382	84.2246	292.3900	13.49	11.56
									NA	46.23
									NA	104.01
6	273.05	5.60	3.35	0	2.79	6.01	125.0215	603.5600	15.96	14.66
									NA	58.65
									NA	131.96
7	323.85	5.60	1.98	1.57	2.41	8.0816	238.7322	925.8100	16.42	16.18
									NA	64.74
									NA	145.66

NA=Not available

For the laminated composite pipe with discontinuity, the data shown in Table 5.9 is considered. The internal surface discontinuities were located at three places along the pipe span, namely $L_c = L/3$, $L/2$, $3L/4$. The geometry of the discontinuity is defined by thickness t_d, length $L_d = 0.15$, and hoop angles θ_1 and θ_2. The discontinuity circumferential coverage was permitted to grow to form full ring or annulus (see Figs. 6.2 and 6.3). The first natural frequency for the pipe with internal wall defect defined by all L_c and $t_d = 3h/4$ is obtained using the present methods and ANSYS. The results are presented in Tables 6.3-6.8, together with the frequency values for the healthy pipe.

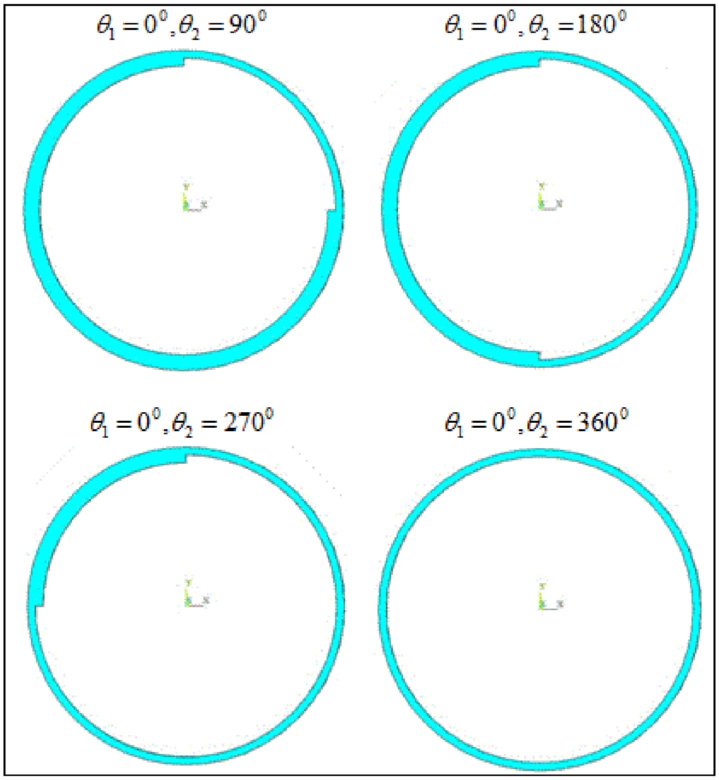

Figure 6.2: Pipe cross-section as discontinuity grows from partial to full ring.

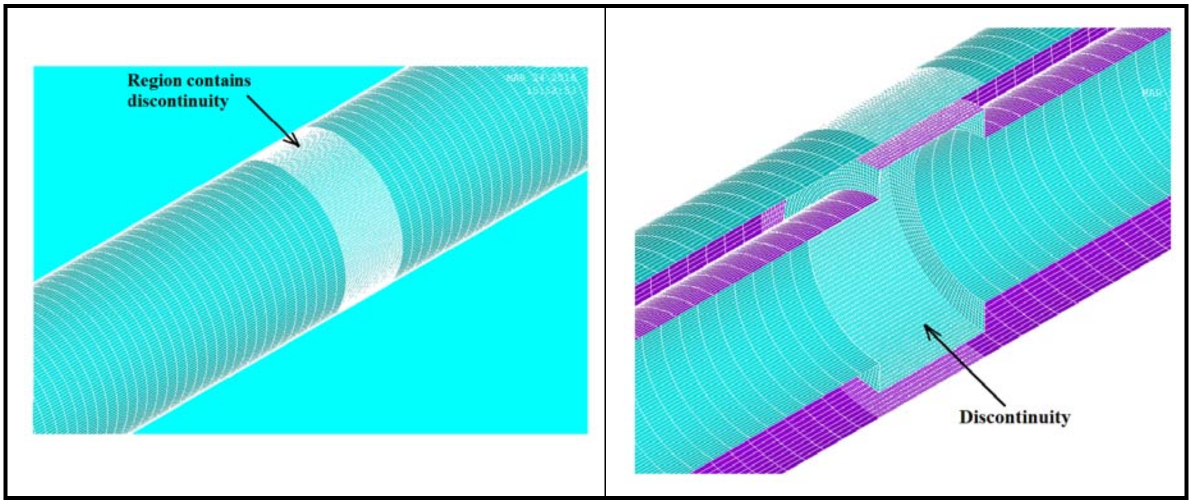

Figure 6.3: Exploded FRP Pipe with annulus discontinuity and its sectional view.

Table 6.3: Natural frequencies (Hz) of FRP pipe with discontinuity at $L_c = L/3$ using B-spline wavelet.

Type	**Discontinuity description**		**WBFEM (B-spline Wavelet)**			
	L_c, t_d **(m)**	θ_1, θ_2 **(Degree)**	LCSS$_1$	LCSS$_2$	LCSS$_3$	LCSS$_4$
Healthy pipe	0, 0	0, 360	37.0869	33.4192	33.4224	33.0117
Pipe with discontinuity	L/3, 3h/4	0, 90	36.9941	33.3359	33.3388	32.9613
		0, 180	36.6540	33.0298	33.0323	32.7283
		0, 270	35.7688	32.2334	32.2346	32.1191
		0, 360	33.2868	30.0017	29.9979	30.5417

Table 6.4: Natural frequencies (Hz) of FRP pipe with discontinuity at $L_c = L/3$ using Trigonometric hermite wavelet.

Type	**Discontinuity description**		**WBFEM (Trigonometric hermite Wavelet)**			
	L_c, t_d **(m)**	θ_1, θ_2 **(Degree)**	LCSS$_1$	LCSS$_2$	LCSS$_3$	LCSS$_4$
Healthy pipe	0, 0	0, 360	37.0868	33.4192	33.4224	33.0117
Pipe with discontinuity	L/3, 3h/4	0, 90	36.9941	33.3359	33.3389	32.9612
		0, 180	36.6540	33.0298	33.0323	32.7283
		0, 270	35.7688	32.2334	32.2346	32.1191
		0, 360	33.2869	30.0017	29.9979	30.5417

Table 6.5: Natural frequencies (Hz) of FRP pipe with discontinuity at $L_c = L/2$ using B-spline wavelet.

Type	Discontinuity description		WBFEM (B-spline Wavelet)				ANSYS
	L_c, t_d **(m)**	θ_1, θ_2 **(Degree)**	LCSS$_1$	LCSS$_2$	LCSS$_3$	LCSS$_4$	**II**
Healthy pipe	0, 0	0, 360	37.0869	33.4192	33.4224	33.0117	33.2680
Pipe with discontinuity	L/2, 3h/4	0, 90	36.9651	33.3098	33.3127	32.9459	33.1290
		0, 180	36.5221	32.9112	32.9135	32.6425	33.0670
		0, 270	35.3895	31.8921	31.8928	31.8593	32.9360
		0, 360	32.3517	29.1603	29.1551	29.8974	32.8340

Table 6.6: Natural frequencies (Hz) of FRP pipe with discontinuity at $L_c = L/2$ using Trigonometric hermite wavelet.

Type	Discontinuity description		WBFEM (Trigonometric hermite Wavelet)				ANSYS
	L_c, t_d **(m)**	θ_1, θ_2 **(Degree)**	LCSS$_1$	LCSS$_2$	LCSS$_3$	LCSS$_4$	**II**
Healthy pipe	0, 0	0, 360	37.0868	33.4192	33.4224	33.0117	33.2680
Pipe with discontinuity	L/2, 3h/4	0, 90	36.9650	33.3098	33.3127	32.9457	33.1290
		0, 180	36.5221	32.9112	32.9134	32.6424	33.0670
		0, 270	35.3895	31.8921	31.8927	31.8593	32.9360
		0, 360	32.3517	29.1602	29.1551	29.8973	32.8340

Table 6.7: Natural frequencies (Hz) of FRP pipe with discontinuity at $L_c = 3L/4$ using B-spline wavelet.

Type	Discontinuity description		WBFEM (B-spline Wavelet)			
	L_c, t_d **(m)**	θ_1, θ_2 **(Degree)**	LCSS$_1$	LCSS$_2$	LCSS$_3$	LCSS$_4$
Healthy pipe	0, 0	0, 360	37.0869	33.4192	33.4224	33.0117
Pipe with discontinuity	3L/4, 3h/4	0, 90	37.0236	33.3624	33.3654	32.9770
		0, 180	36.7896	33.1519	33.1546	32.8165
		0, 270	36.1699	32.5943	32.5961	32.3916
		0, 360	34.3496	30.9577	30.9556	31.2539

Table 6.8: Natural frequencies (Hz) of FRP pipe with discontinuity at $L_c = 3L/4$ using Trigonometric hermite wavelet.

Type	**Discontinuity description**		**WBFEM (Trigonometric hermite Wavelet)**			
	L_c, t_d **(m)**	θ_1, θ_2 **(Degree)**	LCSS_1	LCSS_2	LCSS_3	LCSS_4
Healthy pipe	0, 0	0, 360	37.0868	33.4192	33.4224	33.0117
Pipe with discontinuity	3L/4, 3h/4	0, 90	37.0235	33.3624	33.3655	32.9769
		0, 180	36.7897	33.1519	33.1546	32.8165
		0, 270	36.1699	32.5943	32.5961	32.3916
		0, 360	34.3496	30.9577	30.9556	31.2539

Referring to the results presented in Tables 6.3-6.8, the WBFEM methods used only two and four elements for the healthy pipe and three and five elements for the case with internal wall defect. However, for ANSYS, the corresponding values are 8,800 and over 20,000 elements, respectively. It can be observed that as θ_2 increases from 90^0 to 360^0, the frequency decreases, while the maximum decrement occurred when the discontinuity covers the complete circumference; i.e. at $\theta_2 = 360^o$ for all L_c. Besides, the maximum decrement based on L_c took place when $L_c = L/2$. Similarly, it can be noticed that both B-spline and Trigonometric hermite wavelets produced the same results and LCSS_2 and LCSS_3 results were the same again. Besides, among the LCSS methods, LCSS_1 generated the highest result while LCSS_4 produced the smallest result for the healthy pipe. Thus, henceforth only B-spline wavelet and LCSS_3 were utilized.

In order to study the effect of the discontinuity on higher frequencies, the first eight natural frequencies were examined. In this investigation, both healthy pipe and the pipe with annular discontinuity defined by $L_c = L/2$ and $t_d = 3h/4$ were considered.

The results obtained are presented in Table 6.9. It can be seen that the frequencies of the pipe with thickness discontinuity obtained by the present method and ANSYS are in good agreement and both are lower than that of the healthy pipe due to the softening effect induced by the wall thinning.

Moreover, in previous solutions only $t_d = 3h/4$ with all L_c were considered. Now, the numerical solutions were expanded to include a wider range of the discontinuity parameters t_d and L_c in order to consolidate the effect of the internal surface defects on natural frequencies. In this context, θ_2 is increased gradually from 0^0 to 360^0. The results obtained for the first four natural frequencies for different combinations of the dimensional parameters t_d and L_c are presented in Fig. 6.4. Figure 6.4 shows the effect of the discontinuity on the first four natural frequencies of the laminated composite pipe. The same trend has been observed, as the values of the four frequencies decrease as

Table 6.9: Natural frequencies (Hz) of Simply-supported pipe with annulus discontinuity

S/N	Method			
	WBFEM		ANSYS	
	Healthy pipe	Pipe with Discontinuity	Healthy pipe	Pipe with Discontinuity
1	33.42	29.16	33.27	32.83
2	133.69	133.23	128.63	128.19
3	300.80	282.83	282.57	273.00
4	534.76	528.31	535.39	533.64
5	835.56	816.16	834.90	818.49
6	1203.21	1176.45	1207.50	1185.60
7	1637.71	1634.64	1638.40	1633.90
8	2139.07	2075.32	2139.50	2139.30

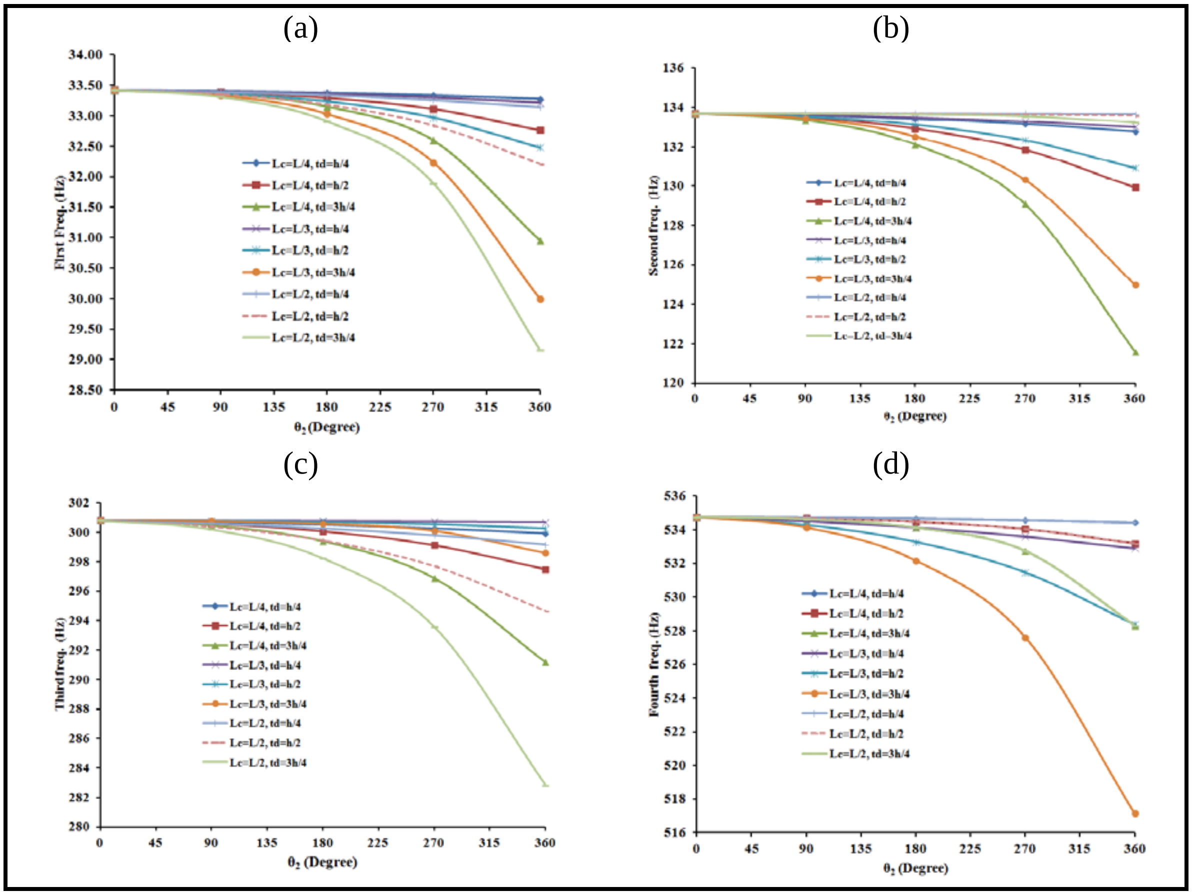

Figure 6.4: Natural frequencies of SS composite pipe with discontinuity: (a) First frequency (b) Second frequency (c) Third frequency and (d) Fourth frequency.

the dimensions of discontinuity increase. That is, an increase in any of the dimensional parameters L_c, L_d and t_d leads to an increase in the size of the wall-thinning, thus resulting in a softening effect, or equivalently a decrease in the natural frequencies.

Furthermore, the effect of the length of the internal surface damage L_d on the modal characteristics of an FRP pipe is also investigated. In this context, the internal surface defect starts at the midpoint of the pipe; i.e. at $L_c = L/2$, and then stretches symmetrically until it covers the entire pipe span. The defect has thickness $t_d = h/2$ and hoop coverage that starts at $\theta_1 = 0^0$ and extends to $\theta_2 = 90^0$, 180^0 and 360^0, respectively.

As depicted in Fig. 6.5, the natural frequency does not monotonically decrease as the length of the surface defect increases, which may seem counterintuitive. However, this behavior can be explained from the mechanics view point. For a fixed length pipe, the

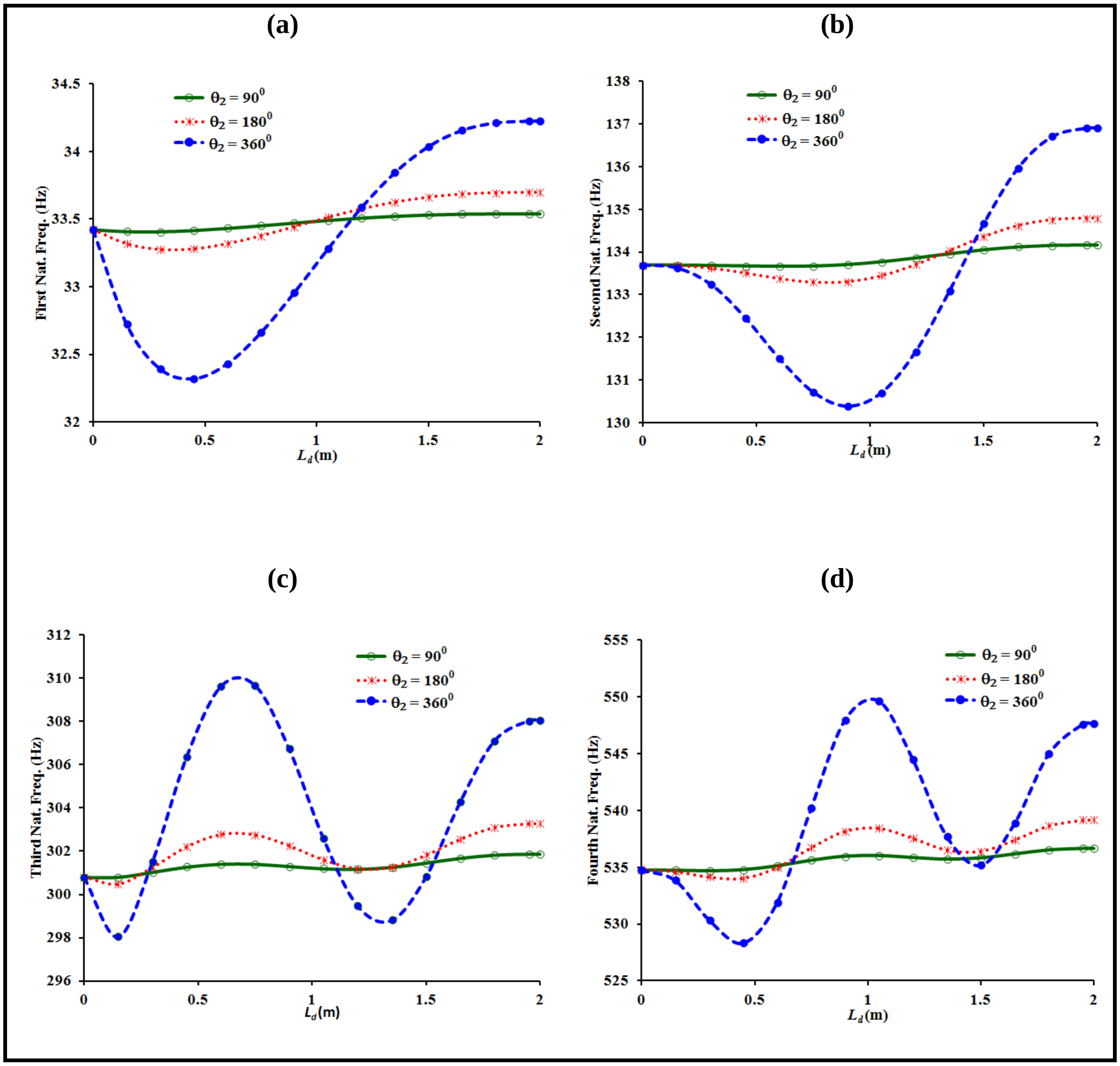

Figure 6.5: Effect of length L_d of the discontinuity on frequency: (a) First natural frequency, (b) Second natural frequency, (c) Third natural frequency, and (d) Fourth natural frequency of SS FRP pipe.

natural bending frequency is directly proportional to the square root of the ratio of flexural stiffness to mass per unit length. Accordingly, when the wall-thinning has a more pronounced effect on stiffness than its effect on mass, the frequency decreases; and vice versa. The same behavior is observed for the first four modes, where the trend of frequency decrease is reversed at certain points. In higher modes, the frequency change appeared to have cycles of decrease and increase across the beam span, yet all the four frequencies experienced increase over their nominal values when the wall-thinning length exceeds three-fourths of the beam span, as shown in Fig. 6.5. Thus, it can be inferred from Fig. 6.5 that for small values of L_d the reduction effect due to wall thinning on stiffness is more than its corresponding reduction effect on mass, and therefore we notice a decrease of frequencies at such smaller values.

It should be noted in Fig. 6.5 that the frequencies at $L_d = 0$ are the nominal values of the healthy pipe. However, by the time $L_d = L$, new pipe (with it's $D_i > D_i$ of original pipe but the same D_o) was produced and its frequencies higher than those of the original pipe as it can be seen in Fig. 6.5.

Finally, the mode shapes of the pipe in the presence of the internal surface discontinuities are examined. The modes shapes of the first four natural frequencies are plotted in Fig. 6.6 for the simply-supported pipe (SS) with surface discontinuities at three different locations. In this case, the geometry of the internal wall-thinning is defined by L_d = 0.15, $\theta_1 = 0^0$ and $\theta_2 = 90^0$. One can observe that the effect of the internal surface defect is depicted for the mode shapes when compared to those of the healthy pipe shown in Fig. 6.6(a). Although, the location of the discontinuity is not directly traceable from

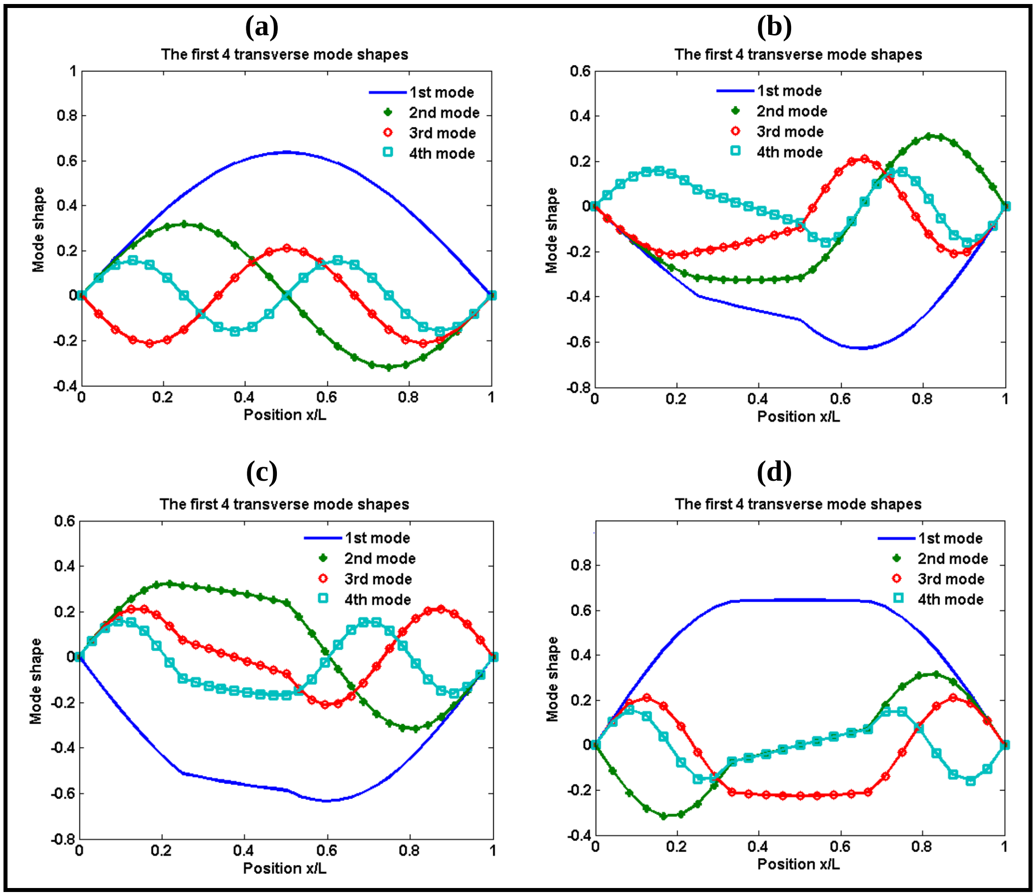

Figure 6.6: Mode shapes for pipes with and without thickness discontinuity: (a) Healthy pipe (b) discontinuity at $L_c = L/4$ (c) discontinuity at $L_c = L/3$ (d) discontinuity at $L_c = L/2$

its effect on the mode shape, both the eigenvalues and eigenvectors carry the signature of the internal surface defect. The results show that vibration frequencies and mode shapes can be utilized for detecting internal pipeline defects, and may be used to complement other proposed vibration-based techniques; e.g.[120].

In this investigation, finite pipe elements were developed using the B-spline and Trigonometric hermite wavelets. The accuracy of the developed finite pipe elements were verified via comparisons with results reported in the available literature for the healthy pipe, as well as results obtained using ANSYS. The efficiency of the WBFEM was demonstrated by the substantially less number of elements used.

The developed elements were utilized in performing vibration analysis of composite pipes with internal wall defects, wherein the effect of the resulting thickness reduction on the natural frequency is evaluated and examined. The observed trend showed a decrease in the values of the natural frequencies as the length of the internal wall thinning increase. It was interesting to note that the trend is not a monotonic decrease, as might be intuitively counter perceived. It was found that all natural frequencies experienced a decrease as the length of the wall-tinning increased, but only for smaller values. As the length of the wall-thinning increased further, the trend of change in the natural frequencies is reversed, thus showing an increasing trend. In general, the trend of frequency changes due to increase in the internal surface defect showed a cyclic behavior. This is consistent with the mechanics of solids; that is the decrease in the cross-sectional area caused by thinning results in a decrease in flexural stiffness, as well as a decrease in mass. The effect of wall thickness reduction on natural frequencies is consequently dependent on the ratio of flexural stiffness to mass. If the resulting decrease in flexural stiffness is more pronounced than that of mass, then frequencies tend to decrease (softening effect), and vice versa. The numerical results showed that all the first four frequencies experienced increase over their nominal values when the wall-thinning length exceeds three-fourths of the beam span.

The plotted mode shapes showed the effect of the internal discontinuity along the span of the pipe. Although, the location of the discontinuity is not directly traceable from its effect on the mode shapes, both the eigenvalues and eigenvectors carry the signature of the internal surface defect.

In the long run, all the $LCSS$ methods and B-spline and Trigonometric wavelets have been used. It was found that while $LCSS_1$ gave the highest results, $LCSS_4$ produced the smallest results. Besides, $LCSS_2$ and $LCSS_3$ not only generated the same results but also their results are in between that of $LCSS_1$ and $LCSS_4$.As a result, from now on, $LCSS_3$ was considered for the rest of the dissertation. On Wavelets, both of them produced almost the same results throughout with different number of elements. However, majorly due to the sensitivity of Trigonometric hermite wavelet to the small element length and its current small MRA compare to B-spline, B-spline wavelets and $LCSS_3$ were used in the remaining part of this dissertation. Hence, in the next chapter, the dynamic analysis of composite pipe with and without inter wall defect conveying fluid was presented.

CHAPTER 7

DYNAMIC ANALYSIS OF COMPOSITE PIPE WITH AND WITHOUT THICKNESS DISCONTINUITY AND CONVEYING FLUID

7.1 Laminated Composite Pipe Conveying Fluid

Figure 7.1 shows a composite (FRP) pipe conveying fluid with velocity $V_x = V_i$ and V_e when entering and existing the pipe. As the fluid flowing through the pipe, the pipe and the fluid will continue to interact with each other with velocity V_p and V_f

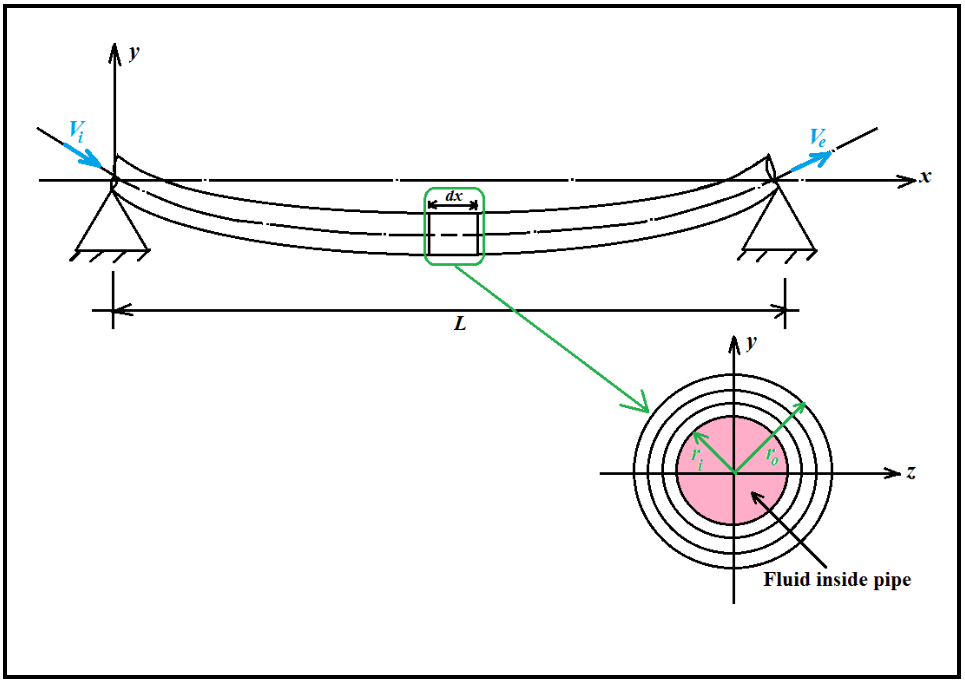

Figure 7.1: Simply supported composite pipe conveying fluid.

respectively. This interaction will probably causing pipe to vibrate with its content. According to [121], the equilibrium of forces for fluid element along x-direction is given as

$$A_f \frac{\partial P}{\partial x} + \tau s = 0 \tag{7.1}$$

where P, s and τ are fluid pressure, inner perimeter of the pipe and the shear stress on the inner surface of the pipe. If element of pipe of length dx in Fig. 7.1 is considered, multiply Eq. (7.1) through by dx will produce

$$A_f \frac{\partial P}{\partial x} dx + \tau s dx = 0 \tag{7.2}$$

where $\tau s dx$ is F_τ. However, $dP/dx = \partial P/\partial x$ and mostly in fluid analysis $dP = P_1 - P_2$, if it was assumed that $dP = P_2 - P_1$, Eq. (7.2) will become

$$F_\tau = A_i \frac{dP}{dx} dx \tag{7.3}$$

Besides, the total T and U of the composite pipe element of length dx conveying fluid can be defined as

$$T = T_p + T_f \tag{7.4}$$

$$U = \frac{1}{2}\int_0^{l_e} \bar{\mathcal{H}}(x)\left(\frac{\partial^2 y}{\partial x^2}\right)^2 dx \tag{7.5}$$

where T_p and T_f are kinetic energies of the composite pipe element and fluid flowing inside the pipe element of the laminated composite pipe element. The components of T defined in Eq. (7.4) can be expressed as

$$T_p = \frac{1}{2}\int_V \rho_p V_p^2 dV = \frac{1}{2}\int_0^{l_e}\iint_{A_p} \rho_p V_p^2 dA_p dx = \frac{1}{2}\int_0^{l_e} \bar{\mathcal{M}}(x) V_p^2 dx$$

$$T_f = \frac{1}{2}\int_V \rho_f V_f^2 dV = \frac{1}{2}\int_0^{l_e}\iint_{A_f} \rho_f V_f^2 dA_f dx = \frac{1}{2}\int_0^{l_e} m_f V_f^2 dx$$

wherein

$$V_p = \frac{\partial y}{\partial t}, V_f = \frac{\partial y}{\partial t} + V\frac{\partial y}{\partial x},\ A_p = \frac{\pi}{4}(D_o^2 - D_i^2),\ A_f = \frac{\pi}{4}D_i^2,\ m_f = \rho_f A_f$$

where $\bar{\mathcal{H}}(x)$ and $\bar{\mathcal{M}}(x)$ are stiffness and mass of pipe element and they are as defined in Chapter 6. Furthermore, forces due to $\bar{T}$ and F_τ will involve as fluid flow through the pipe. The total virtual work done by these forces on the pipe element of length dx can be expressed as

$$\begin{aligned} \delta W &= \delta W_{\bar{T}} + \delta W_{F_\tau} \\ &= \int_0^{l_e} \bar{T}\frac{\partial^2 y}{\partial x^2}\delta y dx - \int_0^{l_e} F_\tau \frac{\partial^2 y}{\partial x^2}\delta y dx \end{aligned} \tag{7.6}$$

or

$$\delta W = -\int_0^{l_e} F_p \frac{\partial^2 y}{\partial x^2}\delta y dx \tag{7.7}$$

where $F_p = F_\tau - \bar{T}$

7.2 Energy Loss in Pipe Conveying Fluid

When fluid is flowing through the pipe it encounters some resistances and as a result part of the fluid energy is lost. Energy losses can be categorized into two: major and minor or local losses. Each of these categories can occur due to the geometry of the pipe and fluid viscosity as shown in Table 7.1. The minor losses occur as a result of

Table 7.1: Energy losses and their causes in pipe flow [122-125]

Energy Losses	Causes
Minor losses	sudden contraction, sudden expansion, pipe fitting, pipe bending, a barrier inside the pipe cross-section, entry to a pipe from reservoir, exit
Major losses	from a pipe to reservoir Friction, motors

energy loss in the components while viscosity in the straight pipe is the cause of major loss [122]. Alternatively, major loss occurs when energy (head) loss due to friction in a pipe while energy loss due to change in velocity responsible for minor loss [124, 125].

7.2.1 Major Energy Head Loss in Fluid Pipe

In a fluid pipe with turbulent flow, the pressure loss depends on pipe (diameter, length, surface roughness) and fluid (density, velocity and viscosity). According to [40], in fully developed flow pressure loss is the main contributor to the energy loss and head loss varies with flow rate. The fluid friction at the pipe walls is the source of the pressure loss. In Fig. 7.2, V_1 and V_2, P_1 and P_2, A_1 and A_2 are the velocities of the fluid, pressures and internal areas at the two sections and h_f is the loss due to the friction. If the real fluid is assumed to be flown in the pipe, application of Bernoulli's equations at the two sections in conjunction with Darcy friction factor will yield

$$h_f = f \frac{L}{D_i} \frac{V^2}{2g} \tag{7.8}$$

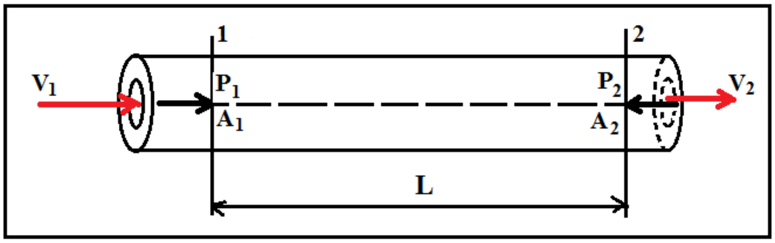

Figure 7.2: Horizontal pipe with flowing fluid.

in which for horizontal pipe

$$\frac{dP}{dx} = -\frac{f \rho V^2}{2D_i} \tag{7.9}$$

However, Eq. (7.9) can be re-expressed as

$$\frac{dP}{dx} = -\frac{f \rho V^2}{2D_i}\left(\frac{Lg}{Lg}\right) = \frac{fLV^2}{D_i 2g}\left(-\frac{\rho g}{L}\right)$$

Upon, substituting Eq. (7.8), it produced

$$\frac{dP}{dx} = h_f\left(-\frac{\rho g}{L}\right) \tag{7.10}$$

Eq. (7.8) is known as Darcy-Weishbach equation. The type of flow (laminar or turbulent) will determine the value of f . The flow can be considered as laminar if [41]

- the characteristic length is appreciably small
- fluid viscosity is high
- fluid velocity is below a certain value

Then, for fully developed laminar flow, f is defined as

$$f = 64 / R_e \text{ for } R_e < 2000 \tag{7.11}$$

where

$$R_e = \frac{\rho V_{avg} D_i}{\mu} = \frac{\rho V_x D_i}{\mu}$$

Unlike in laminar flow, the fluid particles motion is irregular in turbulent flow and as a results Eq. (7.11) is not applicable to turbulent flow that is common in industrial applications and in nature [126]. Hence, to obtain f for turbulent flow, several correlations such as Colebrook, Wood, Jain and Churchill were developed. Among all these correlations, Colebrook is the most well known but difficult to solve because f cannot be expressed explicitly and it was the one used to develop the Moody's diagram. The expressions developed by Colebrook is given as

$$\frac{1}{\sqrt{f}} \approx -2.0 \log_{10}\left[\frac{2.51}{Re\sqrt{f}} + \frac{\varepsilon_p / D_i}{3.7}\right] \tag{7.12}$$

Nevertheless, the difficult involves in order to obtain f from Eq. (7.12) can be prevented by using the explicitly formula given by Haaland [122, 127]

$$\frac{1}{\sqrt{f}} \approx -1.8 \log_{10}\left[\left(\frac{\varepsilon_p / D_i}{3.7}\right)^{1.11} + \frac{6.9}{Re}\right] \tag{7.13}$$

It can be observed in Eq. (7.11) and (7.13) that f in laminar flow is a function of Re only while in turbulent flow it is not only the function of Re but also degree of pipe roughness ε_p [122, 125].

Besides, by substituting Eq. (7.10) in Eq. (7.3), it generated

$$F_\tau = A_f \frac{dP}{dx} dx = A_f \left(-h_f \frac{\rho_f g}{L}\right) dx = -h_f m_f g \tag{7.14}$$

7.2.2 Minor Energy Head Loss in Fluid Pipe

In pipe flow, minor energy (head) losses are always present in addition to major energy head loss. The effects of minor energy losses can be neglected in practice in analysis of long pipeline. Conversely, for short pipelines that contain many valves and bends their effects could be greater than those of major energy losses [122, 124, 125]. Hence, they should be considered in pipe fluid analysis. The pipe contains thickness discontinuity with fluid flowing is shown in Fig. 7.3. In this figure, D_d is the new pipe inner diameter created as a result of internal wall defect in the pipe geometry. In addition, the entire pipe can be divided into three sections whereby A_1, A_2 and A_3 are the internal areas of all sections and V_1, V_2 and V_3 are the fluid velocities at all sections in that order (see Fig. 7.3). Among these sections, second section is the one that contains discontinuity and as a result this region produces two minor head losses: sudden expansion h_e and

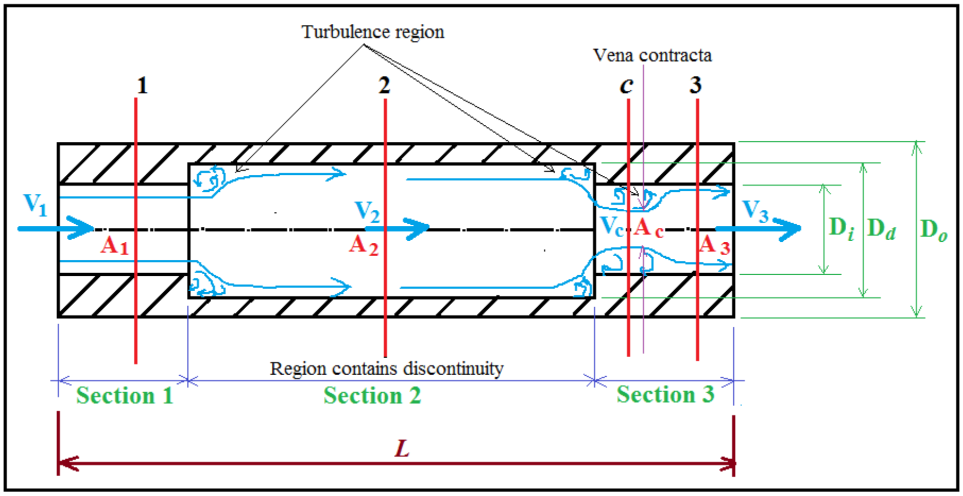

Figure 7.3: Pipe with thickness discontinuity sectional view.

sudden contraction h_c . Due to h_e, the upstream velocity V_1 will be higher than downstream velocity V_2 but pressure will decrease at downstream. Conversely, the upstream velocity V_2 will be lower than downstream velocity V_3 but there will be increase in pressure at downstream as a result of h_c . Minor energy losses will occur due to the change in pipe system geometry/dimension (and or direction) and others (see Table 7.1). Hence, it can be stated that discontinuity in the pipeline is one of the sources of the minor head loss. Thus, only h_e and h_c were considered as minor losses in this work. Among these two minor head losses, head loss due to h_e is relatively higher.

The cross sections of the three regions shown in Fig. 7.3 are as shown in Fig. 7.4. Upon applying Bernoulli's, momentum and continuity equations to first and second regions, second and third regions in Fig. 7.3 one after the other, the generalized minor head losses $\bar{h}_e$ and $\bar{h}_c$ in a pipe with and without thickness discontinuity were obtained as

$$\bar{h}_e = \frac{V_1^2}{2g}\left(1 - \frac{A_1}{A_s}\right)^2 \tag{7.15}$$

$$\bar{h}_c = \frac{V_3^2}{2g}\left(\frac{\bar{V}_c}{V_3} - 1\right)^2 \tag{7.16}$$

Similarly, the h_f in Eq. (7.8) can be generalized as

$$\bar{h}_f = f\,\frac{L}{D_s}\frac{V_s^2}{2g} \tag{7.17}$$

where

$$V_s = A_1 V_1 / A_s,\ \bar{V}_c = A_s V_s / 0.6 A_3,\ A_s = \frac{\pi D_s^2}{4},\ D_s = 2\sqrt{\frac{A_s}{\pi}}$$

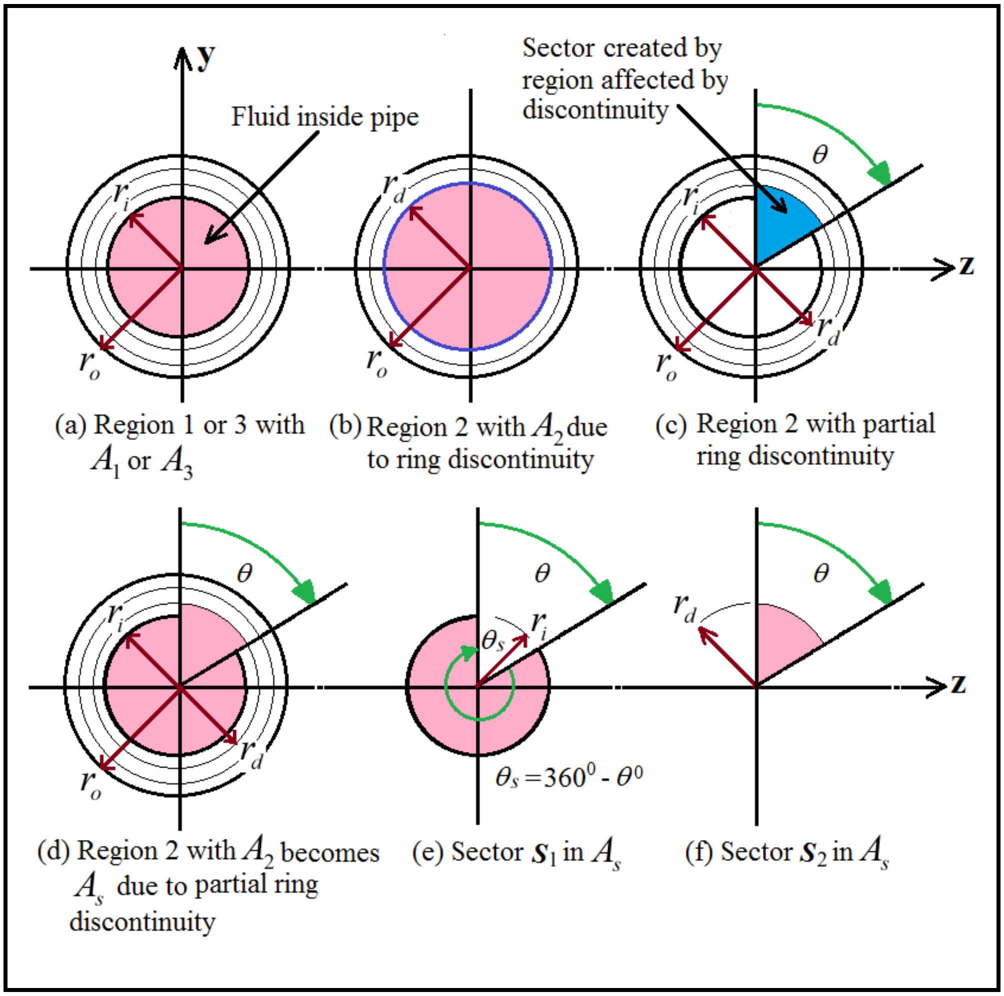

Figure 7.4: FRP Pipe with discontinuity cross-sections at different regions.

Thus, as θ increases A_{s_1} tends to zero, A_{s_2} approaches A_2 (causes A_s to approach A_2 in turn), V_s tends to V_2, $\overline{V}_c$ closes to V_c, D_s gradually becomes D_i. By the time $\theta = 360^0$ or discontinuity becomes full ring or annulus, $A_s = A_2, D_s = D_i, V_s = V_2$, $\overline{V}_c = V_c$, $\overline{h}_e = h_e$, $\overline{h}_c = h_c$, and $\overline{h}_f = h_f$.

Moreover, in a pipeline system either major or minor loses or both can occur as fluid is being conveyed from one point to another. The total energy loss h_t in the pipe shown in Fig. 7.3 can be expressed as

$$h_t = \bar{h}_f + \bar{h}_e + \bar{h}_c \tag{7.18}$$

and as a result, Eq. (7.14) will become

$$F_\tau = -h_t m_f g \tag{7.19}$$

7.3 Equation of Motion of Composite Pipe Conveying Fluid

According to the extended Hamilton's principle

$$\int_{t_1}^{t_2} (\delta U - \delta T - \delta W)dt = 0 \tag{7.20}$$

then, from Eq. (7.4)

$$\delta T = \delta\left(T_p + T_f\right) = \delta T_p + \delta T_f \tag{7.21}$$

By expanding each term in Eq. (7.4), they became

$$\begin{aligned} T_p &= \frac{1}{2}\int_0^{l_e} \bar{\mathcal{M}}(x) V_p^2 dx = \frac{1}{2}\int_0^{l_e} \bar{\mathcal{M}}(x)\left(\frac{\partial y}{\partial t}\right)^2 dx \\ T_f &= \frac{1}{2}\int_0^{l_e} m_f V_f^2 dx = \frac{1}{2}\int_0^{l_e} m_f \left(\left(\frac{\partial y}{\partial t}\right)^2 + 2V_x \frac{\partial^2 y}{\partial t \partial x} + V_x^2\left(\frac{\partial y}{\partial x}\right)^2\right) dx \end{aligned} \tag{7.22}$$

Upon substituting Eq. (7.22) in (7.21) it produced

$$\begin{aligned} \delta T &= \delta\left(\frac{1}{2}\int_0^{l_e} m_e \left(\frac{\partial y}{\partial t}\right)^2 dx + \frac{1}{2}\int_0^{l_e} 2m_f V_x \frac{\partial^2 y}{\partial t \partial x} dx + \frac{1}{2}\int_0^{l_e} m_f V_x^2 \left(\frac{\partial y}{\partial x}\right)^2 dx\right) \\ &= \delta\left(\frac{1}{2}\int_0^{l_e} m_e \left(\frac{\partial y}{\partial t}\right)^2 dx\right) + \delta\left(\frac{1}{2}\int_0^{l_e} 2m_f V_x \frac{\partial^2 y}{\partial t \partial x} dx\right) + \delta\left(\frac{1}{2}\int_0^{l_e} m_f V_x^2 \left(\frac{\partial y}{\partial x}\right)^2 dx\right) \\ &= \delta\left(\frac{1}{2}\int_0^{l_e} m_e \left(\frac{\partial y}{\partial t}\right)^2 dx\right) + \delta\left(\frac{1}{2}\int_0^{l_e} 2m_f V_x \frac{\partial^2 y}{\partial t \partial x} dx\right) - \int_0^{l_e} m_f V_x^2 \frac{\partial^2 y}{\partial x^2} \delta y dx \end{aligned} \tag{7.23}$$

wherein $m_e = \bar{\mathcal{M}}(x) + m_f$. By integrating Eq. (7.23) over the time, it resulted to

$$\begin{aligned}
\delta\int_{t_1}^{t_2} T dt &= \delta\int_{t_1}^{t_2}\left(\left(\frac{1}{2}\int_0^{l_e} m_e\left(\frac{\partial y}{\partial t}\right)^2 dx\right)+\delta\left(\frac{1}{2}\int_0^{l_e} 2m_f V_x\frac{\partial^2 y}{\partial t\partial x}dx\right)-\int_0^{l_e} m_f V_x^2\frac{\partial^2 y}{\partial x^2}\delta y dx\right)dt \\
&= \int_0^{l_e}\delta\left(\int_{t_1}^{t_2}\frac{1}{2}m_e\left(\frac{\partial y}{\partial t}\right)^2 dt\right)dx+\delta\left(\int_0^{l_e}\int_{t_1}^{t_2}\frac{1}{2}2m_f V_x\frac{\partial^2 y}{\partial t\partial x}dtdx\right)-\int_{t_1}^{t_2}\int_0^{l_e} m_f V_x^2\frac{\partial^2 y}{\partial x^2}\delta ydxdt \\
&= -\int_{t_1}^{t_2}\int_0^{l_e} m_e\frac{\partial^2 y}{\partial t^2}\delta ydxdt-\int_{t_1}^{t_2}\int_0^{l_e} 2m_f V_x\frac{\partial^2 y}{\partial t\partial x}\delta ydxdt-\int_{t_1}^{t_2}\int_0^{l_e} m_f V_x^2\frac{\partial^2 y}{\partial x^2}\delta ydxdt \\
&= -\int_{t_1}^{t_2}\left[\int_0^{l_e}\left(m_e\frac{\partial^2 y}{\partial t^2}+2m_f V_x\frac{\partial^2 y}{\partial t\partial x}+m_f V_x^2\frac{\partial^2 y}{\partial x^2}\right)\delta ydx\right]dt
\end{aligned} \qquad (7.24)$$

Similarly, from Eq. (7.5):

$$\delta U=\delta\left(\frac{1}{2}\int_0^{l_e}\bar{\mathcal{H}}(x)\left(\frac{\partial^2 y}{\partial x^2}\right)^2 dx\right)=\int_0^{l_e}\bar{\mathcal{H}}(x)\frac{\partial^4 y}{\partial x^4}\delta ydx \qquad (7.25)$$

Substituting Eqs. (7.7), (7.23) and (7.25) in Eq. (7.20), applied Eq. (7.24) thereafter and then simplified produced equation of motion for the laminated composite pipe as

$$\bar{\mathcal{H}}(x)\frac{\partial^4 y}{\partial x^4}+\left(F_p+m_f V_x^2\right)\frac{\partial^2 y}{\partial x^2}+m_e\frac{\partial^2 y}{\partial t^2}+2m_f V_x\frac{\partial^2 y}{\partial t\partial x}=0 \qquad (7.26)$$

There are four terms in Eq. (7.26): pipe stiffness, centrifugal force that emerges as a result of fluid acceleration through the deformed pipe curvature, pipe inertia and coriolis force which is the force needed to rotate element of fluid with local pipe rotation. Among these terms, centrifugal force will cause decrease in naturally frequency that will finally lead to buckling. In addition, an asymmetric alteration of conventional mode shapes will occur due to coriolis force mixed derivative and this will produce instability like flutter [121].

7.4 Finite Element Formulation of Composite Pipe Conveying Fluid

In order to solve Eq. (7.26), the approximation method was employed due to the fact that derivation of analytical solution to the equation is complex as a result of vibration behavior of the pipeline system. Thus, the composite pipe conveying fluid was discretized using the Euler-Bernoulli pipe element EP in which the only unknown field function is $y(\zeta)$. If the scaling functions of B-spline wavelet on the interval were utilized to express $y(\zeta)$, it would become

$$y(\zeta, t) = \sum_{i=-m+1}^{2^j-1} \beta_{m,i}^j \varphi_{m,i}^j(\zeta) = \{\Psi\}\{\Lambda\} \tag{7.27}$$

wherein $\{\Psi\}$ and $\{\Lambda\}$ are the row vector of the scaling functions and the column vector of the wavelet coefficients to be determined and they are defined as

$$\{\Psi\} = \{\varphi_{m,-m+1}^j(\zeta) \quad \varphi_{m,-m+2}^j(\zeta) \quad \cdots \quad \varphi_{m,2^j-1}^j(\zeta)\}$$

$$\{\Lambda\} = \{\beta_{m,-m+1}^j \quad \beta_{m,-m+2}^j \quad \cdots \quad \beta_{m,2^j-1}^j\}^T$$

Moreover, Eq. (7.27) is in the wavelet-space, then, in order to satisfy the compatibility of the displacement field y each of the element two end nodes (nodes 1 and n_d in Fig. 5.3) will contain two degrees of freedom (y and $\Theta = dy/dx$) in physical space in accordance with Euler-Bernoulli beam theory. Hence, the actual total number of DOF per element will be $n_d + 2$ and the vector of nodal DOF for each element is defined as

$$\{y(t)\}_e = \{y_1 \quad \Theta_1 \quad y_2 \quad y_3 \quad \cdots \quad y_{n_d-2} \quad y_{n_d-1} \quad y_{n_d} \quad \Theta_{n_d}\}^T \tag{7.28}$$

where

$$\Theta_1 = \frac{1}{l_e}\frac{dy(\zeta_1)}{d\zeta}, \quad \Theta_{n_d} = \frac{1}{l_e}\frac{dy(\zeta_{n_d})}{d\zeta}$$

Substituting Eq. (5.43) into Eq. (7.27), one can expressed Eq. (7.28) in matrix form as

$$\{y\}_e = [\Re_B]\{\Lambda\} \tag{7.29}$$

where

$$[\Re_B] = \Big[\{\Psi(\zeta_1)\}^T \quad \left\{\{\Psi(\zeta_1)\}/l_e d\zeta\right\}^T \quad \{\Psi(\zeta_2)\}^T \quad \{\Psi(\zeta_3)\}^T \quad \cdots$$
$$\{\Psi(\zeta_{n_d-2})\}^T \quad \{\Psi(\zeta_{n_d-1})\}^T \quad \{\Psi(\zeta_{n_d})\}^T \quad \left\{\{\Psi(\zeta_{n_d})\}/l_e d\zeta\right\}^T\Big]^T$$

Then, from Eq. (7.29)

$$\{\Lambda\} = [T_B]\{y\}_e\,,\ [T_B] = [\Re_B]^{-1} \tag{7.30}$$

By substituting Eq. (7.30) in Eq. (7.27), we obtained

$$y(\zeta,t) = [N_B]\{y\}_e,\ [N_B] = \{\Psi\}[T_B] \tag{7.31}$$

Then, by substituting Eq. (7.31) in Eq. (7.23), it produced

$$\begin{gathered}\int_0^{l_e}\left(l_e m_e [T_B]^T\{\Psi\}^T\{\Psi\}[T_B]d\zeta\right)\{\ddot{y}\}_e + \int_0^{l_e}\left(2m_f V_x[T_B]^T\{\Psi\}^T\{\Psi^{'}\}[T_B]d\zeta\right)\{\dot{y}\}_e + \\ \int_0^{l_e}\left(\frac{\bar{\mathcal{H}}}{l_e^3}[T_B]^T\{\Psi^{''}\}^T\{\Psi^{''}\}[T_B] - \frac{1}{l_e}\left(F_p + m_f V_x^2\right)[T_B]^T\{\Psi^{'}\}^T\{\Psi^{'}\}[T_B]\right)d\zeta\{y\}_e = 0\end{gathered} \tag{7.32}$$

Eq. (7.32) is the equilibrium equation of motion for the composite pipeline conveying fluid. However, Eq. (7.32), can be re-arranged succinctly as

$$[M]_e\{\ddot{y}\}_e + [B]_e\{\dot{y}\}_e + [K]_e\{y\}_e = 0 \tag{7.33}$$

where

$$[K]_e = [K_p]_e - [K_c]_e$$

$$[K_p]_e = \int_0^{l_e} \frac{\bar{\mathcal{H}}}{l_e^3}[T_B]^T\{\Psi''\}^T\{\Psi''\}[T_B]d\zeta, \quad [K_c]_e = \int_0^{l_e} \frac{1}{l_e} C_k [T_B]^T\{\Psi'\}^T\{\Psi'\}[T_B]d\zeta$$

$$[M]_e = \int_0^{l_e} l_e m_e [T_B]^T\{\Psi\}^T\{\Psi\}[T_B]d\zeta, \quad [B]_e = \int_0^{l_e} C_b [T_B]^T\{\Psi\}^T\{\Psi'\}[T_B]d\zeta,$$

and

$$m_e = \bar{\mathcal{M}} + m_f, \; C_k = F_p + m_f V_x^2, C_b = 2m_f V_x$$

It noteworthy to make it known that $[B]_e$ is an unsymmetric matrix and varies according to the vibration modes, thus it is not the traditional damping matrix [55].

Furthermore, with state vectors $\{\dot{\chi}\}$ and $\{\chi\}$, Eq. (7.33) can be placed in state space form as

$$[\overleftrightarrow{M}]\{\dot{\chi}\} - [\overleftrightarrow{K}]\{\chi\} = 0 \tag{7.34}$$

where

$$[\overleftrightarrow{M}] = \begin{bmatrix} [I] & [0] \\ [0] & [M]_e \end{bmatrix}, \; [\overleftrightarrow{K}] = \begin{bmatrix} [0] & [I] \\ -[K]_e & -[B]_e \end{bmatrix}, \; \{\chi\} = \begin{bmatrix} \{y_1\} \\ \{y_2\} \end{bmatrix}, \; \{\dot{\chi}\} = \begin{bmatrix} \{\dot{y}_1\} \\ \{\dot{y}_2\} \end{bmatrix}$$

Similarly, by assuming the motion of the fluid pipe to be harmonic:

$$\{\chi\} = \{W\}e^{i\omega t}, \{\dot{\chi}\} = i\omega\{W\}e^{i\omega t} \tag{7.35}$$

where ω is frequency and $\lambda = i\omega$. Then, upon substituting Eq. (7.35) in Eq. (7.34) the eignevalue problem was obtained as

$$\left[[\overleftrightarrow{K}] - \lambda[\overleftrightarrow{M}]\right]\{W\} = 0 \tag{7.36}$$

It should be noted that if the size of each matrix in Eq. (7.33) was nxn, the size of each matrix in Eq. (7.36) would be $2nx2n$. In addition, there would be $2n$ values of eigenvalue λ_f that would appear in complex conjugate pairs.

7.5 Results and Discussion

In order to validate the model developed for composite pipe conveying fluid, several pipes were examined. First and foremost, the equation was modified to be able to handle isotropic pipes because of their availability in literature.

7.5.1 Isotropic Pipes Conveying Fluid

In this section, pretension force $\bar{T}$ and loss h_l are neglected and isotropic pipes without internal surface defect conveying fluid were investigated. The first pipe investigated is the one studied in [49] using transfer matrix method (TMM). The nondimensional flow velocity $\bar{V}$, mass ratio β and natural frequencies ω employed were given as

$$\bar{V} = \left(\frac{M}{EI}\right)^{1/2} VL,\ \beta = \frac{M}{M+m},\ \omega = 2\pi\left(\frac{M+m}{EI}\right)^{1/2} L^2\bar{\varpi}$$

where M, m, V and $\bar{\varpi}$ are mass of the fluid per unit length, mass of the pipe per unit length, steady flow velocity and natural frequency of the pipe, respectively. The steel pipe considered has length of 1200 mm, inner diameter of 48 mm, and outer diameter of 51 mm. The pipe is conveying water. The results obtained with two elements and that of [49] with four elements when $\beta = 0.5$ were compared as shown in Fig. 7.5. It can be observed that the results obtained in this study compared well with that of [49]. Besides, the pipe considered in [41] described in Table 7.2 with laminar flow was also studied and the results obtained with two elements and that of [41] are presented in Fig. 7.6. This figure shows that there is good agreement between the present study and that of [41]. The pipe described in Table 7.2 investigated in [128] using analytical method with Wolfram

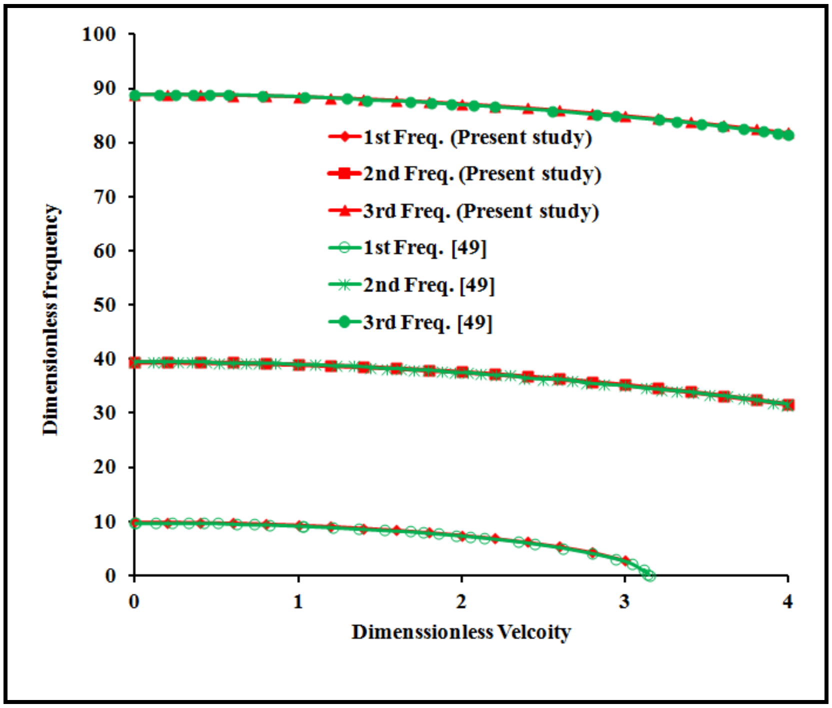

Figure 7.5: The first three frequencies of pinned-pinned pipe with fluid flow.

Table 7.2: Isotropic pipes and fluid properties

Property	**Ref. [41]**	**Ref. [128]**	**Ref. [44]**	**Ref. [129]**
D_i (m)	0.048	0.01	0.162	0.0098
D_o (m)	0.052	0.0102	0.168	0.01
L (m)	1.2	1.0	2.8	2.0
E (GPa)	210	210	70	207
ν	0.3	-	-	-
Pipe density ρ_p (kg/m^3)	7800	7600	2800	8000
Fluid density ρ_f (kg/m^3)	1000	1000	1000	1000

Mathematica 8.0 was examined as well with two elements and the results obtained with that of [128] are shown in Fig. 7.7. It can be seen that the results compared well with that of [128]. In order to examine further the effectiveness of the model presented in this study, the pipe analyzed in [44] using FEM method described in Table 7.2 was investigated until the pipe lost its stability (buckling). The results obtained using four

elements with that of [44] that used twenty five elements are as shown in Fig.7.8 and it can be found that the results obtained agreed with that of [44].

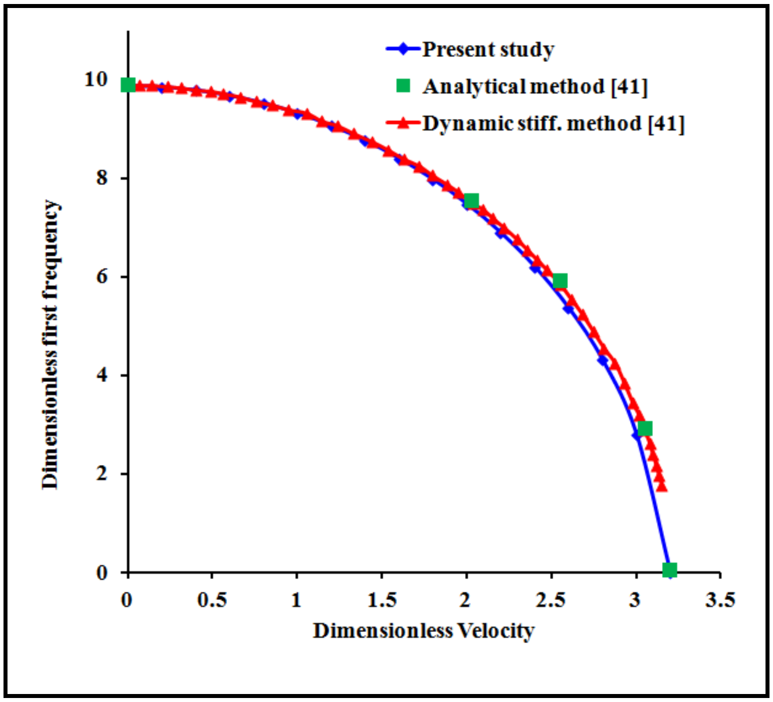

Figure 7.6: First frequency of pinned-pinned pipe with fluid flow using different methods.

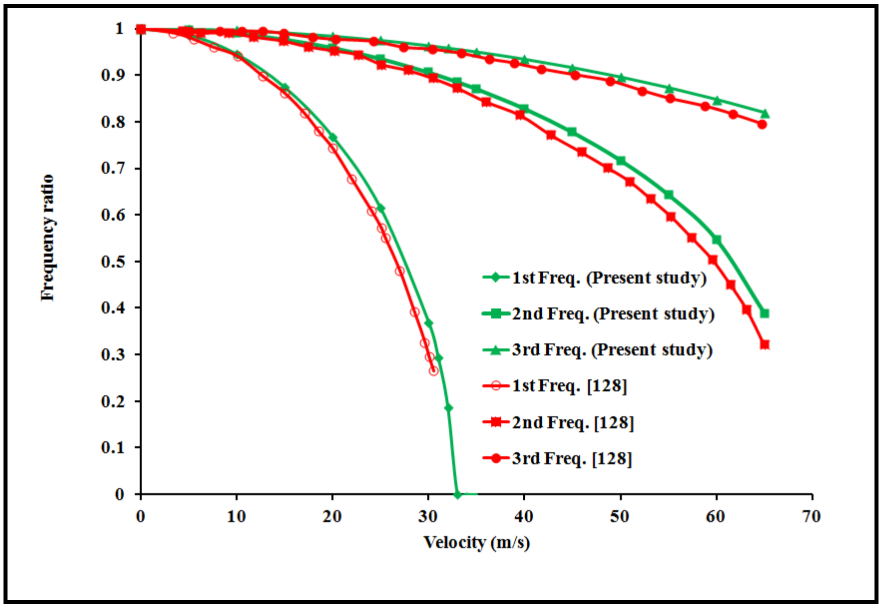

Figure 7.7: The first three frequencies of pinned-pinned pipe with fluid flow.

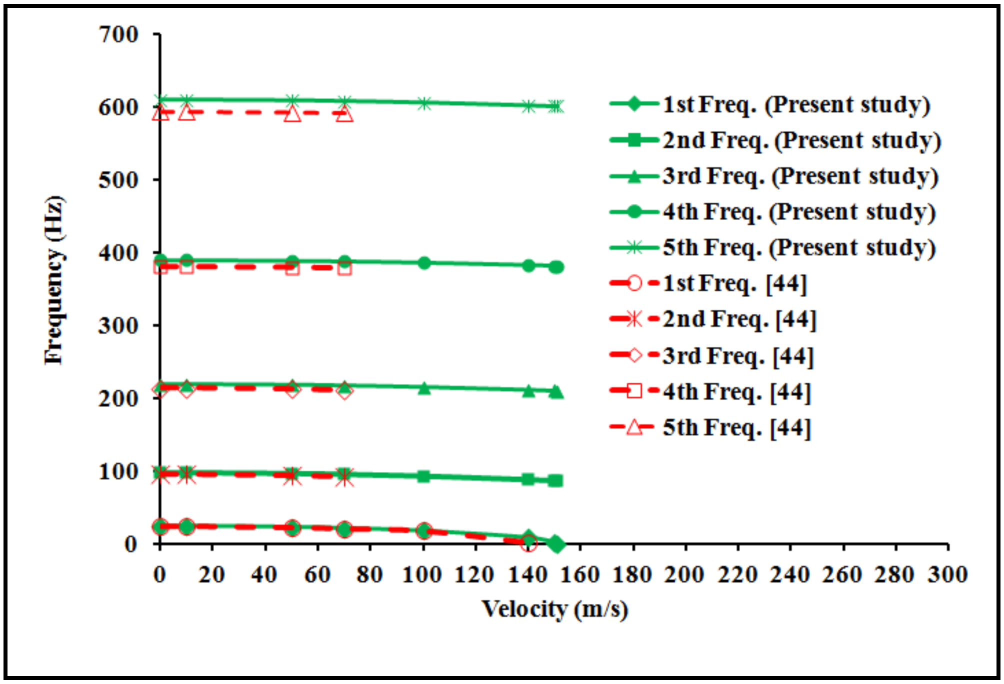

Figure 7.8: The first five frequencies of pinned-pinned pipe with fluid flow.

Another pipe studied under isotropic pipe is the one investigated in [129] using TMM. The pipe is described in Table 7.2 and the results obtained with three elements and that of [129] with ten elements are shown in Fig. 7.9. It can be detected that by comparing Fig. 7.9 to previous figures, the results obtained in this work are more accurate than that of [129].

All the aforementioned pipes are pinned-pinned pipes, however, the present model was also applied to a cantilever pipe considered in [44]. The first three frequencies of the pipe listed in [44] for V =0 m/s include 8.5, 55.4 and 152.6 Hz while from their plot these frequencies can be approximated to be 6.4, 54.3 and 152.3 for V =50 m/s. In this study, the results obtained for the same pipe when V =0 are 8.7, 54.5 and 152.6 Hz and those

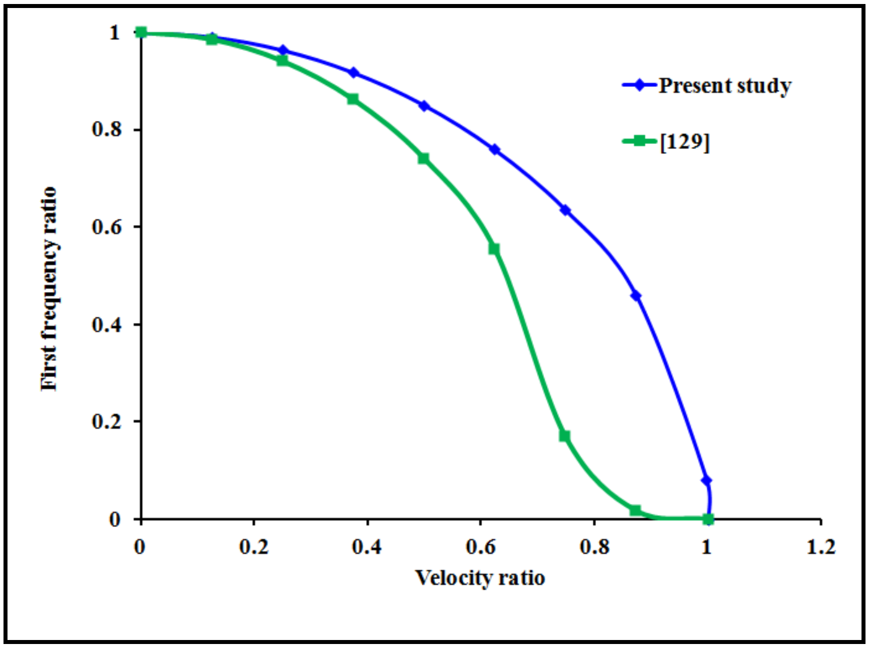

Figure 7.9: First frequency of pinned-pinned pipe with fluid flow.

obtained when V =50 m/s are 4.5, 52.6 and 151.0 Hz in that order. It can be confirmed that the results obtained compared well with those of [44].

Another pipe studied is the variable cross-section pipe supported at two ends by spring (see Fig. 7.10) investigated in [42] using TMM. The flow is laminar and pipe has three segments whereby lengths $L_1 = L_3 = 25cm$ with $L_2 > L_1$. The pipe and fluid properties are as defined in Table 7.3 and Ref. [42] can be consulted for more information. The results obtained are tabulated together with those obtained in[42] for the two fluid considered in Table 7.4. The results in Table 7.4 show that the results obtained in the present study matched well with that of [42]. Further, as it can be discovered in Table 7.4, h_t has no noticeable effect on the frequency under present study. This is due to the fact that the flow under consideration is laminar (very low velocity) and as a results the effect of h_t is immaterial but by the time the flow becomes turbulent (at very high velocity) the effect

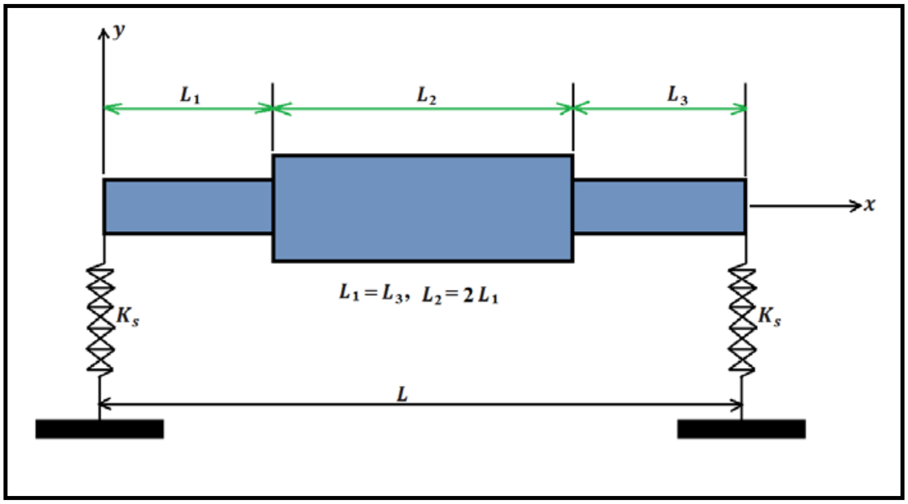

Figure 7.10: Variable cross-section pipe conveying fluid supported by springs.

Table 7.3: Copper pipe and fluid properties [42]

Property	**Value**
Outer diameters, $D_1 \& D_3$	0.0127 m
Outer diameter, D_2	0.0254 m
Reynolds Number, Re	1500
Water density	998.2 kg/m^3
Water dynamic viscosity	0.001003 Pa sec.
Oil density	780 kg/m^3
Oil dynamic viscosity	0.00157 Pa sec.

Table 7.4: Frequencies of pipe with variable cross-sections supported at ends by spring.

S/N	**Pipe Without Fluid**		**Pipe with Fluid**					
			Water			**Oil**		
	Ref. [42]	**Present study**	**Ref. [42]**	**Present study**		**Ref. [42]**	**Present study**	
	20 Elements	**3 Elements**	**20 Elements**	**3 Elements**		**20 Elements**	**3 Elements**	
				$h_t = 0$	$h_t \neq 0$		$h_t = 0$	$h_t \neq 0$
1	31.04	31.07	25.62	25.64	25.64	26.58	26.58	26.58
2	93.11	94.87	79.90	80.80	80.80	82.28	83.34	83.34
3	260.06	260.67	227.59	228.38	228.38	233.64	234.38	234.38

of h_t will become relatively significant. Furthermore, this pipe was studied further by examining the effect of these three lengths on the pipe frequencies if they are altered. In this case, it can be seen in Table 7.5 that as L_1 decreases, L_2 increases and pipe frequency continue to increase with and without fluid (water). This shows that the major percentage of the pipe stiffness is from the second segment, as a result, the longer the L_2, the stiffer the pipe and the higher the frequency and its V_{cr}.

Generally, in most aforementioned examples where several velocities were considered, it can be found that at certain velocity the first frequency became zero. This is due to the effects of increasing in mass of the system by fluid and decreasing in system stiffness due to centrifugal force. Thus, as the velocity V of the fluid increased the stiffness of pipe continued to reduce and at a certain velocity the real part of first eigenvalue became zero. The velocity at which this occurs is regarded as critical velocity V_{cr}. In addition, when the value of velocity was selected arbitrarily and the value selected was greater than V_{cr}, the real part of first eigenvalue remained zero.

Table 7.5: Frequency of pipe with variable cross-sections and lengths supported at ends by spring.

S/N	**L_1= L_3=0.45, L_2=0.1**		**L_1= L_3=0.35, L_2=0.3**		**L_1= L_3=0.25, L_2=0.5**			
	Present study				**Present study**		**Ref. [42]**	
	Pipe without Fluid	**Pipe with Fluid**	**Pipe without Fluid**	**Pipe with Fluid**	**Pipe without Fluid**	**Pipe with Fluid**	**Pipe without Fluid**	**Pipe with Fluid**
	3 Elements	**3 Elements**	**3 Elements**	**3 Elements**	**3 Elements**	**3 Elements**	**20 Elements**	**20 Elements**
1	22.90	19.84	25.36	21.27	31.07	25.64	31.04	25.62
2	88.74	79.55	88.64	77.82	94.87	80.80	93.11	79.90
3	191.38	169.20	232.29	205.66	260.67	228.38	260.06	227.59

7.5.2 Laminated Composite Pipes Conveying Fluid

In this section, composite pipes with internal surface defect were considered. Firstly, the model developed was validated using the works in [55] using Ritz method and the first three frequencies obtained are compared in Table 7.6 where $\mathcal{H} = \Re$. It can be noticed that the results obtained in the present study agreed with that of [55]. It should be noted that pipe configuration is the same as that of the one examined in Table 6.2.

Moreover, the vibrational behavior of a composite pipe conveying fluid, with data as given in Table 5.9 is investigated in the presence of internal surface defect. The fluid is water with density and dynamic viscosity of 998.2 kg/m^3 and 1.003e-3kg/m/s, respectively. The first four frequencies obtained for this FRP pipe without fluid here are as tabulated in Table 6.9.

In order to investigate the effect of fluid on this FRP pipe, the fluid velocity was increased from 0 until the pipe lost its stability with $h_t = 0$ and $h_t \neq 0$, the frequency obtained are presented in Fig. 7.11(a). In Fig. 7.11(b), the first frequency in Fig. 7.11(a) was re-produced for clarity and it can be seen that for uniform pipe there is no significant difference in frequency when $h_t = 0$ and $h_t \neq 0$. However, when the pipe contains thickness discontinuity ($L_c = L/2$, $L_d = 0.15$, $t_d = 3h/4$, $\theta_1 = 0^0$ and $\theta_2 = 90^0$), there was difference between the first frequency when $h_t = 0$ and $h_t \neq 0$ (see Fig. 7.12). This is due to the fact that in Fig. 7.11 when $h_t \neq 0$ only major loss ($\overline{h}_f$) was active and its effect is of no consequence while both major loss and minor loss ($\overline{h}_e$ and $\overline{h}_c$) were active in Fig. 7.12. This shows that in a straight pipe the contribution of $\overline{h}_f$ can be neglected.

Table 7.6: Composite pipe made of fiberglass epoxy with and without fluid flow [55]

S/N	D_o (mm)	L (m)	Pipe wall layup configuration (from outside to inside)			Laminate stiffness			Frequency (Hz)			
									Empty pipe		Pipe with fluid, 12m/s	
			#5 (mm)	#6 (mm)	#7 (mm)	$A_{11}*10^7$ (N/m)	D_{11} (Nm)	$\Re*10^3$ (Nm^2)	Ref. [55]	Present work	Ref. [55]	Present work
1	60.22	1.30	1.98	0	2.41	5.0566	87.1528	3.4632	58.63	57.76	52.85	50.78
									NA	231.03	NA	203.26
									NA	519.83	NA	457.38
2	88.62	1.33	1.98	0	2.36	5.5305	90.8353	11.8550	83.51	83.71	71.31	69.63
									NA	334.85	NA	278.66
									NA	753.41	NA	627.04
3	114.30	5.60	2.24	0	2.21	7.6281	161.5345	28.8050	6.38	6.04	5.183	4.89
									NA	24.17	NA	19.69
									NA	54.37	NA	44.34
4	168.28	5.60	2.41	0	2.54	7.363	216.7862	102.8600	9.28	9.10	7.16	6.93
									NA	36.41	NA	27.84
									NA	81.93	NA	62.67
5	219.08	5.60	3.25	0	2.13	5.0382	84.2246	292.3900	13.49	11.56	9.84	8.89
									NA	46.23	NA	35.66
									NA	104.01	NA	80.26
6	273.05	5.60	3.35	0	2.79	6.01	125.0215	603.5600	15.96	14.66	11.49	10.81
									NA	58.65	NA	43.32
									NA	131.96	NA	97.51
7	323.85	5.60	1.98	1.57	2.41	8.0816	238.7322	925.8100	16.42	16.18	11.86	11.61
									NA	64.74	NA	46.54
									NA	145.66	NA	104.74

NA=Not available

Besides, it can be observed in Fig. 7.12 that when $h_t \neq 0$, V_{cr} at which pipe lost its stability is higher than the V_{cr} its lost stability when $h_t = 0$. One can assume that discontinuity has stabilizing and destabilizing effects depend on its geometry and velocity under consideration. Consequently, it can be deduced that h_t is important when pipe with

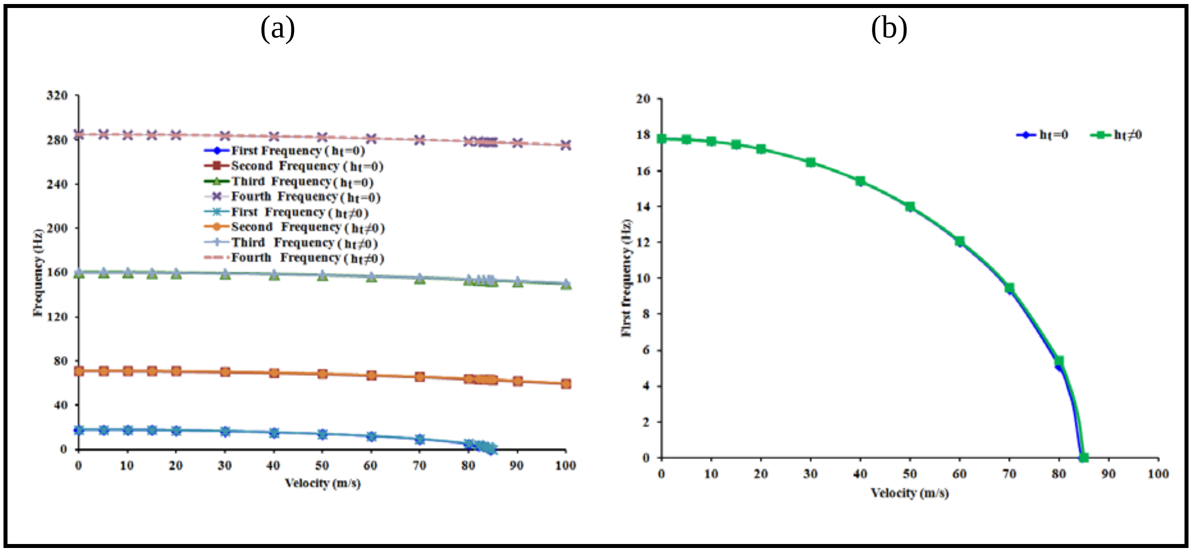

Figure 7.11: Frequency of pinned-pinned FRP pipe conveying fluid: (a) First four frequencies (b) First frequency

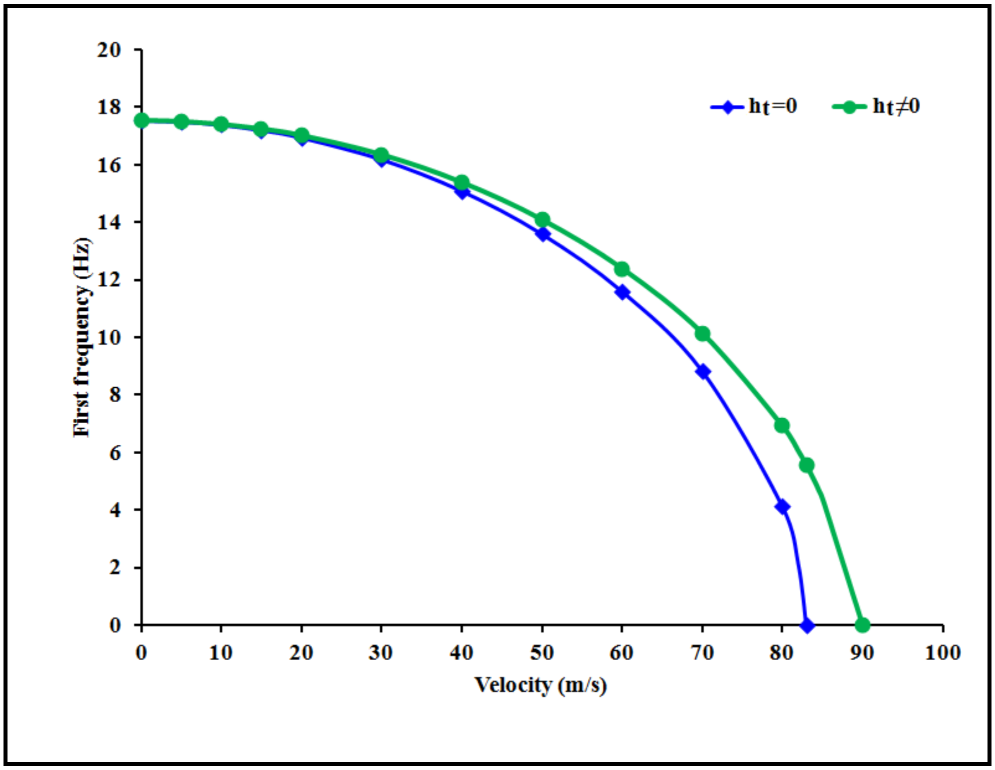

Figure.7.12: First frequency of pinned-pinned FRP pipe with discontinuity conveying fluid.

discontinuity conveying fluid is being investigated, as a results in all the pipes considered from now on, $h_t \neq 0$.

In present investigation, laminated composite pipe with different discontinuity geometries (from partial to full annulus, see Figs. 7.13 and 7.14) were considered and in each of them, $L_c = L/2$ while L_d and t_d are 0.15 and $3h/4$ except otherwise stated. It should be noted that the presence of internal wall defect in the pipe will affect the effects of fluid on the pipe and vice versa. Nevertheless, the combination of the effects of these two phenomena will end up reducing the pipe frequencies.

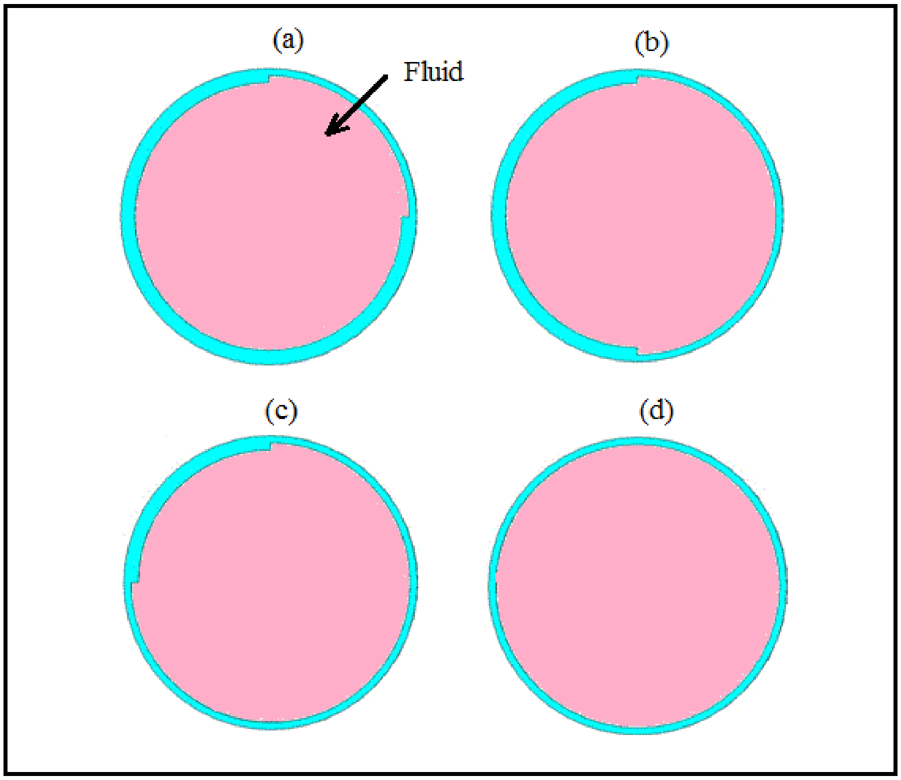

Figure 7.13: Pipe fluid cross-section as internal surface defect grows from partial to full annulus: (a) $\theta_1 = 0^0$, $\theta_2 = 90^0$ (b) $\theta_1 = 0^0$, $\theta_2 = 180^0$ (c) $\theta_1 = 0^0$, $\theta_2 = 270^0$ (d) $\theta_1 = 0^0$, $\theta_2 = 360^0$

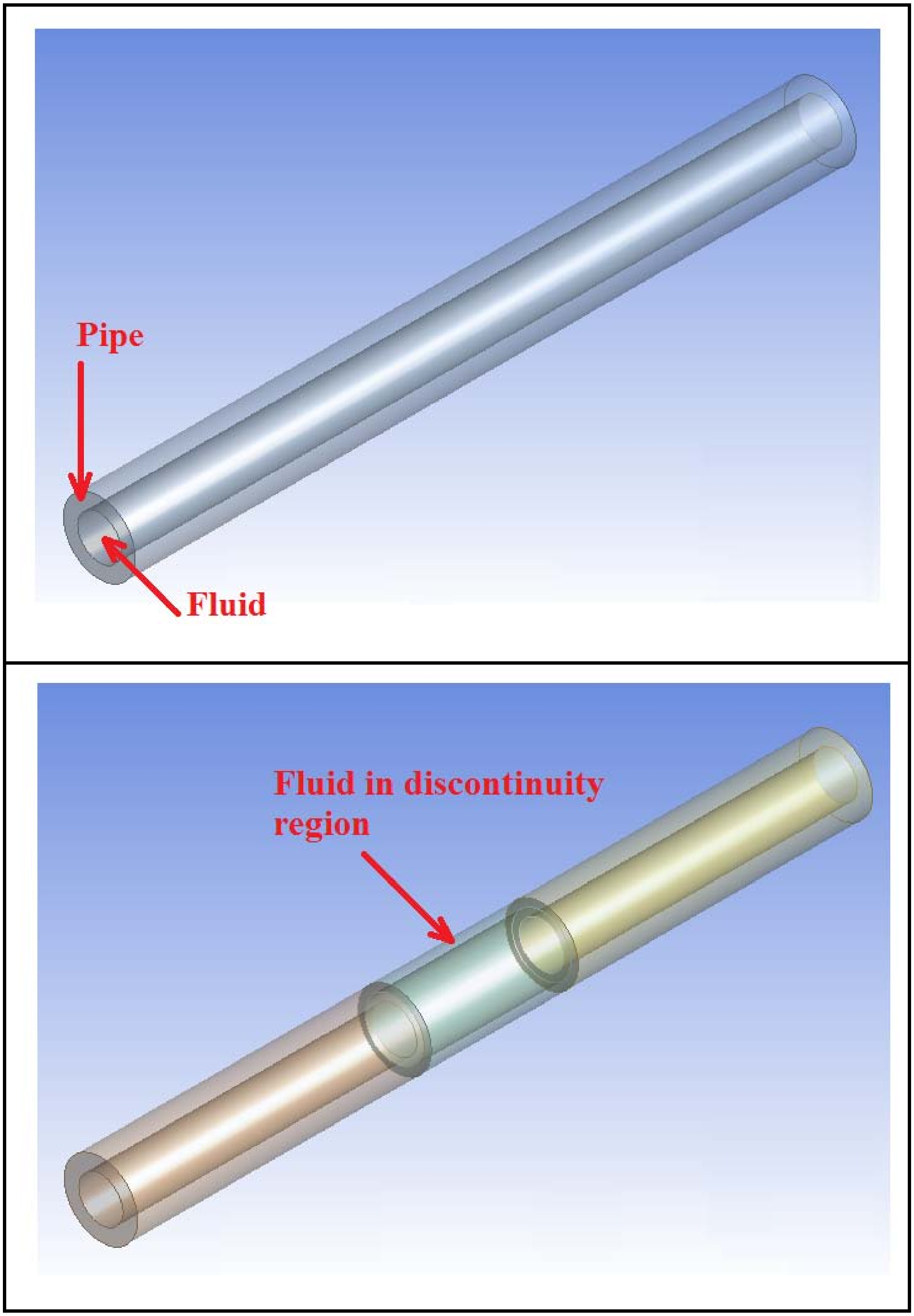

Figure 7.14: Fluid in pipe with and without thickness discontinuity.

Figures 7.15-7.18 show the first four frequencies obtained for each composite pipe with internal defect compared with the one obtained when pipe did not contain thickness discontinuity. It can be seen in these figures that as θ_2 increases, the reduction in frequencies of pipe with discontinuity increases more than that of pipe without discontinuity. This reduction was more in all frequencies except in second frequency. In addition, it can be observed also that as velocity of fluid increases, the frequencies of pipe without thickness discontinuity moved closer to those of pipe with discontinuity. In addition, unlike other frequencies at higher velocities the reduction in second frequency

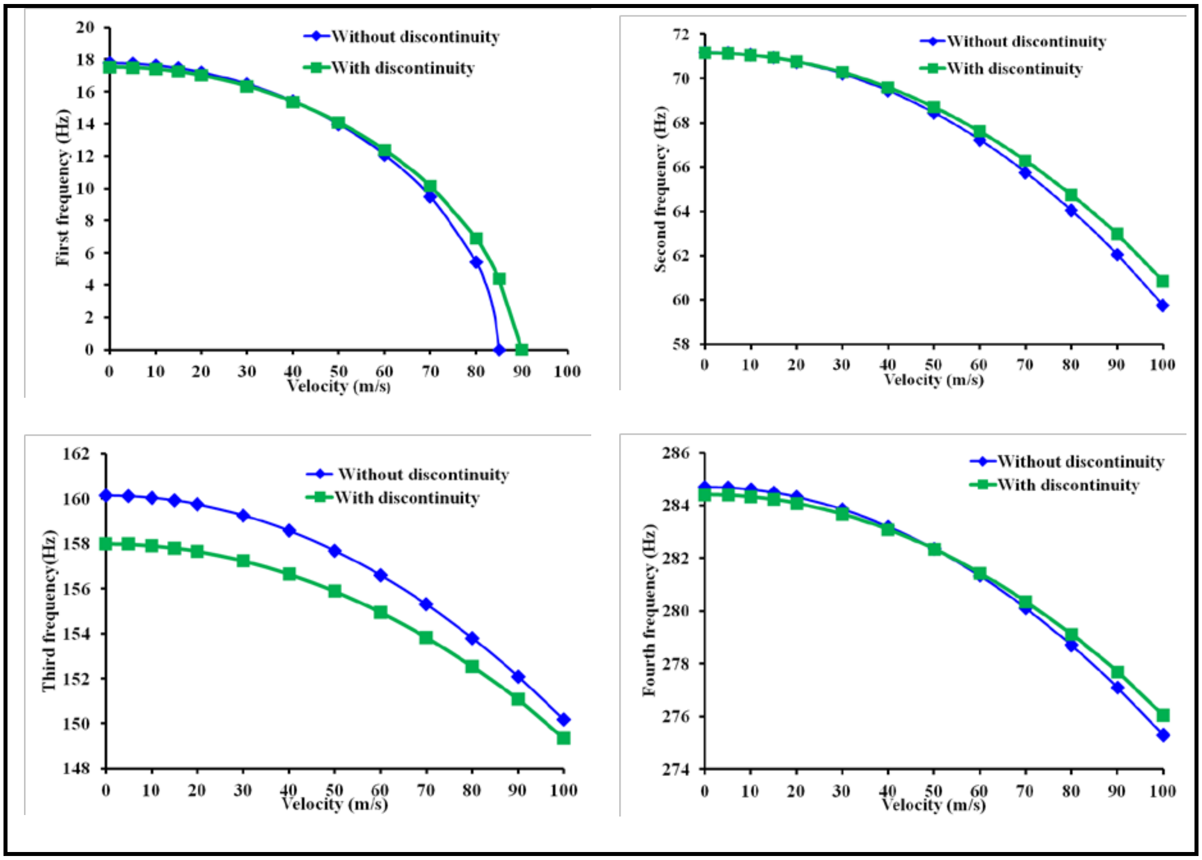

Figure 7.15: Frequency of pinned-pinned FRP pipe with discontinuity conveying fluid when $\theta_1 = 0^0$ and $\theta_2 = 90^0$ (surface defect of Fig. 7.13a).

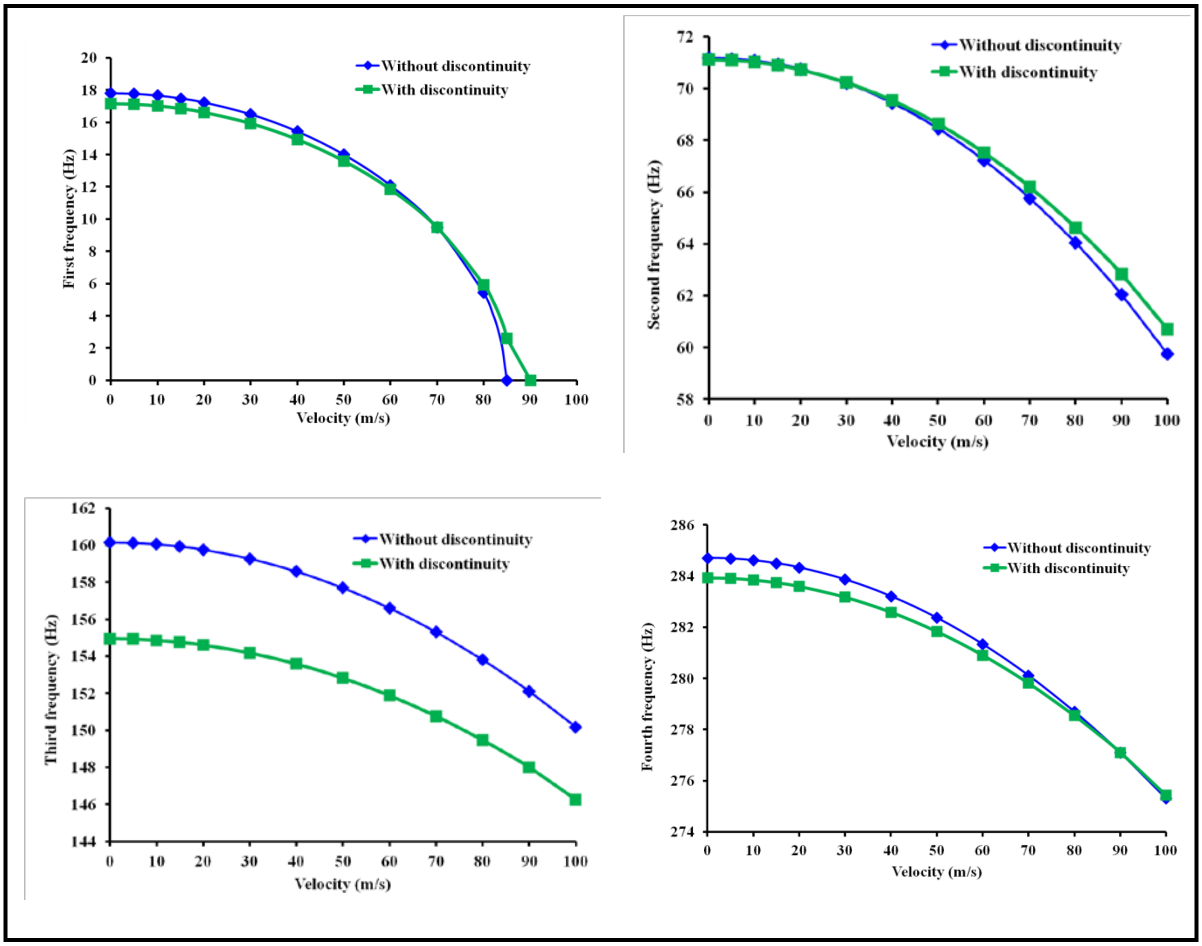

Figure 7.16: Frequency of pinned-pinned FRP pipe with discontinuity conveying fluid when $\theta_1 = 0^0$ and $\theta_2 = 180^0$ (surface defect of Fig. 7.13b).

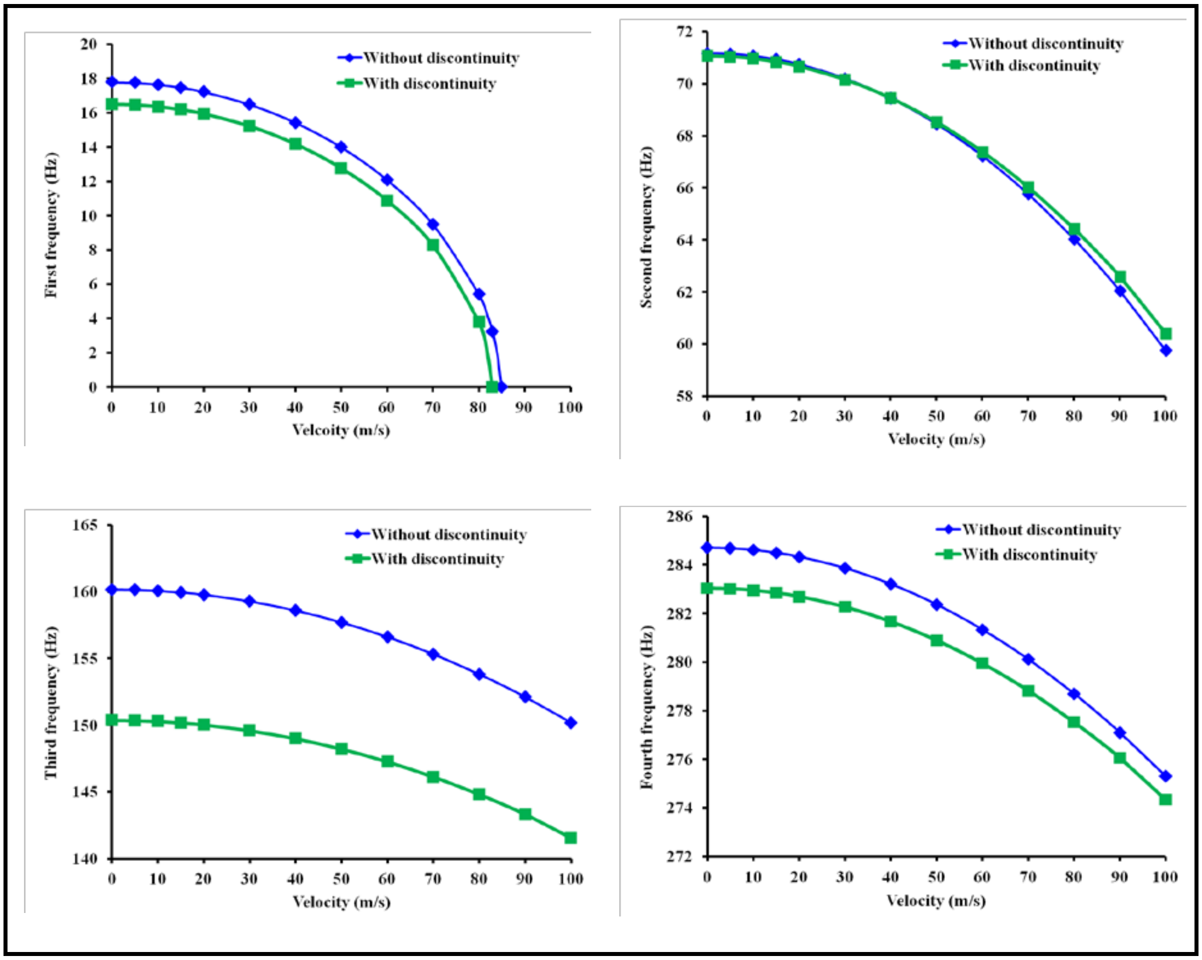

Figure 7.17: Frequency of pinned-pinned FRP pipe with discontinuity conveying fluid when $\theta_1 = 0^0$ and $\theta_2 = 270^0$ (surface defect of Fig. 7.13c).

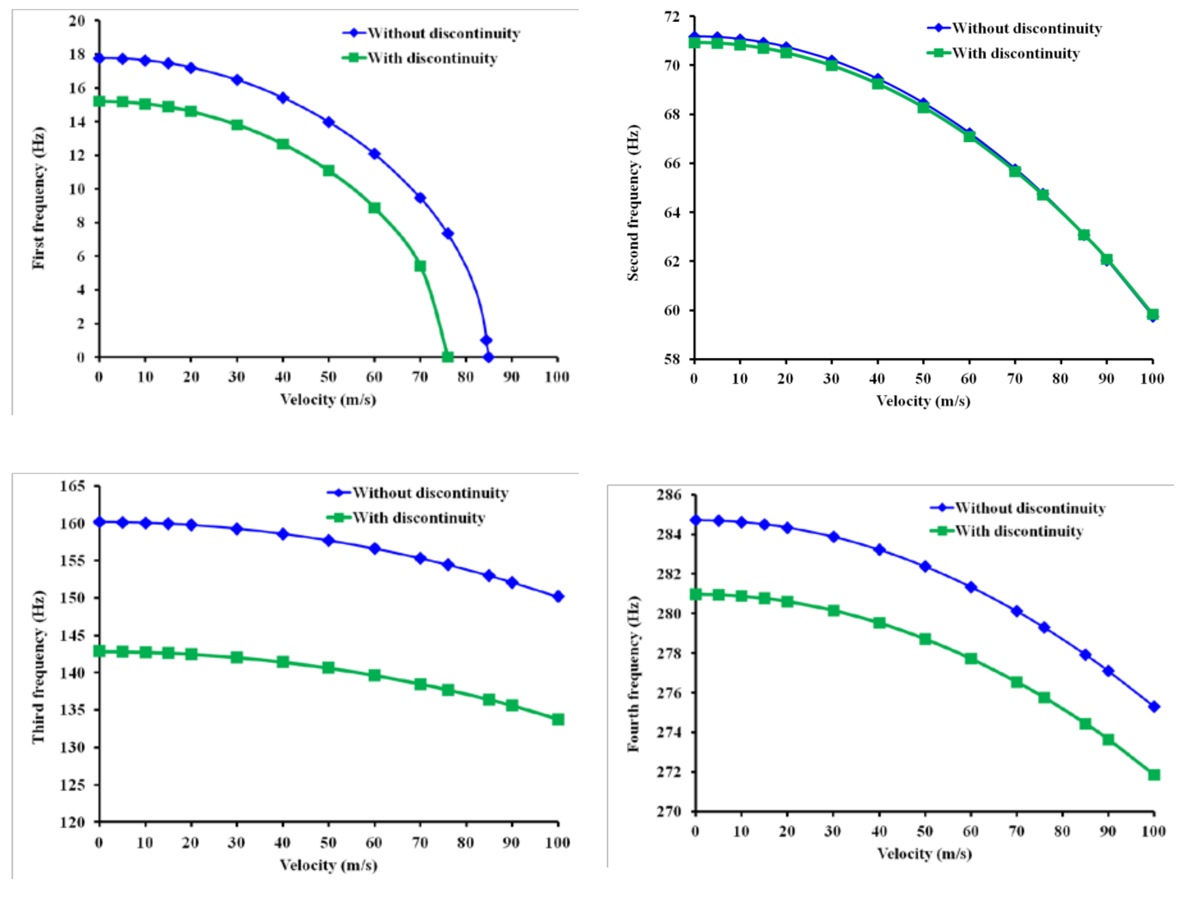

Figure 7.18: Frequency of pinned-pinned FRP pipe with discontinuity conveying fluid when $\theta_1 = 0^0$ and $\theta_2 = 360^0$ (surface defect of Fig. 7.13d).

is more in pipe without discontinuity than that of pipe with discontinuity until discontinuity becomes annulus or $\theta_2 = 360^o$.

Furthermore, in Figs. 7.15-7.18 the thickness $t_d = 3h/4$, the effect of different t_d on pipe frequency was studied next. The results obtained as t_d increases from 0 to $3h/4$ for pipe with annulus internal wall defect and pipe without discontinuity (when $t_d = 0$) are presented in Fig. 7.19. One can see from Fig. 7.19 that as t_d increases, the reduction in frequencies of pipe with discontinuity increases compare to the pipe without

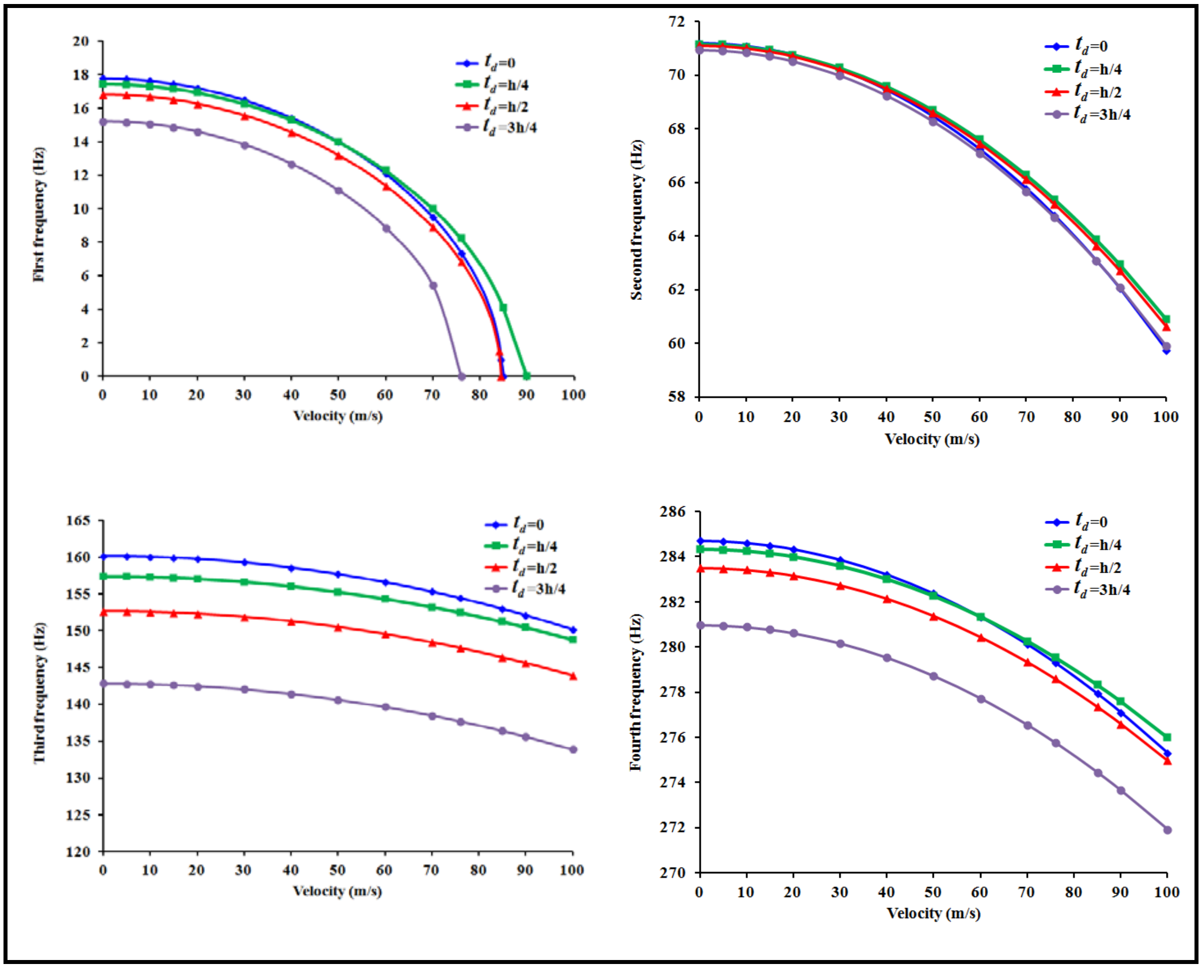

Figure 7.19: Frequency of pinned-pinned FRP pipe with different t_d conveying fluid when $\theta_1 = 0^o$ and $\theta_2 = 360^o$.

discontinuity. The maximum reduction in all four frequencies under consideration occurred when $t_d = 3h/4$. Also, it is only in third frequency that reduction in frequency of pipe with discontinuity more than that of pipe without discontinuity at all t_d considered.

In Figs. 7.15-7.19, the centre L_c of the width of discontinuity considered is $L/2$. Here, the effect of different L_c on pipe frequency was examined and the results obtained are compared with those of pipe without discontinuity (when $L_c = 0$) in Fig. 7.20. One can observe that the frequencies of pipe with thickness discontinuity at all L_c are lower than those of pipe without discontinuity. In addition, each L_c affected the four frequencies under consideration separately. The maximum reduction in first and third frequencies of pipe with discontinuity occurred when $L_c = L/2$ while that of second and fourth frequencies arose when $L_c = 3L/4$ and $L_c = L/3$ respectively.

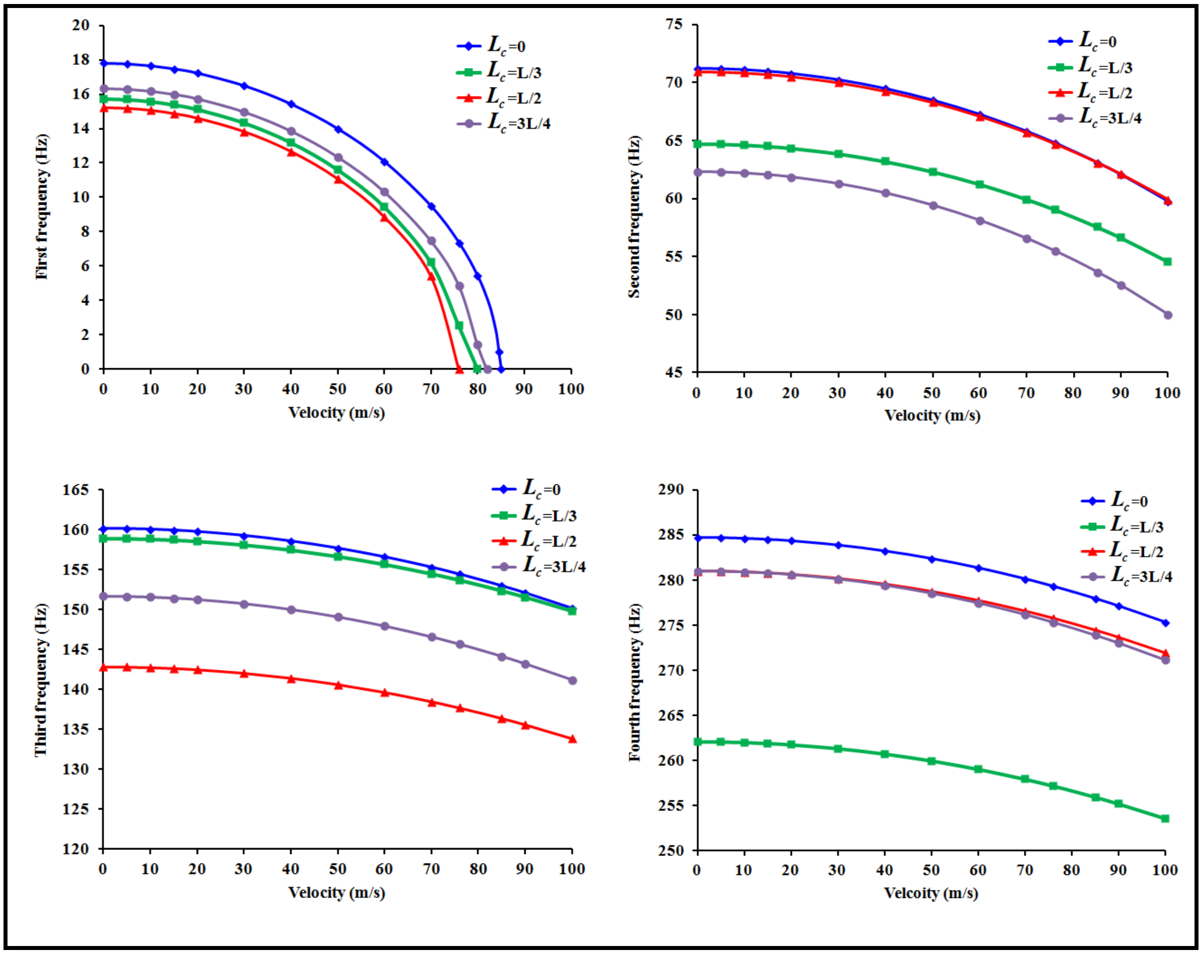

Figure 7.20: Frequency of pinned-pinned FRP pipe with different L_c conveying fluid when $L_d = 0.15$, $\theta_1 = 0^o$ and $\theta_2 = 360^o$.

Besides, in Figs. 7.12-7.20 the width of discontinuity L_d considered is 0.15m. The effect of different L_d on the pipe with thickness discontinuity conveying water was examined next. The centre of thickness discontinuity $L_c = L/2$ and L_d stretches symmetrically until it covers the whole pipe length. The results obtained at different L_d and velocities are presented in Fig. 7.21. This figure shows how the frequencies decrease as L_d increases under any particular velocity. In the same manner, it displays how the frequency reduces as velocity increases for any selected L_d. In addition, one can observe

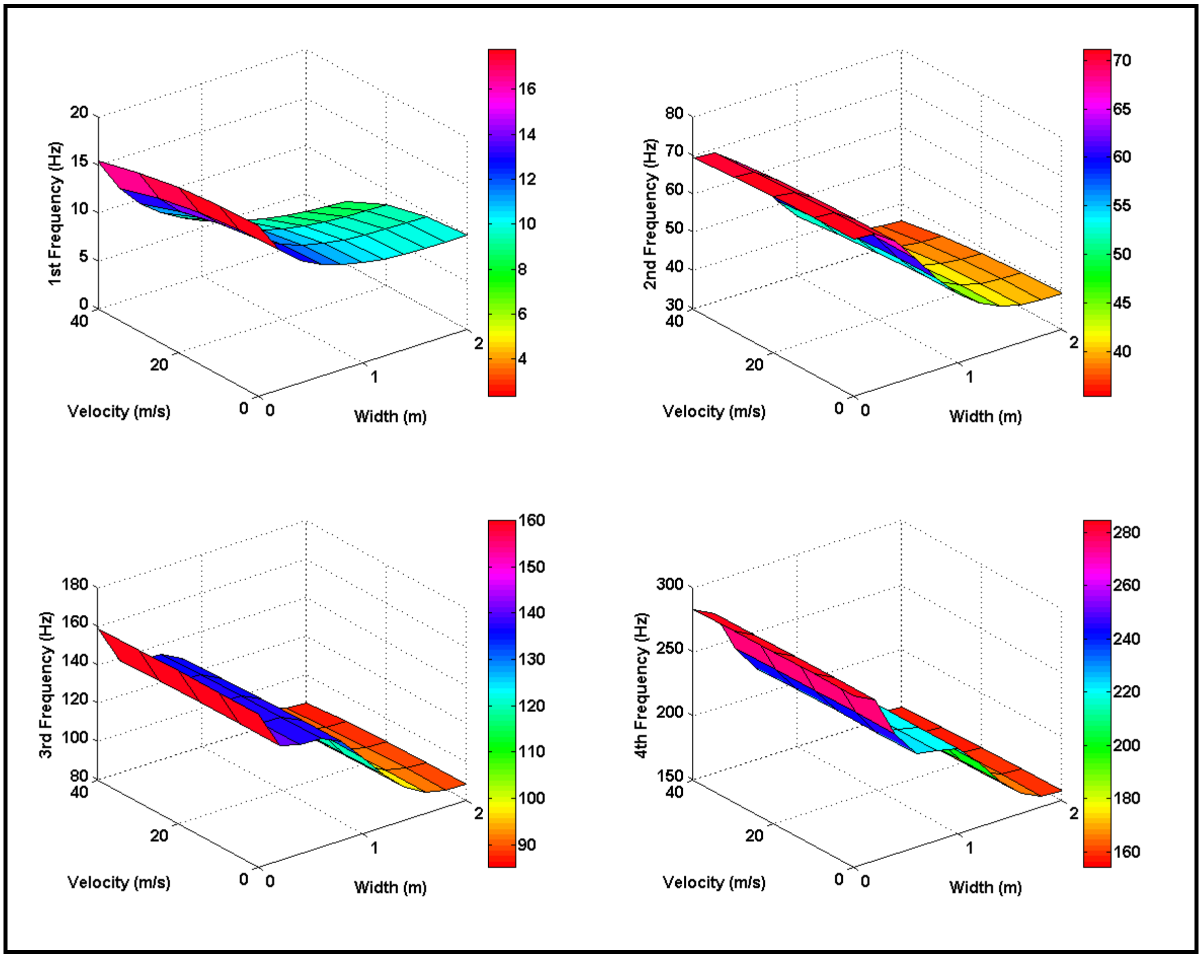

Figure 7.21: Frequency of pinned-pinned FRP pipe with discontinuity conveying fluid at different velocities and width L_d when $\theta_1 = 0^o$ and $\theta_2 = 360^o$.

that there was no noticeable value of L_d where frequency increases unlike when the pipe did not contain fluid that frequency will start to increase at a particular value of L_d as in Chapter 6. Another significant observation that one can observe in Fig. 7.21 is that each frequency plot mimics the shape of its corresponding mode shape. No matter the value of velocity considered in Fig. 7.21, frequency plot will continue to imitate the mode shape and emulate it more as long as values of L_d include 0 and the entire pipe length L.

Besides, the data of another composite pipe considered are given in Table 5.2. The results obtained for this pipe when it is conveying fluid with and without discontinuity are presented in Fig. 7.22. It can be discovered that thickness discontinuity reduced V_{cr}. Also, it can be noticed that the effect of discontinuity and fluid on the pipe frequency is more than the effect of fluid only in all frequencies considered except in the second frequency where reverse is the case at high velocities. In addition, several L_d were also investigated on this pipe and the results obtained are as shown in Fig. 7.23. It can be realized that Fig. 7.23 follows the same trend as Fig. 7.21.

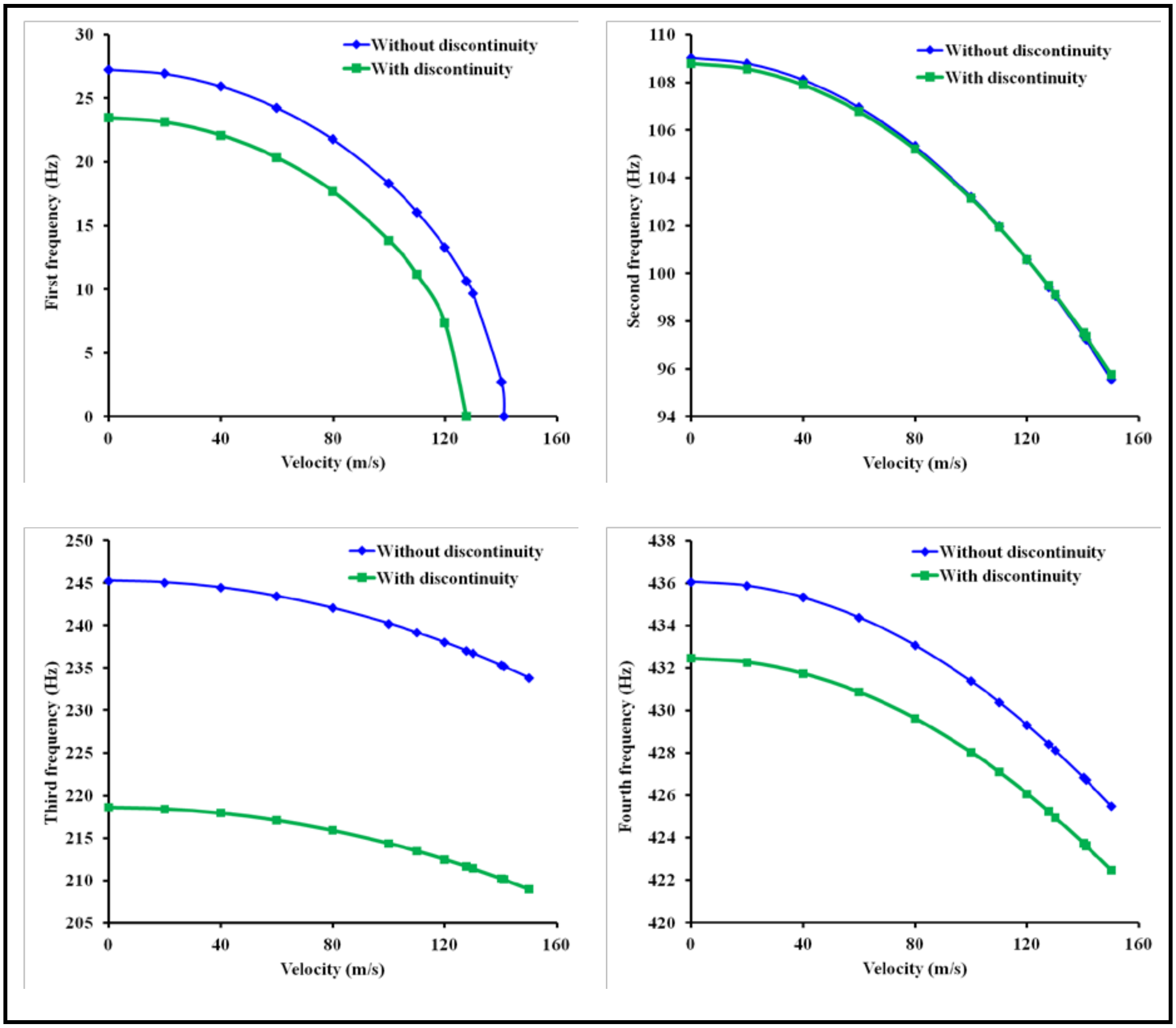

Figure 7.22: Frequency of pinned-pinned Boron-epoxy pipe with discontinuity conveying fluid when $t_d = 3h/4$, $\theta_1 = 0^o$ and $\theta_2 = 360^o$.

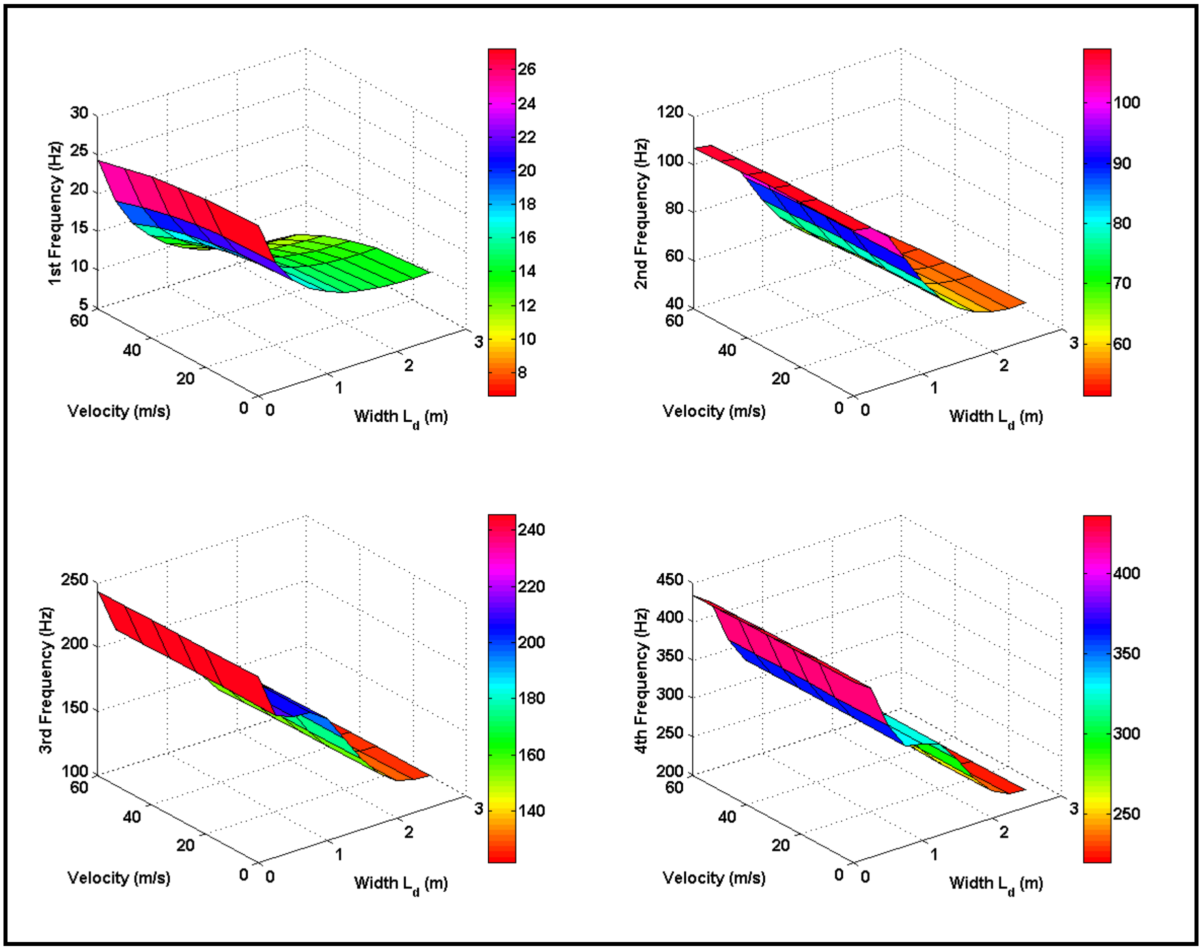

Figure 7.23: Frequency of pinned-pinned Boron-epoxy pipe with discontinuity conveying fluid at different velocities and L_d when $t_d = 3h/4$, $\theta_1 = 0^o$ and $\theta_2 = 360^o$.

Furthermore, the combination of the effect of fluid and thickness discontinuity on mode shape of pipe was also examined using the pipe defined in Table 5.9. Here, fluid has introduced damping into the equation which eventually leads to complex eigenvalues and eigenvectors. Thus, due to the complexity of the eigenvectors, mode shapes cannot be plotted directly and this makes it seems impossible. Nonetheless, the mode shapes can be obtained from complex eigenvectors through three ways: real part, imaginary part and its absolute. These three types of mode shapes were obtained for the first four frequencies when velocities of the fluid were 60 m/s and 84.5 m/s (V_{cr}). The mode shapes obtained are as presented in Figs. 7.24 and 7.25 together with mode shape obtained for healthy pipe without fluid flow. It can be noticed that (a) depicted the expected mode shapes for simply supported pipe while (b), (c) and (d) (that is, real, imaginary and absolute of complex eigenvectors) show the mode shapes in their own ways based on the effect of fluid on the pipe. Although, if one chose to be consistent, any of these three forms of presenting complex mode shapes can be used for further analysis.

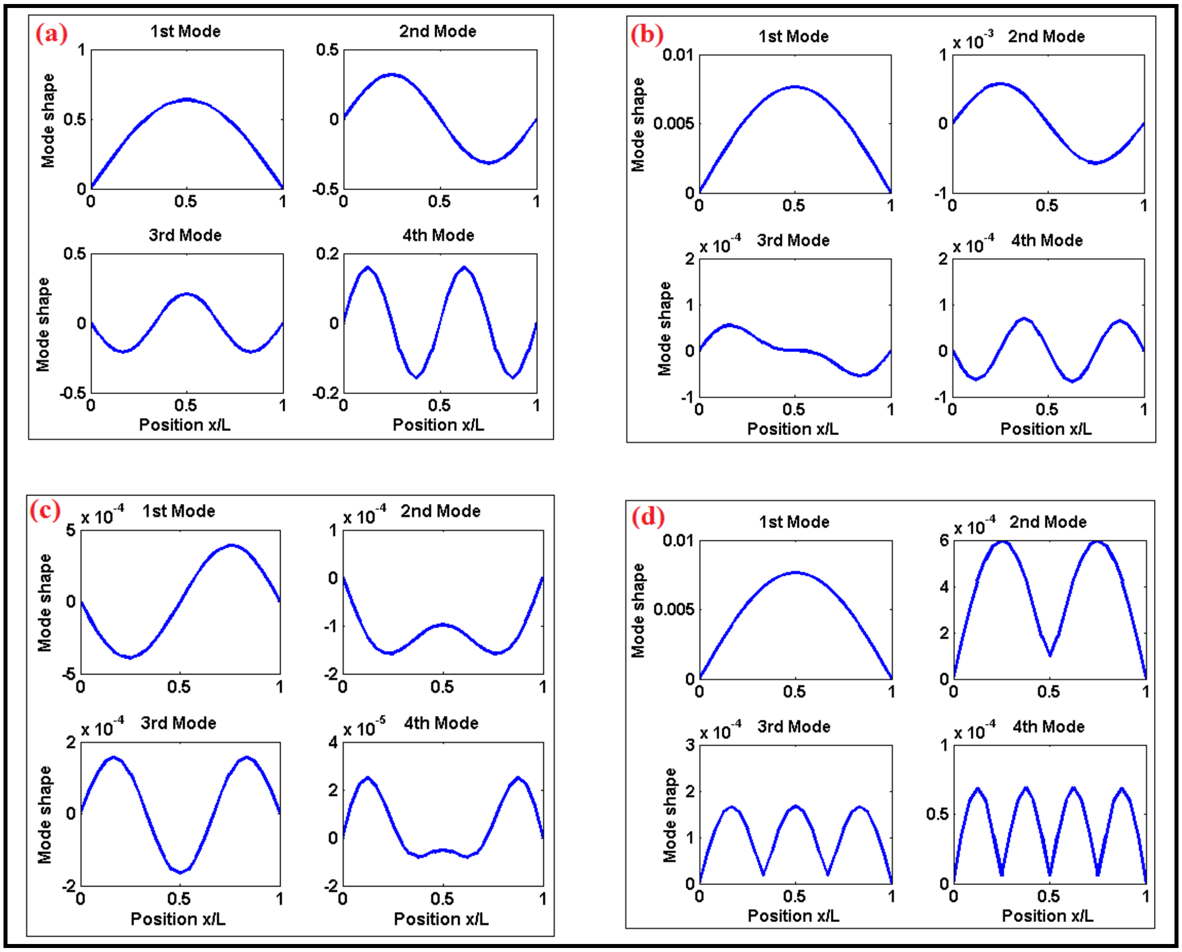

Figure 7.24: Mode shape of health pipe without and with fluid flow at V=60m/s.

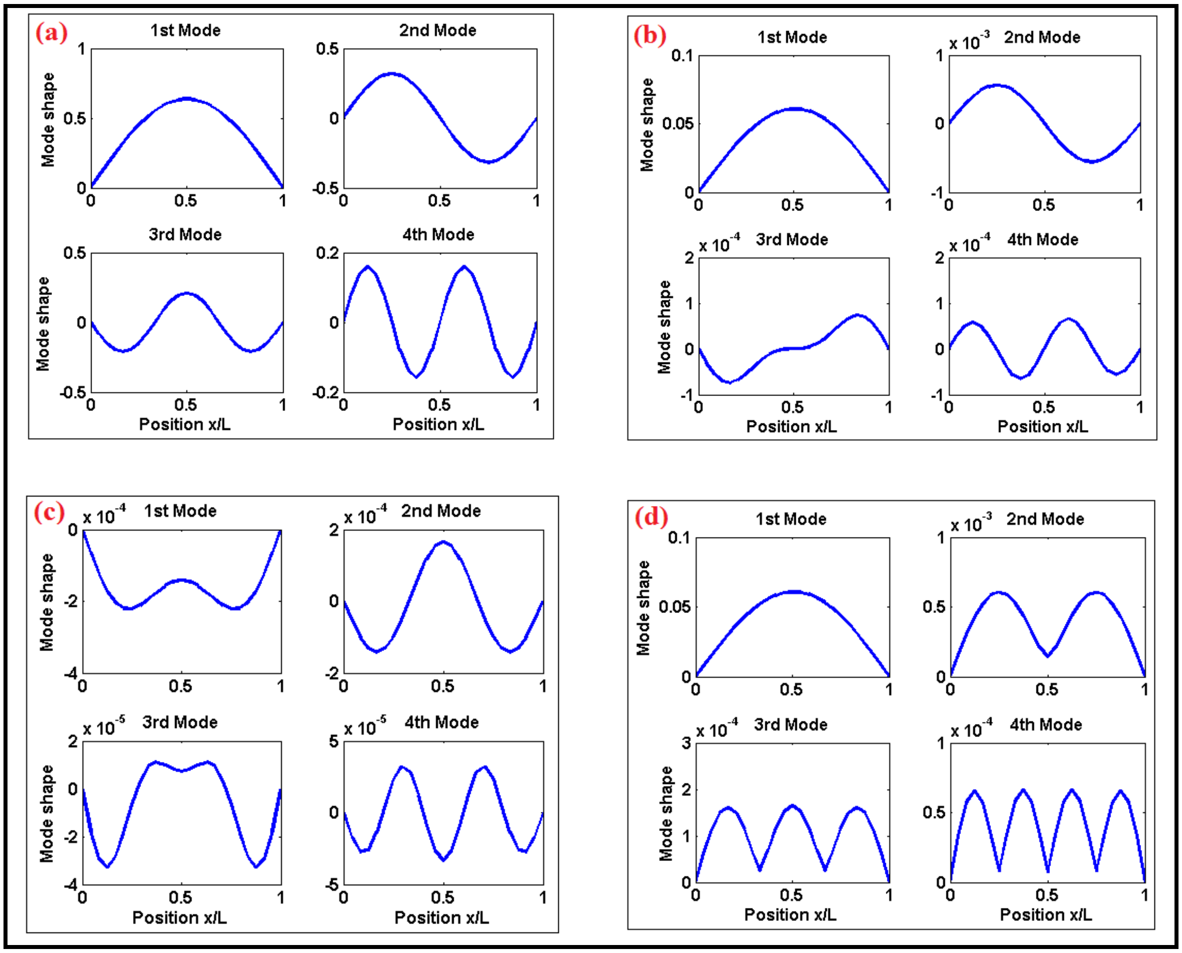

Figure 7.25: Mode shape of health pipe without and with fluid flow at V=84.5m/s.

However, among these methods, (b) is closer to (a) followed by (d). Hence, (b) which is the real part of complex eigenvectors was considered to present the modes shape of FRP with thickness discontinuity with fluid velocity of 60m/s. The geometry of the discontinuity considered was defined by $\theta_1 = 0^o$, $\theta_2 = 90^o$, $t_d = h/2$, $L_d = 0.15$ and $L_c = L/4,\ L/3,\ L/2,\ 3L/4$. The modes shapes obtained for these four locations of the thickness discontinuity are shown in Figs. 7.26-7.29. While (a) is the required mode shape of healthy pipe, the effect of fluid can be observed in (b) and (d). Equally, the influence of thickness discontinuity can be seen in (c) and (d) too. These figures not only show the signature of the effect of thickness discontinuity on the FRP pipe but also display probably area in which discontinuity is located (see (c) and (d) in Figs. 7.26-7.29). It should be noted that in Figs. 7.26-7.29, the second to fourth mode shapes were scaled up for clarity because the fluid effect has reduced the mode shape drastically.

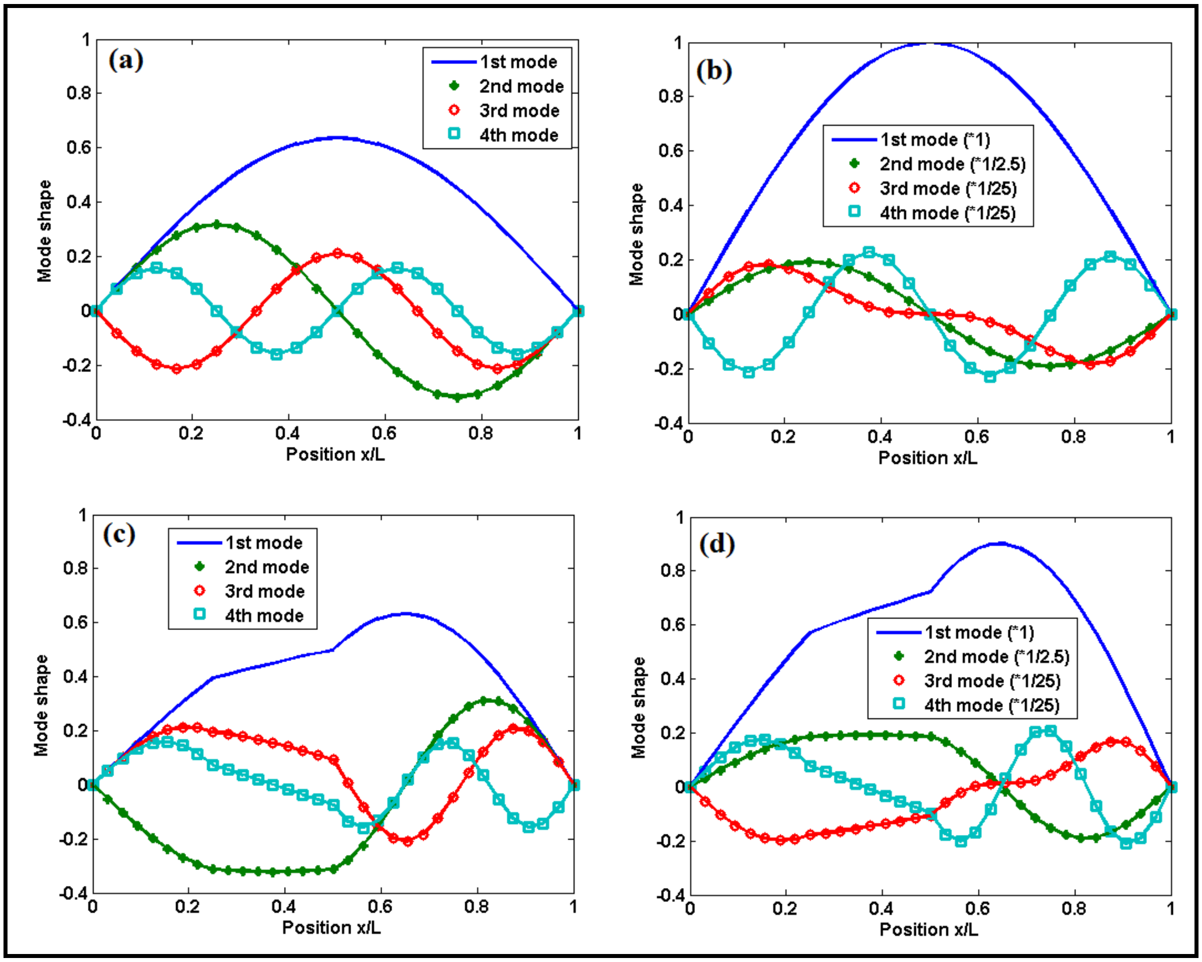

Figure 7.26: Mode shapes of FRP pipe with surface defect at $L_c = L/4$; (a) Empty healthy pipe, (b) Healthy pipe with flow, (c) Empty pipe with defect, (d) Pipe with defect and flow.

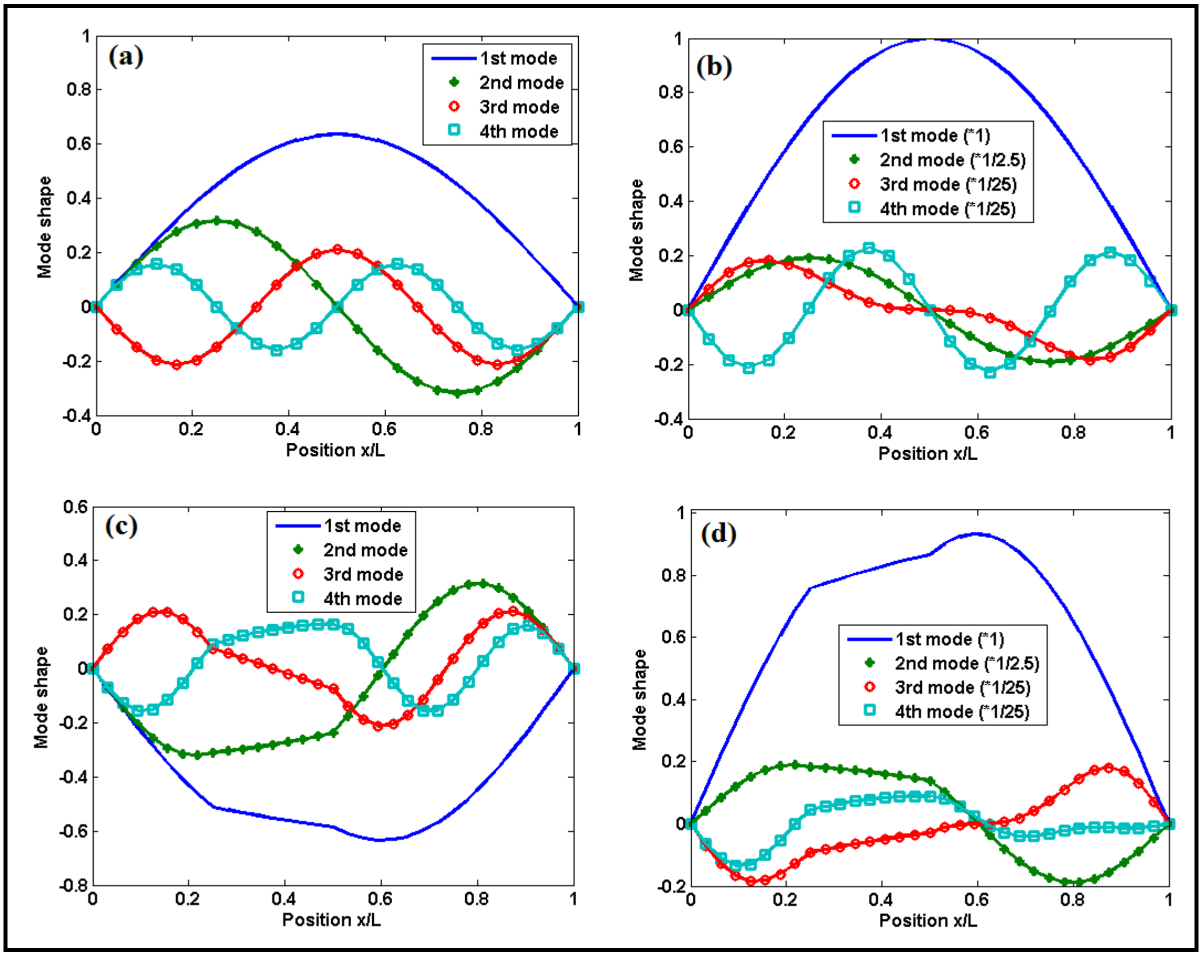

Figure 7.27: Mode shapes of FRP pipe with surface defect at $L_c = L/3$; (a) Empty healthy pipe, (b) Healthy pipe with flow, (c) Empty pipe with defect, (d) Pipe with defect and flow.

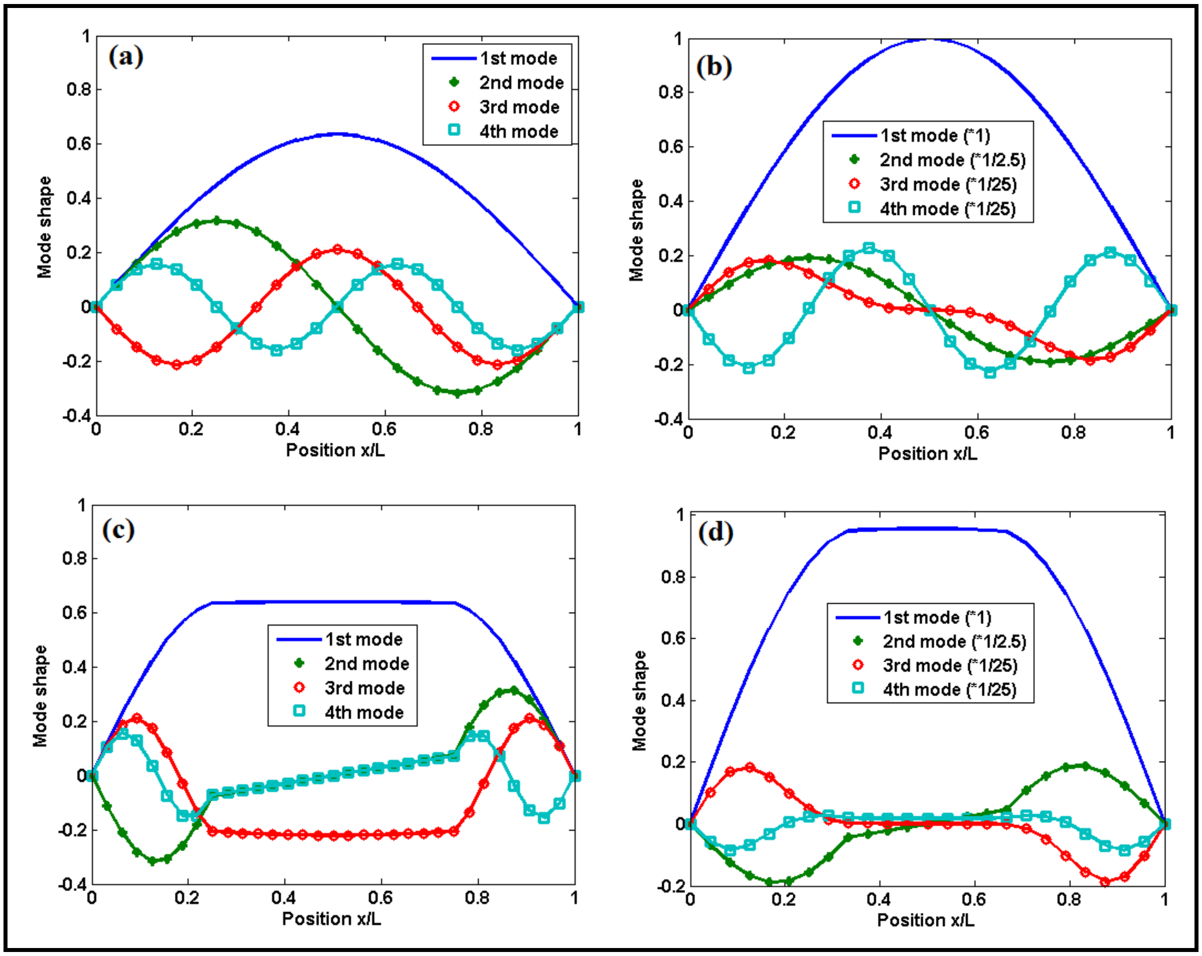

Figure 7.28: Mode shapes of FRP pipe with surface defect at $L_c = L/2$; (a) Empty healthy pipe, (b) Healthy pipe with flow, (c) Empty pipe with defect, (d) Pipe with defect and flow.

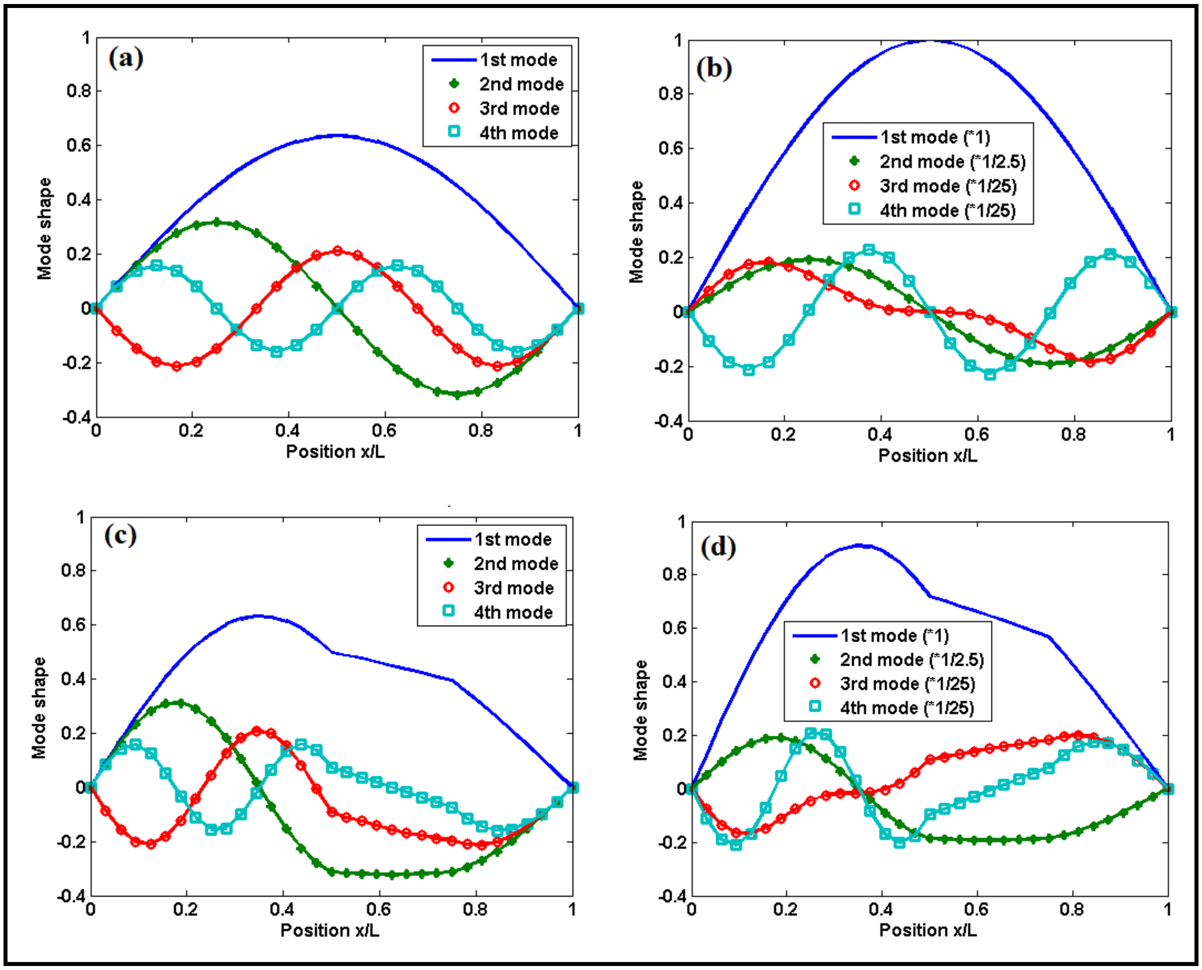

Figure 7.29: Mode shapes of FRP pipe with surface defect at $L_c = 3L/4$; (a) Empty healthy pipe, (b) Healthy pipe with flow, (c) Empty pipe with defect, (d) Pipe with defect and flow.

Finally, in all the aforementioned examples, $\overline{T}$ was neglected. Here, the effect of this force is examined using the pipe described in Table 5.9 and the data of discontinuity geometry employed include $L_c = L/2$, $L_d = 0.15$, $t_d = 3h/4$, $\theta_1 = 0^0$ and $\theta_2 = 360^0$. The results obtained are presented in Figs. 7.30 and 7.31 respectively. One can see in Fig. 7.30 that with or without discontinuity, the pipe frequency increases with $\overline{T}$ and as a result V_{cr} also increases as it can be seen in Fig. 7.31. Similarly, Fig. 7.31 shows that the frequencies of pipe with discontinuity conveying fluid only will decrease drastically more than when there is $\overline{T}$ in addition to discontinuity. In the same way, it can be discovered further that the higher the value of $\overline{T}$ the less the effect of fluid and discontinuity on the pipe and the higher the value of V_{cr}.

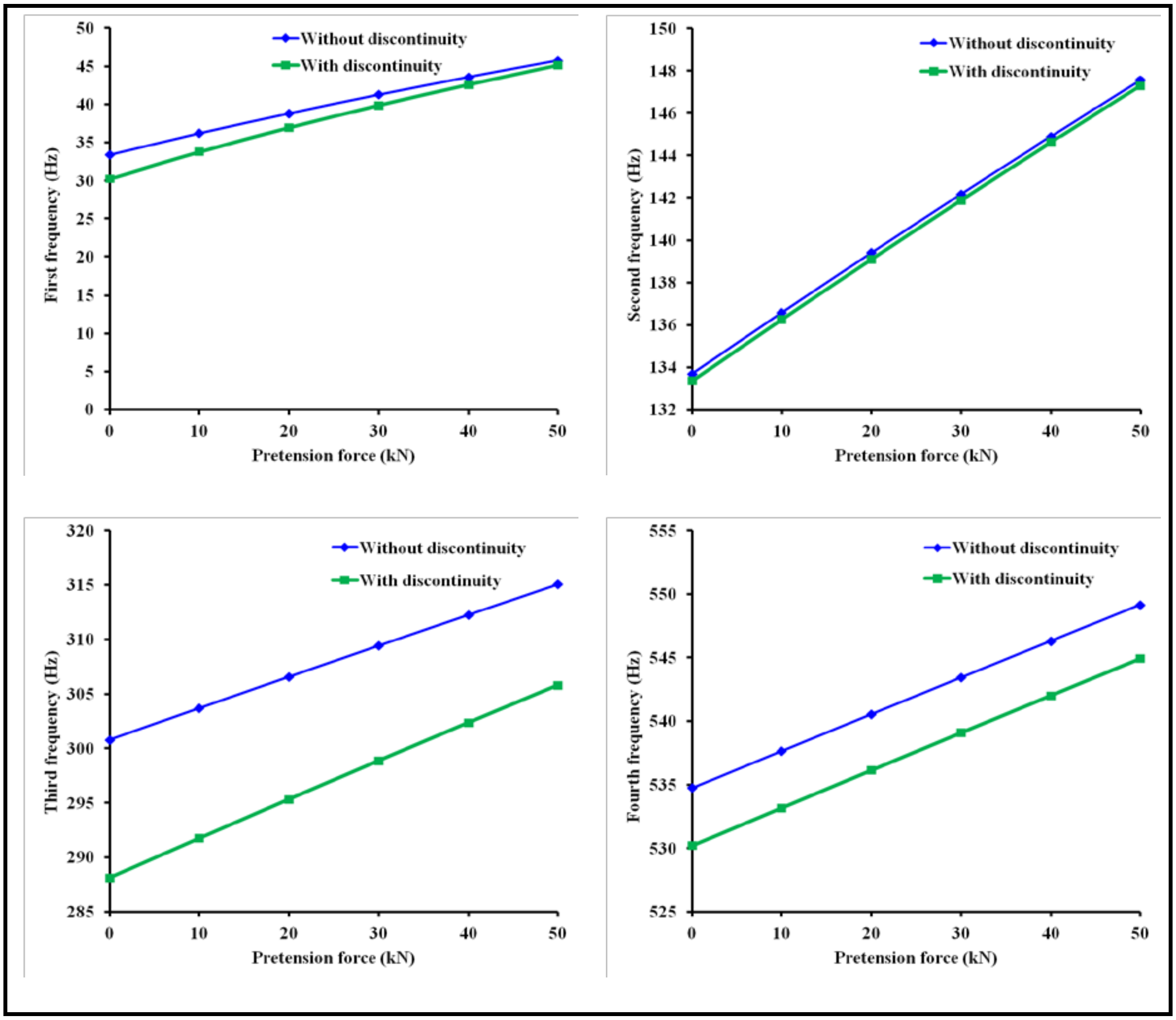

Figure 7.30: Frequency of pinned-pinned pipe with and without discontinuity under different $\overline{T}$.

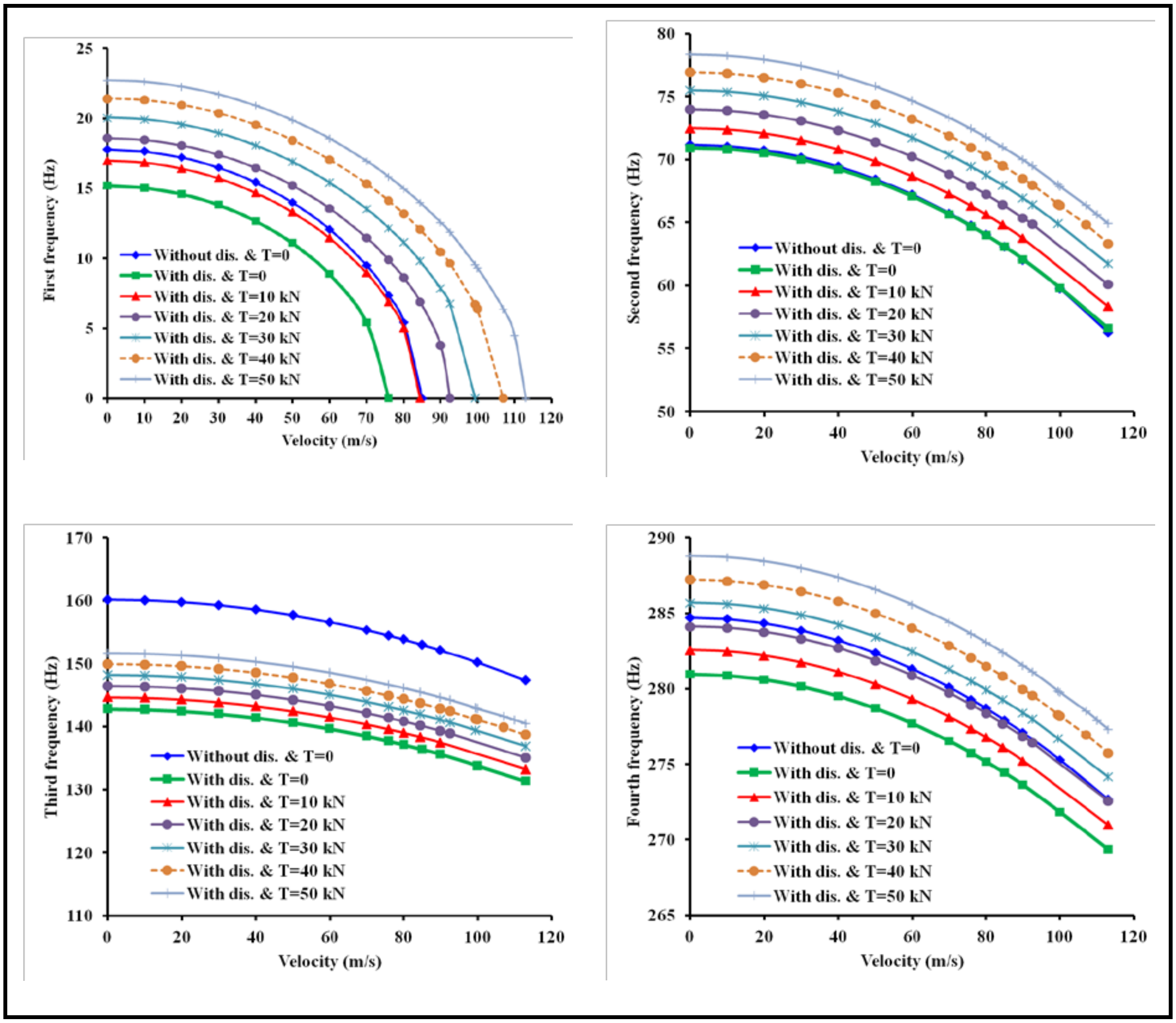

Figure 7.31: Frequency of pinned-pinned pipe with and without discontinuity under different velocity and $\bar{T}$ (dis. = discontinuity).

In this chapter the wavelet based finite element method for composite pipe with thickness discontinuity convening fluid is presented. Several examples were presented to show the effectiveness of the proposed model. It was shown that wavelet based FEM uses very few number of elements without compromising the accuracy. The appreciable decrease in frequencies as the internal surface defect increases in radial and longitudinal directions indicates that the pipe experiences a softening effect. In addition, it can be observed that the defect parameters t_d, L_c and L_d have substantial influence on critical speed V_{cr} or the stability of the pipe as fluid flow rate increases. It was also discovered that V_{cr} of a straight pipe does not only depend on mass ratio, boundary conditions, stiffness of the pipe foundation and pipe viscous properties as mentioned in literature but also depends on discontinuity and pretension force in the pipe. In addition, it has been shown that internal wall defect can serve as either stabilizing or destabilizing factor depends on its geometry and fluid velocity. Besides it was demonstrated that for different values of L_d (with $L_c = L/2$) and velocities, the plot of each frequency will impersonate the shape of its mode shape and this will become clearer when 0 and L are among the values of L_d considered. Thus, this study has set the phase for further analysis of composite pipe with discontinuity conveying fluid.

Nonetheless, in the next chapter the thickness discontinuity or wall-thinning Effect on the impulse response of the FRP Pipe was investigated.

CHAPTER 8

TRANSIENT RESPONSE OF THE FRP PIPE

8.1 Transient Response of FRP Pipe with Internal Wall-thinning

Transient response is initiated by initial conditions on the system states; namely the initial conditions on the displacement and/or velocity vectors. The initial condition on velocities is, in general, a representation of the impulsive excitation. Thus, in this chapter, the effect of internal defect on impulse response of the laminated composite pipe with and without flowing fluid was investigated. The generalized dynamic equation of motion given in Chapter 7 for the composite pipe conveying fluid with and without internal defect is represented in a general form as

$$[M]_e\{\ddot{y}\}_e + [B]_e\{\dot{y}\}_e + [K]_e\{y\}_e = \{F\}_e \tag{8.1}$$

where $\{\ddot{y}\}_e$, $\{\dot{y}\}_e$, $\{y\}_e$ and $\{F\}_e$ are vectors of acceleration, velocity, displacement and applied force respectively. In Eq. (8.1), $[B]_e$ and $\{F\}_e$ will become $[0]_e$ and $\{0\}_e$ when the pipe does not conveying fluid and when no force is applied. In order to obtain, the response of the FRP pipes, Eq. (8.1) can be solved using regular processes for the solution of differential equations with invariable coefficients. Conversely, if the sizes of matrices are large, this approach is no longer advisable because it will become extremely costly. As a result, the approximation methods have been developed as other options. These methods include mode superposition and direct integration [130]. These two methods are almost the same and the choice on which one to be applied depend on its numerical effectiveness.

In this study, two methods: constant-average acceleration (trapezoidal rule) method (CAAM) and ODE45 that belong to direct integration method were considered. They gave the same results but ODE45 was finally adopted because it is already available in MATLAB. Thus, in order to be able to use ODE45 in MATLAB to obtain displacement and velocity responses at desired node, Eq. (8.1) was transformed to the first order system as follows:

$$y = x_1, \quad \dot{y} = \dot{x}_1 = x_2, \quad \ddot{y} = \dot{x}_2 \tag{8.2}$$

upon substituting Eq. (8.2) in (8.1) and rearranged, it produced

$$\{\dot{x}_2\}_e = [M]_e^{-1}\left[-[B]_e\{x_2\}_e - [K]_e\{x_1\}_e + \{F\}_e\right] \tag{8.3}$$

From Eqs. (8.2) and (8.3), one can obtain

$$\begin{bmatrix} \{\dot{x}_1\}_e \\ \{\dot{x}_2\}_e \end{bmatrix} = \begin{bmatrix} [0\ \ ] & [I] \\ -[M]_e^{-1}[K]_e & -[M]_e^{-1}[B]_e \end{bmatrix} \begin{bmatrix} \{x_1\}_e \\ \{x_2\}_e \end{bmatrix} + \begin{bmatrix} \{0\} \\ [M]_e^{-1}\{F\}_e \end{bmatrix}$$

$$\{\dot{X}\} = [H]\{X\} + \{f\} \tag{8.4}$$

where

$$\{\dot{X}\} = \begin{bmatrix} \{\dot{x}_1\}_e \\ \{\dot{x}_2\}_e \end{bmatrix}, \ [H] = \begin{bmatrix} [0] & [I] \\ -[M]_e^{-1}[K]_e & -[M]_e^{-1}[B]_e \end{bmatrix}$$

$$\{X\} = \begin{bmatrix} \{x_1\}_e \\ \{x_2\}_e \end{bmatrix}, \{f\} = \begin{bmatrix} \{0\} \\ [M]_e^{-1}\{F\}_e \end{bmatrix}$$

Hence, in order to be able to solve Eq. (8.4), connection was created between the existing program for this work and ODE45 function available in MATLAB. Through this connection, all the required parameters were supplied to ODE45 and the responses (solutions: displacement and velocity) were received in return for further processes.

8.2 Transient Analysis Initial Conditions

Equation (8.4) requires initial conditions to be able to obtain the required results. In this work, initial conditions on displacement and velocity were utilized. On displacement initial condition, static analysis of FRP pipe was performed. The static deflections of all nodes in the pipe under consideration were then obtained and used as initial displacements. Regarding initial velocity condition, this was done in two ways, namely, by applying initial velocity at a desired node (e.g node located at L/2) and by using pulse excitation (see Fig 8.1) at the same location.

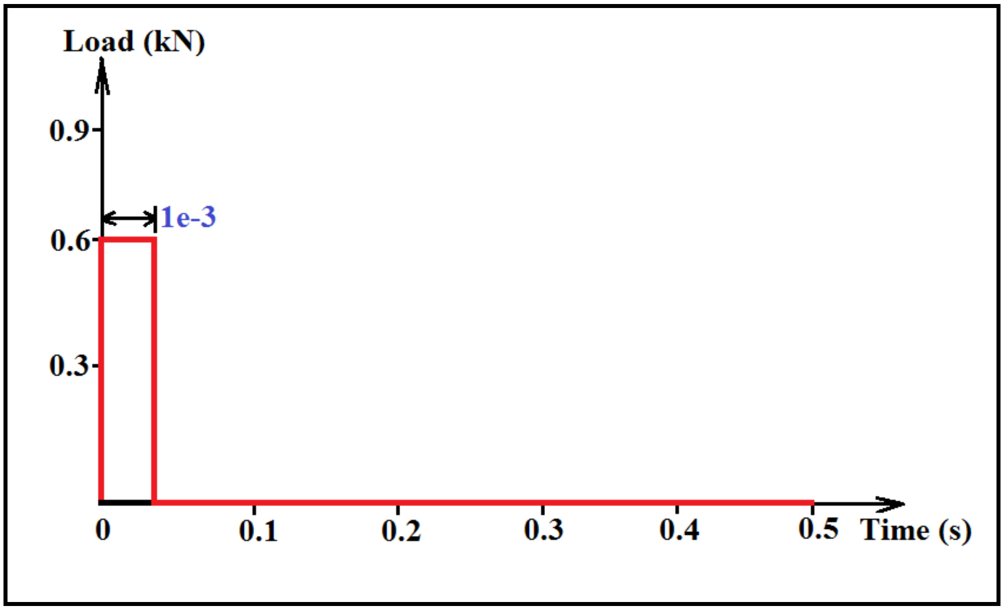

Figure 8.1: A pulse load.

8.3 Results and Discussion

In this section, the FRP pipe described in Table 5.9 was considered with pinned-pinned support and annulus thickness discontinuity geometry ($\theta_1 = 0^0, \theta_2 = 360^0$) was employed. The effect of thickness discontinuity on the impulse response of this FRP pipe with and without fluid flow was investigated. The velocity of fluid flowing inside the pipe considered is 10 m/s and $T_t = 0.5$ seconds. The time step Δt was obtained using $\Delta t = 1/20f$ in which f is the third natural frequency of the healthy FRP pipe. Besides, all the displacement responses were obtained through the node located at $0.5L$.

8.3.1 Impulse Response of Healthy FRP Pipe with and without Fluid Flow

Here, displacement response of pipe without thickness discontinuity was investigated using different initial conditions. The responses obtained are shown in Figs. 8.2 and 8.3 for empty pipe and pipe with fluid flow. It can be noted from the figure that the displacement responses obtained with the two methods of initial velocity condition shown the traces of higher modes. In the same manner, the response obtained with initial displacement condition revealed the traces of lower mode. Hence, in order to ensure that the pipe response contains all modes, ideal impulse is required to excite the pipe. However, this cannot be produced and in order to obtain the responses that is appreciable close to what ideal impulse will produce, initial velocity (pulse excitation) applied at node located at L/2 was utilized in the rest of this chapter.

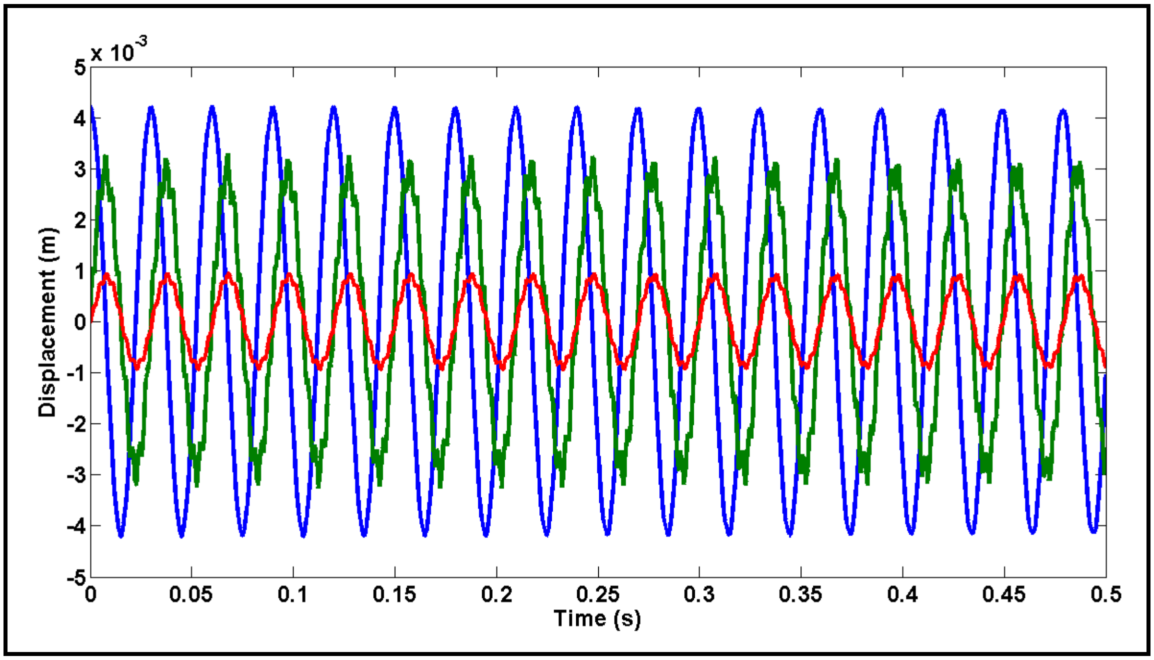

Figure 8.2: Displacement responses of empty healthy FRP pipe.
▬ : Displacement initial condition, ▬ : Velocity initial condition
▬ : Pulse excitation

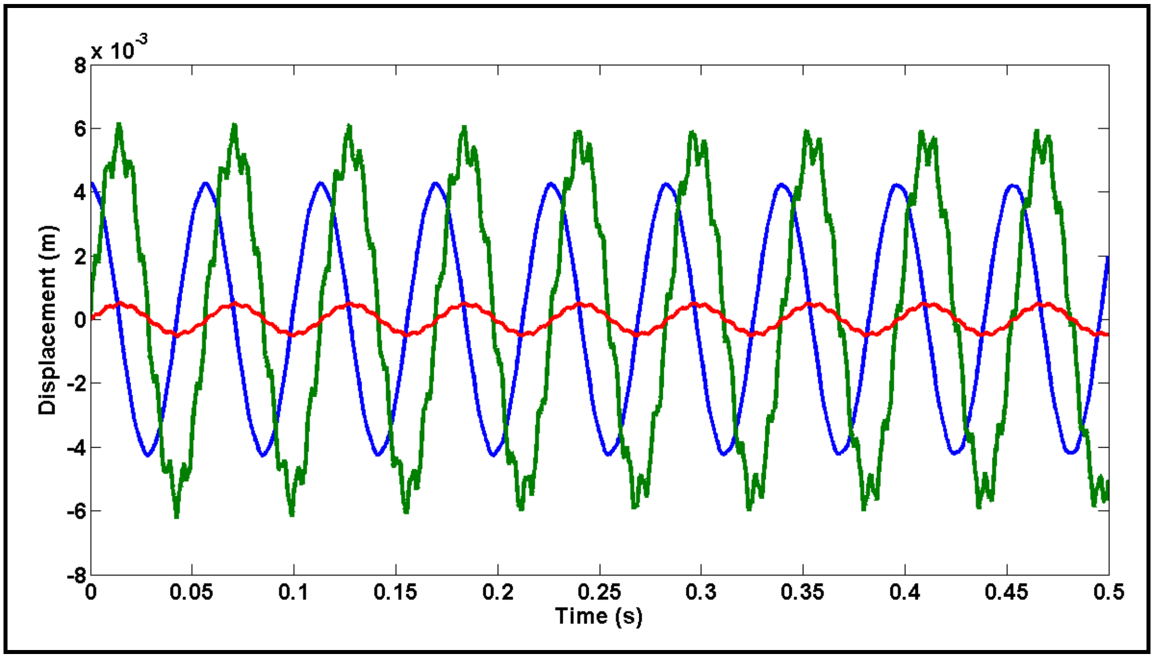

Figure 8.3: Displacement response of healthy FRP pipe with fluid flow.
▬ : Displacement initial condition, ▬ : Velocity initial condition
▬ : Pulse excitation

8.3.2 Empty FRP Pipe with Thickness Discontinuity

Empty pipe with internal defect was examined in this subsection where $L_c = L_d = t_d = 0$ is referring to the healthy pipe. The different L_c considered include 0, $L/4$, $L/2$ and $3L/4$ while t_d and L_d were $3h/4$ and 0.15 respectively. The displacement responses obtained for these L_c are as shown in Fig. 8.4. It can be seen that for pipe with discontinuity there was not only decrease in number of peaks but also appreciable increase in displacement responses of all L_c considered when compared with the response of healthy pipe ($L_c = 0$). The shrinkage in number of peaks, and displacement response depending on the value of L_c. This implies that discontinuity has more effect on stiffness than mass and it indicates that the smaller the stiffness, the larger

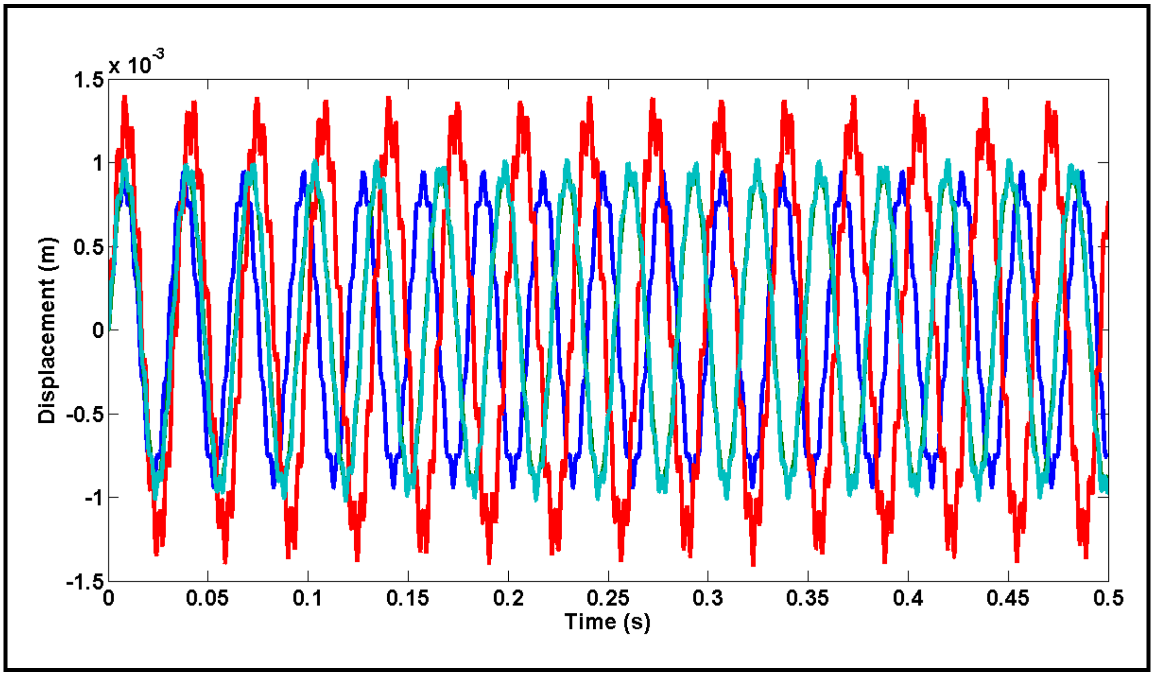

Figure 8.4: Displacement response of empty pipe with thickness discontinuity of $t_d = 3h/4$, $L_d = 0.15$ and different L_c:
━ 0, ━ $L/4$, ━ $L/2$ and ━ $3L/4$

the response and vice versa. This can be explained from the mechanic point of view in which with initial velocity ($\dot{y}^0$), the maximum displacement response depends on $\dot{y}^0 / \omega_n$. In addition, this is also supported by the Hooke's law in which $y = F / k$ and with $F = ma$, the smaller the stiffness k the larger the y and reverse when m is significantly altered.

Moreover, the influence of different t_d of thickness discontinuity with $L_c = L/2$ and $L_d = 0.15$ on the impulse response of FRP pipe was also investigated. The results obtained for displacement responses for pipe with $t_d = 0,\ h/4,\ h/2$, and $3h/4$ are shown in Fig. 8.5. It was found that all the responses increased for all value of t_d when compared

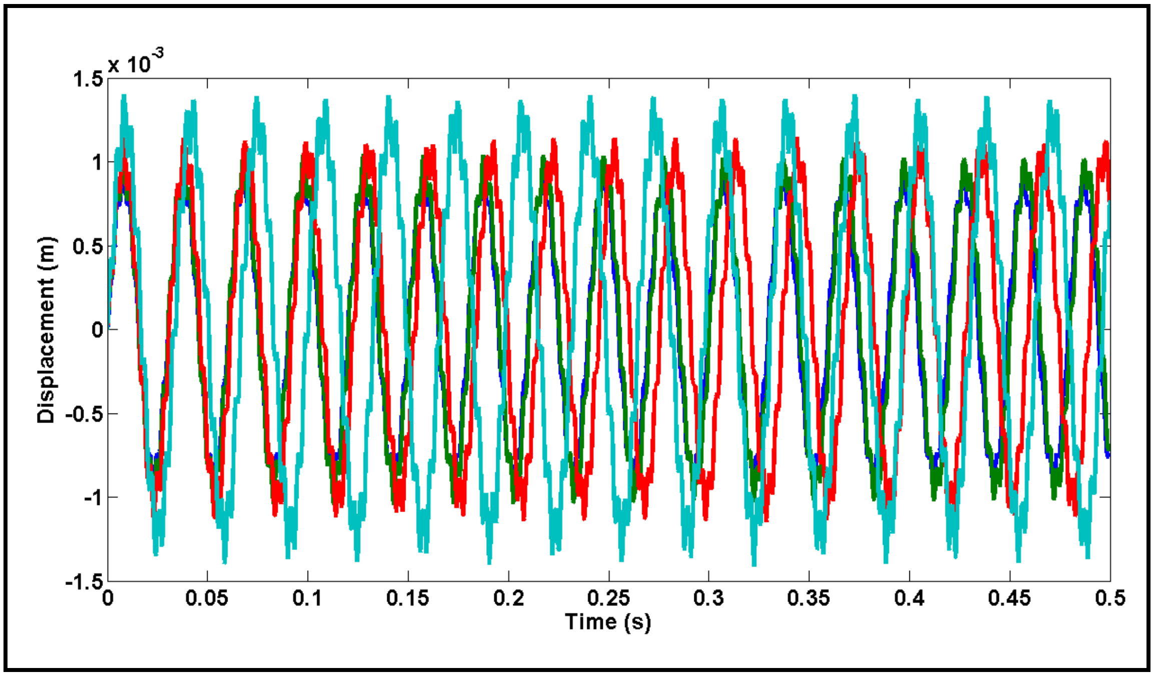

Figure 8.5: Displacement response of empty pipe with thickness discontinuity of $L_c = L/2$, $L_d = 0.15$ and different t_d:
▬ 0, ▬ $h/4$, ▬ $h/2$ and ▬ $3h/4$

with healthy pipe. It can also be found that the higher the t_d, the more the increment in displacement response and decrement in number of peaks. This shows that the effect of increasing in t_d of thickness discontinuity in radial direction affected stiffness more when compare to mass of the pipe. This can also be explained from mechanic point of view discussed earlier that as stiffness increases the response also decreases.

Furthermore, the influence of different L_d of thickness discontinuity with $L_c = L/2$ on the impulse response of FRP pipe was also examined. The results obtained for displacement responses for pipe with $L_d = 0, 0.15, 1.0$ and 2.0 (or L) are shown in Fig. 8.6. It was noticed that all the responses increased for all value of L_d when compared

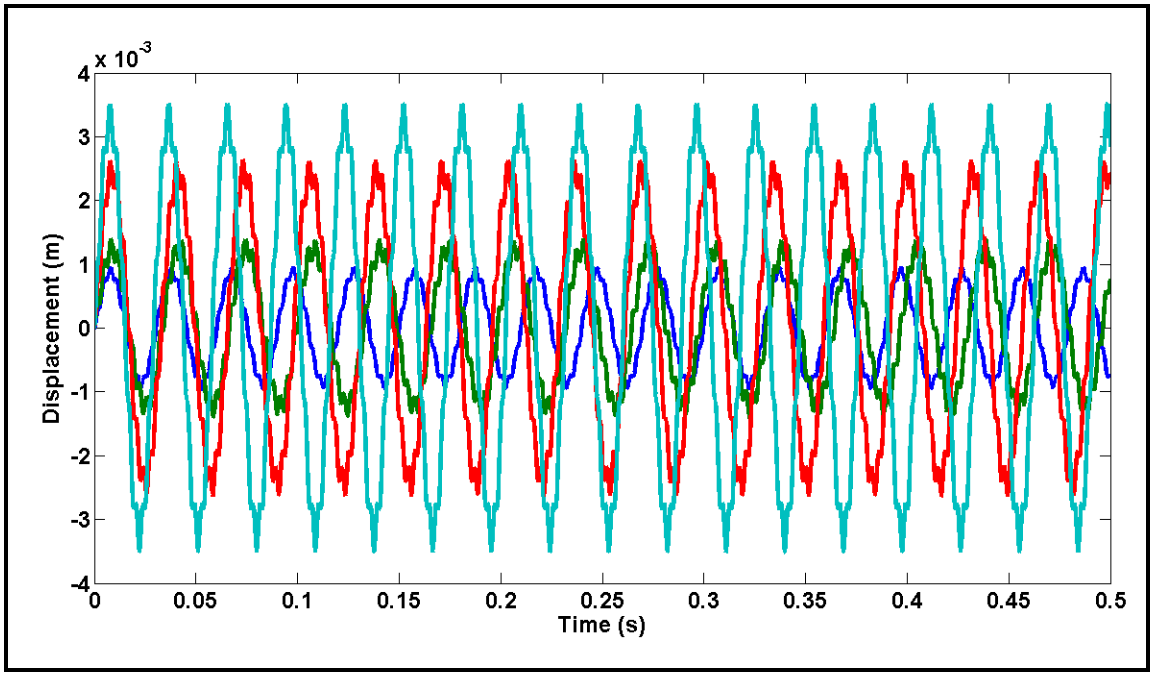

Figure 8.6: Displacement response of empty pipe with thickness discontinuity of $t_d = 3h/4$, $L_c = L/2$ and different L_d:
— 0, — 0.15, — 1.0 and — 2.0

with healthy pipe ($L_d = 0$). This demonstrates that the effect of increasing in L_d of thickness discontinuity in longitudinal direction can also affect stiffness more than mass. However, the rate at which response increased was higher when L_d approaches L or $L_d = L$. This is due to the fact that by the time $L_d = L$ both stiffness and mass have been affected and new pipe has been produced. This new pipe can be treated as pipe without discontinuity and its response is expected to be appreciable more than response of original pipe and responses obtained for other value of L_d. This can also be explained from mechanic point of view discussed earlier that as mass reduces the response also reduces and vice versa when stiffness reduces.

8.3.3 FRP Pipe with Thickness Discontinuity and Flowing Fluid

In this subsection, all the pipes considered in subsection 8.3.2 were considered here with fluid flow. First and foremost, one would expect the response to reduce or closer to zero as t goes to infinity because of damping that introduced into the equation by the fluid and damping should dissipate the energy. Conversely, the damping that fluid added to the equation of motion is not the type that can dissipate the energy but the one that will destabilize the system. This is due to the fact that it was obtained through the velocity of the fluid not from the pipe parameters. Thus, all the responses obtained in this subsection, fluid damping does not reduce them to zero as t goes to infinity. The displacement responses obtained for different values of L_c, t_d and L_d are presented in Fig. 8.7-8.89. It can be recorded that apart from the reduction in number of peaks, all displacement responses also increased for all value of L_c, t_d and L_d considered. This

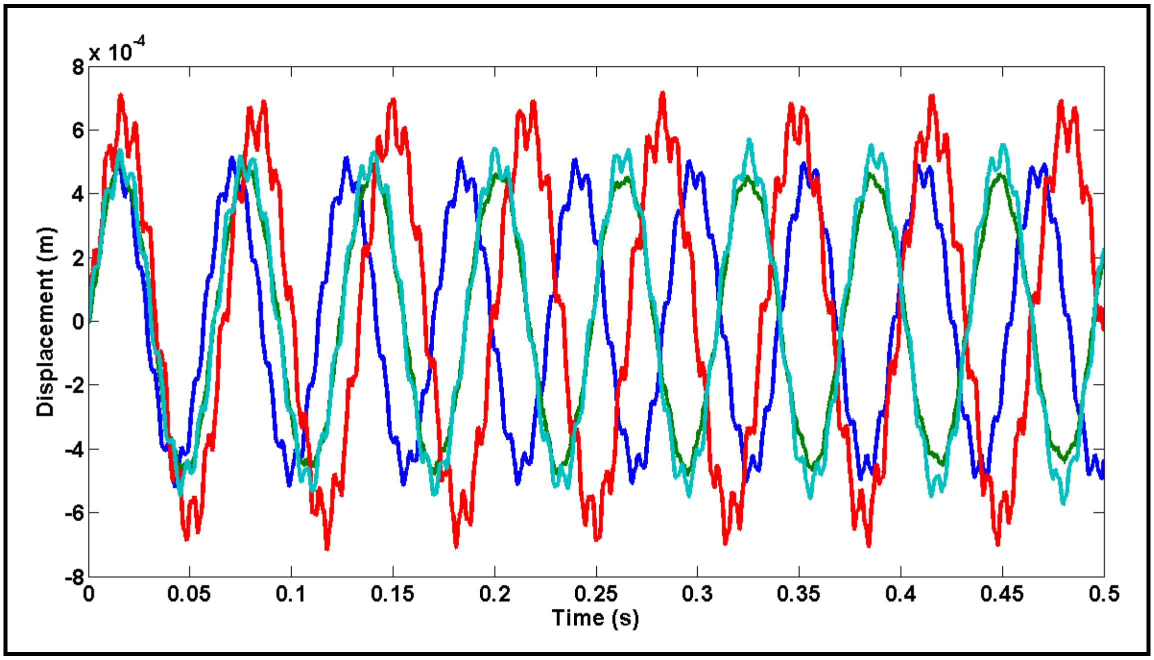

Figure 8.7: Displacement response of FRP pipe with thickness discontinuity of $t_d = 3h/4$ and $L_d = 0.15$ with V=10m/s at different L_c:
▬ 0, ▬ $L/4$, ▬ $L/2$ and ▬ $3L/4$

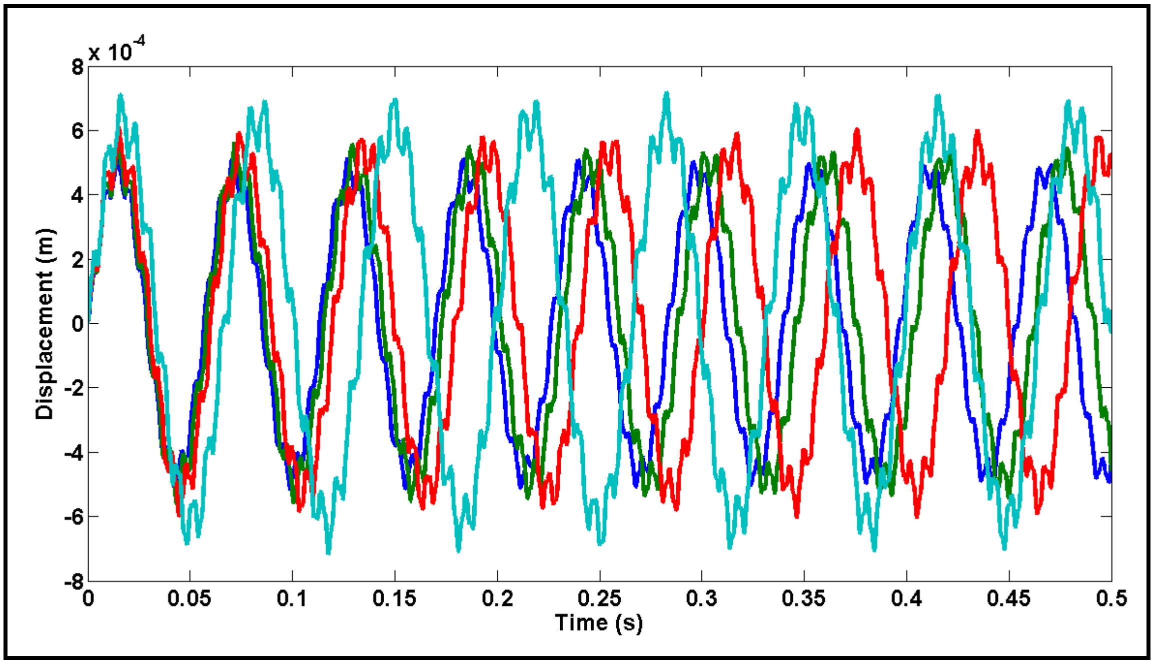

Figure 8.8: Displacement response of FRP pipe with thickness discontinuity of $L_c = L/2$ and $L_d = 0.15$ with V=10 m/s at different t_d:
▬ 0, ▬ $h/4$, ▬ $h/2$ and ▬ $3h/4$

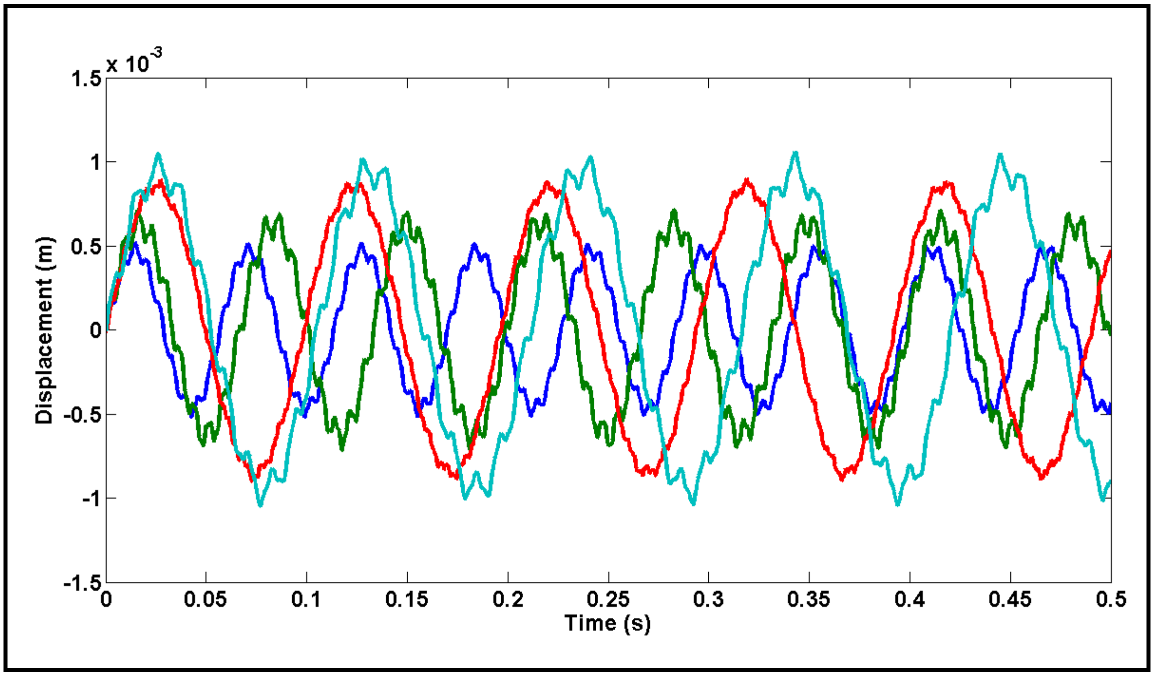

Figure 8.9: Displacement response of FRP pipe with thickness discontinuity of $t_d = 3h/4$ and $L_c = L/2$ with V=10 m/s at different L_d :
▬ 0, ▬ 0.15, ▬ 1.0 and ▬ 2.0

responses obtained are due to the combination of the effects of fluid and thickness discontinuity on pipe parameters. The explanation can also be corroborated from the mechanic point of view discussed in previous section.

In this chapter, three different initial conditions were considered for the transient analysis of FRP with and without fluid flow. It was found that the initial velocity condition in which pulse excitation or initial velocity is applied to a node at L/2 have capacity to excite higher modes. In order to ensure that the pipe response contains all modes, ideal impulse is required to excite the pipe. However, this cannot be produced and in order to obtain the response that is appreciable close to what ideal impulse will produce, the initial velocity condition using pulse excitation was used for the investigation. Besides, the investigation was extended to cover the FRP pipes with thickness discontinuity with and without fluid flow. It was found that all the displacement responses obtained increased when compared to healthy pipe. This can be attributed to the effects of thickness discontinuity with or without fluid or pipe stiffness or mass. It was also noted that when the effects are more on stiffness the response will increase and reverse will be the case when the effects are severe on mass. This can be supported from mechanics in which decrement in stiffness will not only reduce natural frequency but also results to increase in structure response. Also, from mechanic point of view, system will have high response when stiffness is smaller or mass is larger compare to low response when stiffness is higher or mass is smaller.

Finally, it can be concluded from the above discussion that the effect of thickness discontinuity is more on stiffness than mass. In addition, it can be said that thickness discontinuity on the pipes with or without fluid flow has appreciable effect on the impulse response of the FRP pipes and this effect can be recorded from displacement responses when compared with that of healthy pipe. Consequently, the finding in this chapter shows that response of the pipe with thickness discontinuity will increase when compared with healthy pipe. The rate at which response will increase depends on the geometry of the discontinuity or effect of discontinuity on stiffness and mass of the pipe.

CHAPTER 9

CONCLUSIONS AND RECOMMENDATIONS

9.1 Conclusions

The goal of this research work was to appraise the potential of using the vibrational characteristics of the laminated composite pipes (like FRP pipes) in monitoring the erosion-induced thinning or internal defects. In order to achieve this aim, several objectives were set and pursued consistently. In this work, WBFEM has been employed in which Euler-Bernoulli and Timoshenko beam theories were considered. Utlizing these theories in conjunction with B-spline and Trigonometric wavelets, several WBFEM models have been developed for dynamic analysis of laminated composite pipes with and without thickness discontinuity. The fluid flow inside pipes has been also considered. The developed models have been validated and the results obtained were compared with the available results in literature, as well as results obtained via ANSYS simulations.

The dynamic analysis of empty laminated composite pipe with thickness discontinuity showed that as the size of internal wall defect increases the natural frequency of the pipe also decreases. The decrease in pipe frequency is different based on the size of thickness discontinuity parameter that is dominant. If the size of discontinuity is increases in radial direction, that is, t_d is increasing while the width of discontinuity L_d is constant, the frequency of the pipe will continue to decrease. However, if t_d is fixed while L_d is increases, the pipe frequency will continue to decrease to a certain value of L_d and afterward the revise will be the case. This increase in frequency will maintain till $L_d = L$ when new pipe will be created with its frequency more than that of the original pipe. Thus, in general, the trend of frequency changes due to increase in the internal surface defect showed a cyclic behavior. This is consistent with the mechanics of solids; that is, the decrease in the cross-sectional area caused by thinning results in a decrease in flexural stiffness, as well as a decrease in mass. The effect of wall thickness reduction on natural frequencies is consequently dependent on the ratio of flexural stiffness to mass. If the resulting decrease in flexural stiffness is more pronounced than that of mass, then frequencies tend to decrease (softening effect), and vice versa.

Besides, the plotted mode shapes of pipe with thickness discontinuity showed the effect of the internal discontinuity along the span of the pipe. Although, the exact location of the discontinuity is not directly visible from its effect on the mode shapes, but deformed part of mode shape enveloped the location and width of the discontinuity. This implies that both the eigenvalues and eigenvectors carry the signature of the internal surface defect.

However, on the pipe with thickness discontinuity and fluid flow, such increase and decrease in frequency was not noticed. There was decrease in frequency for all the thickness discontinuity geometries considered. Besides it was discovered that for different values of L_d (with $L_c = L/2$) and velocities, the plot of each frequency impersonated the shape of its mode shape and this would become clearer when 0 and L are among the values of L_d considered. Through this plot, the third parameter can be easily predicted once any of the two of the three parameters involved are known. In addition, it was noticed that internal wall defect can serve as either stabilizing or destabilizing factor depends on its geometry and fluid velocity. It was also found that the critical velocity of a straight pipe does not only depend on mass ratio, boundary conditions, stiffness of the pipe foundation and pipe viscous properties as mentioned in literature but also depends on discontinuity and pretension force in the pipe. Besides, the eigenvalues and eigenvectors of the laminated pipe with thickness discontinuity conveying fluid also carry the signature of the internal surface defect similar to that of the empty laminated pipe with wall defect.

Furthermore, this investigation revealed that the internal surface discontinuity in pipes, with or without fluid flow, has an appreciable effect on the impulse response of the FRP pipes. This effect can be recorded from either displacement or velocity responses when compared with that of healthy pipe. Consequently, the finding shows that response of the pipe with thickness discontinuity will increase when compared with healthy pipe. The rate at which response will increase depends on the geometry of the discontinuity. The impulse response is of particular interest for the possible practical implementation of the developed methodology in defect detection. The impulse response analysis serves as the basis for the Experimental Modal Analysis (EMA), which is the experimental means for determining the vibrational characteristics of pipeline networks in the field.

Finally, the results obtained in this study showed that the model developed was not only capable of providing localized information about the compromise of FRP pipe structural integrity but also offered information about the location of the discontinuity. The information obtained can be used to detect the aforementioned effects of thickness discontinuity in industries. Similarly, In addition to presenting some benchmark solutions and new results for the case of a laminated composite pipe with internal wall-thinning with and without fluid flow, this investigation paves the way for future research that aims to utilize vibration measurements in detection of internal erosion-induced wall defects in pipelines.

9.2 Recommendations

In addition to the aforementioned findings this dissertation is providing a platform on which more investigations can be built. The following are some recommendations for future directions of research as extensions to this work:

1. Due to the limited computational speed and storage available with our available ANSYS software, no results could be produced by ANSYS for composite pipes conveying fluid with internal surface defect. This issue needs to be tackled to produce some results by ANSYS for verification purposes, as the current literature lacks any vibration data for composite pipes conveying fluid with internal surface defect.
2. Beam theories were employed in this work, and therefore shell theory and other higher-order theories can be used. Although, previous studies demonstrated that the beam theory is adequate for the analysis of laminated composite pip, higher-order theories need to be investigated to see whether the model accuracy might be improved.
3. In this investigation, the internal surface defect was permitted to grow circumferentially form partial to full ring or annulus, and to occupy any length of the pipe span. However, the defect was assumed to take uniform geometry.

Another extension to this work is to address the problem of pipes with internal surface defects of irregular shapes.

4. The experimental phase of this study is an important extension to this work to further validate the mode and to prove its potential and utilization in future defect-detection and online monitoring schemes in pipelines.
5. The ultimate extension of the work is to utilize it as a basis for a defect-identification scheme based on the measurements of the pipe’s vibrational characteristics. This is basically the inverse problem associated with the dynamic model developed in this dissertation.

APPENDIX A

In other to obtain $\varphi^3_{4,i}(\zeta)$ and $\psi^3_{4,i}(\zeta)$, one can utilize the data presented by Goswami et al. [101] for the scaling and wavelet functions for scale $j=0$ and $m=4$, respectively to generate expressions for $\varphi^0_{m,t}(\zeta)$ and $\psi^0_{m,t}(\zeta)$, for $t=-m+1,-m+2,...,0$. The expressions for $\varphi^0_{m,t}(\zeta)$ are as follows:

$$\varphi^0_{m,t}(\zeta)= \begin{cases} (1-\zeta)^{m-1} & \zeta\in[0,1) \\ 0 & \text{otherwise} \end{cases} \quad \text{for } t=\text{-}m+1, m=2,4 \tag{A1}$$

$$\varphi^0_{m,t}(\zeta)= \sum_{s=0}^{\mathscr{d}} \beta_s\zeta^s, \quad \text{for } t=-m+2,...,0;\ m=4;\ \mathscr{d}=m-1 \tag{A2}$$

where, for $m=4$, $\beta_s\,(s=0,1,2,...,\mathscr{d})$ are tabulated in [101]. In this case, $t=-3,-2,-1,0$ for $m=4$ and $j=0$. When $t=-3$, Eq. (A1) gives

$$\varphi^0_{4,-3}(\zeta)=\frac{1}{6}\begin{cases} 6-18\zeta+18\zeta^2-6\zeta^3 & \zeta\in[0,1) \\ 0 & \text{otherwise} \end{cases} \tag{A3}$$

Also, for $t=-2,-1,0$, Eq. (A2) produces

$$\varphi^0_{4,-2}(\zeta)=\frac{1}{6}\begin{cases} 18\zeta-27\zeta^2+(21/2)\zeta^3 & \zeta\in[0,1) \\ 12-18\zeta+9\zeta^2-(3/2)\zeta^3 & \zeta\in[1,2) \\ 0 & \text{otherwise} \end{cases} \tag{A4}$$

$$\varphi^0_{4,-1}(\zeta)=\frac{1}{6}\begin{cases} 9\zeta^2-(11/2)\zeta^3 & \zeta\in[0,1) \\ -9+27\zeta-18\zeta^2+(7/2)\zeta^3 & \zeta\in[1,2) \\ 27-27\zeta+9\zeta^2-\zeta^3 & \zeta\in[2,3) \\ 0 & \text{otherwise} \end{cases} \tag{A5}$$

and

$$\varphi_{4,0}^{0}(\zeta) = \frac{1}{6}\begin{cases} \zeta^3 & \zeta \in [0,1) \\ 4 - 12\zeta + 12\zeta^2 - 3\zeta^3 & \zeta \in [1,2) \\ -44 + 60\zeta - 24\zeta^2 + 3\zeta^3 & \zeta \in [2,3) \\ 64 - 48\zeta + 12\zeta^2 - \zeta^3 & \zeta \in [3,4) \\ 0 & \text{otherwise} \end{cases} \tag{A6}$$

The same procedures need to be followed to be able to obtain expressions for $\psi_{m,t}^{0}(\zeta)$.

APPENDIX B

Here, upon substituting Eqs. (A3) - (A6) in Eq. (4.12), the following expressions are obtained:

$$\varphi_{4,-3}^{3}(\zeta)=\varphi_{4,-3}^{0}(\zeta)=$$

$$\frac{1}{6}\begin{cases}6-18(2^{3}\zeta)+18(2^{3}\zeta)^{2}-6(2^{3}\zeta)^{3}, & \zeta\in\frac{1}{2^{3}}[0,1)\\ 0 & \text{otherwise}\end{cases} \tag{B1}$$

$$\varphi_{4,-2}^{3}(\zeta)=\varphi_{4,-2}^{0}(\zeta)=$$

$$\frac{1}{6}\begin{cases}18(2^{3}\zeta)-27(2^{3}\zeta)^{2}+\left(21/2\right)(2^{3}\zeta)^{3}, & \zeta\in\frac{1}{2^{3}}[0,1)\\ 12-18(2^{3}\zeta)+9(2^{3}\zeta)^{2}-\left(3/2\right)(2^{3}\zeta)^{3}, & \zeta\in\frac{1}{2^{3}}[1,2)\\ 0 & \text{otherwise}\end{cases} \tag{B2}$$

$$\varphi_{4,-1}^{3}(\zeta)=\varphi_{4,-1}^{0}(\zeta)=$$

$$\frac{1}{6}\begin{cases}9(2^{3}\zeta)^{2}-\left(11/2\right)(2^{3}\zeta)^{3}, & \zeta\in\frac{1}{2^{3}}[0,1)\\ -9+27(2^{3}\zeta)-18(2^{3}\zeta)^{2}+\left(7/2\right)(2^{3}\zeta)^{3}, & \zeta\in\frac{1}{2^{3}}[1,2)\\ 27-27(2^{3}\zeta)+9(2^{3}\zeta)^{2}-(2^{3}\zeta)^{3}, & \zeta\in\frac{1}{2^{3}}[2,3)\\ 0 & \text{otherwise}\end{cases} \tag{B3}$$

$$\varphi_{4,0}^{3}(\zeta)=\varphi_{4,0}^{0}(\zeta)=$$

$$\frac{1}{6}\begin{cases}(2^3\zeta)^3, & \zeta\in\frac{1}{2^3}[0,1)\\ 4-12(2^3\zeta)+12(2^3\zeta)^2-3(2^3\zeta)^3, & \zeta\in\frac{1}{2^3}[1,2)\\ 44+60(2^3\zeta)-24(2^3\zeta)^2+3(2^3\zeta)^3, & \zeta\in\frac{1}{2^3}[2,3)\\ 64-48(2^3\zeta)+12(2^3\zeta)^2-(2^3\zeta)^3, & \zeta\in\frac{1}{2^3}[3,4)\\ 0 & \text{otherwise}\end{cases} \tag{B4}$$

$$\begin{aligned}
\varphi_{4,1}^{3}(\zeta)&=\varphi_{4,0}^{0}(2^3\zeta-1)=\varphi_{4,0}^{3}(\zeta-(1/2^3))\\
\varphi_{4,2}^{3}(\zeta)&=\varphi_{4,0}^{0}(2^3\zeta-2)=\varphi_{4,0}^{3}(\zeta-(2/2^3))\\
\varphi_{4,3}^{3}(\zeta)&=\varphi_{4,0}^{0}(2^3\zeta-3)=\varphi_{4,0}^{3}(\zeta-(3/2^3))\\
\varphi_{4,4}^{3}(\zeta)&=\varphi_{4,0}^{0}(2^3\zeta-4)=\varphi_{4,0}^{3}(\zeta-(4/2^3))\\
\varphi_{4,5}^{3}(\zeta)&=\varphi_{4,-1}^{0}(1-2^3\zeta)=\varphi_{4,-1}^{3}(1-\zeta)\\
\varphi_{4,6}^{3}(\zeta)&=\varphi_{4,-2}^{0}(1-2^3\zeta)=\varphi_{4,-2}^{3}(1-\zeta)\\
\varphi_{4,7}^{3}(\zeta)&=\varphi_{4,-3}^{0}(1-2^3\zeta)=\varphi_{4,-3}^{3}(1-\zeta)
\end{aligned} \tag{B5}$$

NOMENCLATURE

Notation	Unit	Description
d		Degree of curve or degree of polynomial
f		Friction factor
j		Scale
h	m	Total pipe thickness
h_k	m	Thickness of the k^{th} layer
$\overline{h}_c$		Generalized minor head loss due sudden contraction
$\overline{h}_e$		Generalized minor head loss due sudden expansion
$\overline{h}_f$		Generalized major head loss due to friction
κ		Shear deformation coefficient
l_e	m	Element length
m		Order of curve (or order of the polynomial segments of the B-spline curve)
m_f	kg.m^{-1}	Mass of fluid per unit length
n_e		Number of element
r_k	m	Radius of the k^{th} layer
t_d	m	Depth or thickness of the region affected by the discontinuity
$w(x,t)$	m	Transverse displacement of the pipe compared to the centerline
$\gamma(x)$	Kg.m	Rotation inertia
γ_{12}		Shear strain
ε_1		Engineering strain
ε_2		Engineering strain
ε_{12}		Tensorial strain
θ_1	^{o}	First hoop angle
θ_2	^{o}	Second hoop angle
λ	rad^2.sec^{-2}	Eigenvalues
$\hbar$		Number of segment in each element length
ν		Poison's ratio for isotropic material
ν_{12}		Major poison's ratio (poison's ratio in 1-2 plane)
ν_{13}		poison's ratio in 1-3 plane
ν_{16}		Poisson's parameter
ν_{21}		Minor poison's ratio (poison's ratio in 2-1 plane)
ν_{23}		Poison's ratio in 2-3 plane
ν_{26}		Poisson's parameter
ν_{36}		Poisson's parameter

ν_{45}		Poisson's parameter
σ_1	N.m^{-2}	Longitudinal stress
σ_2	N.m^{-2}	Transverse stress
ρ_f	Kg. m^{-3}	Fluid density
ρ_k	Kg. m^{-3}	Density of k^{th} layer
ρ_p	Kg. m^{-3}	Pipe density
ϕ	^{o}	Ply or lamina angle
ω	rad.sec^{-1}	Natural frequency
A	m^{2}	Cross-sectional area of the composite pipe
A_f	m^{2}	Pipe inner area
$[A]$	N.m^{-1}	Extensional (or membrane , in-plane laminate moduli) matrix
$[B]$	N	Bending-coupling (or bending-extensional coupling , in-plane/flexure coupling laminate moduli) matrix
D_s	m	Generalized inner diameter of pipe
D_i	m	Inner diameter of pipe
D_o	m	Outer diameter of pipe
$[D]$	N.m	Bending (or flexural laminate) matrix
E	N.m^{-2}	Modulus of elasticity
E_1	N.m^{-2}	Longitudinal elastic modulus
E_2	N.m^{-2}	Transverse elastic modulus
E_3	N.m^{-2}	Elastic modulus along 3-axis
F_τ	N	Shear friction force
G	N.m^{-2}	shear modulus
G_{12}	N.m^{-2}	In-plane shear modulus
G_{13}	N.m^{-2}	Shear modulus in 1-3 plane
G_{23}	N.m^{-2}	Shear modulus in 2-3 plane
$\mathcal{H}$	N.m^{2}	Bending rigidity of composite pipe
I	m^{4}	Moment of inertia
$[K]_e$	N.m^{-1}	Element stiffness matrix
Θ	radian	Elastic rotation
L	m	Length of pipe
L_c	m	Distance from reference end of the pipe to the center of the discontinuity region
L_d	m	Width or length of the region affected by discontinuity
$[M]_e$	kg	Element mass matrix
$\mathcal{M}$	kg.m^{-1}	Mass per unit length of composite pipe
N		Total number of layer of the composite pipe
$\mathbb{N}$		Natural integer number
$\{N_E\}_e$		Wavelet-based C$_1$ type element shape function for BSWI$_{mj}$

$\{N_T\}_e$		Wavelet-based C_0 type element shape function for $\mathrm{BSWI_{mj}}$
[Q]	$N.m^{-2}$	Reduced stiffness matrix
$[\bar{Q}]$	$N.m^{-2}$	Transformed reduced stiffness matrix
R	m	Radius of mid-surface of the laminate
Re		Reynolds Number
T	$kg.\ m^2.s^{-2}$	Kinetic energy
$\bar{T}$	N	Pretension force
$[T_E]_e$		Wavelet-based C_1 type element transformation matrix for $\mathrm{BSWI_{mj}}$
$[T_H]_e$		Transformation matrix due to trigonometric wavelet
$[T_T]_e$		Wavelet-based C_0 type element transformation matrix for $\mathrm{BSWI_{mj}}$
U	Nm	Strain energy
V_x	$m.\ s^{-1}$	Pipe fluid inlet velocity
$\mathcal{W}(x)$	m	Components of displacement parallel to y direction
$\mathbb{Z}$		Integer number

REFERENCES

[1] Xie, X., Jin, G., Yan, Y., Shi, S. X., and Liu, Z., 2014, "Free vibration analysis of composite laminated cylindrical shells using the Haar wavelet method," Composite Structures, 109, pp. 169-177.

[2] Vidal, P., Gallimard, L., and Polit, O., 2014, "Shell finite element based on the Proper Generalized Decomposition for the modeling of cylindrical composite structures," Computers & structures, 132, pp. 1-11.

[3] Jin, G., Ye, T., Ma, X., Chen, Y., Su, Z., and Xie, X., 2013, "A unified approach for the vibration analysis of moderately thick composite laminated cylindrical shells with arbitrary boundary conditions," International Journal of Mechanical Sciences, 75, pp. 357-376.

[4] Narita, Y., and Ohta, Y., 1993, "Finite element study for natural frequencies of cross-ply laminated cylindrical shells," Composite Structures, 26, pp. 55-62.

[5] Viswanathan, K. K., Aziz, Z. A., Amirah, H. Z., and Javed, S., 2014, "Free vibration of symmetric angle-ply laminated circular cylindrical shells," IOP Conference Series: Earth and Environmental Science, 19, p. 012010.

[6] Jin, G., Ye, T., Chen, Y., Su, Z., and Yan, Y., 2013, "An exact solution for the free vibration analysis of laminated composite cylindrical shells with general elastic boundary conditions," Composite Structures, 106, pp. 114-127.

[7] Farshidianfar, A., and Oliazadeh, P., 2012, "Free Vibration Analysis of Circular Cylindrical Shells: Comparison of Different Shell Theories," International Journal of Mechanics and Applications, 2(5), pp. 74-80.

[8] Khan, S. A., "FRP/RTRP/GRP-Piping system for all Industrial Applications within Middle East from 30 years," Amiantit Fiberglass Industries Ltd-Dammam.

[9] Morton, T. R., 1974, "Fiber-Glass-Reinforced Plastics For Corrosion Resistance-Part 2," Beetle Plastics, Inc.

[10] Reichhold, I., 2009, "FRP Inspection Guide: An Inspection Guide for Fiber-Reinforced Plastic (FRP) Equipment," Reichhold, Inc.

[11] Limited, G. T. P., "P10_What is FRP and Pultruded FRP?," Gactel Turnkey Projects Limited.

[12] P.E., S. D. C., "Fiberglass Pipe ~ Past, Present and Future,"Fiberglass Tank & Pipe Institute.

[13] Suraj, "Fibre Reinforced Plastics (FRP) Ref NDM," http://www.google.com.sa/url?sa=t&rct=j&q=&esrc=s&frm=1&source=web&cd=8&cad=rja&ved=0CGAQFjAH&url=http%3A%2F%2Fwww.sefindia.org%2Fforum%2Fdownload.php%3Fid%3D1665&ei=DoaGUu7tLIKihge0xYH4Aw&usg=AFQjCNH3hiGnSDo1svcq3IzRhXMRWZma6w.

[14] Ltd, P. P., 2012, "GRP PIpe and Fittings:Potable water, non potable water and sewer applications," Promains Pty Ltd.

[15] Group, F. P. I., 2011, "Fiberglass technical overview and design aspects," The Future Pipe Industries Group (FPI).

[16] Reichhold, I., 2009, "FRP Material Selection Guide: An Engineer’s Guide to FRP Technology," Reichhold, Inc.

[17] Corporation, S. R. f. d., "Glass Fiber Reinforced Plastic Pipes," Sabarmati River front development Corporation.

[18] Amiantit, "Flowtite Maintenance Manual," Flowtite Technology AS.

[19] Association, N. O. a. G., "Norwegian Oil and Gas recommended guidelines for NDT of GRP Pipe Systems and Tanks," No. 055, Norwegian Oil and Gas Association, Norway.

[20] Soldatos, K. P., and Messina, A., 1998, "Vibration studies of cross-ply laminated shear deformable circular cylinders on the basis of orthogonal polynomials," Journal of Sound and Vbration, 218(2), pp. 219-243.

[21] Messina, A., and Soldatos, K. P., 1999, "Ritz-type dynamic analysis of cross-ply laminated circular cylinders subjected to different boundary conditions," Journal of Sound and Vbration, 227(4), pp. 749-768.

[22] Civalek, Ö., 2007, "Numerical analysis of free vibrations of laminated composite conical and cylindrical shells: Discrete singular convolution (DSC) approach," Journal of Computational and Applied Mathematics, 205(1), pp. 251-271.

[23] Poore, A. L., Barut, A., and Madenci, E., 2008, "Free vibration of laminated cylindrical shells with a circular cutout," Journal of Sound and Vibration, 312(1-2), pp. 55-73.

[24] Viswanathan, K. K., Kim, K. S., Lee, J. H., Koh, H. S., and Lee, J. B., 2009, "Free vibration of multi-layered circular cylindrical shell with cross-ply walls, including shear deformation by using spline function method," Journal of Mechanical Science and Technology, 22(11), pp. 2062-2075.

[25] Naeem, M. N., Kanwal, S., Shah, A. G., Arshad, S. H., and Mahmood, T., 2012, "Vibration Characteristics of Ring-Stiffened Functionally Graded Circular Cylindrical Shells," ISRN Mechanical Engineering, 2012, pp. 1-13.

[26] Khalifa, A. M., 2011, "Exact solutions for the vibration of circumferentially stepped orthotropic circular cylindrical shells," Comptes Rendus Mécanique, 339(11), pp. 708-718.

[27] Soldatos, K. P., 1984, "Comparison of some shell theories used for the dynamic analysis of cross-ply laminated circular cylinder panels," Journal of Sound and Vbration, 97(2), pp. 305-319.

[28] Ramesh, T. C., and Ganesan, N., 1992, "A finite element based on a discrete layer theory for the free vibration analysis of cylindrical shells," Computers & structures, 43(1), pp. 137-143.

[29] Sun, G., Bennett, P. N., and Willams, F. W., 1993, "An investigation on fundamental frequencies of laminated circular cylinders given by shear deformable finite elements," Journal of Sound and Vbration, 205(3), pp. 265-273.

[30] Singh, S. P., and Gupta, K., 1994, "Free damped flexural vibration analysis of composite cylindrical tubes using beam and shell theories," Journal of Sound and Vbration, 172(2), pp. 171-190.

[31] Timarchi, T., and Soldatos, K. P., 2000, "Vibrations of angle-ply laminated circular cylindrical shells subjected to different sets of edge boundary conditions," Journal of Enginnering Mathematics, 37, pp. 211-230.

[32] Qu, Y., Long, X., Wu, S., and Meng, G., 2013, "A unified formulation for vibration analysis of composite laminated shells of revolution including shear deformation and rotary inertia," Composite Structures, 98, pp. 169-191.

[33] Khdeir, A. A., Reddy, J. N., and Frederick, D., 1989, "A study of bending, vibration and buckling of cross-ply circular cylindrical shells with various shell theories," Int. J. Engng. Sci., 27(11), pp. 1337-1351.

[34] Ye, J., and Soldatos, K. P., 1994, "Three-dimensional vibration of laminated cylinders and cylindrical panels with symmetric or antisymmetric cross-ply lay-up," composite Engineering, 4(4), pp. 429-444.

[35] Ich Thinh, T., and Nguyen, M. C., 2013, "Dynamic stiffness matrix of continuous element for vibration of thick cross-ply laminated composite cylindrical shells," Composite Structures, 98, pp. 93-102.

[36] Koide, R. M., and Luersen, M. A., 2013, "Maximization of fundamental frequency of laminated composite cylindrical shells by Ant Colony Algorithm," Journal of Aerospace Technology and Management, 5(1), pp. 75-82.

[37] Ryu, B.-J., Ryu, S.-U., Kim, G.-H., and Yim, K.-B., 2004, "Vibration and Dynamic Stability of Pipes Conveying Fluid on Elastic Foundations," KSME International Journal, 18(12), pp. 2148-2157.

[38] Reddy, J. N., and Wang, C. M., 2004, "Dynamics of fluid-conveying beams," CORE Report No. 2004-03, National University of Singapore.

[39] Mostafa, N. H., 2014, "Effect of a Viscoelastic Foundation on the Dynamic Stability of a fluid conveying pipe," International Journal of Applied Science and Engineering, 12(1), pp. 59-74.

[40] Hewakandamby, B. N., 2012, A first course in Fluid Mechanics for Engineers, Ventus Publishing ApS.

[41] Wang, L., Gan, J., and Ni, Q., 2013, "Natural frequency analysis of fluid-conveying pipes in the ADINA system," Journal of Physics: Conference Series, 448, p. 012014.

[42] Al-Hashimy, Z. T., Al-Kayiem, H. H., Hasan, F., and Mohmmedd, A. O., 2014, "Effect of Various Fluid Densities on Vibration Characteristics in Variable Cross-section Pipes," Journal of Applied Sciences, 14(18), pp. 2054-2060.

[43] Kutin, J., and Bajsić, I., 2014, "Fluid-dynamic loading of pipes conveying fluid with a laminar mean-flow velocity profile," Journal of Fluids and Structures, 50, pp. 171-183.

[44] Piet-Lahanier, N., and Ohayon, R., 1990, "Finite element analysis of a slender fluid-Structure system," Journal of Fluids and Structures, 4(6), pp. 631-645.

[45] Zhang, Y. L., Gorman, D. G., and Reese, J. M., 1999, "Analysis of the vibration of pipes conveying fluid," Proc Instn Mech Engrs Part C, 213, pp. 849-860.

[46] Hansson, P.-A., and Sandberg, G., 2001, "Dynamic finite element analysis of fluid-filled pipes," Comput. Methods Appl. Mech. Engrg., 190, pp. 3111-3120.

[47] Kaewunruena, S., Chiravatchradejb, J., and Chucheepsakulb, S., 2004, "Nonlinear free vibrations of marine risers/pipes transporting fluid," Ocean Enginnering, pp. 1-24.

[48] Li, Q. S., Yang, K., Zhang, L., and Zhang, N., 2002, "Frequency domain analysis of fluid–structure interaction in liquid-filled pipe systems by transfer matrix method," International Journal of Mechanical Sciences, 44 pp. 2067–2087.

[49] Dai, H. L., Wang, L., Qian, Q., and Gan, J., 2012, "Vibration analysis of three-dimensional pipes conveying fluid with consideration of steady combined force by transfer matrix method," Applied Mathematics and Computation, 219(5), pp. 2453-2464.

[50] Zhong-min, W., Zhen-yu, F., Feng-qun, Z., and Hong-zhao, L., 2000, "Analysis of coupled-mode flutter of pipes conveying fluid on the elastic foundation," Applied Mathematics and Mechanics, 21(10), pp. 1177-1186.

[51] Kuiper, G. L., and Metrikine, A. V., 2004, "On stability of a clamped-pinned pipe conveying fluid," Heron, 49(3), pp. 211-232.

[52] Tornabene, F., Marzani, A., Viola, E., and Elishakoff, I., 2010, "Critical flow speeds of pipes conveying fluid using the generalized differential quadrature method," Adv. Theor. Appl. Mech, 3(3), pp. 121-138.

[53] García Planas, M. I., and Mediano Valiente, B., 2014, "Stability analysis of a clamped-pinned pipeline conveying fluid," WSEAS Transactions on Systems, 13, pp. 54-64.

[54] Chang, J.-S., and Chiou, W.-J., 1995, "Natural frequencies and critical velocities of fixed-fixed laminated circular cylindrical shells conveying fluids," Journal of Computers & Structures, 57(5), pp. 929-939.

[55] Zou, G. P., Cheraghi, N., and Taheri, F., 2005, "Fluid-induced vibration of composite natural gas pipelines," International Journal of Solids and Structures, 42(3-4), pp. 1253-1268.

[56] Duarte, H. V., Donadon, L. V., and Ávila, A. F., "Composite piping dynamics under internal flow," Proc. 11th Pan-American Congress of Applied Mechanics - PACAM XI.

[57] Mohammad, R., Kotousov, A., Codrington, J., and Blazewicz, A., 2011, "Effect of flowing medium for a simply supported pipe subjected to impulse loading," Australian Journal of Mechanical Engineering, 8(2), pp. 133-144.

[58] Mohammad, R., Kotousov, A., and Codrington, J., 2011, "Analytical modelling of a pipe with flowing medium subjected to an impulse load," International Journal of Impact Engineering, 38(2-3), pp. 115-122.

[59] Duan, H. F., Lee, P. J., and Tuck, J., 2014, "Experimental Investigation of Wave Scattering Effect of Pipe Blockages on Transient Analysis," Procedia Engineering, 89, pp. 1314-1320.

[60] Zheng, C., Liu, H., Kouretzis, G. P., Sloan, S. W., and Ding, X., 2015, "Vertical response of a thin-walled pipe pile embedded in viscoelastic soil to a transient point load with application to low-strain integrity testing," Computers and Geotechnics, 70, pp. 50-59.

[61] Zhang, X., Chen, X., Wang, X., and He, Z., 2010, "Multivariable finite elements based on B-spline wavelet on the interval for thin plate static and vibration analysis," Finite Elements in Analysis and Design, 46(5), pp. 416-427.

[62] Xiang, J. W., Chen, X. F., He, Z. J., and Dong, H. B., 2006, "The construction of 1D wavelet finite elements for structural analysis," Computational Mechanics, 40(2), pp. 325-339.

[63] Chen, X., Yang, Z., Zhang, X., and He, Z., 2012, "Modeling of wave propagation in one-dimension structures using B-spline wavelet on interval finite element," Finite Elements in Analysis and Design, 51, pp. 1-9.

[64] Jiawei, X., Zhengjia, H., and Xuefeng, C., 2006, "The construction of wavelet-based truncated conical shell element using B-spline wavelet on the interval," Acta Mechanica Solida Sinica, 19(4), pp. 316-326.

[65] Daniel, I. M., and Ishai, O., 1994, Engineering Mechanics of Composite Materials, Oxford University Press, New York.

[66] Kolla´R, L. A. O. P., and Springer, G. S., 2003, Mechanics Of Composite Structures, Cambridge University Press, New York.

[67] Niu, M. C. Y., 1992, Composite Airframe Structures - Practical Design Information and Data, AD Adaso/Adastra Engineering LLC.

[68] Nettles, A. T., 1994, "Basic mechanics of laminated composite plates," No. M-764, George C. Marshall Space Flight Center, NASA, Alabama 35812.

[69] Gibson, R. F., 1994, Principles Of Composite Material Mechanics, McGraw-Hill, Inc., London.

[70] Mororo, L. A., Melo, A. M. C., Junior, E. P., Holanda, A. S., and Almeida, D. C., 2010, "Global analysis of laminated tubes," Meccanica Computacional, XXIX, pp. 1367-1383.

[71] Reddy, J. N., 2004, Mechanics of Laminated Composite Plates and Shells: Theory and Analysis, CRC Press, London.

[72] Barbero, E. J., 1999, Introduction to Composite Materials Design, Taylor & Francis Group, Great Britain.

[73] Jones, R. M., 1999, Mechanics of composite materials, Taylor & Francis, Inc., USA.

[74] Kaw, A. K., 2006, Mechanics of Composite Materials, CRC Press, New York.

[75] Motavalli, M., "Laminate Theory," http://www.empa.ch/plugin/template/empa/*/54078.

[76] Resnikoff, H. L., and Raymond O. Wells, J., 1998, Wavelet Analysis: The Scalable Structure of Information, Springer-Verlag New York, Inc., New York.

[77] Han, J.-G., Ren, W.-X., and Huang, Y., 2005, "A multivariable wavelet-based finite element method and its application to thick plates," Finite Elements in Analysis and Design, 41(9-10), pp. 821-833.

[78] Chen, X., Yang, S., Ma, J., and He, Z., 2004, "The construction of wavelet finite element and its application," Finite Elements in Analysis and Design, 40(5-6), pp. 541-554.

[79] Youhe, Z., Jizeng, W., and Xiaojing, Z., 1998, "Applications of wavelet Galerkin FEM to bending of beam and plate structures," Applied Mathematical and Mechanics, 19(8), pp. 745-755.

[80] Williams, J. R., and Amaratunga, K., 1994, "Introduction to wavelets in engineering," International Journal for Numerical Methods in Engineering, 37(14), pp. 2365-2388.

[81] Restrepo, J. M., and Leaf, G. K., 1997, "Inner Product Computations Using Periodized Daubechies Wavelets," International Journal for Numerical Methods in Engineering, 40, pp. 3557-3578.

[82] Liu, Y., Qin, F., Liu, Y., and Cen, Z., 2010, "A Daubechies wavelet-based method for elastic problems," Engineering Analysis with Boundary Elements, 34(2), pp. 114-121.

[83] Chen, X., He, Z., Xiang, J., and Li, B., 2006, "A dynamic multiscale lifting computation method using Daubechies wavelet," Journal of Computational and Applied Mathematics, 188(2), pp. 228-245.

[84] Daubechies, I., 1992, Ten lectures on wavelets, Society for industrial and applied mathematics, Philadelphia.

[85] Spanos, P. D., Failla, G., and Politis, N. P., 2005, "Wavelets — Concepts and Applications," Vibration and Shock Handbook, C. W. d. Silva, ed., CRC Press, U.S.A, pp. 11 11-11 24.

[86] Soman, K. P., Ramachandran, K. I., and Resmi, N. G., 2004, Insight Into Wavelets From Theory to Practice, Prentice-Hall of India, New Delhi.

[87] Chun-Lin, L., 2010, "A tutorial of the wavelet transform," NTUEE, Taiwan.

[88] Donald, D. A., Everingham, Y. L., McKinna, L. W., and Coomans, D., 2009, "Feature Selection in the Wavelet Domain: Adaptive Wavelets," Comprehensive Chemometrics, D. B. Editors-in-Chief: Stephen, T. Romà, and W. Beata, eds., Elsevier, Oxford, pp. 647-679.

[89] Chui, C. K., 1997, Wavelets: A Mathematical Tool for Signal Analysis, The Society for Industrial and Applied Mathematics (SIAM), Philadelphia.

[90] Mix, D. F., and Olejniczak, K. J., 2003, Elements of wavelets for engineers and scientists, John Wiley & Sons.

[91] Chen, C., and Hsiao, C., "Haar wavelet method for solving lumped and distributed-parameter systems," Proc. Control Theory and Applications, IEE Proceedings-, IET, pp. 87-94.

[92] Vidacovic, B., and Meuller, P., 1991, "Wavelets for Kids. A Tutorial Introduction," AMS Subject Classification, Duke University.

[93] He, W.-Y., and Ren, W.-X., 2012, "Finite element analysis of beam structures based on trigonometric wavelet," Finite Elements in Analysis and Design, 51, pp. 59-66.

[94] He, W.-Y., and Ren, W.-X., 2013, "Trigonometric wavelet-based method for elastic thin plate analysis," Applied Mathematical Modelling, 37(4), pp. 1607-1617.

[95] Bashmal, S., Oke, W. A., and Khulief, Y., 2015, "Vibration analysis of an elastically restrained microcantilever beam under electrostatic loading using wavelet-based finite element method," Micro & Nano Letters, 10(3), pp. 147-152.

[96] He, W.-Y., and Ren, W.-X., 2013, "Adaptive Trigonometric Hermite Wavelet Finite Element Method for Structural Analysis," International Journal of Structural Stability and Dynamics, 13(01), p. 1350007.

[97] Chui, C. K., 1992, An introduction to Wavelets, Academic press, London.

[98] Yang, Z., Chen, X., He, Y., He, Z., and Zhang, J., 2014, "The Analysis of Curved Beam Using B-Spline Wavelet on Interval Finite Element Method," Shock and Vibration, 2014, pp. 1-9.

[99] Xiang, J., Zhong, Y., Chen, X., and He, Z., 2008, "Crack detection in a shaft by combination of wavelet-based elements and genetic algorithm," International Journal of Solids and Structures, 45(17), pp. 4782-4795.

[100] Chui, C. K., and Quak, E., 1992, "Wavelets on a bounded interval," Numerical methods in approximation theory, D. Braess, and L. L. Schumaker, eds., Birkhäuser Verlag Basel, Switzerland, pp. 53-57.

[101] Goswami, J. C., Chan, A. K., and Chui, C. K., 1995, "On solving first-kind integral equations using wavelets on a bounded interval," IEEE transaction on antennas and propagation, 43(6), pp. 614-622.

[102] Quak, E., and Weyrich, N., 1994, "Decomposition and reconstruction algorithms for spline wavelets on a bounded interval," Applied Computational Harmonic Analysis 1(3), pp. 217-231.

[103] Gallier, J., 2013, Curves and surfaces in geometric modeling: Theory and algorithms, Jean Gallier, Philadelphia,USA.

[104] Wang, Y., Chen, X., and He, Z., 2012, "A second-generation wavelet-based finite element method for the solution of partial differential equations," Applied Mathematics Letters, 25(11), pp. 1608-1613.

[105] Ma, J., Xue, J., Yang, S., and He, Z., 2003, "A study of the construction and application of a Daubechies wavelet-based beam element," Finite Elements in Analysis and Design, 39(10), pp. 965-975.

[106] ZHANG, X.-M., LIU, K.-A., and LIU, J.-Q., 2005, "A Wavelet Finite Element Method for 2-D Wave Equation in the Fluid-Saturated Porous Media," Chinese Journal of Geophysics, 48(5), pp. 1234-1246.

[107] Romine, C., and Peyton, B., 1997, "Computing connection coefficients of compactly supported wavelets on bounded intervals," US Department of Energy, Report No. ORNL/TM-13413.

[108] "Laminated Composites-I," http://nptel.ac.in/courses/105108124/pdf/Lecture_Notes/LNm5.pdf.

[109] Salim, H. A., and Davalos, J. F., 2005, "Torsion of Open and Closed Thin-Walled Laminated Composite Sections," Journal of Composite Materials, 39(6), pp. 497-524.

[110] Wu, X., and Sun, C. T., 1991, "Vibration analysis of laminated composite thin-walled beams using finite elements," AIAA Journal, 29(5), pp. 736-742.

[111] Massa, J. C., and Barbero, E. J., 1998, "A Strength.ofMaterials Formulation for Walled Composite Beams with Torsion," Journal of Composite Materials, 32(17), pp. 1560-1594.

[112] Vinson, J. R., and Sierakowski, R. L., 2008, The behavior of structures composed of composite materials, Springer, Netherlands.

[113] Hajianmaleki, M., and Qatu, M. S., 2011, "Mechanics of Composite Beams," Advances in Composite Materials - Analysis of Natural and Man-Made Material, P. Těšinova, ed., InTech, pp. 527-546.

[114] Zienkiewicz, O. C., and Taylor, R. L., 1961, The Finite Element Method, McGraw-Hill Book Company, London.

[115] S., T., H., Y. D., and W., J. W., 1928, Vibration Problems in Engineering, Wiley, New York, USA.

[116] Qatu, M. S., and Iqbal, J., 2010, "Transverse vibration of a two-segment cross-ply composite shafts with a lumped mass," Composite Structures, 92(5), pp. 1126-1131.

[117] Kim, C.-D., and Bert, C. W., 1993, "Critical speed analysis of laminated composite, hollow drive shafts," Chemical Engineering, 3(7-8), pp. 633-643.

[118] Chang, M.-Y., Chen, J.-K., and Chang, C.-Y., 2004, "A simple spinning laminated composite shaft model," International Journal of Solids and Structures, 41(3-4), pp. 637-662.

[119] W., B. C., and Chun-Do, K., 1995, "Whirling of Composite-Material Driveshafts including Bending-Twisting Coupling and Transverse Shear Deformation," Journal of Vibration and Acoustics, 117(1), pp. 17–21.

[120] PENG, X.-L., and HAO, H., 2012, "A Numerical Study Of Damage Detection Of Underwater Pipeline Using Vibration-Based Method," International Journal of Structural Stability and Dynamics, 12(03), p. 1250021.

[121] Blevins, R. D., 2001, Flow-Induced Vibration, Krieger Publishing Company, Malabar, Florida.

[122] Young, D. F., Munson, B. R., Okiishi, T. H., and Huebsch, W. W., 2011, A Brief Introduction to Fluid Mechanics, John Wiley & Sons, Inc., USA.

[123] Romeo, E., Royo, C., and Monzón, A., 2002, "Improved explicit equations for estimation of the friction factor in rough and smooth pipes," Chemical Engineering Journal, 86(3), pp. 369-374.

[124] Bansal, R. K., 2010, A Textbook of Fluid Mechanics and Hydraulic Machines, Laxmi Publications (P) Ltd, New Delhi, India.

[125] Brater, E. F., King, H. W., Lindell, J. E., and Wei, C. Y., 1996, Handbook of Hydraulics, McGraw-Hill, New York, USA.

[126] Lin, Y.-H., and Chu, C.-L., 2001, "Active Modal Control of Timoshenko Pipes," Journal of the Chinese Institute of Engineers, 24(1), pp. 65-74.

[127] White, F. M., 2006, Viscous Fluid Flow, McGraw-Hill, New York, America.

[128] Hengstler, J. A., 2013, "Influence of the fluid-structure interaction on the vibrations of structures," PhD, Diss., Eidgenössische Technische Hochschule ETH Zürich, Nr. 21645, 2013.

[129] Grant, I., 2010, "Flow induced vibrations in pipes, a finite element approach," MS, Cleveland State University.

[130] Barkanov, E., 2001, Introduction to the Finite Element Method.

VITA

Name: Wasiu Adeyemi Oke

Nationality: Nigerian

Date of Birth: March 23, 1976

Present Address: Department of Mechanical Engineering, P. O. Box 8611, King Fahd University of Petroleum and Mineral (KFUPM), Dhahran-31261, Saudi Arabia.

Permanent Address: Ikolaba Compound, Off Ado-Awaye Road, Malete, Koso, Iseyin, Oyo State, Nigeria.

Email Address: wasiuad@yahoo.com, wasiu.oke@gmail.com, wasiuad@kfupm.edu.sa

Educational Qualification:

PhD Mechanical Engineering

King Fahd University of Petroleum & Minerals, Dhahran, Saudi Arabia (May, 2016)

MS Mechanical Engineering

King Fahd University of Petroleum & Minerals, Dhahran, Saudi Arabia (January, 2012)

B.Sc. Mechanical Engineering

University of Ibadan, Nigeria (March, 2005)

National Diploma (ND) Mechanical Engineering

The Federal Polytechnic Bida, Nigeria (May, 1998)

Publications:

- Khulief, Y. A., El-Gebeily, M. A., Oke, W. A., and Ahmed, W. H., 2015, "Modal frequencies of fiber-reinforced polymer pipes with wall-thinning using a wavelet-based finite element model, "Proceedings of the Institution of Mechanical Engineers, Part C: Journal of Mechanical Engineering Science, 229(13), pp. 2377-2386.
- Oke, W. A., and Khulief, Y. A., 2016, "Vibration analysis of composite pipes using the finite element method with B-spline wavelets," Journal of Mechanical Science and Technology, 30(2), pp. 623-635.
- Oke, W. A and Khulief, Y. A, B-Spline wavelet-based finite element vibration analysis of composite pipes with internal surface defects of different geometries; ***accepted*** (International Journal of Structural Stability and Dynamics).
- Oke, W. A., and Khulief, Y. A., Effect of internal surface damage on vibration behavior of a composite pipe conveying fluid ***(submitted)***.